UNIVERSITY OF SOUTHAMPTON

Time Domain Non Linear Strip Theory for Ship Motions

by
Yun Tao Fan
BEng, MSc.

A thesis submitted for the degree of
Doctor of Philosophy

Fluid Structure Interaction Research Group
School of Engineering Sciences
Faculty of Engineering, Science and Mathematics

December 2004

UNIVERSITY OF SOUTHAMPTON

ABSTRACT

THE FACULTY OF ENGINEERING, SCIENCE AND MATHEMATICS

SCHOOL OF ENGINEERING SCIENCES

Doctor of Philosophy

Time-Domain Non-Linear Strip Theory for Ship Motions

by Yun Tao Fan

A new time-domain strip theory is developed in this thesis. Compared with traditional strip theory, the main difference is that the calculation is carried out in the time domain. Exciting forces and hydrodynamic coefficients are computed on the instantaneous wetted ship hull surface at each time step, which makes this new method possible to cope with relatively large-amplitude motions and non-constant forward speed problems.

The basis of this new method lies in the strip theory of Salvesen, *et al* [56] and the early work of Westlake and Wilson [72]. The newly developed conformal mapping method enables the two-dimensional hydrodynamic coefficients of the sections with any type of shape to be computed accurately and efficiently. This new method is applied to calculate the hydrodynamic coefficients and motions of a Series 60 ($C_B = 0.7$) ship model in regular waves. By comparing the results with experimental data and numerical results provided by other contemporary analytical techniques, important improvements are found within a certain range of wave frequencies.

The numerical schemes are carefully verified and validated in a systematic manner to make sure that the correct results are obtained.

Contents

List of Figures iv

List of Tables xi

List of Symbols xii

Acknowledgements xx

1 Introduction 1

2 Literature Review 5

2.1 Two-Dimensional Theories 6

2.1.1 Thin-Ship Theory 6

2.1.2 Slender-Body Theory 7

2.1.3 Strip Theory 8

2.1.4 Unified Slender-Body Theory 8

2.2 Three-Dimensional Methods 9

2.2.1 Green Function Method 10

2.2.2 Rankine Panel Method 10

2.3 Time-Domain Methods 11

2.3.1 Time-Domain Green Function Method 12

2.3.2 Time-Domain Rankine Panel Method 13

3 Problem Formulation and Solution 14

3.1 Introduction 14
3.2 The Boundary-Value Problem 16
3.2.1 Definitions and Coordinate Systems 16
3.2.2 Governing Equations and Boundary Conditions 19
3.3 The Linearised Problem 22
3.3.1 Decomposition of Velocity Potential 23
3.3.2 Linearisation of Free-Surface Boundary Condition 24
3.3.3 Linearisation of Ship Body Surface Boundary Condition . . 27
3.4 Solution of Unsteady Potential 29
3.4.1 Linear Decomposition of the Unsteady Potential 29
3.4.2 Incident Wave Potential 30
3.4.3 Diffraction Wave Potential 31
3.4.4 Radiation Wave Potential 32
3.5 Two-Dimensional Problem and Conformal Mapping 37
3.6 Hydrodynamic and Hydrostatic Forces 47
3.6.1 Radiation Forces and Hydrodynamic Coefficients 48
3.6.2 Exciting Forces 54
3.6.3 Hydrostatic Restoring Forces 56
3.7 Ship Motion Equations & Time-Domain Method 59

4 Hydrodynamic Coefficients **62**
4.1 Introduction 62
4.2 Numerical Description of a Ship's Hull 63
4.3 Extraction of Wetted Hull 64
4.4 The Conformal Mapping 70
4.5 Two-Dimensional Hydrodynamic Coefficients 85
4.5.1 Effects of Mapping Coefficient Number 86
4.5.2 Effects of Heel Angle 90
4.6 Three-Dimensional Hydrodynamic Coefficients 110

4.6.1 Symmetric Hydrodynamic Coefficients 111
4.6.2 Anti-Symmetric Hydrodynamic Coefficients 112
4.6.3 Hydrodynamic Coefficients of a Heeled Series 60 (C_B = 0.70) Model 114

5 Motion Prediction in Regular Seaways **147**
5.1 Introduction 147
5.2 Froude-Kriloff Forces 148
5.3 Diffraction Forces 150
5.4 Newmark-β Direct Integration Method 154
5.5 Motion Prediction in Head Seas 163
5.5.1 Curve Fitting with Sinusoidal Function 165
5.5.2 Phasing of Displacement, Velocity and Acceleration 170
5.5.3 Comparisons with Experimental Data 172
5.5.4 Effect of the Incident Wave Amplitude 176
5.6 Motion Prediction in Oblique Seas 176

6 Concluding Remarks **187**
6.1 Summary of Investigation 187
6.2 Future Developments 190

A Intersection of Reference Plane and Ship Hull **192**

B Geometric Data of the Sections of a Rationalised Series 60 Hull Form **198**

Bibliography **200**

List of Figures

3.1 Boundary Value Problem. 17

3.2 Harmonic Wave Definitions. 17

3.3 Coordinate System. 18

3.4 The Coordinate Systems of Conformal Mapping. 39

3.5 Two-Dimensional Boundary Value Problem. 42

4.1 Original Series 60 Hull Form. 64

4.2 Rationalised Series 60 Hull Form. 65

4.3 Reference Planes in Equilibrium Coordinate System. 66

4.4 Intersections of Hull and Reference Planes ($\xi_5 = 0°, \xi_6 = 20°$). 69

4.5 Conformal Mapping of the Sections of Series 60 Hull Form (10 waterlines and 5 mapping coefficients). 73

4.6 Conformal Mapping of the Sections of Series 60 Hull Form (10 waterlines and 8 mapping coefficients). 74

4.7 Conformal Mapping of the Sections of Series 60 Hull Form (10 waterlines and 11 mapping coefficients). 75

4.8 Conformal Mapping of the Sections of Series 60 Hull Form (10 waterlines and 14 mapping coefficients). 76

4.9 Conformal Mapping of the Heeled Sections of Series 60 Hull Form (10 waterlines, 5 mapping coefficients and heeling angle 20°). . . . 77

4.10 Conformal Mapping of the Heeled Sections of Series 60 Hull Form (10 waterlines, 8 mapping coefficients and heeling angle 20°). . . . 78
4.11 Conformal Mapping of the Heeled Sections of Series 60 Hull Form (10 waterlines, 11 mapping coefficients and heeling angle 20°). . . . 79
4.12 Conformal Mapping of the Heeled Sections of Series 60 Hull Form (10 waterlines, 14 mapping coefficients and heeling angle 20°). . . . 80
4.13 Multi-Parameter Mapping with a Large Number of Coefficients. . . 81
4.14 Numerical Instability of the Multi-Parameter Conformal Mapping with a Large Number of Coefficients. 82
4.15 Comparison of Two Mapping Methods for the Symmetric Sections (14 coefficients used in multi-parameter mapping). 83
4.16 Comparison of Two Mapping Methods for the Asymmetric Sections (14 coefficients used in multi-parameter mapping). 84
4.17 Sway Hydrodynamic Coefficients of Section 10 of Series 60 Hull Form without Heel Angle. 92
4.18 Sway Hydrodynamic Coefficients of Section 18 of Series 60 Hull Form without Heel Angle. 93
4.19 Sway Hydrodynamic Coefficients of Section 20 of Series 60 Hull Form without Heel Angle. 94
4.20 Heave Hydrodynamic Coefficients of Section 10 of Series 60 Hull Form without Heel Angle. 95
4.21 Heave Hydrodynamic Coefficients of Section 18 of Series 60 Hull Form without Heel Angle. 96
4.22 Heave Hydrodynamic Coefficients of Section 20 of Series 60 Hull Form without Heel Angle. 97
4.23 Roll Hydrodynamic Coefficients of Section 10 of Series 60 Hull Form without Heel Angle. 98

4.24 Roll Hydrodynamic Coefficients of Section 18 of Series 60 Hull Form without Heel Angle. 99
4.25 Roll Hydrodynamic Coefficients of Section 20 of Series 60 Hull Form without Heel Angle. 100
4.26 Sway-Roll and Roll-Sway Coupling Hydrodynamic Coefficients of Section 10 of Series 60 Hull Form without Heel Angle. 101
4.27 Sway-Roll and Roll-Sway Hydrodynamic Coefficients of Section 18 of Series 60 Hull Form without Heel Angle. 102
4.28 Sway-Roll and Roll-Sway Hydrodynamic Coefficients of Section 20 of Series 60 Hull Form without Heel Angle. 103
4.29 Sway Hydrodynamic Coefficients of Section 20 of Series 60 Hull Form with Heel Angles 0°, 10° and 20°. 104
4.30 Heave Hydrodynamic Coefficients of Section 20 of Series 60 Hull Form with Heel Angles 0°, 10° and 20°. 105
4.31 Roll Hydrodynamic Coefficients of Section 20 of Series 60 Hull Form with Heel Angles 0°, 10° and 20°. 106
4.32 Sway-Roll and Roll-Sway Coupling Coefficients of Section 20 of Series 60 Hull Form with Heel Angles 0°, 10° and 20°. 107
4.33 Sway-Heave and Heave-Sway Coupling Coefficients of Section 20 of Series 60 Hull Form with Heel Angles 0°, 10° and 20°. 108
4.34 Heave-Roll and Roll-Heave Coupling Coefficients of Section 20 of Series 60 Hull Form with Heel Angles 0°, 10° and 20°. 109
4.35 Comparison of the Predicted and Measured Heave Hydrodynamic Coefficients of Series 60 Ship Model. 117
4.36 Comparison of the Predicted and Measured Pitch Hydrodynamic Coefficients of Series 60 Ship Model. 118
4.37 Comparison of the Predicted and Measured Heave-Pitch Coupling Hydrodynamic Coefficients of Series 60 Ship Model. 119

4.38 Comparison of the Predicted and Measured Pitch-Heave Coupling Hydrodynamic Coefficients of Series 60 Ship Model. 120
4.39 Comparison of the Predicted and Measured Sway Hydrodynamic Coefficients of Series 60 Ship Ship Model. 121
4.40 Comparison of the Predicted and Measured Yaw Hydrodynamic Coefficients of Series 60 Ship Model. 122
4.41 Comparison of the Predicted and Measured Sway-Yaw Coupling Hydrodynamic Coefficients of Series 60 Ship Model. 123
4.42 Comparison of the Predicted and Measured Yaw-Sway Coupling Hydrodynamic Coefficients of Series 60 Ship Model. 124
4.43 Comparison of the Predicted and Measured Roll Hydrodynamic Coefficients of Series 60 Ship Model. 125
4.44 Comparison of Heave Coefficients of Series 60 Ship Model at Heel Angles 0°, 10° and 20°. 126
4.45 Comparison of Pitch Coefficients of Series 60 Ship Model at Heel Angles 0°, 10° and 20°. 127
4.46 Comparison of Pitch-Heave Coupling Coefficients of Series 60 Ship Model at Heel Angles 0°, 10° and 20°. 128
4.47 Comparison of Heave-Pitch Coupling Coefficients of Series 60 Ship Model at Heel Angles 0°, 10° and 20°. 129
4.48 Comparison of Sway Coefficients of Series 60 Ship Model at Heel Angles 0°, 10° and 20°. 130
4.49 Comparison of Yaw Coefficients of Series 60 Ship Model at Heel Angles 0°, 10° and 20°. 131
4.50 Comparison of Sway-Yaw Coupling Coefficients of Series 60 Ship Model at Heel Angles 0°, 10° and 20°. 132
4.51 Comparison of Yaw-Sway Coupling Coefficients of Series 60 Ship Model at Heel Angles 0°, 10° and 20°. 133

4.52 Comparison of Roll Coefficients of Series 60 Ship Model at Heel Angles 0°, 10° and 20°. 134
4.53 Comparison of Sway-Roll/Roll-Away Coupling Coefficients of Series 60 Ship Model at Heel Angles 0°, 10° and 20°. 135
4.54 Comparison of Roll-Yaw Coupling Coefficients of Series 60 Ship Model at Heel Angles 0°, 10° and 20°. 136
4.55 Comparison of Yaw-Roll Coupling Coefficients of Series 60 Ship Model at Heel Angles 0°, 10° and 20°. 137
4.56 Comparison of Sway-Pitch/Pitch-Sway Coupling Coefficients of Series 60 Ship Model at Heel Angles 0°, 10° and 20°. 138
4.57 Comparison of Sway-Pitch Coupling Coefficients of Series 60 Ship Model at Heel Angles 0°, 10° and 20°. 139
4.58 Comparison of Heave-Roll/Roll-Heave Coupling Coefficients of Series 60 Ship Model at Heel Angles 0°, 10° and 20°. 140
4.59 Comparison of Heave-Yaw Coupling Coefficients of Series 60 Ship Model at Heel Angles 0°, 10° and 20°. 141
4.60 Comparison of Roll-Pitch Coupling Coefficients of Series 60 Ship Model at Heel Angles 0°, 10° and 20°. 142
4.61 Comparison of Pitch-Sway Coupling Coefficients of Series 60 Ship Model at Heel Angles 0°, 10° and 20°. 143
4.62 Pitch-Roll Coupling Coefficients of Series 60 Ship Model at Heel Angles 0°, 10° and 20°. 144
4.63 Comparison of Pitch-Yaw/Yaw-Pitch Coupling Coefficients of Series 60 Ship Model at Heel Angles 0°, 10° and 20°. 145
4.64 Comparison of Yaw-Heave Coupling Coefficients of Series 60 Ship Model at Heel Angles 0°, 10° and 20°. 146

5.1 Froude-Kriloff Forces of a Series 60 ($C_B = 0.7$) Model Travelling with Forward Speed $F_n = 0.2$. 151

5.2 Phases of Froude-Kriloff Forces of a Series 60 ($C_B = 0.7$) Model Travelling with Forward Speed $F_n = 0.2$. 152
5.3 Diffraction Forces of a Series 60 ($C_B = 0.7$) Model Travelling with Forward Speed $F_n = 0.2$. 155
5.4 Phases of Diffraction Forces of a Series 60 ($C_B = 0.7$) Model Travelling with Forward Speed $F_n = 0.2$. 156
5.5 Total Exciting Forces of a Series 60 ($C_B = 0.7$) Model Travelling with Forward Speed $F_n = 0.2$. 157
5.6 Phases of Total Exciting Forces of a Series 60 ($C_B = 0.7$) Model Travelling with Forward Speed $F_n = 0.2$. 158
5.7 Stability of Newmark Direct Integration Method. 161
5.8 Solutions of Unforced Motions. 164
5.9 Motion Histories of a Series 60 ($C_B = 0.7$) Model Travelling with Forward Speed $F_n = 0.2$ in Head Waves ($\omega_0 = 4.0\ rad/s$). 166
5.10 Displacement Histories and Corresponding Fitted Curves of a Series 60 ($C_B = 0.7$) Model Travelling with Forward Speed $F_n = 0.2$ in Head Waves ($\omega_0 = 4.0\ rad/s$). 169
5.11 Phasing of the Predicted Motions of a Series 60 ($C_B = 0.7$) Model Travelling with Forward Speed $F_n = 0.2$ in Head Waves ($\omega_0 = 4.0\ rad/s$). 171
5.12 Comparison of the Motions of a Series 60 ($C_B = 0.7$) Model Travelling with Forward Speed $F_n = 0.2$ in Head Waves. 174
5.13 Comparison of the Motions of a Series 60 ($C_B = 0.7$) Model Travelling with Forward Speed $F_n = 0.3$ in Head Waves. 175
5.14 Effect of Wave Amplitude on the Motions of a Series 60 ($C_B = 0.7$) Model Travelling with Forward Speed $F_n = 0.2$ in Head Waves. . . 177
5.15 Effect of Wave Amplitude on the Motions of a Series 60 ($C_B = 0.7$) Model Travelling with Forward Speed $F_n = 0.3$ in Head Waves. . . 178

5.16 Comparison of the Motions of a Series 60 ($C_B = 0.7$) Model Travelling with Forward Speed $F_n = 0.2$ in Oblique Waves ($\mu = 135°$). . . 179

5.17 Motion Histories of a Series 60 ($C_B = 0.7$) Model Travelling with Forward Speed $F_n = 0.2$ in Oblique Waves ($\mu = 135°, \omega_0 = 4.0\ rad/s$).181

5.17 Continued. 182

5.17 Continued. 183

5.18 Motion Histories of a Series 60 ($C_B = 0.7$) Model Travelling with Forward Speed $F_n = 0.2$ in Oblique Waves ($\mu = 90°, \omega_0 = 4.0\ rad/s$). 184

5.18 Continued. 185

5.18 Continued. 186

A.1 Intersections of Hull and Reference Planes ($\xi_5 = 0°, \xi_6 = 50°$) 193

A.2 Intersections of Hull and Reference Planes ($\xi_5 = 20°, \xi_6 = 0°$) 194

A.3 Intersections of Hull and Reference Planes ($\xi_5 = 50°, \xi_6 = 0°$) 195

A.4 Intersections of Hull and Reference Planes ($\xi_5 = 20°, \xi_6 = 20°$) 196

A.5 Intersections of Hull and Reference Planes ($\xi_5 = 50°, \xi_6 = 50°$) 197

List of Tables

4.1 Principal Particulars of the Series 60 Hull Form. 65

4.2 Lewis Mapping Data of Section 10, 18 and 20 of the Series 60 Hull Form. 72

4.3 Factors Used to Render the Sectional Hydrodynamic Coefficients Non-Dimensional. 85

4.4 Factors Used to Render the Hydrodynamic Coefficients of the Series 60 ($C_B = 0.70$) Model Non-Dimensional. 111

5.1 Values of the Coefficients of the Heave and Pitch Motion Equations. 162

5.2 Values of the Coefficients of the Fitted Curves of the Motion Histories of the Series 60 ($C_B = 0.7$) Model Travelling with Forward Speed $F_n = 0.2$ in Head Waves ($\omega_0 = 4.0\ rad/s$). 170

5.3 Phase Angles of the Motions of the Series 60 ($C_B = 0.7$) Model Travelling with Forward Speed $F_n = 0.2$ in Head Waves ($\omega_0 = 4.0\ rad/s$). 170

B.1 The Series 60 Hull Form Sectional Geometric Data 199

List of Symbols

a,$a_{(2k)}$,$a_{(2k+1)}$	Real part of the complex coefficients of conformal mapping
b,$b_{(2k)}$,$b_{(2k+1)}$	Imaginary part of the complex coefficients of conformal mapping
c,$c_{(2k)}$,$c_{(2k+1)}$	Complex coefficients of conformal mapping
$\vec{e}_i$	Cartesian basis vectors, $i = 1, 2, 3$
e_{ijk}	*Levi-Civita* symbol (*e-Permutation* symbol)
g	Acceleration due to gravity
$\bar{h}$	Water depth with respected to the coordinate system $\bar{o}(\bar{x}_1, \bar{x}_2, \bar{x}_3)$
h_G	Mean height of the centre of gravity of ship above still water surface
$\imath$	Imaginary unit
$\underline{\ell}$	Arc length
m	Ship mass
$\bar{n}_i$	Unit normal vector pointing out of the fluid domain in the coordinate system $\bar{o}(\bar{x}_1, \bar{x}_2, \bar{x}_3)$, $i = 1, 2, 3$
n_i	Unit normal vector pointing out of the fluid domain in the coordinate system $o(x_1, x_2, x_3)$, $i = 1, 2, 3$
$\underline{n}_i$	Two-dimensional unit normal vector in x_2, x_3-plane

$\widetilde{n}_i$	Generalised unit normal vector, $i = 1, 2, \ldots, 6$
$\widetilde{\underline{n}}_i$	Generalised two-dimensional unit normal vector in x_2, x_3-plane, $i = 1, 2, 3, 4$
$\bar{o}(\bar{x}_1, \bar{x}_2, \bar{x}_3)$	Coordinate system fixed in space
$o'(x'_1, x'_2, x'_3)$	Coordinate system fixed to the ship
$o(x_1, x_2, x_3)$	Coordinate system moving in steady translation with the mean forward velocity of ship
$\bar{p}$	Fluid pressure in the coordinate system $\bar{o}(\bar{x}_1, \bar{x}_2, \bar{x}_3)$
p	Fluid pressure in the coordinate system $o(x_1, x_2, x_3)$
p_a	Atmospheric pressure
r	Complex modulus
t	Time
$\bar{v}_i$	Velocity of the ship's wetted surface with respect to the coordinate system $\bar{o}(\bar{x}_1, \bar{x}_2, \bar{x}_3)$, $i = 1, 2, 3$
v_i	Velocity of the ship's wetted surface with respect to the coordinate system $o(x_1, x_2, x_3)$, $i = 1, 2, 3$
w_i	Velocity of the steady state flow with respect to the coordinate system $o(x_1, x_2, x_3)$, $i = 1, 2, 3$
$\bar{x}_i$	Position vector in the coordinate system $\bar{o}(\bar{x}_1, \bar{x}_2, \bar{x}_3)$, $i = 1, 2, 3$
x'_i	Position vector in the coordinate system $o'(x'_1, x'_2, x'_3)$, $i = 1, 2, 3$
x_i	Position vector in the coordinate system $o(\bar{x}_1, \bar{x}_2, \bar{x}_3)$, $i = 1, 2, 3$
A_{ji}	Three-dimensional added-mass coefficient in jth direction due to unit motion in ith mode

$\underline{A}_{ji}$	Two-dimensional added-mass coefficient in jth direction due to unit motion in ith mode
$\underline{A}^a_{ji}$	Two-dimensional added-mass coefficient of the aftermost section
B	Ship beam
B_{ji}	Three-dimensional hydrodynamic damping coefficient in jth direction due to unit motion in ith mode
$\underline{B}_{ji}$	Two-dimensional hydrodynamic damping coefficient in jth direction due to unit motion in ith mode
$\underline{B}^a_{ji}$	Two-dimensional hydrodynamic damping coefficient of the aftermost section
C_B	Block coefficient
C_{ji}	Element of hydrostatic restoring matrix
F_j	Total force or moment acting on ship hull in jth mode of motion
F_j^D	Force or moment acting on ship hull due to diffraction wave in jth mode of motion
F_j^I	Force or moment acting on ship hull due to incident wave in jth mode of motion
F_j^R	Force or moment acting on ship hull due to radiation waves in jth mode of motion
F_j^S	Buoyancy restoring force or moment in jth mode of motion
F_n	Froude number
$\boldsymbol{F}_j^D$	Complex amplitude of F_j^D
$\boldsymbol{F}_j^I$	Complex amplitude of F_j^I

$\underline{F}_j^D$	Two-dimensional force or moment acting on a cross section due to diffraction wave in jth mode of ship motion
$\underline{F}_j^R$	Two-dimensional force or moment acting on a cross section due to radiation waves in jth mode of ship motion
$\underline{F}_j^{Da}$	Two-dimensional force or moment acting on the aftermost section due to diffraction waves in jth mode of ship motion
$\underline{F}_j^I$	Two-dimensional force or moment acting on a cross section due to incident wave in jth mode of ship motion
GM_T	Metacentric height
I_{ij}	Element of the moment of inertia matrix of ship
K_0	Wave number of incident wave
K_e	Wave number of encounter wave
LCB	Longitudinal centre of buoyancy
LCG	Longitudinal centre of gravity
L_{ship}	Ship length
M_{ji}	Element of the generalised mass matrix
N_{an}	Number of the complex arguments used to determine the coefficients of multipole expansion
N_{cm}	Number of conformal mapping coefficients
N_{mp}	Number of multipole potentials
N_{pt}	Number of ship section definition points used in conformal mapping
$\vec{N}'$	Unit normal vector of the reference plane in the coordinate system

	$o'(x_1', x_2', x_3')$
P_i	Intersection point of x_1'-axis and ith ship cross section
$\underset{\sim}{P}_{i(2j)}$,$\underset{\sim}{P}_{i(2j+1)}$	Coefficients of multipole potentials
$\underset{\sim}{P}_{i0}$	Coefficient of source potential
$\underset{\sim}{P}_{i1}$	Coefficient of dipole potential
$S^{W'}$	Waterplane area in the coordinate system $o'(x_1, x_2', x_3')$
$S_i^{W'}$,$S_{ij}^{W'}$	Waterplane moments in the coordinate system $o'(x_1, x_2', x_3')$
$\bar{S}_b$	Wetted hull surface in the coordinate system $\bar{o}(\bar{x}_1, \bar{x}_2, \bar{x}_3)$
S_b	Wetted hull surface in the coordinate system $o(x_1, x_2, x_3)$
$\bar{S}_f$	Free surface outside the ship body waterplane in the coordinate system $\bar{o}(\bar{x}_1, \bar{x}_2, \bar{x}_3)$
S_f	Free surface outside the ship body waterplane in the coordinate system $o(x_1, x_2, x_3)$
$\bar{S}_h$	Sea bed surface in the coordinate system $\bar{o}(\bar{x}_1, \bar{x}_2, \bar{x}_3)$
$\bar{S}_\infty$	Enclosing contour at infinity in the coordinate system $\bar{o}(\bar{x}_1, \bar{x}_2, \bar{x}_3)$
S_{bs}	Steady state hull surface
S_{fs}	Steady state free surface
$\underset{\sim}{S}_{bs}$	Two-dimensional contour of the underwater part of ship cross section in x_2, x_3-plane
$\underset{\sim}{S}_{bsa}$	Two-dimensional contour of the underwater part of the aftermost ship cross section in x_2, x_3-plane
$\underset{\sim}{S}_f$	Two-dimensional free-surface contour in x_2, x_3-plane
$\underset{\sim}{S}_h$	Two-dimensional sea bed contour in x_2, x_3-plane

S_∞	Two-dimensional enclosing contour at the infinity in x_2, x_3-plane
T	Ship draught
U	Steady forward speed of ship
VCG	Vertical centre of gravity
V_{bs}	Volume enclosed by hull surface S_{bs} and waterplane surface
V_{dsp}	Displacement of ship
V_{ship}	Ship volume
$X_i^{B'}$	Centre of buoyancy of ship in the coordinate system $o'(x_1, x_2', x_3')$, $i = 1, 2, 3$
$X_i^{G'}$	Centre of gravity of ship in the coordinate system $o'(x_1, x_2', x_3')$, $i = 1, 2, 3$
X_i^G	Centre of gravity of ship in the coordinate system $o(x_1, x_2, x_3)$, $i = 1, 2, 3$
X_1^a	Position of the aftermost section on x_1-axis
$\vec{X}^{P_i'}$	Position of the ith intersection point P_i in the coordinate system $o'(x_1', x_2', x_3')$
$\vec{X}^{P_i}$	Position of the ith intersection point P_i in the coordinate system $o(x_1, x_2, x_3)$
β, ϵ	Parameters of Newmark-β direct integration method
δ_{ij}	Kronecker delta
$\bar{\phi}$	General velocity potential in the coordinate system $\bar{o}(\bar{x}_1, \bar{x}_2, \bar{x}_3)$
ϕ	General velocity potential in the coordinate system $o(x_1, x_2, x_3)$
ϕ^S	Velocity potential associated with steady motion

ϕ^T	Velocity potential associated with unsteady motion
ϕ_0	Incident wave velocity potential
ϕ_7	Velocity potential associated with the diffraction wave
ϕ_i	Velocity potential associated with the radiation wave due to the ith mode of ship motion
$\underset{\sim}{\varphi}_{(2j)}$, $\underset{\sim}{\varphi}_{(2j+1)}$	Multipole potentials
$\underset{\sim}{\varphi}_0$	Source potential
$\underset{\sim}{\varphi}_1$	Dipole potential
γ	Euler's constant
$\bar{\eta}$	Free-surface elevation in the coordinate system $\bar{o}(\bar{x}_1, \bar{x}_2, \bar{x}_3)$
η	Free-surface elevation in the coordinate system $o(x_1, x_2, x_3)$
η_0	Incident wave amplitude
η_s	Steady state free-surface elevation
λ	Wave length
μ	Heading angle of incident wave
ϑ	Complex argument or phase
ϱ	Fluid mass-density
ϱ_{ship}	Ship mass-density
ω_0	Frequency of incident wave
ω_e	Frequency of encounter
ξ_i^R	Displacement vector of rotational motion, $i = 1, 2, 3$
ξ_i^T	Displacement vector of translational motion, $i = 1, 2, 3$

ξ_i	Displacement of ship motion in ith mode
$\underset{\sim}{\psi}_{(2j)}$	Conjugate stream function of velocity potential $\underset{\sim}{\varphi}_{(2j)}$
$\underset{\sim}{\psi}_{(2j+1)}$	Conjugate stream function of velocity potential $\underset{\sim}{\varphi}_{(2j+1)}$
$\underset{\sim}{\psi}_0$	Conjugate stream function of velocity potential $\underset{\sim}{\varphi}_0$
$\underset{\sim}{\psi}_1$	Conjugate stream functions of velocity potential $\underset{\sim}{\varphi}_1$
Φ_0	Complex amplitude of incident wave potential ϕ_0
Φ_7	Complex amplitude of diffraction wave potential ϕ_7
Φ_i	Complex amplitude of radiation wave potential ϕ_i
Φ_i^U	Speed-dependent part of radiation potential Φ_i
Φ_i^0	Speed-independent part of radiation potential Φ_i
$\underline{\Phi}_i$	Speed-independent part of radiation potential Φ_i, $\underline{\Phi}_i \equiv \Phi_i^0$
$\underset{\sim}{\underline{\Phi}}_i$	Mapped velocity potential corresponding to velocity potential $\underline{\Phi}_i$
$\underline{\Omega}$	Two-dimensional fluid domain bounded by $\underline{S}_f$, $\underline{S}_{bs}$, $\underline{S}_h$ and $\underline{S}_\infty$
Ω	Fluid domain bounded by surfaces $\bar{S}_f$, $\bar{S}_b$, $\bar{S}_h$ and $\bar{S}_\infty$
Ξ_i	Complex amplitude of the displacement of ship motion ξ_i
$\underset{\sim}{\Psi}_i$	Conjugate stream function of velocity potential $\underset{\sim}{\Phi}_i$
Ψ_i^0	Conjugate stream function of velocity potential Φ_i^0

Acknowledgements

I wish to express my gratitude to all the people who have helped, supported and encouraged me throughout my study. Without them it could not be possible for me to come this far.

I am very grateful to my supervisor Professor P. A. Wilson for his keen insight, clear guidance and warm encouragement. Particularly, I want to thank him for his enduring my many times of delay of delivering this thesis.

I also would like to thank Dr. Du, Dr. Tan and Prof. Zheng. Without their help and suggestion, it would be much difficult for me to start the seakeeping study. I very appreciate that Dr. Hudson provided me with his programs and experimental data.

Finally, I am deeply indebted to my parents and sister for their unconditional love throughout so many years. My special thanks and appreciation go to my wife Na for her love, understanding and support in the most difficult time of my study.

Chapter 1

Introduction

Ships are built for the purpose of carrying people, material, and/or weapons upon the sea. In order to accomplish this mission, a ship must possess several basic characteristics. It must float in a stable upright position, move with sufficient speed, be able to manoeuvre at sea and in restricted waters, and be strong enough to withstand the rigours of heavy weather and wave impact. By a simple knowledge of hydrostatics, ship is easily to be ensured floating upright in clam water. However ships rarely sail in calm water, therefore prediction of ship dynamical characteristics in a realistic seaway becomes necessary during ship design. Wave loadings, induced by realistic ocean waves, are the main exciting source of ship dynamical motions. The research of interaction between ship and waves is named *seakeeping*.

For more than a hundred years, many seakeeping theories and methods have been established. The major difficulties in seakeeping computations are the non-linearities, which exist in almost every phase.

i. There are non-linearities associated with the fluid in the form of viscosity. In most hydrodynamic studies, viscosity is negligible compared to the inertia and gravity of the fluid. However, viscosity has an important effect on the

roll motion, especially at resonance in the beam seas.

ii. Bernoulli's equation used to compute the hydrodynamic pressure contains velocity squared terms.

iii. The free-surface boundary condition is strongly non-linear containing a combination of non-linear terms of unknown quantities and applied on an unknown surface, which itself is a part of the solution.

iv. The non-linearity exists in solving incident wave potential due to the non-linear free-surface boundary condition.

v. The body boundary condition imposed upon an unknown body surface introduces important non-linear effects, such as the interaction between the steady and unsteady wave flows.

vi. The body geometry often causes non-linear hydrostatic restoring forces.

Fully non-linear seakeeping problem is beyond the computational state-of-the-art at the present time. Consequently, approximations must be made in order to have a tractable mathematical problem. Viscosity and the velocity squared terms in Bernoulli's equation are the first non-linear factors to be neglected. *Neumann-Kelvin* and *Dawson* approaches are two most commonly used methods of linearising free-surface boundary condition. The body boundary condition and hydrostatic restoring forces can be linearised by being expanded about the calm water surface using Taylor's series. Moreover, because of the forward speed ships always tend to be long and slender with smooth variations along their length. This geometric feature of typical ships is the basis of many other further approximations that have allowed various seakeeping theories to be developed.

Recently a so-called *body-exact* approach to treat the body boundary condition has emerged, in which the exact body boundary condition is applied on the instantaneous wetted surface of the body. The body boundary condition is

linear when it is applied on the instantaneous wetted surface. This results in a time varying linear system rather then a time invariant system. Except for some very simple cases, the body-exact problem must be solved in the time domain. In most of the reported works a three-dimensional method, either time-domain Green function method or time-domain Rankine plane method is adopted. The objective of this thesis is to extend the traditional frequency-domain strip theory into the time domain, so that the body-exact approach can be used. The hydrodynamic coefficients and forces are able to be computed over an exact wetted body surface.

The three-dimensional methods have been proved to give, in general, better agreement with experimental data. However, strip theory is still the most popular theory. Beck and Reed [3] estimated that probably 80 percent of all the current calculations related to ships with forward speed are still made by using strip theory. This is because strip theory has distinctive benefits compared with three-dimensional methods. Firstly, it is reliable and requires much less numerical calculation than the three-dimensional methods, whilst its accuracy is quite reasonable for engineering applications. Secondly, strip theory just requires the offset data on ship sections, while the three-dimensional methods need the three-dimensional ship surface data. This makes strip theory more feasible for the analysis of the seakeeping performance in the initial ship design stage. In the last decade, strip theory seems to be neglected, all the efforts have been focused on the development of time-domain three-dimensional methods, yet few works on refining strip theory can be found.

Generally the steady-state time-harmonic ship motions (surge ξ_1, sway ξ_2, heave ξ_3, roll ξ_4, pitch ξ_5, yaw ξ_6) can be described by a set of second order equations

$$\sum_{i=1}^{6}(M_{ji}+A_{ji})\ddot{\xi}_i+\sum_{i=1}^{6}B_{ji}\dot{\xi}_i+\sum_{i=1}^{6}C_{ji}\xi_i=F_j \qquad j=1,2,\ldots,6,$$

where M_{ji} is the generalised mass matrix, A_{ji} and B_{ji} are the added-mass and damping coefficient matrix, C_{ji} is the hydrostatic coefficient matrix and F_j is exciting force and moment vector. In the derivation of these equations using strip theory [56], it is assumed that motions are small. Not only is the free-surface boundary condition linearised about the undisturbed water surface, but is the body boundary condition expanded about the mean position. For large-amplitude motions in the severe seas, the influence of the varying underwater part of the hull will be significant, so this linearisation of body boundary condition may not be justified. This weakness may be rectified by applying a body-exact approach. At each time step, the exact submerged part of each section is extracted, hydrodynamic coefficients and forces are then calculated based on this instantaneous body boundary. A fully time-domain method is *NOT* adopted, because it requires the evaluation of convolution integrals over all previous time steps. This may cause strip theory to lose its numerical simplicity over other methods. Instead, a coupled time and frequency domain method is presented in this thesis from the engineering practice point of view. With the restriction of time-harmonic exciting forces, the equations of ship motions are assumed still to keep as simple form as the above equations at each time instant, but the coefficients M_{ji}, A_{ji}, B_{ji}, C_{ji} and the forces F_j are varying.

Chapter 2

Literature Review

The research of ship motions and wave loadings was started by William Froude [17] in 1861, studying the rolling motion of the first steam ship. Several decades later, Kriloff [33] studied the pitch and heave motions of ships. Froude and Kriloff derived differential equations of ship motion which consisted of only mass, linearised restoring forces, and wave-induce force exerted on the ship. The wave-induced force was evaluated from the pressure field of the undisturbed incident waves, the hydrodynamic disturbance associated with the presence of the ship hull was neglected. This force is now named *Froude-Kriloff Force*. Modern computations began with two development in the 1950's. The first was the use of random process theory to determine the statistics of the ship responses in a seaway. The second was the development of linear ship motion theories to predict the response of the ship to regular waves. Detailed histories of the development can be found in many sources including Newman [45], Ogilvie [51] and Beck [3].

St. Denis and Pierson [60] proposed a method to predict the statistics of ship responses to a realistic seaway. Two critical assumptions were made:

i. the ship can be represented by a linear system, and

ii. the sea surface is a Gaussian random process with zero mean.

The linear system assumption allows the superposition principle to be used. The response of ship to the irregular waves could be considered as the summation of the response to regular waves of all frequencies. This simplifies the prediction of ship motions in realistic seaways into two relatively easy problems: the prediction of the ship motions and loads in regular sinusoidal waves and the prediction of the statistical response in irregular waves using the regular wave results. The second assumption enables the probability density function of the ship response to be completely characterized by the variance, which is simply the area under the spectral density of the response. Once the probability density function for a given response is known, all the desired statistics of the response can easily be determined. The spectral density of any given response can be found by multiplying the incident wave spectrum by the square of the response amplitude operator of the desired response. St. Denis and Pierson's research indicates that seakeeping research could be focused on analysing solutions in regular waves only.

In the early period, analytic techniques for predicting ship motions in regular waves were linear and two-dimensional. Lately, with the arrival of faster and larger computers, non-linear and three-dimensional techniques have been developed.

2.1 Two-Dimensional Theories

2.1.1 Thin-Ship Theory

Thin-Ship Theory was probably the first analytic technique developed in 1950's. It originated from the thin-ship approximation of Michell [38] in his steady-state wave-resistance theory. Ships were assumed to have vanishingly small beam compared to length, draught, and ambient wave length ($B \leq L_{ship}, T, \lambda$). Michell

realised the possibility of extending his theory to ship motions, but a promised paper was never published. It was Peters and Stoker [54] who extended this theory to include unsteady motions to find non-resonant behaviour of ship responses. A systematic perturbation procedure was adopted with the ship's beam and the unsteady motions assumed to be of the same small order of magnitude. The first-order theory was rather trivial in that the Froude-Kriloff exciting force was the only hydrodynamic force. Unbounded resonance existed in heave, pitch, and roll because of the lack of hydrodynamic damping. Newman [42] refined Peters and Stoker's thin-ship theory by introducing a more accurate statement of the boundary condition on the oscillatory ship hull and using a systematic expansion in multiple small parameters. Although the unphysical motion responses predicted by Peters and Stoker were reconciled, the computed results from Newman's theory did not compare well with experiments.

2.1.2 Slender-Body Theory

Typical ship hulls are usually elongated with beam and draught of the same order of magnitude and of smaller order then ship length ($B, T \leq L_{ship}$), which are closer to slender bodies than thin ships. *Slender-Body Theory* was established in the aerodynamic studies of the flow around airships in the 1920's. In the 1950's it was applied to ships by Joosen [27], Newman [43], Newman and Tuck [48]. The wavelength of the incident wave or the waves radiated from the body is of the same order or greater than the ship's length. Unfortunately, as in the thin-ship theory, most non-trivial hydrodynamics effects are of higher order compared to the hydrodynamic restoring force and the Froude-Kriloff exciting force. Moreover, the leading-order equations of motions are non-resonant because the inertial force due to the body mass is of high order.

2.1.3 Strip Theory

At the same time that the slender-body theories were being studied, an alternative *Strip-Theory* was also being investigated. Using a combination of slender-body theory and good physical insight, Korvin-Kroukovsky [31] and Korvin-Kroukovsky and Jacobs [32] developed a strip-theory for predicting heave and pitch motions in heave waves, which was the first ship motion theory suitable for numerical computations and had adequate accuracy for engineering applications. Unfortunately inconsistent mathematics was found in this theory later, in particular it did not satisfy the Timman-Newman relationships [63]. Modified versions of strip theory have since been proposed, of which, that developed by Salvesen, Tuck and Faltinsen [56] is mostly widely used in ship design. It provides satisfactory performance in the prediction of the motions of conventional ships as well as computational simplicity.

A mathematically consistent strip theory was developed by Ogilvie and Tuck [52] (or see Ogilvie [51]) using slender-body theory. Unfortunately, in their theory some integral terms over the free-surface are very difficult to compute.

2.1.4 Unified Slender-Body Theory

Strip theory is a short wavelength theory, whilst slender-body theory is a long wavelength theory. In order to bridge the gap between these two theories, Newman [45] developed a unified slender-body theory which accounted for three dimensionality in a more consistent manner than pure strip theory and slender-body theory. The ship beam B and draft T are restricted to be small compared to the length L_{ship} by factors of order $\varepsilon \ll 1$, *i.e.* $L_{ship} = \mathcal{O}(1)$, $B = \mathcal{O}(\varepsilon)$ and $T = \mathcal{O}(\varepsilon)$. The fluid domain is divided into an inner region where $(x_2, x_3) = \mathcal{O}(\varepsilon)$

and an outer region where $(x_2, x_3) = \mathcal{O}(1)^*$. In the inner region the velocity potential is governed by the two-dimensional Laplace's equation and two-dimensional linearised speed-independent free-surface boundary condition, which are similar to the strip theory. In the outer region three-dimensional Laplace's equation governs the solution, subject to linearised speed-dependent free-surface boundary condition and the radiation condition of outgoing waves at infinity. Since both solutions in the inner region and in the outer region are not unique, they are matched in a suitable overlap region $\varepsilon \ll (x_2, x_3) \ll 1$ to solve the uniqueness.

Unified slender-body theory was successfully applied to seakeeping of ships by Newman and Sclavounos [47]. Comparisons with experimental results have indicated improved predictions relative to strip theory predictions. Sclavounos [57] later extended it to the diffraction problem. This theory was further refined recently by Kashiwagi, *et al* [29]. His work shows that for a VLCC the unified slender-body theory and strip theory give essentially equivalent predictions for heave and pitch motions at various heading angles.

2.2 Three-Dimensional Methods

Since early 80's, due to the revolutionary advent of powerful computers, seakeeping research on a complete three-dimensional numerical solution has blossomed. Unlike the two-dimensional theories (strip theory, slender-body theory, *etc.*), the three-dimensional methods can give detailed hydrodynamic pressure distributions over the hull surface, and can be applied to large structures which are no longer 'slender' in all dimensions. No restriction on the wavelength is in principle imposed by a three-dimensional method.

*The coordinate systems are defined in §3.2.1

2.2.1 Green Function Method

Green Function Method was first used to solve Neumann-Kelvin problem, where the body boundary condition is applied on the mean position of the exact body surface and the linearised free-surface boundary condition is used. By combining fundamental singularities with other analytic functions, it is possible to develop Green functions that satisfy all the boundary conditions of the problem except on the body surface. The solution of Neumann-Kelvin problem can then be formulated in terms of integrals of free-surface Green functions over the body surface. Wehausen and Laitone [70] established various Green functions for wave problems.

The difficulty of extending frequency-domain Green function to ships is due to the forward speed. The forward-speed free-surface Green function, involving single and double integrals of functions dependent on forward speed and frequency of encounter, is extremely difficult to compute in the frequency domain. Early efforts were contributed by Chang [9], and Inglis and Price [25, 26]. Later developments of this method are made by Wu and Eatock Taylor [73], and Chen, *et al* [10].

2.2.2 Rankine Panel Method

An alternative three-dimensional method is *Rankine Panel Method* which was initiated by Dawson [13]. Instead of linearising the free-surface boundary condition about the free-stream velocity, Dawson linearised the free-surface boundary condition about the so-called *double-body flow*. The free-surface boundary conditions are now a function of geometrically dependent double-body flow, thus a single free-surface Green function is no longer applicable. To solve this boundary value problem, Dawson distributed *Rankine sources* on both the body surface and calm

water surface. The Rankine source $G(\vec{x}, \vec{\varsigma})$ is define as

$$G(\vec{x}, \vec{\varsigma}) = \frac{1}{2\pi} \frac{1}{|\vec{x} - \vec{\varsigma}|},$$

where $\vec{x}$ is the field point and $\vec{\varsigma}$ is the source point.

Sclavounos and Nakos [59] and Nakos and Sclavounos [39] studied the numerical properties of the Rankine panel method used to simulate steady and unsteady free surface flows and developed rational stability criteria guiding the selection of the panel aspect ratio as a function of the ship speed and the wave frequency. The implementation of these numerical algorithms to the seakeeping problem of realistic ships was carried out by Nakos and Sclavounos [39, 40].

Rankine panel method allows a more general free-surface condition to be used. It also removes the complexity of computing the free-surface Green function and the irregular frequency problem in the Green function method. The drawback is that it requires many more panels than the Green function method and its stability is a question.

2.3 Time-Domain Methods

In all the theories or methods discussed in previous sections, the problem is formulated in the frequency domain leading to equations that have meaning only if the body motions are strictly sinusoidal in time. An alternative to the frequency-domain approach is to formulate the problem in the time domain, which are applicable to unsteady transient problems. Cummins [12] and Ogilvie [50] first discussed the use of time-domain analysis to solve unsteady body motion problems in the presence of a free surface. For fully linear problems at constant or zero forward speed, the time-domain and frequency-domain solutions are related by

Fourier transforms.

2.3.1 Time-Domain Green Function Method

Based on the early work of Finkelstein [15], Wehausen [69] provided the rigorous theoretical basis for using a time-domain Green function to solve the unsteady ship motion problems at zero forward speed. Computations directly from this method for two-dimensional problems were presented by Yeung [74] and Newman [46]. Three-dimensional computations were then given by Beck and Liapis [4] for the zero speed radiation problem, and by King, *et al* [30] for the non-zero forward speed seakeeping problem. Bingham, *et al* [5] also made similar investigations and developed a technique for approximating the asymptotic of the solution, which was used to reduce the required length of the computation.

Working in one domain or the other might have advantages for a particular problem. At zero forward speed evaluation of time-domain Green function requires approximately the same amount of computational effort as zero-speed frequency domain Green function. However in the case that the body's forward speed is included, time-domain Green function method is found much more effective than frequency-domain Green function method. This is because that forward-speed frequency-domain Green function is very complicated and extremely difficult to calculate, whilst forward-speed time-domain Green function retains the same relatively simple form as zero-speed frequency-domain Green function regardless of the body's velocity.

Another important advantage of time-domain methods is that they could be extended to solve large-amplitude motions by applying the exact body boundary condition on the instantaneous wetted hull surface. If the free-surface boundary condition remains linearised, this body-exact approach is time variant linear. Example of body-exact time-domain Green function method was given by Lin and

Yue [36].

2.3.2 Time-Domain Rankine Panel Method

Like the frequency-domain Green function method, Rankine panel method can be extended to time domain as well. Nakos, *et al* [41] presented the design, implementation and application of a Rankine panel method for the solution of transient wave-body interactions in three dimensions. Since the free-surface computational domain in Rankine panel method is finite, given a sufficiently long computational time, the waves generated by the ship will propagate outwards and interact with the truncation of the free-surface computational domain. The effect of the free-surface truncation may be interpreted as reflection by a horizontal rigid lid laid over the free-surface, outside the computational domain. Therefore an artificial wave-absorbing beach was designed for avoiding wave reflection.

Pawlowski [53] proposed a *Weak-Scatter* hypothesis, in which only the ship-generated disturbances are assumed to be small and linearisable about the large amplitude of ship motions and incoming waves. By employing this hypothesis, Kring, *et al* [34], Sclavounos, *et al* [58], and Huang and Sclavounos [23] have developed a body-exact time-domain Rankine panel method, in which the linearisation of the ship generated wave disturbance are done around the ambient wave profile with a body-exact condition on the ship hull.

Chapter 3

Problem Formulation and Solution

3.1 Introduction

In seakeeping research, a ship is usually regarded as an unrestrained rigid body with six degrees of freedom. As long as the forces exerted on its surface by the water are determined, the ship's motions in sea waves may be able to predicted consequently by classic rigid body dynamics theory. To calculate these forces, the analytical representation for the fluid flow is inevitably needed. In principle, Navier-Stokes equation (conservation of momentum), continuity equation (conservation of mass) and energy equation (conservation of energy) suffice to describe the motion of all fluid flow subject only to the assumption of a Newtonian stress-strain relationship, which is justified for all practical purposes in the case of most fluids, including water and air. The difficulty comes in attempting to solve the Navier-Stokes equations. They form a coupled system of non-linear partial differential equations and have only been solved analytically for some very simple geometrical configurations, principally those in which the non-linear convective acceleration terms $u_{i,j}u_j$ can be assumed to vanish. However, we neither can nor want to solve Navier-Stokes equations in seakeeping research, at least at

present.

Therefore, the fluid flow around ships is usually considered to be potential; that is, incompressible, inviscid and irrotational. The governing equations of fluid flow can then be reduced to Laplace's equation and Bernoulli's equation. This assumption is reasonable since the effects of viscous damping on ship motions are small. One exception is the roll motion, where viscous damping has significant effects due to the periodical separation of the boundary layer from the hull. For accurate prediction of roll motion, viscous roll damping effect must be carefully considered. In practice, an empirical correction coefficient, which depends on the wave frequency, the viscosity, the bilge-keel dimension and the hull geometry, is introduced to scale up the roll damping [56]. Laplace's equation is linear, and may be solved if proper boundary conditions are imposed. Once it is solved, Bernoulli's equation is applied to find the pressure distribution over the ship's hull. The pressure is then integrated to yield the total hydrodynamic forces and moments acting on the ship's body.

Cartesian coordinates and index notation are used in this chapter. Vectors, matrices and tensors are denoted in terms of components relative to a set of Cartesian basis vectors $\{\vec{e}_1, \vec{e}_2, \vec{e}_3\}$, for example,

$$\vec{x} = \sum_{i=1}^{3} x_i \vec{e}_i.$$

Whenever a lower case Latin index does not appear repeated, *i.e.*, it is a *free index*, it is understood to take on values 1, 2 and 3, unless otherwise indicated. *E.g.*, the symbolism x_i stands for the collection x_1, x_2, x_3. Whenever a lower case Latin index appears repeated once in tensors or a product of vectors, *i.e.*, it appears exactly twice, then summation convention (Einstein convention) is implied over the repeated index. The range of summation is from 1 to 3, unless otherwise

indicated. Thus

$$\vec{x} = \sum_{i=1}^{3} x_i \vec{e}_i \equiv \vec{x} = x_i \vec{e}_i. \tag{3.1}$$

When no confusion arises, the vectors are expressed for brevity sake as number triples, *e.g.* $\vec{x} = \{x_1, x_2, x_3\}$, or simply x_i. A comma subscript denotes derivatives, for example,

$$\phi_{,i} = \frac{\partial \phi}{\partial x_i},$$
$$\phi_{,jk} = \frac{\partial^2 \phi}{\partial x_j x_k}.$$

3.2 The Boundary-Value Problem

3.2.1 Definitions and Coordinate Systems

For a real ship in a seaway, the fluid domain is effectively unbounded relative to the scale of the ship. Figure (3.1) depicts the geometry and coordinate system of this fluid domain used in the computation. Ω represents the fluid volume bounded above by the free surface $\bar{S}_f$ and body surface $\bar{S}_b$, below by the sea bed surface $\bar{S}_h$, and at the infinity by an enclosing contour $\bar{S}_\infty$. $\vec{\bar{n}} = \{\bar{n}_1, \bar{n}_2, \bar{n}_3\}$ is the unit normal vector of the boundary surface pointing out of the fluid domain. A right-handed coordinate system $\bar{o}(\bar{x}_1, \bar{x}_2, \bar{x}_3)$ is fixed in space. The $\bar{x}_1, \bar{x}_2$-plane lies in the still water surface. The still water surface is the average water surface level or surface of the water where no waves were present. $\bar{x}_1$-axis is directed as the ship mean forward speed. $\bar{x}_3$-axis points vertically down.

Figure (3.2) shows a snapshot of a harmonic sea wave defined in the coordinate system $\bar{o}(\bar{x}_1, \bar{x}_2, \bar{x}_3)$. The water depth $\bar{h}$ is measured between the sea bed and the still water level, η_0 is the amplitude of the harmonic wave. The horizontal distance (measured in the direction of wave propagation) between any two suc-

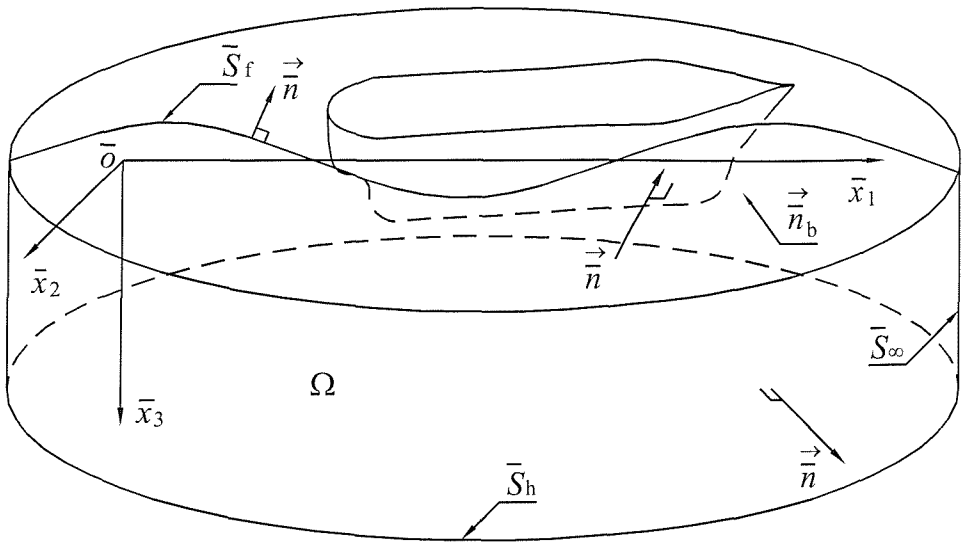

Figure 3.1: *Boundary Value Problem.*

cessive wave crests is the wave length λ. The ratio of wave height to wave length is often referred to as the dimensionless wave steepness $2\eta_0/\lambda$.

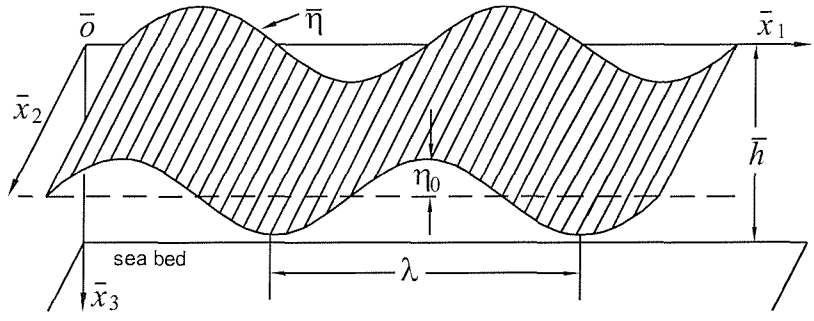

Figure 3.2: *Harmonic Wave Definitions.*

Suppose that a ship is travelling horizontally with constant forward speed U through this harmonic wave. Let $o(x_1, x_2, x_3)$ be a right-handed coordinate system moving in steady translation with the mean forward velocity of the ship, with x_1, x_2-plane lying parallel to the still water surface, x_1-axis pointing in the direction of ship forward speed and x_3-axis pointing vertically down as shown in Figure (3.3). The origin o remains at a fixed height h_G above the still water surface

and is sited at the time-averaged position of the centre of gravity of the ship. It is helpful to define a third coordinate system $o'(x_1', x_2', x_3')$, which is fixed to the ship and its origin o' is situated at the ship's centre of gravity. x_1'-axis is in the longitudinal forward direction, x_2' is in the lateral starboard side direction, and x_3' is vertically down. Thus, in the calm water, coordinate system $o'(x_1', x_2', x_3')$ is coincident with coordinate system $o(x_1, x_2, x_3)$. After a time Δt, $o(x_1, x_2, x_3)$ has moved a distance $U\Delta t$ from the $\bar{o}$ along the $\bar{x}_1$-axis.

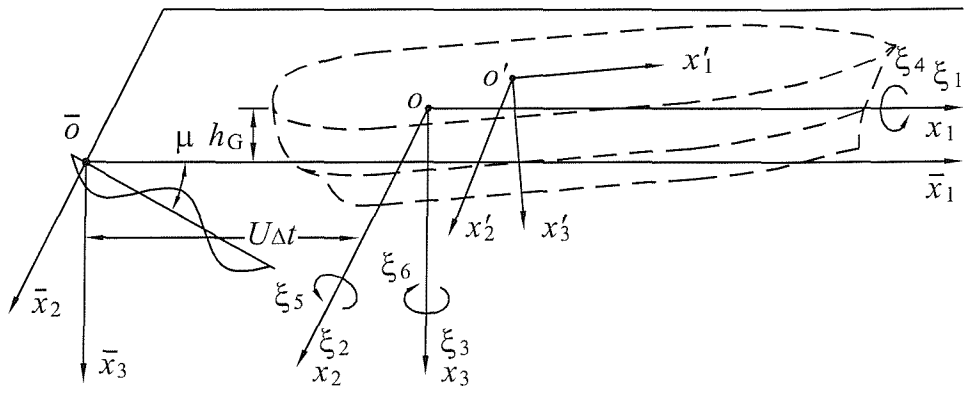

Figure 3.3: *Coordinate System.*

Within the coordinate system $\bar{o}(\bar{x}_1, \bar{x}_2, \bar{x}_3)$, the incident harmonic wave is defined to have a wavelength λ, an amplitude η_0, and a heading angle of μ relative to the $\bar{x}_1$-axis ($\mu = 0$ for following waves).

Due to the presence of sea waves, the ship carries out oscillations around the steady translating coordinate system $o(x_1, x_2, x_3)$, which may be described by the translational motions surge ξ_1, sway ξ_2 and heave ξ_3 along the x_1, x_2 and x_3 axes respectively, and rotational motions roll ξ_4, pitch ξ_5 and yaw ξ_6 about the same axes respectively.

If the oscillatory motion is small, coordinate system $\bar{o}(\bar{x}_1, \bar{x}_2, \bar{x}_3)$, $o(x_1, x_2, x_3)$

and $o'(x'_1, x'_2, x'_3)$ can be related by

$$\vec{\bar{x}} = \{U\Delta t, 0, -h_G\} + \vec{x}, \tag{3.2}$$

$$x_i = \xi_i^T + e_{ijk}\xi_j^R x'_k, \tag{3.3}$$

where $\vec{\bar{x}} = \{\bar{x}_1, \bar{x}_2, \bar{x}_3\}$, $\vec{x} = \{x_1, x_2, x_3\}$ and $\vec{x}' = \{x'_1, x'_2, x'_3\}$ are the position vectors in the coordinate system $\bar{o}(\bar{x}_1, \bar{x}_2, \bar{x}_3)$, $o(x_1, x_2, x_3)$ and $o'(x'_1, x'_2, x'_3)$ respectively. Vector $\vec{\xi}^T = \{\xi_1^T, \xi_2^T, \xi_3^T\} = \{\xi_1, \xi_2, \xi_3\}$ represents the linear translations, and vector $\vec{\xi}^R = \{\xi_1^R, \xi_2^R, \xi_3^R\} = \{\xi_4, \xi_5, \xi_6\}$ represents the rotational motions. e_{ijk} is *Levi-Civita* symbol or *e-Permutation* symbol, and has values

$$e_{ijk} = \begin{cases} 1 & \text{if } ijk \text{ is an even permutation of the integers 123.} \\ -1 & \text{if } ijk \text{ is an odd permutation of the integers 123.} \\ 0 & \text{in all other cases.} \end{cases} \tag{3.4}$$

3.2.2 Governing Equations and Boundary Conditions

Governing Equations

Assuming that the fluid is inviscid and incompressible, the fluid flow motion for an irrotational flow may be described using potential theory. By defining a scalar fluid velocity potential $\bar{\phi} = \bar{\phi}(x_i, t)$, $i = 1, 2, 3$ the continuity equation reduces to Laplace's equation and the momentum equations reduce to Bernoulli's equation. Therefore, the governing equations are

$$\bar{\phi}_{,ii} = 0 \qquad \bar{x}_i \in \Omega, \tag{3.5}$$

$$\frac{\partial \bar{\phi}}{\partial t} + \frac{1}{2}\bar{\phi}_{,i}\bar{\phi}_{,i} + \frac{1}{\varrho}(\bar{p} - p_a) - g\bar{x}_3 = 0 \qquad \bar{x}_i \in \Omega, \tag{3.6}$$

where p_a is the atmospheric pressure, which is assumed constant and hereafter is omitted. With this formulation, the potential $\bar{\phi}$ and pressure $\bar{p}$ are uncoupled. Typically a solution for $\bar{\phi}$ is found by satisfying Equation (3.5) along with appropriate boundary conditions. Then $\bar{p}$ is easily computed using Equation (3.6).

Boundary Conditions

As defined in §3.2.1, the boundary of the fluid domain consists of four surfaces: $\bar{S}_b$, $\bar{S}_f$, $\bar{S}_h$ and $\bar{S}_\infty$. In the seakeeping research, sea bottom $\bar{S}_h$ is usually assumed be to a horizontal flat plane and the depth of the water is usually considered as infinity, that is $\bar{x}_3 = \infty$.

On solid boundary surfaces such as the ship hull $\bar{S}_b$ and sea bottom $\bar{S}_h$, a kinematic condition requiring no flow normal to the boundary is imposed. Since the flow is assumed inviscid, there is no condition on flow tangential to the boundary. The boundary condition for the ship hull surface is

$$\frac{\partial \bar{\phi}}{\partial \bar{n}} = \bar{\phi}_{,i}\bar{n}_i = \bar{v}_i\bar{n}_i \qquad \bar{x}_i \in \bar{S}_b, \tag{3.7}$$

where $\bar{v}_i$, $i = 1, 2, 3$ is the velocity of the ship's wetted surface. On the sea bottom surface the boundary condition is,

$$\frac{\partial \bar{\phi}}{\partial \bar{n}} = \bar{\phi}_{,3} = 0 \qquad \bar{x}_i \in \bar{x}_3 = \infty, \tag{3.8}$$

Suppose the free surface $\bar{S}_f$ is defined by its elevation $\bar{x}_3 = \bar{\eta}(\bar{x}_1, \bar{x}_2, t)$. On this surface, the kinematic boundary condition requires that a point on the surface remains on the surface, that is

$$\frac{D}{Dt}(\bar{x}_3 - \bar{\eta}) = \frac{\partial \bar{\eta}}{\partial t} + \frac{\partial \bar{\phi}}{\partial \bar{x}_1}\frac{\partial \bar{\eta}}{\partial \bar{x}_1} + \frac{\partial \bar{\phi}}{\partial \bar{x}_2}\frac{\partial \bar{\eta}}{\partial \bar{x}_2} - \frac{\partial \bar{\phi}}{\partial \bar{x}_3} = 0 \qquad \bar{x}_i \in \bar{S}_f. \tag{3.9}$$

Since the position of the free surface in unknown, an additional dynamics boundary condition is necessary, that the pressure on the free surface is equal to the atmospheric pressure p_a (which may be assumed to be zero). From Bernoulli's equation (3.6) it follows that

$$\frac{\partial \bar{\phi}}{\partial t} + \frac{1}{2}\bar{\phi}_{,i}\bar{\phi}_{,i} + \frac{\bar{p}}{\varrho} - g\bar{x}_3 = 0 \qquad \bar{x}_i \in \bar{S}_f. \tag{3.10}$$

Equations (3.9) and (3.10) can be combined together to give an alternative boundary condition for the velocity potential on the free surface,

$$\frac{\partial^2 \bar{\phi}}{\partial t^2} + 2\bar{\phi}_{,i}\frac{\partial \bar{\phi}_{,i}}{\partial t} + \frac{1}{2}(\phi_{,i}\phi_{,i})_{,j}\phi_{,j} - g\bar{\phi}_{,3} = 0 \qquad \bar{x}_i \in \bar{S}_f. \tag{3.11}$$

Finally, a radiation condition is required at infinity (on surface $\bar{S}_\infty$) to guarantee an unique solution for this boundary value problem. This boundary condition may have various different mathematical forms depending on the nature of the velocity potential and the methods of solving this boundary value problem (time-domain or frequency-domain method). Hence it will be discussed later in §3.4.4.

Coordinate Transformation

It is usually more convenient to carry out the calculation in the steady-moving coordinate system $o(x_1, x_2, x_3)$. The velocity potential $\phi = \phi(x_i, t)$, $i = 1, 2, 3$ in this equilibrium coordinate system is redefined in the form

$$\phi(x_i, t) = \bar{\phi}(x_i + \delta_{1i}Ut - \delta_{3i}h_G, t) = \bar{\phi}(\bar{x}_i, t), \tag{3.12}$$

where δ_{ij} is Kronecker delta and defined as

$$\delta_{ij} = \begin{cases} 1 & \text{if } i = j. \\ 0 & \text{if } i \neq j. \end{cases} \tag{3.13}$$

Using Lorentz transformation, the governing equations (3.5) and (3.6) become

$$\phi_{,ii} = 0 \qquad x_i \in \Omega, \tag{3.14}$$

$$\frac{\partial \phi}{\partial t} - U\phi_{,1} + \frac{1}{2}\phi_{,i}\phi_{,i} + \frac{p}{\varrho} - g(x_3 - h_G) = 0 \qquad x_i \in \Omega, \tag{3.15}$$

with respect to the coordinate system $o(x_1, x_2, x_3)$. Similarly the boundary conditions (3.7), (3.8) and (3.11) can be written as

$$\phi_{,i}n_i = v_i n_i + U\delta_{1i}n_i \qquad x_i \in S_b, \tag{3.16}$$

$$\phi_{,3} = 0 \qquad x_i \in x_3 = \infty, \tag{3.17}$$

$$\frac{\partial^2 \phi}{\partial t^2} - 2U\frac{\partial \phi_{,1}}{\partial t} + 2\phi_{,i}\left(\frac{\partial \phi}{\partial t} - U\phi_{,1}\right)_{,i} + U^2\phi_{,11} + \frac{1}{2}(\phi_{,i}\phi_{,i})_{,j}\phi_{,j} - g\phi_{,3} = 0 \qquad x_i \in S_f, \tag{3.18}$$

where v_i, $i = 1, 2, 3$ is the oscillatory velocity of ship relative to the coordinate system $o(x, y, z)$, and n_i, $i = 1, 2, 3$ is the unit normal vector defined same as $\bar{n}_i$, $i = 1, 2, 3$ but related to the coordinate system $o(x, y, z)$. The free surface S_f is defined by its elevation $x_3 = \eta(x_1, x_2, t)$.

3.3 The Linearised Problem

The Laplace's equation (3.14) is linear, however, the boundary conditions (3.16) and (3.18) are non-linear. To solve such a system of partial differential equations

is rather difficult. In most of the cases, the boundary conditions (3.16) and (3.18) have to be linearised.

3.3.1 Decomposition of Velocity Potential

Three topics are of interest in ship hydrodynamics. The first topic is the steady-state flow field due to the steady forward motion of a ship travelling in calm water, which is often associated with the calculation of wave resistance; The second topic is the interactions between the incident wave and vessel which has no mean velocity; The third topic is the problem of ship motions in waves, which can be regarded as a superposition of the first and second case. Hence, the velocity potential ϕ is assumed to be the sum of two components: the steady potential $U\phi^S(x_i)$, $i = 1, 2, 3$ and the unsteady potential $\phi^T(x_i, t)$, $i = 1, 2, 3$, that is

$$\phi(x_i, t) = U\phi^S(x_i) + \phi^T(x_i, t). \tag{3.19}$$

$U\phi^S$ is the steady state flow potential due to the steady forward motion of the ship in calm water without the presence of incident waves. ϕ^T is unsteady flow potential associated with oscillatory motion of the ship in the incident waves. The hydrodynamic interactions that exist between $U\phi^S$ and ϕ^T will complicate the more general problem.

Based on these assumption and decomposition, it is easy to obtain the governing equations and boundary conditions for the steady velocity potential $U\phi^S$. It must satisfy the Laplace's equation (3.14), together with the ship body boundary condition (3.16), sea bottom boundary condition (3.17) and the free-surface boundary condition (3.18), as follows:

$$\phi^S_{,ii} = 0 \qquad\qquad x_i \in \Omega, \tag{3.20}$$

$$\phi^S_{,i} n_i = n_1 \qquad x_i \in S_{bs}, \tag{3.21}$$

$$\phi^S_{,3} = 0 \qquad x_i \in x_3 = \infty, \tag{3.22}$$

$$U^2[\phi^S_{,11} - 2\phi^S_{,i}\phi^S_{,1i} + \phi^S_{,i}(\phi^S_{,j}\phi^S_{,j})_{,i}] - g\phi^S_{,3} = 0 \qquad x_i \in S_{fs}, \tag{3.23}$$

where S_{bs} is the steady state position of the ship hull surface, S_{fs} is the steady free-surface elevation, which takes the form $x_3 = \eta_s(x_1, x_2)$ and is given by the implicit formula

$$\eta_s = h_G + \frac{U^2}{2g}(\phi^S_{,i}\phi^S_{,i} - 2\phi^S_{,1})\Big|_{x_3=\eta_s}, \tag{3.24}$$

which is obtained by substituting $U\phi^S$ into Bernoulli's equation (3.15).

3.3.2 Linearisation of Free-Surface Boundary Condition

Linearisation of free-surface boundary condition (3.18) involves linearising both steady potential ϕ^S and unsteady potential ϕ^T.

In the theory of water waves the amplitude of the incident wave is commonly assumed small in comparison to the wavelength, so that the oscillatory motion of the ship and the surrounding fluid flow potential can be assumed small, and linearisation of unsteady problem can be introduced. However, linearisation of the steady state potential is more complicated, because it not only depends on the steady forward speed of the ship, but also depends on the geometry of the ship. In most of the cases, the ship shape must satisfy certain conditions, such that perturbations of the steady state flow are small, then the linearisation of steady potential ϕ^S can be justified. Complete reduction of linearised free-surface boundary condition was given by Newman [45].

Linearising only ϕ^T

If only oscillatory flow potential ϕ^T is linearised, by substituting the total potential Equation (3.19) into Equation (3.18), the free-surface boundary condition can be written as

$$\frac{\partial^2\phi_T}{\partial t^2} + 2w_i\Big(\frac{\partial\phi_T}{\partial t}\Big)_{,i} + w_i(w_j\phi^T_{,j})_{,i} + \frac{1}{2}\phi^T_{,i}(w_jw_j)_{,i} + \frac{1}{2}w_i(w_jw_j)_{,i} - Ug\phi^S_{,3} - g\phi^T_{,3} = 0 \qquad x_i \in S_f, \quad (3.25)$$

where second-order terms in ϕ^T are neglected. w_i, $i = 1, 2, 3$ is the velocity vector of the steady flow relative to the moving reference frame $o(x_1, x_2, x_3)$, defined as

$$w_i = U(\phi^S_{,i} - \delta_{1i}). \quad (3.26)$$

This equation governs the unsteady velocity potential ϕ^T provided that the steady flow velocity w_i or steady flow potential ϕ^S is known.

Although w_i can be determined by Equations (3.20 - 3.23) and (3.26), one problem still remains in Equation (3.25), that is the free-surface elevation S_f is time-variant, which is difficult to be tackled. Since the difference between S_f and S_{fs} is small, it is possible to obtain the free-surface boundary condition for ϕ^T applied on the time-invariant surface S_{fs} by Taylor-series expansion. The expression for the free-surface elevation S_f is

$$\eta = h_G + \frac{1}{g}\Big[\frac{\partial\phi^T}{\partial t} + \frac{1}{2}(w_iw_i - U^2) + w_i\phi^T_{,i}\Big]\Big|_{x_3=\eta}, \quad (3.27)$$

$$= \eta_s + \frac{1}{g}\Big(\frac{\partial\phi^T}{\partial t} + w_i\phi^T_{,i}\Big)\Big|_{x_3=\eta_s} + \frac{1}{g}(\eta - \eta_s)(w_iw_{i,3})\Big|_{x_3=\eta_s}, \quad (3.28)$$

where Taylor-series expansion is applied about the steady flow free-surface ele-

vation S_{fs}. Now the difference $(\eta - \eta_s)$ can be obtained,

$$\eta - \eta_s = \Big(\frac{\partial \phi^T}{\partial t} + w_i \phi^T_{,i}\Big) \Big/ (g - w_i w_{i,3})\Big|_{x_3=\eta_s}. \tag{3.29}$$

Hence expanding all the terms in Equation (3.25) from S_f to S_{fs}, and neglecting all the second order quantities, it follows that

$$\frac{\partial^2 \phi^T}{\partial t^2} + 2w_i\Big(\frac{\partial \phi^T}{\partial t}\Big)_{,i} + w_i(w_j \phi^T_{,j})_{,i} + \frac{1}{2}\phi^T_{,i}(w_j w_j)_{,i} - g\phi^T_{,3} + (\eta - \eta_s)\Big[\frac{1}{2}w_i(w_j w_j)_{,i} - Ug\phi^S_{,3}\Big]_{,3} = 0 \qquad x_i \in S_{fs}. \tag{3.30}$$

Linearising both ϕ^T and ϕ^S

The steady flow field w_i, $i = 1, 2, 3$ is the major complexity in the free-surface boundary condition (3.30). Moreover, in order to obtain w_i, it is necessary to solve the non-linear equations of steady flow ϕ^S, which is very difficult. Thus, in almost all seakeeping theories or methods, the free-surface boundary condition (3.30) is further linearised.

Suppose that certain geometry restrictions are imposed on the ship's shape, for example, the hull shape is restricted to be a small perturbation from a plane which contains the x_1-axis, so that the steady state potential ϕ^S and its derivatives are small. Neglecting the perturbation of steady flow, the steady flow velocity becomes $w_i = -U\delta_{1i}$. The free-surface boundary condition (3.30) reduces to

$$\frac{\partial^2 \phi^T}{\partial t^2} - 2U\Big(\frac{\partial \phi^T}{\partial t}\Big)_{,1} + U^2 \phi^T_{,11} - g\phi^T_{,3} = 0 \qquad x_i \in x_3 = h_G. \tag{3.31}$$

The steady free-surface elevation S_{fs} Equation (3.24) simply becomes $x_3 = h_G$.

It should be noted that this assumption is not consistent with the basic assumption of slender-body theory which states that the derivatives in the trans-

verse direction are larger than the longitudinal derivatives. The assumption applied here lead to equations of motion in a form which can be quite easily solved numerically, while the use of slender-body theory results in a similar strip theory but with some additional integral terms which are difficult to evaluate [52].

3.3.3 Linearisation of Ship Body Surface Boundary Condition

The boundary condition on the ship hull needs to be linearised similarly.

Considering ship as a rigid body, the unsteady ship motion v_i, $i = 1, 2, 3$ in the hull boundary condition (3.16) is simply defined by the unsteady translation ξ_i^T, $i = 1, 2, 3$ and rotation ξ_i^R, $i = 1, 2, 3$ of the ship. Since ξ_i^T and ξ_i^R are small, it has

$$v_i = \dot{\alpha}_i = \dot{\xi}_i^T + e_{ijk}\dot{\xi}_j^R x_k', \tag{3.32}$$

where

$$\alpha_i = \xi_i^T + e_{ijk}\xi_j^R x_k' \tag{3.33}$$

is the local oscillatory displacement of the ship's surface, and the overdot denotes time differentiation in the reference frame $o(x_1, x_2, x_3)$.

Substitution of Equations (3.19), (3.26) and (3.32) into Equation (3.16) gives the boundary condition of unsteady potential ϕ^T on ship's hull,

$$\phi_{,i}^T n_i = \dot{\alpha}_i n_i - w_i n_i \qquad x_i \in S_b. \tag{3.34}$$

The unit normal vector n_i, $i = 1, 2, 3$ of the body wetted surface in its instantaneous position S_b can be expressed by that of the body wetted surface in its steady mean position S_{bs} through the first order contribution from the rotation ξ_i^R, as

$$n_i|_{S_b} = n_i|_{S_{bs}} + e_{ijk}\xi_j^R n_k|_{S_{bs}}. \tag{3.35}$$

The steady flow velocity w_i, $i = 1, 2, 3$ on the instantaneous hull surface can also be expressed by the steady flow velocity on the hull surface at steady mean position,

$$w_i|_{S_b} = (w_i + w_{i,j}\alpha_j)|_{S_{bs}}, \tag{3.36}$$

where Taylor-series expansion is applied at the direction of α_i.

Substituting Equations (3.35) and (3.36) in Equation (3.34), and neglecting second order terms in α_i and ξ_i^R, it follows that

$$\phi_{,i}^T n_i = \dot{\alpha}_i n_i + e_{ijk}\xi_j^R w_k n_i - w_{i,j}\alpha_j n_i \qquad x_i \in S_{bs}. \tag{3.37}$$

This formula was first derived by Timman and Newman [63]. From Equations (3.33) and (3.37), an alternative hull boundary condition can be derived in the form

$$\phi_{,j}^T n_j = \widetilde{n}_i \dot{\xi}_i + \widetilde{m}_i \xi_i \qquad i = 1, 2, \ldots, 6,\ x_j \in S_{bs}, \tag{3.38}$$

where $\widetilde{n}_i$, $i = 1, 2, \ldots, 6$ is the generalised unit normal vector, $\widetilde{m}_i$, $i = 1, 2, \ldots, 6$ is the gradient of the steady velocity in the normal direction, defined by

$$\widetilde{n}_i = n_i, \tag{3.39}$$

$$\widetilde{m}_i = -w_{i,j} n_j, \tag{3.40}$$

$$\widetilde{n}_{i+3} = e_{ijk} x_j n_k, \tag{3.41}$$

$$\widetilde{m}_{i+3} = e_{ijk} x_j m_k + e_{ijk} w_j n_k, \tag{3.42}$$

where $i, j, k = 1, 2, 3$, and $x_j \in S_{bs}$.

Once again, the perturbation of the steady flow field due to the ship is neglected giving $w_i = -U\delta_{1i}$, hence $\widetilde{m}_i$ reduces to

$$\{0, 0, 0, 0, Un_3, -Un_2\}.$$

3.4 Solution of Unsteady Potential

In the previous section, the linearisation of free-surface boundary condition and ship body surface boundary condition has been discussed. It appears that if the perturbation of the steady flow field can be neglected, all the terms concerning ϕ^S in both free-surface boundary condition and ship body surface boundary condition will disappear, and leave behind only those linear terms of ϕ^T. Therefore, the equations governing ϕ^T are linear, as follows:

$$\phi^T_{,ii} = 0 \qquad x_j \in \Omega, \tag{3.43}$$

$$\phi^T_{,3} = 0 \qquad x_j \in x_3 = \infty, \tag{3.44}$$

$$\frac{\partial^2 \phi^T}{\partial t^2} - 2U\left(\frac{\partial \phi^T}{\partial t}\right)_{,1} + U^2 \phi^T_{,11} - g\phi^T_{,3} = 0 \qquad x_j \in x_3 = h_G, \tag{3.45}$$

$$\phi^T_{,j} n_j = \widetilde{n}_i \dot{\xi}_i + \widetilde{m}_i \xi_i \qquad i = 1, 2, \ldots, 6, \quad x_j \in S_{bs}, \tag{3.46}$$

where

$$\{\widetilde{n}_1, \widetilde{n}_2, \widetilde{n}_3\} = \{n_1, n_2, n_3\}, \tag{3.47}$$

$$\{\widetilde{n}_4, \widetilde{n}_5, \widetilde{n}_6\} = \{x_2 n_3 - x_3 n_2, x_3 n_1 - x_1 n_3, x_1 n_2 - x_2 n_1\}, \tag{3.48}$$

$$\{\widetilde{m}_1, \widetilde{m}_2, \widetilde{m}_3] = \{0, 0, 0\}, \tag{3.49}$$

$$\{\widetilde{m}_4, \widetilde{m}_5, \widetilde{m}_6] = \{0, Un_3, -Un_2\}. \tag{3.50}$$

3.4.1 Linear Decomposition of the Unsteady Potential

Since the unsteady motions of the ship and surrounding fluid has been assumed small, linear superposition can be applied. The unsteady velocity potential problem hence can be treated as a superposition of three separate problems: the incident wave potential problem; the radiation wave potential problem, where the ship undergoes prescribed oscillatory motions in otherwise calm water; and the

diffraction wave potential problem, where incident wave acts upon the ship in its equilibrium position. Interactions between these three first-order problems are of second order in the oscillatory amplitudes, and may be neglected in the linear theory. The radiation potential may be decomposed further, by considering separately the six degrees of freedom defined above. In each of these modes, outgoing radiated waves will exist on the free surface.

$$\phi^T = \phi_0 + \phi_7 + \sum_{i=1}^{6} \phi_i, \tag{3.51}$$

where ϕ_0 represents the incident wave potential, ϕ_7 is the diffraction wave potential, and ϕ_i, $i = 1, 2, \ldots, 6$ are the potential due to the body motions surge, sway, heave, roll, pitch and yaw, respectively. This decomposition was first performed by Haskind [22], and it greatly simplifies the analysis of unsteady wave potential.

3.4.2 Incident Wave Potential

By linear gravity-wave theory [61], the potential for an incident plane-progressive wave of constant amplitude η_0 and a sinusoidal profile in the water of infinite depth satisfying the equations

$$\phi_{0,ii} = 0 \qquad x_i \in \Omega, \tag{3.52}$$

$$\phi_{0,3} = 0 \qquad x_i \in x_3 = \infty, \tag{3.53}$$

$$\frac{\partial^2 \phi_0}{\partial t^2} - 2U\left(\frac{\partial \phi_0}{\partial t}\right)_{,1} + U^2 \phi_{0,11} - g\phi_{0,3} = 0 \qquad x_i \in x_3 = h_G, \tag{3.54}$$

is given by

$$\begin{aligned} \phi_0 &= \Re[\Phi_0(x_i) e^{\imath \omega_e t}] \\ &= \Re\left[\frac{ig\eta_0}{\omega_0} e^{-K_0(x_3 - h_G + \imath x_1 \cos\mu - \imath x_2 \sin\mu)} e^{\imath \omega_e t}\right], \end{aligned} \tag{3.55}$$

where μ is the heading angle, $K_0 = 2\pi/\lambda$ is the wave number, λ is the wave length, and $\omega_0 = \sqrt{gK_0}$ is the wave frequency, which is related to the frequency of encounter ω_e by

$$\omega_e = \omega_0 - K_0 U \cos\mu. \tag{3.56}$$

By definition, the incident wave potential ϕ_0 is not required to satisfy any boundary condition at infinity.

3.4.3 Diffraction Wave Potential

The diffraction wave is induced by the incident wave. It satisfies the Laplace's equation, the sea bottom boundary condition, and the linearised free-surface boundary condition,

$$\phi_{7,ii} = 0 \qquad x_i \in \Omega, \tag{3.57}$$

$$\phi_{7,3} = 0 \qquad x_i \in x_3 = \infty, \tag{3.58}$$

$$\frac{\partial^2\phi_7}{\partial t^2} - 2U\left(\frac{\partial\phi_7}{\partial t}\right)_{,1} + U^2\phi_{7,11} - g\phi_{7,3} = 0 \qquad x_i \in x_3 = h_G. \tag{3.59}$$

Meanwhile, on the ship hull surface, it has to satisfy the boundary condition

$$\phi_{7,i}n_i = -\phi_{0,j}n_j \qquad x_i \in S_{bs}, \tag{3.60}$$

which suggests that the diffraction wave potential can be expressed in the form similar to the incident wave potential,

$$\phi_7 = \Re[\Phi_7(x_i)e^{\imath\omega_e t}]. \tag{3.61}$$

With a boundary condition at infinity (it represents outgoing waves scattered by the ship body), it forms a proper boundary value problem and its solution can

be obtained analytically or numerically. The detailed discussion of diffraction problem was given by Ogilvie [51], Newman [43, 45], Sclavounos [57] and *etc.* Solving the diffraction problem is of importance for some practical problems, for example, the prediction of the relative displacement and velocity between the ship and the water surface. However if the radiation problem defined in §3.4.4 has been solved and only the total force acted on the ship hull is required, solving the diffraction problem can be avoided.

3.4.4 Radiation Wave Potential

Assuming that the vessel motion has been going on over an infinite time interval $[-\infty, t]$ excited by a incident regular wave, such that the transient motion has vanished and the ship is undertaking steady oscillation sinusoidal in time with the frequency of encounter ω_e. Hence the ship's motions are of the form

$$\xi_i = \Re\left(\Xi_i e^{\imath\omega_e t}\right) \qquad i = 1, 2, \ldots, 6, \tag{3.62}$$

where Ξ_i is the complex amplitude of each oscillatory motion ξ_i. Naturally, the resulting radiation wave potential ϕ_i can be defined as

$$\phi_i = \Re\left[\Xi_i \Phi_i(x_i) e^{\imath\omega_e t}\right] \qquad i = 1, 2, \ldots, 6. \tag{3.63}$$

As usual, the radiation potential ϕ_i must satisfy the Laplace's equation, the sea bottom boundary condition and the free-surface boundary condition, it follows

$$\Phi_{i,jj} = 0 \qquad x_j \in \Omega, \tag{3.64}$$

$$\Phi_{i,3} = 0 \qquad x_j \in x_3 = \infty, \tag{3.65}$$

$$-\omega_e^2\Phi_i - 2\imath\omega_e U\Phi_{i,1} + U^2\Phi_{i,11} - g\Phi_{i,3} = 0 \qquad x_j \in x_3 = h_G, \tag{3.66}$$

where $i = 1, 2, \ldots, 6$.

Considering Equations (3.51) and (3.60), the boundary condition for Φ_i on the ship surface can be derived from Equation (3.46), that is

$$\Phi_{i,j}n_j = \imath\omega_e\widetilde{n}_i + \widetilde{m}_i \qquad i = 1, 2, \ldots, 6,\ x_j \in S_{bs}. \tag{3.67}$$

A radiation boundary condition at infinity is required to ensure the existence and uniqueness of the potential Φ_i. Physically this boundary condition represents the energy flux of waves associated with the disturbance of the ship body and is directed away from the ship to infinity, the conservation of energy is to be satisfied. At zero forward speed, Newman [44] described the radiation condition in the following forms:

i. for two-dimensional flows,

$$\Phi_i \propto e^{\mp\imath K_0 x_2} \qquad \text{as } x_2 \to \pm\infty,\ i = 1, 2, \ldots, 6. \tag{3.68}$$

ii. for three-dimensional flows,

$$\Phi_i \propto R^{-1/2}e^{-\imath K_0 R} \qquad \text{as } R \to \infty,\ i = 1, 2, \ldots, 6. \tag{3.69}$$

Here $R = \sqrt{x_1^2 + x_2^2}$, and the constants of proportionality in Equations (3.68) and (3.69) may depend on the remaining coordinates, but not on x_1 or R, respectively. At non-zero forward speed, the radiation condition at infinity is implicitly satisfied via the use of Green's function. In fact, the diffraction wave potential Φ_7 should satisfy the same radiation condition as that discussed above.

In order to further simplify the boundary condition (3.67), the radiation potentials Φ_i are linearly separated into speed-independent parts Φ_i^0 and speed-dependent parts Φ_i^U, that is

$$\Phi_i = \Phi_i^0 + \frac{\Phi_i^U}{\imath\omega_e} \qquad i = 1, 2, \ldots, 6, \tag{3.70}$$

and let Φ_i^0 and Φ_i^U satisfy the boundary conditions

$$\Phi_{i,j}^0 n_j = \imath\omega_e \widetilde{n}_i \qquad i = 1, 2, \ldots, 6,\ x_j \in S_{bs}, \tag{3.71}$$

$$\Phi_{i,j}^U n_j = \imath\omega_e \widetilde{m}_i \qquad i = 1, 2, \ldots, 6,\ x_j \in S_{bs}. \tag{3.72}$$

This separation was proposed by Salvesen, *et al* [56]. From Equations (3.71) and (3.72), it can be found that

$$\Phi_i^U = 0, \tag{3.73}$$

$$\Phi_5^U = U\Phi_3^0, \tag{3.74}$$

$$\Phi_6^U = -U\Phi_2^0, \tag{3.75}$$

where $i = 1, 2, 3, 4$. Thus

$$\Phi_i = \Phi_i^0 + \frac{U}{\imath\omega_e}\delta_{5i}\Phi_3^0 - \frac{U}{\imath\omega_e}\delta_{6i}\Phi_2^0 \qquad i = 1, 2, \ldots, 6. \tag{3.76}$$

Apart from the ship body boundary condition (3.71), Φ_i^0 must satisfy the Laplace's equation, the sea bottom boundary condition, the free-surface boundary condition and the radiation condition at infinity,

$$\Phi_{i,jj}^0 = 0 \qquad x_j \in \Omega, \tag{3.77}$$

$$\Phi_{i,3}^0 = 0 \qquad x_j \in x_3 = \infty \tag{3.78}$$

$$-\omega_e^2\Phi_i^0 - 2\imath\omega_e U\Phi_{i,1}^0 + U^2\Phi_{i,11}^0 - g\Phi_{i,3}^0 = 0 \qquad x_j \in z = h_G, \tag{3.79}$$

$$\Phi_i^0 \propto R^{-1/2} e^{-\imath K_0 R} \qquad \text{as } R \to \infty, \tag{3.80}$$

where $i = 1, 2, \ldots, 6$. Strictly speaking, the potentials Φ_i^0 are not speed independent at this point, instead, they depend on the forward speed U through the free-surface boundary condition (3.79). However, it can be found later that Φ_i^0 are approximately independent of U according to the high-frequency assumption.

The next step is to simplify further the speed-independent potentials Φ_i^0 to the forms suitable for numerical evaluation, by applying "strip theory" approximations, which can also be found in the work of Salvesen, *et al* [56]. They are so critical that it is worth writing out here, as follows:

i. The ship is assumed to be long and slender, such that the component of the hull normal vector n_i in the x_1-direction is much smaller then the components in the x_2- and x_3-directions, $n_2 \gg n_1$ and $n_3 \gg n_1$. Therefore, n_1 can be set as $n_1 = 0$, the three-dimensional normal components n_2 and n_3 can be replaced with $\underline{n}_2$ and $\underline{n}_3$, respectively. $\underline{n}_2$ and $\underline{n}_3$ are the components in the x_2 and x_3 directions of the two-dimensional unit normal vector in the x_2, x_3-plane. Thus the generalised normal $\widetilde{n}_i$ on the right hand side of Equation (3.71) becomes

$$\{\widetilde{n}_1, \widetilde{n}_2, \widetilde{n}_3\} = \{0, \underline{n}_2, \underline{n}_3\}, \tag{3.81}$$

$$\{\widetilde{n}_4, \widetilde{n}_5, \widetilde{n}_6\} = \{x_2\underline{n}_3 - x_3\underline{n}_2, -x_1\underline{n}_3, x_1\underline{n}_2\}. \tag{3.82}$$

This implies that

$$\Phi_1^0 = 0, \tag{3.83}$$

$$\Phi_5^0 = -x_1\Phi_3^0, \tag{3.84}$$

$$\Phi_6^0 = x_1\Phi_2^0. \tag{3.85}$$

Consequently, only Φ_2^0, Φ_3^0 and Φ_4^0 are needed to be solved. The boundary condition (3.71) becomes

$$\Phi_{i,2}^0 \underline{n}_2 + \Phi_{i,3}^0 \underline{n}_3 = \imath\omega_e \widetilde{\underline{n}}_i \qquad i = 2,3,4,\ x_j \in S_{bs}, \tag{3.86}$$

where $\widetilde{\underline{n}}_i$ is the generalised two-dimensional normal vector in the x_2, x_3-plane,

$$\{\widetilde{\underline{n}}_1, \widetilde{\underline{n}}_2, \widetilde{\underline{n}}_3, \widetilde{\underline{n}}_4\} = \{0, \underline{n}_2, \underline{n}_3, x_2\underline{n}_3 - x_3\underline{n}_2\}. \tag{3.87}$$

ii. The ship is assumed to be long and slender, such that $\partial/\partial y \gg \partial/\partial x$ and $\partial/\partial z \gg \partial/\partial x$ in the neighbourhood of the hull. The Laplace's equation (3.77) becomes

$$\Phi_{i,22}^0 + \Phi_{i,33}^0 = 0 \qquad i = 2,3,4,\ x_j \in \Omega. \tag{3.88}$$

iii. The wave length is assumed to be approximately of the same order as the ship beam, such that the frequency of encounter ω_e is high, $\omega_e \gg U(\partial/\partial x)$. Free-surface boundary condition (3.79) becomes approximately

$$\omega_e^2 \Phi_i^0 + g\Phi_{i,3}^0 = 0 \qquad i = 2,3,4,\ x_j \in z = h_G, \tag{3.89}$$

It must be emphasized that this assumption makes the theoretical justification for the strip theory questionable in the low-frequency range.

By examination of Equations (3.86), (3.88) and (3.89), it can be found that the three-dimensional problem of potential Φ_i has been effectively reduced to a set of two-dimensional problems of potentials Φ_i^0. The solutions can be found analytically or numerically. Apparently the solution at each x_2, x_3-plane (cross section of ship body) is independent of the solutions at all other cross sections.

3.5 Two-Dimensional Problem and Conformal Mapping

It is found in §3.4.4 that three-dimensional unsteady potential ϕ^T can be obtained by solving two-dimensional potentials Φ_i^0 at each cross plane of ship body, which are independent of ship forward speed and governed by Equations (3.86), (3.88) and (3.89). There are three methods commonly in use for computing these two-dimensional potentials:

i. The Lewis conformal mapping method,

ii. The Tasai-Porter multi-parameter conformal mapping method,

iii. The Frank close-fit method.

Frank close-fit method [16] is a boundary element method, in which the ship section contour is represented by straight-line segments between the offset points. The velocity potential is obtained by distributing pulsating source singularities with constant strength over each of the straight segments.

Lewis and Tasai-Porter methods are based on conformal mapping technique in complex analysis. Suppose that ζ-plane and z-plane are two complex planes and a velocity potential $\Phi_\zeta(\zeta)$ of a fluid flow bounded by a complicated geometrical boundary Ω_ζ in ζ-plane is needed to be found. If there exists an analytic function $z = f(\zeta)$ which maps this complicated boundary Ω_ζ onto a simpler one Ω_z in z-plane and replaces the fluid flow in ζ-plane with the fluid flow in z-plane, where velocity potential $\Phi_z(z)$ is known or easy to be obtained, then the potential Φ_ζ can be obtained by analytic function theory, $\Phi_\zeta = \Phi_z[f(\zeta)]$. Therefore, in order to find Φ_i^0, the first objective is to map the ship section contour in physical x_2, x_3-plane (ζ-plane) onto a simple contour, which is usually a semi-circle, in a reference plane (z-plane).

The Riemann mapping theorem states that this analytic function $z = f(\zeta)$ and its reverse function $\zeta = f^{-1}(z)$ always exist, however, they are not always easy to be found in practice. In the Lewis method [35], the Lewis mapping function can only map a Lewis form, which is used to mathematically represent the geometrical shape of a ship section and only has the same beam, draught and cross sectional area as the given section, onto a semi-circle. Therefore, it usually can not be applied, for example, to sections with large bulbs or to sections with very small sectional area. However, for many common ship section forms, this method is fast and quite accurate. In the Tasai-Porter method [55, 62], the ship sections are conformally mapped onto a circle by applying a mapping function with many more coefficients than Lewis mapping function in order to get the desired close-fit accuracy. A bibliography of conformal mapping techniques was provided by Conceição, *et al* [11] and the various methods of obtaining the transform coefficients were discussed by Bishop, *et al* [6].

Westlake and Wilson [71] developed a conformal mapping function similar to that of Tasai and Porter. The difference lies in the iteration procedure used to compute the coefficients of the conformal mapping function. By employing "line length method" to relate the assumed angles ϑ_z in the z-plane to the angles ϑ_ζ subtended by the points mapped by function $\zeta = f^{-1}(z)$ in the ζ-plane, Westlake and Wilson's method allows the mapping of almost any section shape including re-entrant sections.

Since only the force exerted on ship section by water flow is eventually needed, it can be found later on that the explicit solution of Φ_i^0 in physical x_2, x_3-plane is not necessary. The force can be evaluated in the reference z-plane by coordinate transformation. This fact means that the reverse function $\zeta = f^{-1}(z)$ is more important than the function $z = f(\zeta)$ itself.

In accordance with Westlake and Wilson's work, the mapping function $\zeta = f^{-1}(z)$ takes the form

$$\zeta = c\Big(z + \sum_{k=0}^{\infty} c_k z^{-k}\Big), \tag{3.90}$$

where $\zeta = x_2 + \imath x_3$ is in the physical x_2, x_3-plane (ζ-plane), $z = \imath r e^{-\imath\vartheta}$ is in the reference plane (z-plane), and c, c_k are the complex transformation parameters, $c = a + \imath b$, $c_k = a_k + \imath b_k$. The coordinate systems are depicted in Figure (3.4).

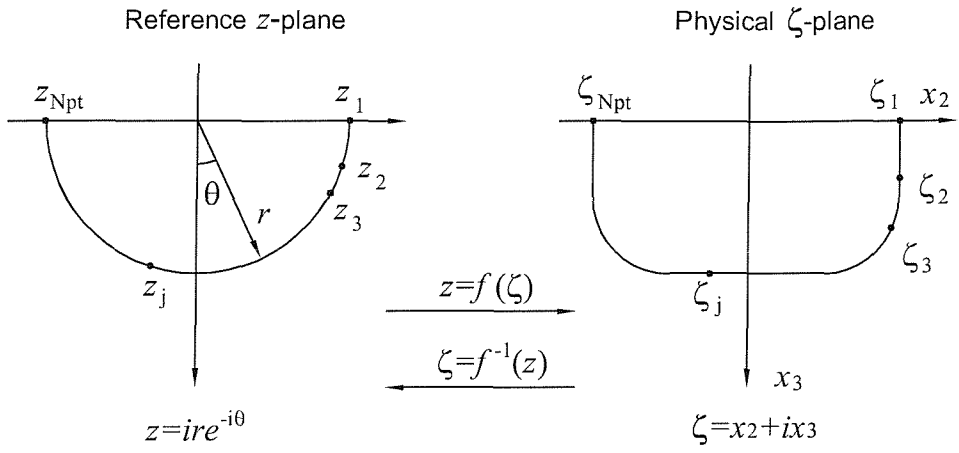

Figure 3.4: *The Coordinate Systems of Conformal Mapping.*

As only the region $x_3 \geq 0$ is considered, this transformation can be simplified by assuming the x_2-axis is a line of symmetry. The symmetry relation is

$$\zeta = f^{-1}(z) = \overline{f^{-1}(\bar{z})}, \tag{3.91}$$

where the overline indicates a conjugate operator. Using this relationship it can be shown that $b = 0$ and $b_k = 0$, $k = 0, 1, 2, \ldots, \infty$. If the real and imaginary parts are separated, Equation (3.90) may then be expressed as

$$\begin{aligned} x_2 &= \boldsymbol{x}_2(r, \vartheta) \\ &= a\Big\{r\sin\vartheta + \sum_{k=0}^{\infty}(-1)^k\Big[\frac{a_{(2k)}}{(r)^{2k}}\cos 2k\vartheta + \frac{a_{(2k+1)}}{(r)^{2k+1}}\sin(2k+1)\vartheta\Big]\Big\}, \end{aligned} \tag{3.92}$$

$$
\begin{aligned}
x_3 &= \boldsymbol{x}_3(r,\vartheta) \\
&= a\Big\{r\cos\vartheta + \sum_{k=0}^{\infty}(-1)^k\Big[\frac{a_{(2k)}}{(r)^{2k}}\sin 2k\vartheta - \frac{a_{(2k+1)}}{(r)^{2k+1}}\cos(2k+1)\vartheta\Big]\Big\}.
\end{aligned}
\tag{3.93}
$$

In practice the series has to be truncated to N_{cm} terms.

Normally the definition of a ship section takes the form of a set of discrete points $\zeta_j(x_{2j}, x_{3j})$, $j = 1, 2, \ldots, N_{pt}$. If a section is mapped onto a unit semi-circle*, for each definition point there exists a corresponding point $z_j(1, \vartheta_j)$ in z-plane. Hence the conformal mapping coefficients a, $a_{(2k)}$, $a_{(2k+1)}$ are determined by,

$$
x_{2j} = a\Big\{\sin\vartheta_j + \sum_{k=0}^{N_{cm}}(-1)^k[a_{(2k)}\cos 2k\vartheta_j + a_{(2k+1)}\sin(2k+1)\vartheta_j]\Big\}, \tag{3.94}
$$

$$
x_{3j} = a\Big\{\cos\vartheta_j + \sum_{k=0}^{N_{cm}}(-1)^k[a_{(2k)}\sin 2k\vartheta_j - a_{(2k+1)}\cos(2k+1)\vartheta_j]\Big\}. \tag{3.95}
$$

Usually points $\zeta_1(x_{21}, x_{31})$ and $\zeta_{N_{pt}}(x_{2N_{pt}}, x_{3N_{pt}})$ are on the waterline, *i.e.* $x_{31} = 0$, $x_{3N_{pt}} = 0$, and they are mapped onto points $(1, \pi/2)$ and $(1, -\pi/2)$ respectively. Since trivial solutions exit at these two positions, only $2N_{pt} - 2$ non-linear equations are available for solving $2N_{cm} + 3$ unknown transformation coefficients and $N_{pt} - 2$ unknown angles ϑ_j. The number of offset points N_{pt} and the number N_{cm} must satisfy the relationship

$$
2N_{pt} - 2 \geq 2N_{cm} + 3 + N_{pt} - 2 \tag{3.96}
$$

or

$$
N_{pt} \geq 2N_{cm} + 3. \tag{3.97}
$$

*Only the underwater part of the section is mapped onto the unit semi-circle, so points ζ_j are those on the underwater part of the section.

Now consider a ship cross section at any particular position x_1. Since Φ_i^0 is irrelevant to coordinate x_1, by defining

$$\underline{\Phi}_i \equiv \Phi_i^0 = \Phi_i^0(x_2, x_3), \tag{3.98}$$

Equations (3.86), (3.88) and (3.89) can be rewritten as

$$\underline{\Phi}_{i,22} + \underline{\Phi}_{i,33} = 0 \qquad (x_2, x_3) \in \underline{\Omega}, \tag{3.99}$$

$$\underline{\Phi}_{i,2}\underline{n}_2 + \underline{\Phi}_{i,3}\underline{n}_3 = \imath\omega_e\widetilde{\underline{n}}_i \qquad (x_2, x_3) \in \underline{S}_{bs}, \tag{3.100}$$

$$\omega_e^2\underline{\Phi}_i + g\underline{\Phi}_{i,3} = 0 \qquad (x_2, x_3) \in x_3 = h_G, \tag{3.101}$$

where $i = 2, 3, 4$, $\underline{S}_{bs}$ is the wetted ship cross section contour, $\underline{\Omega}$ is the two-dimensional fluid domain bounded by free-surface $\underline{S}_f$, $\underline{S}_{bs}$, sea bed $\underline{S}_h$ $(x_3 = \infty)$ and a virtual enclosing contour $\underline{S}_\infty$ at the infinity, as shown in Figure (3.5). The boundary condition on sea bottom Equation (3.78) remains unchanged, however, the three-dimensional radiation condition at infinity Equation (3.80) should be replaced with the two-dimensional one,

$$\underline{\Phi}_i \propto e^{\mp\imath K_0 x_2} \qquad \text{as } x_2 \to \pm\infty,\ i = 2, 3, 4, \tag{3.102}$$

The boundary condition (3.100) can also be expressed in terms of stream function. Suppose that $\underline{\Psi}_i$ is the conjugate stream function of the potential $\underline{\Phi}_i$, it has

$$\frac{\partial\underline{\Psi}_i^0}{\partial\underline{\ell}} = \frac{\partial\underline{\Phi}_i^0}{\partial\underline{n}} \qquad (x_2, x_3) \in \underline{S}_{bs}, \tag{3.103}$$

where $\underline{\ell}$ is the arc length along the curve $\underline{S}_{bs}$, $\vec{n}$ is the unit normal vector $\{\underline{n}_2, \underline{n}_3\}$ shown in Figure (3.5), which can be defined as

$$\underline{n}_2 = \frac{\partial x_3}{\partial\underline{\ell}}, \tag{3.104}$$

$$\underline{n}_3 = -\frac{\partial x_2}{\partial \underline{\ell}}. \tag{3.105}$$

Therefore,

$$\frac{\partial \underline{\Psi}_2}{\partial \underline{\ell}} = w\omega_e \frac{\partial x_3}{\partial \underline{\ell}} \qquad (x_2, x_3) \in \underline{S}_{bs}, \tag{3.106}$$

$$\frac{\partial \underline{\Psi}_3}{\partial \underline{\ell}} = -w\omega_e \frac{\partial x_2}{\partial \underline{\ell}} \qquad (x_2, x_3) \in \underline{S}_{bs}, \tag{3.107}$$

$$\frac{\partial \underline{\Psi}_4}{\partial \underline{\ell}} = -w\omega_e \left[x_2 \frac{\partial x_2}{\partial \underline{\ell}} + x_3 \frac{\partial x_3}{\partial \underline{\ell}} \right] \qquad (x_2, x_3) \in \underline{S}_{bs}. \tag{3.108}$$

After integration, the stream functions $\underline{\Psi}_i$ can be written in the form

$$\underline{\Psi}_2 = w\omega_e x_3 + C_2(t) \qquad (x_2, x_3) \in \underline{S}_{bs}, \tag{3.109}$$

$$\underline{\Psi}_3 = -w\omega_e x_2 + C_3(t) \qquad (x_2, x_3) \in \underline{S}_{bs}, \tag{3.110}$$

$$\underline{\Psi}_4 = -\frac{w\omega_e}{2}(x_2^2 + x_3^2) + C_4(t) \qquad (x_2, x_3) \in \underline{S}_{bs}, \tag{3.111}$$

where C_2, C_3, and C_4 are the integration constants, which may depend on the time t.

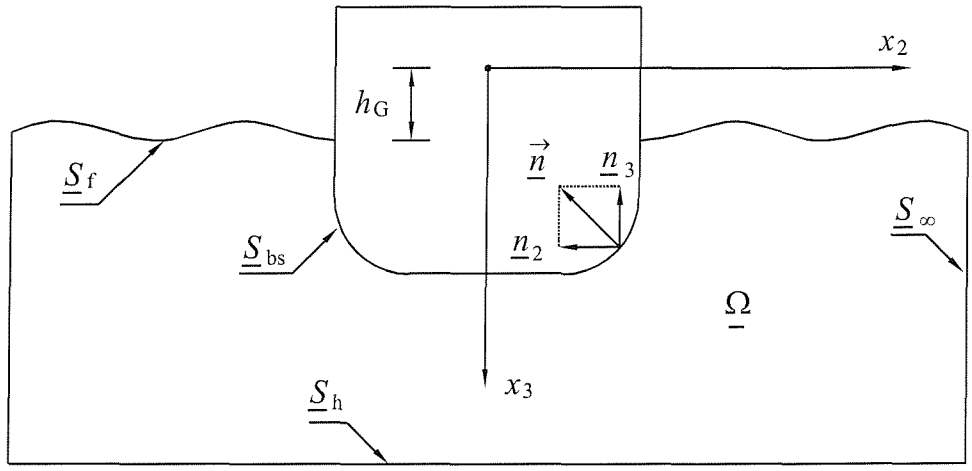

Figure 3.5: *Two-Dimensional Boundary Value Problem.*

Using the conformal mapping Equations (3.92) and (3.93), cross section $\underset{\sim}{S}_{bs}$ is mapped onto a unit semi-circle in the reference plane, the fluid flow of velocity potential $\underset{\sim}{\Phi}_i$ in x_2, x_3-plane is replaced with the fluid flow of velocity potential $\underset{\sim}{\Phi}_i$ in the reference plane. By applying the same mapping transformation to Equations (3.78), (3.101), (3.99), (3.102), (3.109), (3.110) and (3.111), the governing equations for $\underset{\sim}{\Phi}_i$ can be obtained†,

$$\frac{\partial}{\partial r}\left(r\frac{\partial \underset{\sim}{\Phi}_i}{\partial r}\right)+\frac{1}{r}\frac{\partial^2 \underset{\sim}{\Phi}_i}{\partial \vartheta^2}=0 \qquad \vartheta\in\left(-\frac{\pi}{2},\frac{\pi}{2}\right),\ r\in(1,+\infty], \tag{3.112}$$

$$\begin{cases} \underset{\sim}{\Psi}_2=\imath\omega_e(\boldsymbol{x}_3+h_G)+C_2(t) \\ \underset{\sim}{\Psi}_3=-\imath\omega_e\boldsymbol{x}_2+C_3(t) \\ \underset{\sim}{\Psi}_4=-\dfrac{\imath\omega_e}{2}[\boldsymbol{x}_2^2+(\boldsymbol{x}_3+h_G)^2]+C_4(t) \end{cases} \qquad \vartheta\in\left[-\frac{\pi}{2},\frac{\pi}{2}\right],\ r=1, \tag{3.113}$$

$$\omega_e^2\frac{\partial \boldsymbol{x}_3}{\partial \vartheta}\underset{\sim}{\Phi}_i+g\frac{\partial \underset{\sim}{\Phi}_i}{\partial \vartheta}=0 \qquad \vartheta=\pm\frac{\pi}{2},\ r\in(1,+\infty] \tag{3.114}$$

$$\frac{\partial \underset{\sim}{\Phi}_i}{\partial \boldsymbol{x}_3}=0 \qquad \text{as } \boldsymbol{x}_3\to\infty, \tag{3.115}$$

$$\underset{\sim}{\Phi}_i\propto e^{\mp\imath K_0\boldsymbol{x}_2} \qquad \text{as } \boldsymbol{x}_2\to\pm\infty, \tag{3.116}$$

where $i=2,3,4$, and $\underset{\sim}{\Psi}_i$ are the conjugate stream functions of potentials $\underset{\sim}{\Phi}_i$.

Ursell [65, 66] derived a potential flow solution, which satisfies the Laplace's equation (3.99) and the boundary conditions (3.100) and (3.101), for a circular cylinder oscillating harmonically with arbitrary frequency in the free surface. Eatock Taylor and Hu [14] gave a generalised version of Ursell's solution, which can be applied to both floating and submerged bodies.

Similar to the Ursell's method but in complex plane, the velocity potential $\underset{\sim}{\Phi}_i$ is also composed of a source potential, a dipole potential and a series of linear

†The origin of the coordinate system used in the conformal mapping (3.92) and (3.93) is located on the still water surface. However, the origin of the coordinate system used in Equation (3.78), (3.101), (3.99), (3.102), (3.109), (3.110) and (3.111) is located at the centre of the gravity of the ship, which is h_G metres above the still water surface, therefore it has to be moved down to the still water surface before using the conformal mapping.

multipole potentials,

$$\underset{\sim}{\Phi}_i = \underset{\sim}{P}_{i0}\underset{\sim}{\varphi}_0 + \underset{\sim}{P}_{i1}\underset{\sim}{\varphi}_1 + \sum_{j=1}^{\infty}(\underset{\sim}{P}_{i(2j)}\underset{\sim}{\varphi}_{(2j)} + \underset{\sim}{P}_{i(2j+1)}\underset{\sim}{\varphi}_{(2j+1)}), \tag{3.117}$$

where $\underset{\sim}{\varphi}_0$ and $\underset{\sim}{\varphi}_1$ are the potentials of a source and of a dipole situated at the origin, $\underset{\sim}{\varphi}_{(2j)}$ and $\underset{\sim}{\varphi}_{(2j+1)}$ are the multipole potentials,

$$\underset{\sim}{\varphi}_0 = \int_0^{\infty} \frac{K_e \sin(\rho \boldsymbol{x}_3) - \rho\cos(\rho \boldsymbol{x}_3)}{K_e^2 + \rho^2} e^{-\rho|\boldsymbol{x}_2|} d\rho + \imath\pi e^{-K_e(\boldsymbol{x}_3 + \imath|\boldsymbol{x}_2|)}, \tag{3.118}$$

$$\begin{aligned}\underset{\sim}{\varphi}_1 = \mp \int_0^{\infty} \frac{K_e \cos(\rho \boldsymbol{x}_3) + \rho\sin(\rho \boldsymbol{x}_3)}{K_e^2 + \rho^2} e^{-\rho|\boldsymbol{x}_2|} d\rho \pm \pi e^{-K_e(\boldsymbol{x}_3 + \imath|\boldsymbol{x}_2|)} \\ + \frac{\boldsymbol{x}_2}{K_e(\boldsymbol{x}_2^2 + \boldsymbol{x}_3^2)} \qquad \boldsymbol{x}_2 \gtrless 0,\end{aligned} \tag{3.119}$$

$$\begin{aligned}\underset{\sim}{\varphi}_{(2j)} = \frac{\cos(2j\vartheta)}{(r)^{2j}} + aK_e\Bigg\{ \frac{\cos[(2j-1)\vartheta]}{(2j-1)(r)^{2j-1}} - \sum_{k=0}^{N_{cm}}(-1)^k \Bigg[2k a_{(2k)} \\ \frac{\sin[(2j+2k)\vartheta]}{(2j+2k)(r)^{2j+2k}} - (2k+1)a_{(2k+1)} \frac{\cos[(2j+2k+1)\vartheta]}{(2j+2k+1)(r)^{2j+2k+1}}\Bigg]\Bigg\},\end{aligned} \tag{3.120}$$

$$\begin{aligned}\underset{\sim}{\varphi}_{(2j+1)} = \frac{\sin[(2j+1)\vartheta]}{(r)^{2j+1}} + aK_e\Bigg\{ \frac{\sin(2j\vartheta)}{2j(r)^{2j}} + \sum_{k=0}^{N_{cm}}(-1)^k \Bigg[2k a_{(2k)} \\ \frac{\cos[(2j+2k+1)\vartheta]}{(2j+2k+1)(r)^{2j+2k+1}} + (2k+1)a_{(2k+1)} \frac{\sin[(2j+2k+2)\vartheta]}{(2j+2k+2)(r)^{2j+2k+2}}\Bigg]\Bigg\}.\end{aligned} \tag{3.121}$$

where K_e is the wave number of encounter wave,

$$K_e = \frac{\omega_e^2}{g} \tag{3.122}$$

All the above potentials satisfy the Laplace's equation (3.112), the free-surface boundary condition (3.114), the sea bottom boundary condition (3.115) and the radiation condition at infinity (3.116). The complex valued unknown constants $\underset{\sim}{P}_{i0}$, $\underset{\sim}{P}_{i1}$, $\underset{\sim}{P}_{i(2j)}$ and $\underset{\sim}{P}_{i(2j+1)}$ are chosen such that the boundary condition (3.113) is satisfied. In practice, the infinite series (3.117) in the multipole expansion is

truncated to a finite number N_{mp}.

It appears that the integrals in Equations (3.118) and (3.119) converge very slowly when they are calculated in a numerical way. They are usually replaced with the following power series expansion,

$$\int_0^\infty \frac{K_e \sin(\rho \boldsymbol{x}_3) - \rho \cos(\rho \boldsymbol{x}_3)}{K_e^2 + \rho^2} e^{-\rho|\boldsymbol{x}_2|} d\rho \tag{3.123}$$
$$= e^{-K_e \boldsymbol{x}_3}[\boldsymbol{Q} \cos(K_e \boldsymbol{x}_2) + \boldsymbol{S} \sin(K_e|\boldsymbol{x}_2|)] - \pi e^{-K_e \boldsymbol{x}_3} \sin(K_e|\boldsymbol{x}_2|),$$

$$\int_0^\infty \frac{K_e \cos(\rho \boldsymbol{x}_3) + \rho \sin(\rho \boldsymbol{x}_3)}{K_e^2 + \rho^2} e^{-\rho|\boldsymbol{x}_2|} d\rho \tag{3.124}$$
$$= e^{-K_e \boldsymbol{x}_3}[\boldsymbol{Q} \sin(K_e|\boldsymbol{x}_2|) - \boldsymbol{S} \cos(K_e \boldsymbol{x}_2)] + \pi e^{-K_e \boldsymbol{x}_3} \cos(K_e \boldsymbol{x}_2)$$

where

$$\boldsymbol{Q} = \gamma + \ln(K_e \boldsymbol{R}) + \sum_{n=1}^{\infty} \frac{K_e^n \boldsymbol{R}^n}{n! n} \cos(n\chi), \tag{3.125}$$

$$\boldsymbol{S} = \chi + \sum_{n=1}^{\infty} \frac{K_e^n \boldsymbol{R}^n}{n! n} \sin(n\chi), \tag{3.126}$$

$$\chi = \arctan\left(\frac{\boldsymbol{x}_2}{\boldsymbol{x}_3}\right), \tag{3.127}$$

$$\boldsymbol{R} = \sqrt{\boldsymbol{x}_2^2 + \boldsymbol{x}_3^2}, \tag{3.128}$$

$$\gamma = \text{Euler's constant.} \tag{3.129}$$

By means of the Cauchy-Riemann relations, the conjugate stream function of the potential function (3.117) can be obtained,

$$\underset{\sim}{\Psi}_i = \underset{\sim}{P}_{i0} \underset{\sim}{\psi}_0 + \underset{\sim}{P}_{i1} \underset{\sim}{\psi}_1 + \sum_{j=1}^{N_{mp}} (\underset{\sim}{P}_{i(2j)} \underset{\sim}{\psi}_{(2j)} + \underset{\sim}{P}_{i(2j+1)} \underset{\sim}{\psi}_{(2j+1)}), \tag{3.130}$$

where $\underset{\sim}{\psi}_0$, $\underset{\sim}{\psi}_1$, $\underset{\sim}{\psi}_{(2j)}$ and $\underset{\sim}{\psi}_{(2j+1)}$ are the conjugate stream functions of the potentials $\underset{\sim}{\varphi}_0$, $\underset{\sim}{\varphi}_1$, $\underset{\sim}{\varphi}_{(2j)}$ and $\underset{\sim}{\varphi}_{(2j+1)}$ respectively, defined as follows,

$$\begin{aligned}\underset{\sim}{\psi}_0 &= \pm\int_0^\infty \frac{K_e\cos(\rho \boldsymbol{x}_3)+\rho\sin(\rho \boldsymbol{x}_3)}{K_e^2+\rho^2}e^{-\rho|\boldsymbol{x}_2|}d\rho \mp \pi e^{-K_e(\boldsymbol{x}_3+\imath|\boldsymbol{x}_2|)}\\ &= \pm e^{-K_3\boldsymbol{x}_3}[\boldsymbol{Q}\sin(K_e|\boldsymbol{x}_2|)-\boldsymbol{S}\cos(K_e\boldsymbol{x}_2)]+\imath\pi e^{-K_3\boldsymbol{x}_3}\sin(K_e\boldsymbol{x}_2)\\ &\quad \boldsymbol{x}_2 \gtrless 0,\end{aligned} \tag{3.131}$$

$$\begin{aligned}\underset{\sim}{\psi}_1 &= \int_0^\infty \frac{K_e\sin(\rho \boldsymbol{x}_3)-\rho\cos(\rho \boldsymbol{x}_3)}{K_e^2+\rho^2}e^{-\rho|\boldsymbol{x}_2|}d\rho + \imath\pi e^{-K_e(\boldsymbol{x}_3+\imath|\boldsymbol{x}_2|)}\\ &\quad -\frac{\boldsymbol{x}_3}{K_e(\boldsymbol{x}_2^2+\boldsymbol{x}_3^2)}\\ &= e^{-K_3\boldsymbol{x}_3}[\boldsymbol{Q}\cos(K_e\boldsymbol{x}_2)+\boldsymbol{S}\sin(K_e|\boldsymbol{x}_2|)]+\imath\pi e^{-K_3\boldsymbol{x}_3}\cos(K_e\boldsymbol{x}_2)\\ &\quad -\frac{\boldsymbol{x}_3}{K_e(\boldsymbol{x}_2^2+\boldsymbol{x}_3^2)},\end{aligned} \tag{3.132}$$

$$\begin{aligned}\underset{\sim}{\psi}_{(2j)} &= \frac{\sin(2j\vartheta)}{(r)^{2j}}+aK_e\Bigg\{\frac{\sin[(2j-1)\vartheta]}{(2j-1)(r)^{2j-1}}+\sum_{k=0}^{N_{cm}}(-1)^k\Bigg[2ka_{(2k)}\\ &\quad \frac{\cos[(2j+2k)\vartheta]}{(2j+2k)(r)^{2j+2k}}+(2k+1)a_{(2k+1)}\frac{\sin[(2j+2k+1)\vartheta]}{(2j+2k+1)(r)^{2j+2k+1}}\Bigg]\Bigg\},\end{aligned} \tag{3.133}$$

$$\begin{aligned}\underset{\sim}{\psi}_{(2j+1)} &= -\frac{\cos[(2j+1)\vartheta]}{(r)^{2j+1}}+aK_e\Bigg\{-\frac{\cos(2j\vartheta)}{2j(r)^{2j}}+\sum_{k=0}^{N_{cm}}(-1)^k\Bigg[2ka_{(2k)}\\ &\quad \frac{\sin[(2j+2k+1)\vartheta]}{(2j+2k+1)(r)^{2j+2k+1}}-(2k+1)a_{(2k+1)}\frac{\cos[(2j+2k+2)\vartheta]}{(2j+2k+2)(r)^{2j+2k+2}}\Bigg]\Bigg\}.\end{aligned} \tag{3.134}$$

Suppose that ϑ_k, $k=1,2,\ldots,N_{an}$ are N_{an} arbitrary angles and $-\pi/2 \le \vartheta_k < \pi/2$. On the surface of the circular cylinder, $\underset{\sim}{\Psi}_i$ must satisfy the boundary condition (3.113), this gives N_{an} linear equations for each of $\underset{\sim}{\Psi}_i$, $i=2,3,4$,

$$\underset{\sim}{P}_{i0}\underset{\sim}{Q}_{0k}+\underset{\sim}{P}_{i1}\underset{\sim}{Q}_{1k}+\sum_{j=1}^{N_{mp}}(\underset{\sim}{P}_{i(2j)}\underset{\sim}{Q}_{(2j)k}+\underset{\sim}{P}_{i(2j+1)}\underset{\sim}{Q}_{(2j+1)k})=\underset{\sim}{R}_{ik}, \tag{3.135}$$

where

$$\underset{\sim}{Q}_{0k} = \underset{\sim}{\psi}_0(1,\vartheta_k) - \underset{\sim}{\psi}_0(1,\pi/2), \tag{3.136}$$

$$\underset{\sim}{Q}_{1k} = \underset{\sim}{\psi}_1(1,\vartheta_k) - \underset{\sim}{\psi}_1(1,\pi/2), \tag{3.137}$$

$$\underset{\sim}{Q}_{(2j)k} = \underset{\sim}{\psi}_{(2j)}(1,\vartheta_k) - \underset{\sim}{\psi}_{(2j)}(1,\pi/2), \tag{3.138}$$

$$\underset{\sim}{Q}_{(2j+1)k} = \underset{\sim}{\psi}_{(2j+1)}(1,\vartheta_k) - \underset{\sim}{\psi}_{(2j+1)}(1,\pi/2), \tag{3.139}$$

$$\underset{\sim}{R}_{2k} = \imath\omega \boldsymbol{x}_3(1,\vartheta_k), \tag{3.140}$$

$$\underset{\sim}{R}_{3k} = -\imath\omega[\boldsymbol{x}_2(1,\vartheta_k) - \boldsymbol{x}_2(1,\pi/2)], \tag{3.141}$$

$$\underset{\sim}{R}_{4k} = -\frac{\imath\omega}{2}[\boldsymbol{x}_2^2(1,\vartheta_k) - \boldsymbol{x}_2^2(1,\pi/2) + \boldsymbol{x}_3^2(1,\vartheta_k) + 2\boldsymbol{x}_3^2(1,\vartheta_k)h_G]. \tag{3.142}$$

The number of angles N_{an} must be greater then $2N_{mp}+2$ to ensure there are sufficient equations for solving the coefficients $\underset{\sim}{P}_{i0}$, $\underset{\sim}{P}_{i1}$, $\underset{\sim}{P}_{i(2j)}$ and $\underset{\sim}{P}_{i(2j+1)}$. Usually $N_{an} \gg 2N_{mp}+2$, the coefficients are solved in a least square sense.

3.6 Hydrodynamic and Hydrostatic Forces

Once the velocity potential ϕ is solved, pressure p can be obtained by Bernoulli's equation (3.15). The forces and moments acting on the ship can be calculated by integrating the pressure p over the ship wetted hull surface S_{bs},

$$\begin{aligned} F_j &= \iint_{S_{bs}} p\widetilde{n}_j ds \\ &= -\varrho \iint_{S_{bs}} \Big[\frac{\partial \phi^T}{\partial t} - U\phi^T_{,1} + \frac{1}{2}\phi^T_{,i}\phi^T_{,i} + U\phi^S_{,i}\phi^T_{,i} - g(x_3 - h_G)\Big] n_j ds \\ &\quad + \varrho \iint_{S_{bs}} \Big[U^2\phi^S_{,1} - \frac{1}{2}U^2\phi^S_{,i}\phi^S_{,i}\Big] n_j ds \qquad j = 1,2,\ldots 6, \end{aligned} \tag{3.143}$$

where F_1, F_2, and F_3 are the forces and F_4, F_5, F_6 are the moments. The second integral in Equation (3.143) is a steady force component and will be exactly offset

by the steady propulsive force, for it is assumed that the perturbations occur in a system which is otherwise in equilibrium.

Neglecting the steady pressure terms and the high-order terms in ϕ^S and ϕ^T in the Bernoulli's equation, the forces and moments (3.143) can be evaluated as

$$\begin{aligned} F_j &= -\varrho \iint_{S_{bs}} \left[\frac{\partial \phi^T}{\partial t} - U\phi^T_{,1} - g(x_3 - h_G)\right] n_j ds \\ &= \Re(F_j^I + F_j^D + F_j^R) + F_j^S \qquad j = 1, 2, \ldots, 6, \end{aligned} \tag{3.144}$$

where F_j^I are the forces and moments due to incident wave, F_j^D are the forces and moments due to diffraction wave, F_j^R are the forces and moments due to radiation wave produced by six degrees of ship body motion, and F_j^S are the ordinary buoyancy restoring forces and moments,

$$F_j^I = -\varrho e^{\imath\omega_e t} \iint_{S_{bs}} (\imath\omega_e \Phi_0 - U\Phi_{0,1})\widetilde{n}_j ds, \tag{3.145}$$

$$F_j^D = -\varrho e^{\imath\omega_e t} \iint_{S_{bs}} (\imath\omega_e \Phi_7 - U\Phi_{7,1})\widetilde{n}_j ds, \tag{3.146}$$

$$F_j^R = -\varrho e^{\imath\omega_e t} \iint_{S_{bs}} (\imath\omega_e \Xi_i \Phi_i - U\Xi_i \Phi_{i,1})\widetilde{n}_j ds, \qquad i = 1, 2, \ldots, 6, \tag{3.147}$$

$$F_j^S = \varrho g \iint_{S_{bs}} (x_3 - h_G)\widetilde{n}_j ds. \tag{3.148}$$

3.6.1 Radiation Forces and Hydrodynamic Coefficients

The details of calculating radiation forces and moments F_j^R can be found in the work of Salvesen, *et al* [56].

$$F_j^R = -\varrho e^{\imath\omega_e t} \iint_{S_{bs}} (\imath\omega_e \Xi_i \Phi_i - U\Xi_i \Phi_{i,1})\widetilde{n}_j ds$$

$$
\begin{aligned}
&= e^{\imath\omega_e t}\Big(-\imath\omega_e\varrho \iint\limits_{S_{bs}} \Xi_i\Phi_i\widetilde{n}_j ds + \varrho \iint\limits_{S_{bs}} \Xi_i\Phi_i\widetilde{m}_j ds - \varrho U \int\limits_{\underline{S}_{bsa}} \Xi_i\Phi_i\widetilde{n}_j d\underline{\ell}\Big) \\
&= e^{\imath\omega_e t}\Big(-\imath\omega_e\varrho \iint\limits_{S_{bs}} \Xi_i\Phi_i\widetilde{n}_j ds + \varrho U \iint\limits_{S_{bs}} \delta_{5j}\Xi_i\Phi_i\widetilde{n}_3 ds \\
&\quad - \varrho U \iint\limits_{S_{bs}} \delta_{6j}\Xi_i\Phi_i\widetilde{n}_2 ds - \varrho U \int\limits_{\underline{S}_{bsa}} \Xi_i\Phi_i\widetilde{n}_j d\underline{\ell}\Big),
\end{aligned}
\tag{3.149}
$$

where $i = 1, 2, \ldots, 6$, $\underline{S}_{bsa}$ refers to the underwater contour of the aftermost section of the ship. Considering Equation (3.76), Equation (3.149) can be expressed as

$$
\begin{aligned}
F_j^R = \Xi_i e^{\imath\omega_e t}\Big(&-\imath\omega_e\varrho \iint\limits_{S_{bs}} \Phi_i^0\widetilde{n}_j ds - \delta_{5i}\varrho U \iint\limits_{S_{bs}} \Phi_3^0\widetilde{n}_j ds + \delta_{6i}\varrho U \iint\limits_{S_{bs}} \Phi_2^0\widetilde{n}_j ds \\
&+ \delta_{5j}\varrho U \iint\limits_{S_{bs}} \Phi_i^0\widetilde{n}_3 ds + \delta_{5j}\delta_{5i}\frac{\varrho U^2}{\imath\omega_e} \iint\limits_{S_{bs}} \Phi_3^0\widetilde{n}_3 ds - \delta_{5j}\delta_{6i}\frac{\varrho U^2}{\imath\omega_e} \iint\limits_{S_{bs}} \Phi_2^0\widetilde{n}_3 ds \\
&- \delta_{6j}\varrho U \iint\limits_{S_{bs}} \Phi_i^0\widetilde{n}_2 ds - \delta_{6j}\delta_{5i}\frac{\varrho U^2}{\imath\omega_e} \iint\limits_{S_{bs}} \Phi_3^0\widetilde{n}_2 ds + \delta_{6j}\delta_{6i}\frac{\varrho U^2}{\imath\omega_e} \iint\limits_{S_{bs}} \Phi_2^0\widetilde{n}_2 ds \\
&- \varrho U \int\limits_{\underline{S}_{bsa}} \Phi_i^0\widetilde{n}_j d\underline{\ell} - \delta_{5i}\frac{\varrho U^2}{\imath\omega_e} \int\limits_{\underline{S}_{bsa}} \Phi_3^0\widetilde{n}_j d\underline{\ell} + \delta_{6i}\frac{\varrho U^2}{\imath\omega_e} \int\limits_{\underline{S}_{bsa}} \Phi_2^0\widetilde{n}_j d\underline{\ell}\Big),
\end{aligned}
\tag{3.150}
$$

where $i, j = 1, 2, \ldots, 6$. Completely complying with the "strip theory" assumptions in §3.4.4, the surface integrals of Φ_i^0 in Equation (3.150) can be computed as

$$
\begin{aligned}
\iint\limits_{S_{bs}} \Phi_i^0\widetilde{n}_j ds &= -\frac{1}{\imath\varrho\omega_e} \int\limits_{L_{ship}} \Big(-\imath\varrho\omega_e \int\limits_{\underline{S}_{bs}} \Phi_i^0\widetilde{n}_j d\underline{\ell}\Big) dx_1 \\
&= \begin{cases}
0 & j = 1 \\
-\dfrac{1}{\imath\varrho\omega_e} \displaystyle\int\limits_{L_{ship}} \Big(-\imath\varrho\omega_e \int\limits_{\underline{S}_{bs}} \underline{\Phi}_i\widetilde{\underline{n}}_j d\underline{\ell}\Big) dx_1 & j = 2, 3, 4 \\
\dfrac{1}{\imath\varrho\omega_e} \displaystyle\int\limits_{L_{ship}} \Big(-\imath\varrho\omega_e \int\limits_{\underline{S}_{bs}} \underline{\Phi}_i\widetilde{\underline{n}}_3 d\underline{\ell}\Big) x_1 dx_1 & j = 5 \\
-\dfrac{1}{\imath\varrho\omega_e} \displaystyle\int\limits_{L_{ship}} \Big(-\imath\varrho\omega_e \int\limits_{\underline{S}_{bs}} \underline{\Phi}_i\widetilde{\underline{n}}_2 d\underline{\ell}\Big) x_1 dx_1 & j = 6
\end{cases}
\end{aligned}
\tag{3.151}
$$

$$
= \begin{cases}
-\dfrac{1}{\imath\varrho\omega_e}\displaystyle\int_{L_{ship}}\Big(-\imath\varrho\omega_e\int_{\underline{S}_{bs}}\underline{\Phi}_i\widetilde{\underline{n}}_j d\underline{\ell}\Big)dx_1 & j,i=2,3,4,\\
\dfrac{1}{\imath\varrho\omega_e}\displaystyle\int_{L_{ship}}\Big(-\imath\varrho\omega_e\int_{\underline{S}_{bs}}\underline{\Phi}_3\widetilde{\underline{n}}_j d\underline{\ell}\Big)x_1dx_1 & j=2,3,4,\ i=5,\\
-\dfrac{1}{\imath\varrho\omega_e}\displaystyle\int_{L_{ship}}\Big(-\imath\varrho\omega_e\int_{\underline{S}_{bs}}\underline{\Phi}_2\widetilde{\underline{n}}_j d\underline{\ell}\Big)x_1dx_1 & j=2,3,4,\ i=6,\\
\dfrac{1}{\imath\varrho\omega_e}\displaystyle\int_{L_{ship}}\Big(-\imath\varrho\omega_e\int_{\underline{S}_{bs}}\underline{\Phi}_i\widetilde{\underline{n}}_3 d\underline{\ell}\Big)x_1dx_1 & j=5,\ i=2,3,4,\\
-\dfrac{1}{\imath\varrho\omega_e}\displaystyle\int_{L_{ship}}\Big(-\imath\varrho\omega_e\int_{\underline{S}_{bs}}\underline{\Phi}_3\widetilde{\underline{n}}_3 d\underline{\ell}\Big)x_1^2dx_1 & j,i=5,\\
\dfrac{1}{\imath\varrho\omega_e}\displaystyle\int_{L_{ship}}\Big(-\imath\varrho\omega_e\int_{\underline{S}_{bs}}\underline{\Phi}_2\widetilde{\underline{n}}_3 d\underline{\ell}\Big)x_1^2dx_1 & j=5,\ i=6,\\
-\dfrac{1}{\imath\varrho\omega_e}\displaystyle\int_{L_{ship}}\Big(-\imath\varrho\omega_e\int_{\underline{S}_{bs}}\underline{\Phi}_i\widetilde{\underline{n}}_2 d\underline{\ell}\Big)x_1dx_1 & j=6,\ i=2,3,4,\\
\dfrac{1}{\imath\varrho\omega_e}\displaystyle\int_{L_{ship}}\Big(-\imath\varrho\omega_e\int_{\underline{S}_{bs}}\underline{\Phi}_3\widetilde{\underline{n}}_2 d\underline{\ell}\Big)x_1^2dx_1 & j=6,\ i=5,\\
-\dfrac{1}{\imath\varrho\omega_e}\displaystyle\int_{L_{ship}}\Big(-\imath\varrho\omega_e\int_{\underline{S}_{bs}}\underline{\Phi}_2\widetilde{\underline{n}}_2 d\underline{\ell}\Big)x_1^2dx_1 & j,i=6,\\
0 & i,j=\text{all other values},
\end{cases}
$$

where $\underline{\Phi}_i$, $i=2,3,4$ are the two-dimensional velocity potential at each cross section, L_{ship} is the ship length, $\underline{S}_{bs}$ is the underwater part of the contour of each cross section, and $\widetilde{\underline{n}}_i$, $i=2,3,4$ is the generalised normal vector in the cross section plane (x_2,x_3-plane). It is now clear that the three-dimensional radiation forces (3.150) eventually are the functions of the two-dimensional integrals

$$
-\imath\omega_e\varrho\int_{\underline{S}_{bs}}\underline{\Phi}_i\widetilde{\underline{n}}_j d\underline{\ell}.
$$

By applying the conformal mapping Equations (3.92) and (3.93), those integrals can be computed as

i. for $j = 2, i = 2, 3, 4,$

$$\begin{aligned} -\imath\omega_e\varrho \int_{\underline{S}_{bs}} \underline{\Phi}_i \underline{\widetilde{n}}_2 d\underline{\ell} &= -\imath\omega_e\varrho \int_{\underline{S}_{bs}} \underline{\Phi}_i \frac{\partial x_3}{\partial \underline{\ell}} d\underline{\ell} \\ &= -\imath\omega_e\varrho \int_{\underline{S}_{bs}} \underline{\Phi}_i dx_3 \\ &= -\imath\omega_e\varrho \int_{-\frac{\pi}{2}}^{\frac{\pi}{2}} \underset{\sim}{\Phi}_i \frac{\partial \boldsymbol{x}_3}{\partial \vartheta}\Big|_{r=1} d\vartheta. \end{aligned} \tag{3.152}$$

ii. for $j = 3, i = 2, 3, 4,$

$$\begin{aligned} -\imath\omega_e\varrho \int_{\underline{S}_{bs}} \underline{\Phi}_i \underline{\widetilde{n}}_3 d\underline{\ell} &= \imath\omega_e\varrho \int_{\underline{S}_{bs}} \underline{\Phi}_i \frac{\partial x_2}{\partial \underline{\ell}} d\underline{\ell} \\ &= \imath\omega_e\varrho \int_{\underline{S}_{bs}} \underline{\Phi}_i dx_2 \\ &= \imath\omega_e\varrho \int_{-\frac{\pi}{2}}^{\frac{\pi}{2}} \underset{\sim}{\Phi}_i \frac{\partial \boldsymbol{x}_2}{\partial \vartheta}\Big|_{r=1} d\vartheta. \end{aligned} \tag{3.153}$$

iii. for $j = 4, i = 2, 3, 4,$

$$\begin{aligned} -\imath\omega_e\varrho \int_{\underline{S}_{bs}} \underline{\Phi}_i \underline{\widetilde{n}}_4 d\underline{\ell} &= \imath\omega_e\varrho \int_{\underline{S}_{bs}} \underline{\Phi}_i \Big[x_2 \frac{\partial x_2}{\partial \underline{\ell}} + x_3 \frac{\partial x_3}{\partial \underline{\ell}}\Big] d\underline{\ell} \\ &= \imath\omega_e\varrho \int_{\underline{S}_{bs}} \underline{\Phi}_i (x_2 dx_2 + x_3 dx_3) \\ &= \imath\omega_e\varrho \int_{-\frac{\pi}{2}}^{\frac{\pi}{2}} \underset{\sim}{\Phi}_i \Big[\boldsymbol{x}_2 \frac{\partial \boldsymbol{x}_2}{\partial \vartheta} + (\boldsymbol{x}_3 + h_G) \frac{\partial \boldsymbol{x}_3}{\partial \vartheta}\Big]_{r=1} d\vartheta. \end{aligned} \tag{3.154}$$

$\underline{\Phi}_i e^{\imath\omega_e t}$ can be considered as the velocity potential due to the unit amplitude oscillatory motion $e^{\imath\omega_e t}$ of a cross section in the ith mode. Let $\underline{F}_j^R$ be the hydrody-

namic forces acting on a cross section, it follows

$$\begin{aligned} \underline{F}_j^R &= e^{\imath\omega_e t}\sum_{i=2}^{4}\Big(-\imath\omega_e\varrho\int_{\underline{S}_{bs}}\underline{\Phi}_i\widetilde{\underline{n}}_j d\underline{\ell}\Big) \\ &= -e^{\imath\omega_e t}\sum_{i=2}^{4}(-\omega_e^2\underline{A}_{ji}+\imath\omega_e\underline{B}_{ji}), \end{aligned} \tag{3.155}$$

where the integrals are separated into real and imaginary parts. The coefficients $\underline{A}_{ji}$, $\underline{B}_{ji}$ are real and correspond, respectively, to the force components due to acceleration and velocity of the section. So that $\underline{A}_{ji}$ are two-dimensional added-mass coefficients and $\underline{B}_{ji}$ are two-dimensional damping coefficients of a section.

Similarly, radiation forces F_j^R (3.150) can be expressed in terms of their real and imaginary parts as well,

$$F_j^R = -(-\omega_e^2 A_{ji}+\imath\omega_e B_{ji})\Xi_i e^{\imath\omega_e t} \qquad i,j=1,2,\ldots,6, \tag{3.156}$$

where A_{ji} and B_{ji} are three-dimensional added-mass and damping coefficients, and correspond to the force components due to acceleration $-\omega_e^2\Xi_i e^{\imath\omega_e t}$ and velocity $\imath\omega_e\Xi_i e^{\imath\omega_e t}$ of the ship respectively. By Equations (3.150), (3.151) and (3.155), the non-zero three-dimensional hydrodynamic coefficients A_{ji}, B_{ji} can be computed from two-dimensional hydrodynamic coefficients $\underline{A}_{ji}$, $\underline{B}_{ji}$ as follows:

i. for $j=2,3,4$

$$A_{ji} = \int_{L_{ship}}\underline{A}_{ji}dx_1 - \frac{U}{\omega_e^2}\underline{B}^a_{ji} \qquad i=2,3,4, \tag{3.157}$$

$$B_{ji} = \int_{L_{ship}}\underline{B}_{ji}dx_1 + U\underline{A}^a_{ji} \qquad i=2,3,4, \tag{3.158}$$

$$A_{j5} = -\int_{L_{ship}}x_1\underline{A}_{j3}dx_1 - \frac{U}{\omega_e^2}\int_{L_{ship}}\underline{B}_{j3}dx_1 + \frac{U}{\omega_e^2}X_1^a\underline{B}^a_{j3} - \frac{U^2}{\omega_e^2}\underline{A}^a_{j3}, \tag{3.159}$$

$$B_{j5} = -\int_{L_{ship}} x_1 \underline{B}_{j3} dx_1 + U \int_{L_{ship}} \underline{A}_{j3} dx_1 - U X_1^a \underline{A}_{j3}^a - \frac{U^2}{\omega_e^2} \underline{B}_{j3}^a, \tag{3.160}$$

$$A_{j6} = \int_{L_{ship}} x_1 \underline{A}_{j2} dx_1 + \frac{U}{\omega_e^2} \int_{L_{ship}} \underline{B}_{j2} dx_1 - \frac{U}{\omega_e^2} X_1^a \underline{B}_{j2}^a + \frac{U^2}{\omega_e^2} \underline{A}_{j2}^a, \tag{3.161}$$

$$B_{j6} = \int_{L_{ship}} x_1 \underline{B}_{j2} dx_1 - U \int_{L_{ship}} \underline{A}_{j2} dx_1 + U X_1^a \underline{A}_{j2}^a + \frac{U^2}{\omega_e^2} \underline{B}_{j2}^a, \tag{3.162}$$

ii. for $j = 5, 6$

$$A_{5i} = -\int_{L_{ship}} x_1 \underline{A}_{3i} dx_1 + \frac{U}{\omega_e^2} \int_{L_{ship}} \underline{B}_{3i} dx_1 + \frac{U}{\omega_e^2} X_1^a \underline{B}_{3i}^a \qquad i = 2, 3, 4, \tag{3.163}$$

$$B_{5i} = -\int_{L_{ship}} x_1 \underline{B}_{3i} dx_1 - U \int_{L_{ship}} \underline{A}_{3i} dx_1 - U X_1^a \underline{A}_{3i}^a \qquad i = 2, 3, 4, \tag{3.164}$$

$$A_{55} = \int_{L_{ship}} x_1^2 \underline{A}_{33} dx_1 + \frac{U^2}{\omega_e^2} \int_{L_{ship}} \underline{A}_{33} dx_1 - \frac{U}{\omega_e^2} (X_1^a)^2 \underline{B}_{33}^a + \frac{U^2}{\omega_e^2} X_1^a \underline{A}_{33}^a, \tag{3.165}$$

$$B_{55} = \int_{L_{ship}} x_1^2 \underline{B}_{33} dx_1 + \frac{U^2}{\omega_e^2} \int_{L_{ship}} \underline{B}_{33} dx_1 + U (X_1^a)^2 \underline{A}_{33}^a + \frac{U^2}{\omega_e^2} X_1^a \underline{B}_{33}^a, \tag{3.166}$$

$$A_{56} = -\int_{L_{ship}} x_1^2 \underline{A}_{32} dx_1 - \frac{U^2}{\omega_e^2} \int_{L_{ship}} \underline{A}_{32} dx_1 + \frac{U}{\omega_e^2} (X_1^a)^2 \underline{B}_{32}^a - \frac{U^2}{\omega_e^2} X_1^a \underline{A}_{32}^a, \tag{3.167}$$

$$B_{56} = -\int_{L_{ship}} x_1^2 \underline{B}_{32} dx_1 - \frac{U^2}{\omega_e^2} \int_{L_{ship}} \underline{B}_{32} dx_1 - U (X_1^a)^2 \underline{A}_{32}^a - \frac{U^2}{\omega_e^2} X_1^a \underline{B}_{32}^a, \tag{3.168}$$

$$A_{6i} = \int_{L_{ship}} x_1 \underline{A}_{2i} dx_1 - \frac{U}{\omega_e^2} \int_{L_{ship}} \underline{B}_{2i} dx_1 - \frac{U}{\omega_e^2} X_1^a \underline{B}_{2i}^a \qquad i = 2, 3, 4, \tag{3.169}$$

$$B_{6i} = \int_{L_{ship}} x_1 \underline{B}_{2i} dx_1 + U \int_{L_{ship}} \underline{A}_{2i} dx_1 + U X_1^a \underline{A}_{2i}^a \qquad i = 2, 3, 4, \tag{3.170}$$

$$A_{65} = -\int_{L_{ship}} x_1^2 \underline{A}_{23} dx_1 - \frac{U^2}{\omega_e^2} \int_{L_{ship}} \underline{A}_{23} dx_1 + \frac{U}{\omega_e^2} (X_1^a)^2 \underline{B}_{23}^a - \frac{U^2}{\omega_e^2} X_1^a \underline{A}_{23}^a, \tag{3.171}$$

$$B_{65} = -\int_{L_{ship}} x_1^2 \underline{B}_{23} dx_1 - \frac{U^2}{\omega_e^2} \int_{L_{ship}} \underline{B}_{23} dx_1 - U (X_1^a)^2 \underline{A}_{23}^a - \frac{U^2}{\omega_e^2} X_1^a \underline{B}_{23}^a, \tag{3.172}$$

$$A_{66} = \int_{L_{ship}} x_1^2 \underline{A}_{22} dx_1 + \frac{U^2}{\omega_e^2} \int_{L_{ship}} \underline{A}_{22} dx_1 - \frac{U}{\omega_e^2} (X_1^a)^2 \underline{B}_{22}^a + \frac{U^2}{\omega_e^2} X_1^a \underline{A}_{22}^a, \tag{3.173}$$

$$B_{66} = \int_{L_{ship}} x_1^2 \underline{B}_{22} dx_1 + \frac{U^2}{\omega_e^2} \int_{L_{ship}} \underline{B}_{22} dx_1 + U(X_1^a)^2 \underline{A}_{22}^a + \frac{U^2}{\omega_e^2} X_1^a \underline{B}_{22}^a, \tag{3.174}$$

where $\underline{A}_{ji}^a$ and $\underline{B}_{ji}^a$ refer to the added-mass and damping coefficients of the aftermost section, and X_1^a is the position of the aftermost section on x_1-axis.

3.6.2 Exciting Forces

Incident wave forces F_j^I, $j = 1, 2, \ldots, 6$ and diffraction forces F_j^D, $j = 1, 2, \ldots, 6$ are the exciting forces concerned in seakeeping research.

Introducing the incident wave potential (3.55) into the expression of the incident wave forces and moments (3.145) gives

$$\begin{aligned} F_j^I &= \boldsymbol{F}_j^I e^{\imath\omega_e t} = -\imath\varrho\omega_0 e^{\imath w_e t} \iint_{S_{bs}} \Phi_0 \widetilde{n}_j ds \\ &= \varrho\eta_0 g e^{\imath w_e t} \iint_{S_{bs}} e^{-K_0(x_3 - h_G + \imath x_1 \cos\mu - \imath x_2 \sin\mu)} \widetilde{n}_j ds \\ &= \begin{cases} 0 & j = 1, \\ \varrho\eta_0 e^{\imath w_e t} \int_{L_{ship}} \underline{F}_j^I dx_1 & j = 2, 3, 4, \\ -\varrho\eta_0 e^{\imath w_e t} \int_{L_{ship}} x_1 \underline{F}_3^I dx_1 & j = 5, \\ \varrho\eta_0 e^{\imath w_e t} \int_{L_{ship}} x_1 \underline{F}_2^I dx_1 & j = 6, \end{cases} \end{aligned} \tag{3.175}$$

where the "strip theory" assumptions in §3.4.4 are used, $\underline{F}_j^I$ are the sectional incident wave forces given by

$$\underline{F}_j^I = g e^{-\imath K_0 x_1 \cos\mu} \int_{\underline{S}_{bs}} e^{K_0(\imath x_2 \sin\mu - x_3 + h_G)} \underline{\widetilde{n}}_j d\underline{\ell} \qquad j = 2, 3, 4. \tag{3.176}$$

As has been discussed earlier, the explicit solution for the diffraction wave potential is not always necessary. By using Haskind relationship, Salvesen, *et al* [56] gave the computation of diffraction force, in the form

$$
\begin{aligned}
F_j^D &= \boldsymbol{F}_j^D e^{\imath\omega_e t} = -\varrho e^{\imath\omega_e t} \iint_{S_{bs}} (\imath\omega_e \Phi_7 - U\Phi_{7,1})\widetilde{n}_j ds, \\
&= -\varrho e^{\imath\omega_e t} \iint_{S_{bs}} (\imath\omega_e \widetilde{n}_j - \widetilde{m}_j)\Phi_7 ds - \varrho U e^{\imath\omega_e t} \int_{\underline{S}_{bsa}} \Phi_7 \widetilde{n}_j d\underline{\ell} \\
&= -\varrho e^{\imath\omega_e t} \iint_{S_{bs}} (\Phi^0_{j,i} n_i - \frac{1}{\imath\omega_e}\Phi^U_{j,i} n_i)\Phi_7 ds - \frac{\varrho U}{\imath\omega_e} e^{\imath\omega_e t} \int_{\underline{S}_{bsa}} \Phi_7 \Phi_{j,i} n_i d\underline{\ell} \\
&= -\varrho e^{\imath\omega_e t} \iint_{S_{bs}} (\Phi^0_j - \frac{1}{\imath\omega_e}\Phi^U_j)\Phi_{7,i} n_i ds - \frac{\varrho U}{\imath\omega_e} e^{\imath\omega_e t} \int_{\underline{S}_{bsa}} \Phi^0_j \Phi_{7,i} n_i d\underline{\ell} \\
&= \varrho e^{\imath\omega_e t} \iint_{S_{bs}} (\Phi^0_j - \frac{1}{\imath\omega_e}\Phi^U_j)\Phi_{0,i} n_i ds + \frac{\varrho U}{\imath\omega_e} e^{\imath\omega_e t} \int_{\underline{S}_{bsa}} \Phi^0_j \Phi_{0,i} n_i d\underline{\ell} \\
&= \varrho e^{\imath\omega_e t} \iint_{S_{bs}} (\Phi^0_j - \frac{1}{\imath\omega_e}\Phi^U_j)(\imath n_2 \sin\mu + n_3) K_0 \Phi_0 ds \\
&\quad + \frac{\varrho U}{\imath\omega_e} e^{\imath\omega_e t} \int_{\underline{S}_{bsa}} \Phi^0_j (\imath n_2 \sin\mu + n_3) K_0 \Phi_0 d\underline{\ell}.
\end{aligned}
\tag{3.177}
$$

Using Equations (3.73-3.75), as well as the same "strip theory" assumptions, the diffraction forces (3.177) becomes

$$
\boldsymbol{F}_j^D = \begin{cases}
0 & j = 0, \\
\varrho\eta_0 \Big[\int_{L_{ship}} \underline{F}_j^D dx + \frac{U}{\imath\omega_e} \underline{F}_j^{Da} \Big] & j = 2, 3, 4, \\
-\varrho\eta_0 \Big[\int_{L_{ship}} (x_1 \underline{F}_3^D + \frac{U}{\imath\omega_e} \underline{F}_3^{Da}) dx_1 + \frac{U}{\imath\omega_e} X_1^a \underline{F}_3^{Da} \Big] & j = 5, \\
\varrho\eta_0 \Big[\int_{L_{ship}} (x_1 \underline{F}_2^D + \frac{U}{\imath\omega_e} \underline{F}_2^{Da}) dx_1 + \frac{U}{\imath\omega_e} X_1^a \underline{F}_2^{Da} \Big] & j = 6,
\end{cases}
\tag{3.178}
$$

where $\underline{F}_j^D$ are defined as sectional diffraction forces, and given by

$$\underline{F}_j^D = \omega_0 e^{-\imath x_1 K_0 \cos\mu} \int_{\underline{S}_{bs}} (\imath \underline{n}_3 - \underline{n}_2 \sin\mu) e^{K_0(\imath x_2 \sin\mu - x_3 + h_G)} \underline{\Phi}_j d\underline{\ell} \quad j = 2,3,4. \tag{3.179}$$

$\underline{F}_j^{Da}$ refers to $\underline{F}_j^D$ evaluated at the aftermost section.

3.6.3 Hydrostatic Restoring Forces

Newman [44] has given the expressions for the hydrostatic forces F_j^S. Applying Gauss's theorem to Equation (3.148) and considering the forces and moments separately yields

$$\vec{F}^{SF} = -\vec{e}_3 \varrho g \iiint_{V_{bs}} dv, \tag{3.180}$$

$$\vec{F}^{SM} = -\varrho g \iiint_{V_{bs}} (\vec{e}_1 x_2 - \vec{e}_2 x_1) dv, \tag{3.181}$$

where $\vec{e}_i$, $i = 1,2,3$ are unit base vectors of coordinate system $o(x_1, x_2, x_3)$, V_{bs} is the displaced volume of ship body enclosed by the surface S_{bs} and plane $x_3 = h_G$.

Since the centre of gravity moves with the ship, it is convenient to replace the moment $\vec{F}^{SM}$ in Equation (3.181) by the moment $\vec{F}^{SM'}$ about the origin of the body-fixed coordinate system $o'(x_1', x_2', x_3')$,

$$\vec{F}^{SM'} = \varrho g \iiint_{V_{bs}} [\vec{e}_1(-x_2 + \xi_2) + \vec{e}_2(x_1 - \xi_1)] dv, \tag{3.182}$$

The volume integral in Equation (3.182) can be evaluated in terms of the body-fixed coordinate system $o'(x_1', x_2', x_3')$, in which the volume V_{bs} can be decomposed into the static volume V_0' beneath the plane $x_3' = h_G$ and the thin layer bounded

by the planes $x_3' = h_G$ and $x_3 = h_G$. Thus

$$\begin{aligned}
\vec{F}^{SM'} &= \varrho g \iiint_{V_0'} [\vec{e}_1(-x_2' - \xi_6 x_1' + \xi_4 x_3' - \xi_4 h_G) + \vec{e}_2(x_1' + \xi_5 x_3' - \xi_5 h_G - \xi_6 x_2')] dv \\
&\quad + \varrho g \iint_{S_0'} [\vec{e}_1(-x_2' - \xi_6 x_1' + \xi_4 x_3' - \xi_4 h_G) + \vec{e}_2(x_1' + \xi_5 x_3' - \xi_5 h_G \\
&\qquad - \xi_6 x_2')](\xi_3 + \xi_4 x_2' - \xi_5 x_1') dx_1' dx_2' \\
&= \varrho g \iiint_{V_0'} [\vec{e}_1(-x_2' - \xi_6 x_1' + \xi_4 x_3' - \xi_4 h_G) + \vec{e}_2(x_1' + \xi_5 x_3' - \xi_5 h_G - \xi_6 x_2')] dv \\
&\quad + \varrho g \iint_{S_0'} [\vec{e}_1(-\xi_3 x_2' - \xi_4 x_2'^2 + \xi_5 x_1' x_2') + \vec{e}_2(\xi_3 x_1' + \xi_4 x_1' x_2' - \xi_5 x_1'^2)] dx_1' dx_2' \\
&= \varrho g V_{dsp} [\vec{e}_1(-X_1^{B'} \xi_6 - X_2^{B'} + X_3^{B'} \xi_4) + \vec{e}_2(X_1^{B'} - X_2^{B'} \xi_6 + X_3^{B'} \xi_5)] \\
&\quad + \varrho g [\vec{e}_1(-S_2^{W'} \xi_3 - S_{22}^{W'} \xi_4 + S_{12}^{W'} \xi_5) + \vec{e}_2(S_1^{W'} \xi_3 + S_{12}^{W'} \xi_4 - S_{11}^{W'} \xi_5)],
\end{aligned} \tag{3.183}$$

where V_{dsp} is the displaced volume, $S_i^{W'}$ and $S_{ij}^{W'}$ are the waterplane moments defined as

$$S_i^{W'} = \iint_{S_0'} x_i' dx_1' dx_2', \tag{3.184}$$

$$S_{ij}^{W'} = \iint_{S_0'} x_i' x_j' dx_1' dx_2', \tag{3.185}$$

and $X_i^{B'}$ is the centre of buoyancy,

$$X_i^{B'} = \frac{1}{V_{dsp}} \iiint_{V_0'} x_i' dv. \tag{3.186}$$

Similarly, $\vec{F}^{SF}$ in Equation (3.180) can be computed in the form

$$\begin{aligned}\vec{F}^{SF} &= -\vec{e}_3 \varrho g V_{dsp} - \vec{e}_3 \varrho g \iint_{S_0'} (\xi_3 + x_2'\xi_4 - x_1'\xi_5) dx_1' dx_2' \\ &= \vec{e}_3(-\varrho g V_{dsp} - \varrho g S^{W'}\xi_3 - \varrho g S_2^{W'}\xi_4 + \varrho g S_1^{W'}\xi_5),\end{aligned} \tag{3.187}$$

where $S^{W'}$ denotes the waterplane area.

For convenience the force and moment due to the weight of the ship body are usually incorporated into hydrostatic force and moment. The force associated with the body weight is $\{0, 0, mg\}$, where m is the ship body mass. The corresponding moment is given by the vector

$$\{X_1^{G'}\xi_6 + X_2^{G'} - X_3^{G'}\xi_4, -X_1^{G'} + X_2^{G'}\xi_6 - X_3^{G'}\xi_5, 0\},$$

where $X_i^{G'}$ is the centre of gravity.

By defining hydrostatic force coefficient matrix C_{ji} as

$$C_{ji} = \begin{Bmatrix} 0 & 0 & 0 & 0 & 0 & 0 \\ 0 & 0 & 0 & 0 & 0 & 0 \\ 0 & 0 & \varrho g S^{W'} & \varrho g S_2^{W'} & -\varrho g S_1^{W'} & 0 \\ 0 & 0 & \varrho g S_2^{W'} & \varrho g S_{22}^{W'} + mgX_3^{G'} - \varrho g V_{dsp} X_3^{B'} & -\varrho g S_{12}^{W'} & -mX_1^{G'} + \varrho g V_{dsp} X_1^{B'} \\ 0 & 0 & -\varrho g S_1^{W'} & -\varrho g S_{12}^{W'} & \varrho g S_{11}^{W'} + mgX_3^{G'} - \varrho g V_{dsp} X_3^{B'} & -mX_2^{G'} + \varrho g V_{dsp} X_2^{B'} \\ 0 & 0 & 0 & 0 & 0 & 0 \end{Bmatrix}, \tag{3.188}$$

the total hydrostatic force (3.148) can be expressed in the form

$$F_j^S = -C_{ji}\xi_i \qquad i, j = 1, 2, \ldots, 6. \tag{3.189}$$

3.7 Ship Motion Equations & Time-Domain Method

If the ship is considered as a rigid body with six degrees of freedom, with respect to the moving coordinate system $o(x, y, z)$, its motions can now be determined by Newton's Second Law of motion,

$$M_{ji}\frac{d^2\xi_i}{dt^2} = \Re(F_j^I + F_j^D + F_j^R) + F_j^S \qquad i, j = 1, 2, \ldots, 6, \tag{3.190}$$

where M_{ji} is the generalised mass matrix for the ship,

$$M_{ji} = \begin{Bmatrix} m & 0 & 0 & 0 & mX_3^G & -mX_2^G \\ 0 & m & 0 & -mX_3^G & 0 & mX_1^G \\ 0 & 0 & m & mX_2^G & -mX_1^G & 0 \\ 0 & -mX_3^G & mX_2^G & I_{11} & I_{12} & I_{13} \\ mX_3^G & 0 & -mX_1^G & I_{21} & I_{22} & I_{23} \\ -mX_2^G & mX_1^G & 0 & I_{31} & I_{32} & I_{33} \end{Bmatrix}, \tag{3.191}$$

where X_i^G is the location of centre of gravity with respect to the coordinate system $o(x_1, x_2, x_3)$, I_{ji} are the moments of inertia,

$$I_{ij} = \iiint_{V_{ship}} \varrho_{ship}(\delta_{ij}x_k x_k - x_i x_j)dv, \tag{3.192}$$

V_{ship} denotes the volume of ship and ϱ_{ship} is ship mass-density.

By combining Equations (3.62), (3.156), (3.177), (3.178) and (3.189), the ship motion Equation (3.190) turns into

$$[-\omega_e^2(M_{ji} + A_{ji}) + i\omega_e B_{ji} + C_{ji}]\Xi_i = \boldsymbol{F}_j^I + \boldsymbol{F}_j^D \qquad i, j = 1, 2, \ldots, 6. \tag{3.193}$$

There are six simultaneous linear equations, which can be solved for the body

motions Ξ_i by standard matrix-inversion techniques.

It can be noticed that all the forces (3.145 - 3.147) are computed by integrating pressure over the steady-state wetted surface S_{bs}, which is the underwater part of the hull when the ship is advancing in the calm water at speed U. This surface is assumed to keep unchanged throughout the calculation. When a ship is in severe seas, the underwater part of the hull may vary significantly with the time, which may result in significant differences between the quantities, such as added-mass and damping coefficients, calculated on S_{bs} and those calculated on instantaneous wetted surface. This accounts for an important reason that the present linear seakeeping theories fail to give satisfying prediction of a ship's motion in severe seas. It is only in time domain that the forces and hydrodynamic coefficients could be possibly calculated on exact wetted surface. Lin and Yue [36] extended time-domain Green function method to calculate large motions and waves loads of ships in severe seas, where the exact body boundary condition was used at any instantaneous time. Meanwhile Kring, *et al* [34] extended time-domain Rankine panel method. Both of these methods still have numerical difficulties and are very much time-consuming even when used in powerful computers. Therefore, the objective of this thesis is to extended traditional "strip-theory" from frequency domain to time domain, so that, not only all the added-mass, damping coefficients, and forces can be computed on the actual underwater part of the hull surface, but also the computation time can be saved.

Equation (3.193) has to be rewritten in the time-dependent form

$$(M_{ji} + A_{ji})\frac{d^2\xi_i}{dt^2} + B_{ji}\frac{d\xi_i}{dt} + C_{ji}\xi_i = \Re(F_j^I + F_j^D) \qquad i, j = 1, 2, \ldots, 6. \tag{3.194}$$

A time-stepping scheme, *e.g.* Newmark-β direct integration scheme, can then be employed to solve these equations. The incident wave forces F_j^I at each time step can be obtained straightforwardly by replacing the integral surface S_{bs} in the

Equation (3.177) with the instantaneous wetted surface S_b, because the incident wave potential Φ_0 is irrelevant to the underwater hull surface.

On the instantaneous wetted surface S_b, the diffraction wave potential Φ_7 must satisfy the same boundary as that on S_{bs} Equation (3.60) without any doubt. Meanwhile, Newman [45] has pointed out that the hull boundary condition for unsteady wave potential ϕ^T Equation (3.46) can be applied either on S_b or S_{bs} with the difference $\mathcal{O}(\alpha_i^2)$. Hence the formulation in §3.4.4 should remain unchanged if S_{bs} is replaced with S_b in every equation, that means Φ_j^0 can be computed by the same set of equations. Therefore, at any instantaneous time the diffraction force F_j^D and the radiation forces F_j^R (added-mass and damping coefficients) can be calculated by the same equations, Equation (3.177) and Equation (3.150) respectively, as long as S_{bs} is replaced with S_b in those equations.

The generalised mass matrix M_{ji} must also be calculated at each time step, since the centre of gravity X_i^G is moving in the coordinate system $o(x_1, x_2, x_3)$. All the moments of inertia I_{ji} remain, because the ship is no longer symmetric about x_1-axis all the time.

It seems that the ship motion equations (3.194) are ready to be solved now. However, it must be pointed out that these equations have been derived assuming the motions are sinusoidal in time, as evidenced by the fact that the added-mass A_{ji} and damping coefficients B_{ji} depend on the frequency ω_e. It can not be directly extended to the case where the time-dependence is more general. Thus, the exciting forces and ship motions are restricted to be sinusoidal in time in this thesis.

Chapter 4

Hydrodynamic Coefficients

4.1 Introduction

In the previous chapter the theory (*Time-Domain Strip Theory*) for predicting the ship's motions in the time domain has been established. This chapter presents the hydrodynamic coefficients computed using the program developed in accordance with the time-domain strip theory. A numerical scheme of extracting underwater hull is also presented. Two-dimensional (sectional) added-mass and damping coefficients are computed using Westlake and Wilson's multi-parameter conformal mapping method [71], and the results are compared with those computed by the Lewis conformal mapping method. The program is verified by comparing the numerical results of three-dimensional added-mass and damping coefficients with the experimental data and with the results produced by a Green function method program. The influences of heel angle on both the sectional hydrodynamic coefficients and the total three-dimensional hydrodynamic coefficients are accessed.

4.2 Numerical Description of a Ship's Hull

The ship's hull is usually represented by a number of parallel sections that are perpendicular to the longitudinal line, and each section is defined by a number of offsets. Sections may be positioned arbitrarily along the ship length. There are usually more sections at ship's fore and aft body then at mid body. Since the Simpson's integration rule is used to calculate the three-dimensional hydrodynamic coefficients from sectional hydrodynamic coefficients, the sections have to be equally spaced. Firstly a specified number of waterlines are interpolated from the definition of each section. The waterlines are not equally spaced, but closer to keel are more concentrated in order to capture the rapid change of hull profile there. From there waterlines the equally spaced sections are created simply by interpolation. It usually uses 21 sections in the traditional frequency-domain strip theory. However, the program developed with this thesis does not impose any limit on the number of sections as long as the computer has enough memory. In theory the more sections that are used, the more accurate results will be given, but the more computational time is needed as well.

Figure (4.1) presents the Series 60 hull form of block coefficient $C_B = 0.70$ [64]. The original data is given by Hudson [24] in *shipshape*'s HFG file format*. Eight waterlines and twelve sections, together with stem and stern profiles, are defined. Series 60 hull form represents traditional cruiser-stern commercial ships. It has sections of various typical shapes, *e.g.* rectangular, round and fine. Hence it is used in this chapter to validate conformal mapping program. Figure (4.2) is the rationalised Series 60 hull form with 21 equally spaced sections (between fore and aft perpendiculars), and for the sake of clarity only twelve waterlines (including keel and deck line) are shown. The number of waterlines are usually much more then twelve in real computation. Hull form is truncated at aft perpendicular.

*A commercial software for defining, fairing and drawing a set of ship's lines, developed by the Wolfson Unit for Marine Technology and Industrial Aerodynamics.

Table (4.1) presents the principal particulars of Series 60 hull form.

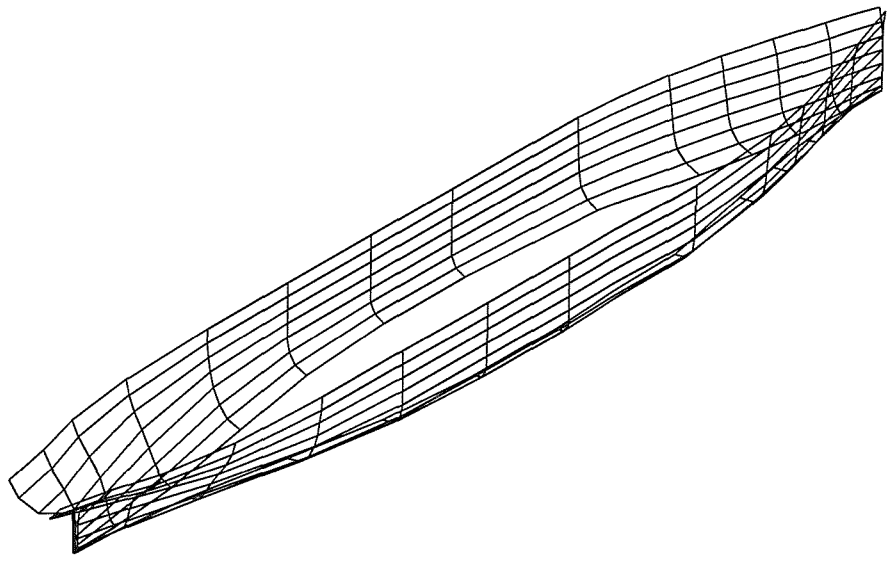

Figure 4.1: *Original Series 60 Hull Form.*

4.3 Extraction of Wetted Hull

Sections are usually defined in the body-fixed coordinate system $o'(x_1', x_2', x_3')$. In the frequency-domain strip theory, the underwater part of the hull is independent of time and extracted at equilibrium position, where the coordinate system $o'(x_1', x_2', x_3')$ is identical to the equilibrium coordinate system $o(x_1, x_2, x_3)$. The integration along the ship length therefore can be replaced with the integration along the x_1-axis (see Equation (3.151) in §3.6). However, in time-domain method the body-fixed coordinate system $o'(x_1', x_2', x_3')$ and the sections are oscillating with respect to the equilibrium coordinate system $o(x_1, x_2, x_3)$, sections are no longer perpendicular to the x_1-axis. The forces and hydrodynamics coefficients may have to be computed in the non-equilibrium coordinate system $o'(x_1', x_2', x_3')$, then transformed into equilibrium coordinate system $o(x_1, x_2, x_3)$. This proved to

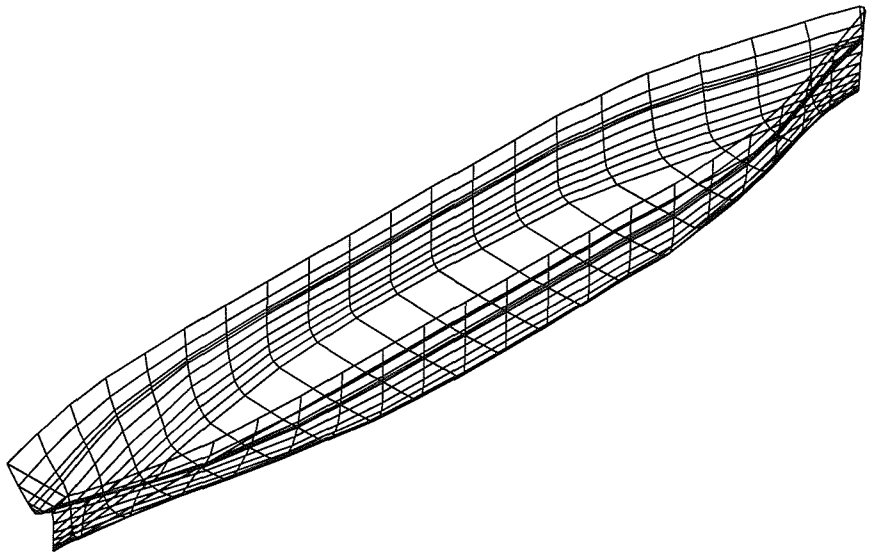

Figure 4.2: *Rationalised Series 60 Hull Form.*

Quantity	Symbol	Value
Length(between perpendiculars)	L_{ship}	$3.048m$
Beam	B	$0.435m$
Draught	T	$0.174m$
Displacement	V_{dsp}	$0.1616m^3$
Block Coefficient	C_B	0.70
Centre of Buoyancy(fwd. of midship)	LCB	$0.015m$
Longitudinal Centre of Gravity(fwd. of midship)	LCG	$0.015m$
Vertical Centre of Gravity(above keel)	VCG	$0.146m$
Metacentric Height	GM_T	$0.30m$

Table 4.1: *Principal Particulars of the Series 60 Hull Form.*

be very difficult. An alternative method is to replace the original sections with some equivalent sections, which are perpendicular to the x_1-axis at each time step. The sectional hydrodynamic coefficients and forces are calculated on those equivalent sections. The three-dimensional hydrodynamic coefficients and forces with respect to the equilibrium coordinate system $o(x_1, x_2, x_3)$ can then be computed in the same way as the frequency-domain strip theory, that is by integrating those sectional hydrodynamic coefficients and forces along the x_1-axis.

In order to find the equivalent sections, a number of reference planes have to be set up in the coordinate system $o(x_1, x_2, x_3)$ at first, such that the reference planes are perpendicular to the x_1-axis and pass through, respectively, the intersection points of x_1'-axis and the the original sections. The ith reference plane can be described by

$$\vec{e}_1 \cdot (\vec{x} - \vec{X}^{P_i}) = 0 \tag{4.1}$$

where $\vec{X}^{P_i}$ is position vector of the intersection point P_i in the coordinate system $o(x_1, x_2, x_3)$, shown in Figure (4.3). The equivalent sections are the intersections of these reference planes with the ship hull.

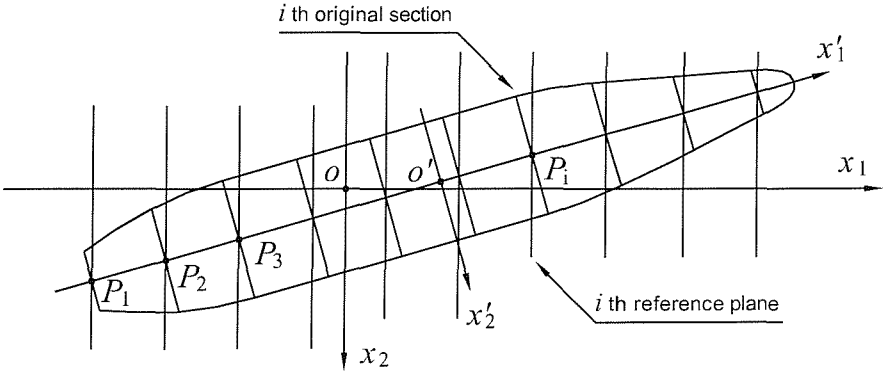

Figure 4.3: *Reference Planes in Equilibrium Coordinate System.*

The reference planes can also be defined with respect to the body-fixed coor-

dinate system $o'(x_1', x_2', x_3')$ by the equation

$$\vec{N}' \cdot (\vec{x}' - \vec{X}^{P_i'}) = 0, \tag{4.2}$$

where $\vec{X}^{P_i'} = \{X_1^{P_i'}, 0, 0\}$ is position vector of the intersection point P_i in the body-fixed coordinate system $o'(x_1', x_2', x_3')$, and $\vec{N}'$ is the normal vector of the reference planes in the body-fixed coordinate system $o'(x_1', x_2', x_3')$,

$$\vec{N}' = \begin{Bmatrix} \cos\xi_5 \cos\xi_6 \\ \sin\xi_4 \sin\xi_5 \cos\xi_6 - \cos\xi_4 \sin\xi_6 \\ \cos\xi_4 \sin\xi_5 \cos\xi_6 + \sin\xi_4 \sin\xi_6 \end{Bmatrix}. \tag{4.3}$$

For computational simplicity, the intersections of the hull and references planes are calculated in the body-fixed coordinate system $o'(x_1', x_2', x_3')$, then transformed into the equilibrium coordinate system $o(x_1, x_2, x_3)$ using the following equation,

$$\begin{Bmatrix} x_1 \\ x_2 \\ x_3 \end{Bmatrix} = \begin{Bmatrix} \cos\xi_5 \cos\xi_6 & \sin\xi_4 \sin\xi_5 \cos\xi_6 & \cos\xi_4 \sin\xi_5 \cos\xi_6 \\ & - \cos\xi_4 \sin\xi_6 & + \sin\xi_4 \sin\xi_6 \\ \cos\xi_5 \sin\xi_6 & \sin\xi_4 \sin\xi_5 \sin\xi_6 & \cos\xi_4 \sin\xi_5 \sin\xi_6 \\ & + \cos\xi_4 \cos\xi_6 & - \sin\xi_4 \cos\xi_6 \\ - \sin\xi_5 & \sin\xi_4 \cos\xi_5 & \cos\xi_4 \cos\xi_5 \end{Bmatrix} \begin{Bmatrix} x_1' \\ x_2' \\ x_3' \end{Bmatrix} + \begin{Bmatrix} \xi_1 \\ \xi_2 \\ \xi_3 \end{Bmatrix} \tag{4.4}$$

After the equivalent sections are found, the wetted part of each section can be extracted easily. In the present investigation, this is defined to be the part of each section which is below the undisturbed free surface $x_3 = h_G$.

The rationalised hull can be considered as a *mesh*, which is composed of points and line segments. Meshes are widely used in geometric modelling in computer graphics or finite-element analysis. Finding the intersection of two arbitrary meshes is an important research topic in computer graphics. Fortunately,

only the algorithm for finding the intersection of a mesh and a plane is needed in this thesis. Let $\langle \vec{Q}_k, \vec{Q}_{k+1} \rangle$ denote a line segment with end points $\vec{Q}_k$ and $\vec{Q}_{k+1}$ in the hull mesh, and let $\underline{\vec{Q}}_k^i$ be the intersection point of this line segment and the ith reference plane defined by Equation (4.2),

$$\underline{\vec{Q}}_k^i = (1 - \sigma_k^i)\vec{Q}_k + \sigma_k^i \vec{Q}_{k+1} \qquad \text{for some } \sigma_k^i \in [0, 1]. \tag{4.5}$$

Substituting (4.5) into the plane Equation (4.2) and solving for σ leads to

$$\sigma_k^i = \frac{\vec{N}' \cdot (\vec{Q}_k - \vec{X}^{P_i'})}{\vec{N}' \cdot (\vec{Q}_k - \vec{Q}_{k+1})}, \tag{4.6}$$

The line segment $\langle \vec{Q}_k, \vec{Q}_{k+1} \rangle$ intersects the ith reference plane if $\vec{N}' \cdot (\vec{Q}_k - \vec{X}^{P_i'}) > 0$ and $\vec{N}' \cdot (\vec{Q}_{k+1} - \vec{X}^{P_i'}) < 0$, or if $\vec{N}' \cdot (\vec{Q}_k - \vec{X}^{P_i'}) < 0$ and $\vec{N}' \cdot (\vec{Q}_{k+1} - \vec{X}^{P_i'}) > 0$. The special case is that $\vec{N}' \cdot (\vec{Q}_k - \vec{X}^{P_i'}) = 0$ and $\vec{N}' \cdot (\vec{Q}_{k+1} - \vec{X}^{P_i'}) = 0$, which means the line segment lies entirely in the reference plane, and this is treated individually in the program.

All the intersection points $\underline{\vec{Q}}_k^i$ are transformed into the equilibrium coordinate system $o(x_1, x_2, x_3)$ by Equation (4.4), which then forms the ith equivalent section of ith original section. Figure (4.4) shows the intersection of the reference plane and ship hull with a 20° yaw angle. The original sections are shown as solid lines and the intersections are shown as dashed lines. The program has been tested and verified extensively with a pitch and/or a yaw angle ranging from 0° to 50°. The algorithm has been proved very robust. More examples can be found in Appendix A, Figures (A.1 - A.5). Some of the cases, for example $\xi_5 = 50°$ and/or $\xi_6 = 50°$, will never occur in reality, but they are presented there to demonstrate the robustness of the program. It is understood that the translational motions ξ_1, ξ_2, ξ_3 and roll angles ξ_4 have no significance for testing the program, they are therefore omitted.

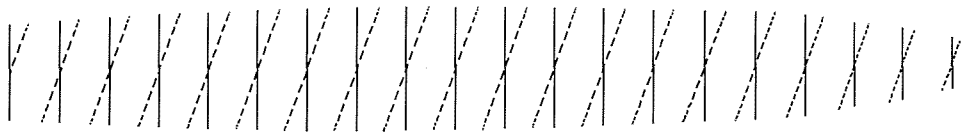

(a) Top View

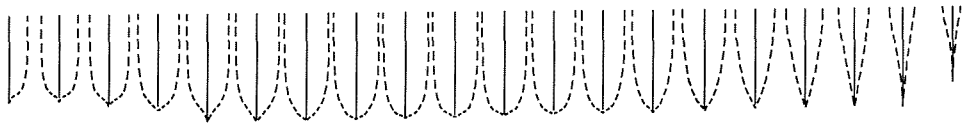

(b) Starboard View

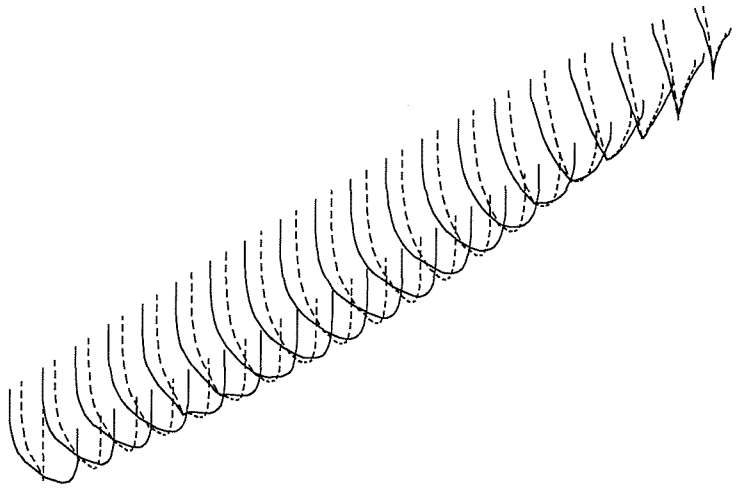

(c) 3D View

Figure 4.4: *Intersections of Hull and Reference Planes* ($\xi_5 = 0°$, $\xi_6 = 20°$).

4.4 The Conformal Mapping

The versatility of conformal mapping technique has been demonstrated by Westlake and Wilson [71]. By a suitable choice of the conformal mapping coefficient number N_{cm}, a large number of ship-shaped sections may be mapped to the desired degree of accuracy. Figures (6-9) in [71] are of particular interest, which prove Westlake and Wilson's conformal mapping method is capable of mapping re-entrant sections (*e.g.* a bulbous section heeled to an angle 15^0) with as many as 48 mapping coefficients. For simple sections, it is not advisable to choose a very large number of mapping coefficients because they demand excessive computations. The actual number of mapping coefficients is usually ascertained on a trial and error basis. In this section, three typical sections (Section 10, 18 and 20) of a rationalised Series 60 hull form are chosen to determine a reasonable mapping coefficient number N_{cm}. Section 10 is a rectangular section with small round bilge, Section 20 is a fine section, and Section 18 is roughly close to a round section.

Figures (4.5 - 4.8) show the mapping results of these sections with 5, 8, 11 and 14 coefficients respectively. The contour curve generated by the multi-parameter conformal mapping does not necessarily pass through all the given offset points but the curve does fit the given data as closely as possible. This is contrary to the contour generated by Lewis mapping which always passes through the coordinates of the draught and beam of the section. The mapped points of all three sections move closer to the given offset points as the number of coefficients increases. It shows that the rectangular Section 10 can be mapped very accurately with as few as 8 mapping coefficients. However, for the fine Section 20, it may require 11 or more coefficients to accurately map the bottom perimeter. Comparing Figure (4.7) and Figure (4.8) shows that further increase of conformal mapping coefficients brings no improvement of mapping accuracy.

Figures (4.9 - 4.12) illustrate the mapping results of the same sections, how-

ever they are heeled to an angle 20°. Once again, it shows that 11 coefficients are sufficient to achieve reasonable mapping accuracy even for asymmetric sections. When a ship is undergoing motions in six degree of freedom, the underwater part of a section can be of arbitrary shape. It is impossible to check the mapping results of all the cases. However, from the results shown in these figures, it may be safe to claim that 14 to 20 conformal mapping coefficients are adequate for Series 60 hull form.

For a large number of mapping coefficients, extra points may have to be interpolated between each pair of successive given offsets to give a sufficient number of equations. Using too many mapping coefficients not only results in unnecessary computations, but also creates unpredictable numerical instability. Figure (4.13) illustrates the conformal mapping with a large number of coefficients (26, 27 and 28 coefficients), which provides an accurate fit at the section definition points of Section 10, but a poor fit between them. Figure (4.14(a)) shows numerical instability occurs with a further increase of the number of coefficients, where both the section definition points and the points between them can not be mapped. A test curve, which is created by mapping the randomly chosen points $(1, \vartheta_i)$ in the reference plane into physical plane, is drawn in each figure to ensure the points between the given section offsets are correctly mapped. It seems that evenly distributing section definition points around the contour can greatly improved the numerical stability. Figures (4.14(b)) and (4.14(c)) show the Sections 18 and 20, which have a more even distribution of points defining section than Section 10, can still be mapped very accurately with 30 mapping coefficients.

Figures (4.15) and (4.16) compare the mapping results obtained by the Lewis method and those obtained by the multi-parameter method. The data needed in the Lewis mapping are given in Table (4.2)†, in which B is sectional beam at the waterline, T is draught, A is the sectional area under waterline, H is the

†The beam, draught and area for all other sections can be found in Appendix B, Table (B.1).

beam/draught ratio, and σ is the section area coefficient,

$$H = \frac{B}{T}, \qquad \sigma = \frac{A}{B \cdot T}. \tag{4.7}$$

The area coefficient of Section 18 is within the permissible range of Lewis mapping, while the area coefficients of Section 10 is slightly greater the upper limit and that of Section 20 is out of the lower limit [37].

Section	B	T	A	H	σ
10	0.4350	0.174	0.07353	2.5000	0.9715
18	0.3424	0.174	0.04012	1.9680	0.6734
20	0.1576	0.174	0.01077	0.9057	0.3927

Table 4.2: *Lewis Mapping Data of Section 10, 18 and 20 of the Series 60 Hull Form.*

It shows multi-parameter method has great advantages over Lewis method, especially of mapping the fine section in Figure (4.15(c)), where Lewis mapping even fails to distinguish the basic characteristic of the original section. For those asymmetric sections in Figure (4.16), the contours generated by Lewis method are still symmetric as expected from the theory.

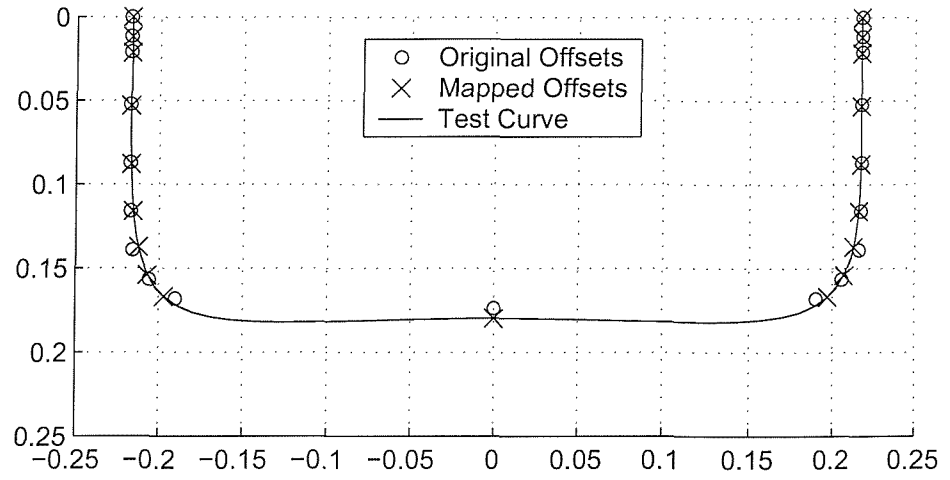

(a) Section 10

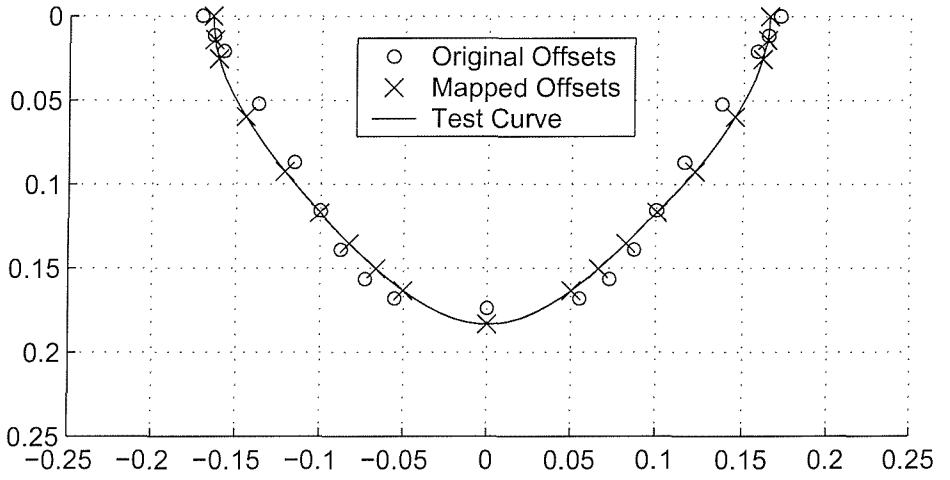

(b) Section 18

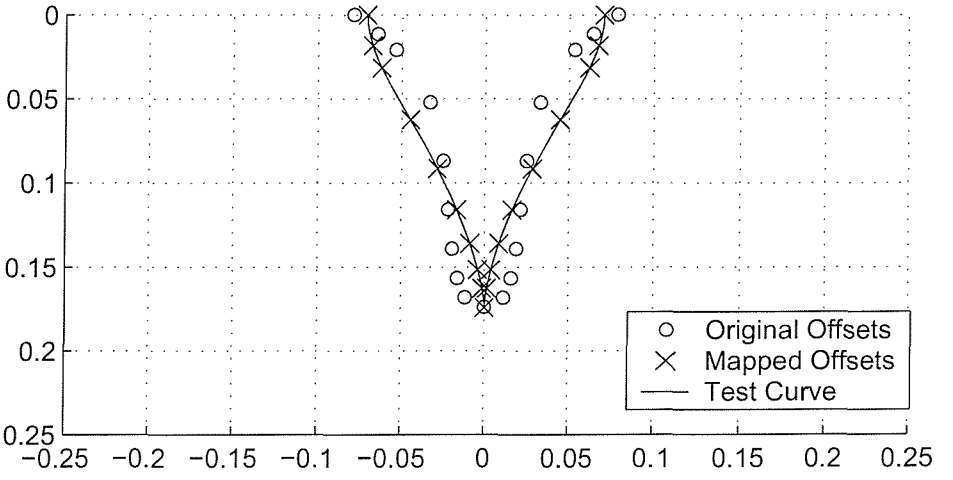

(c) Section 20

Figure 4.5: *Conformal Mapping of the Sections of Series 60 Hull Form (10 waterlines and 5 mapping coefficients).*

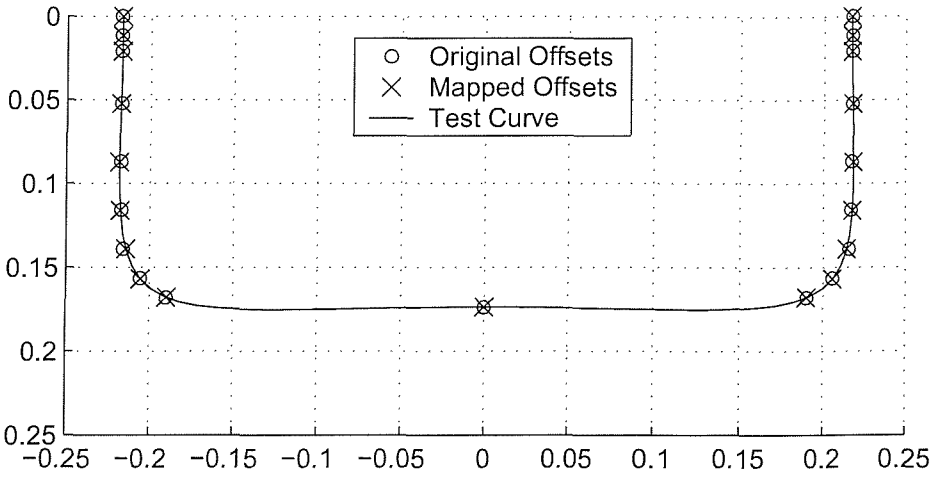

(a) Section 10

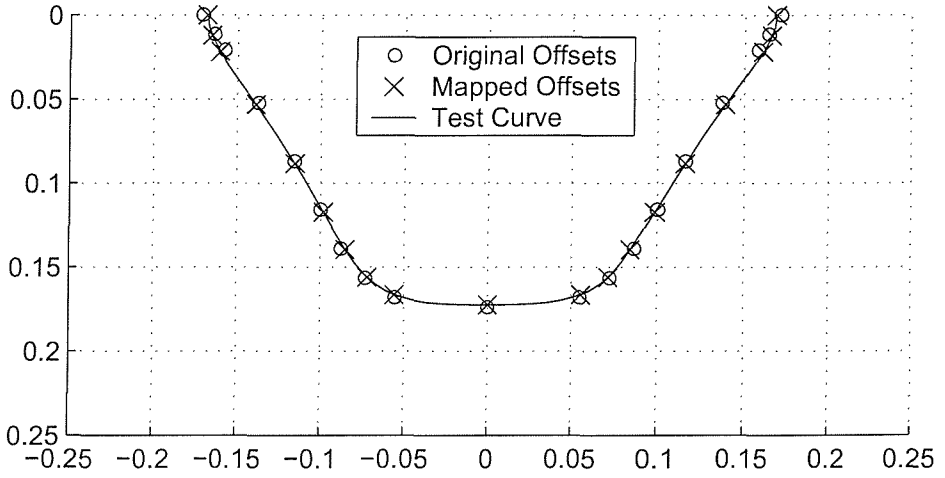

(b) Section 18

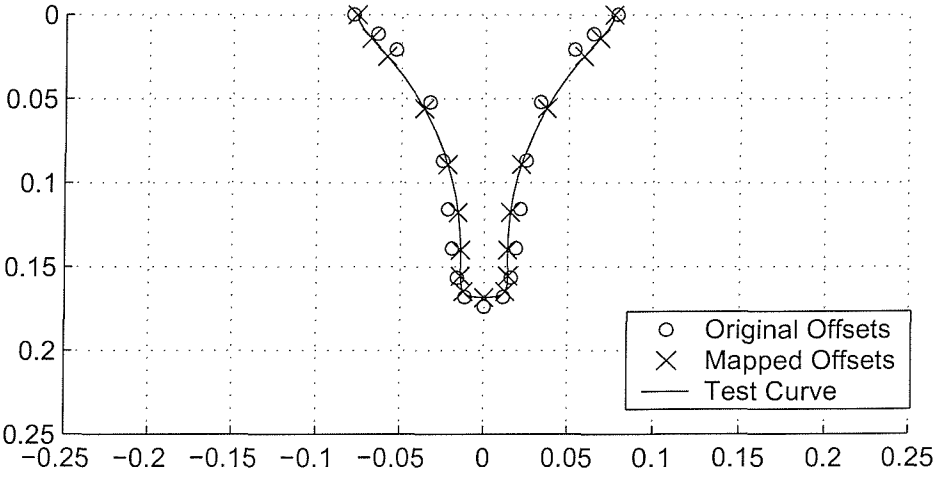

(c) Section 20

Figure 4.6: *Conformal Mapping of the Sections of Series 60 Hull Form (10 waterlines and 8 mapping coefficients).*

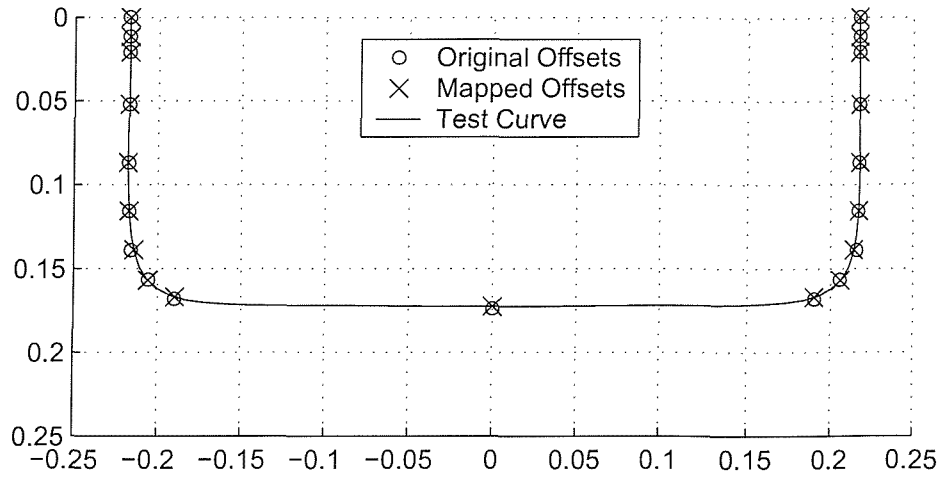

(a) Section 10

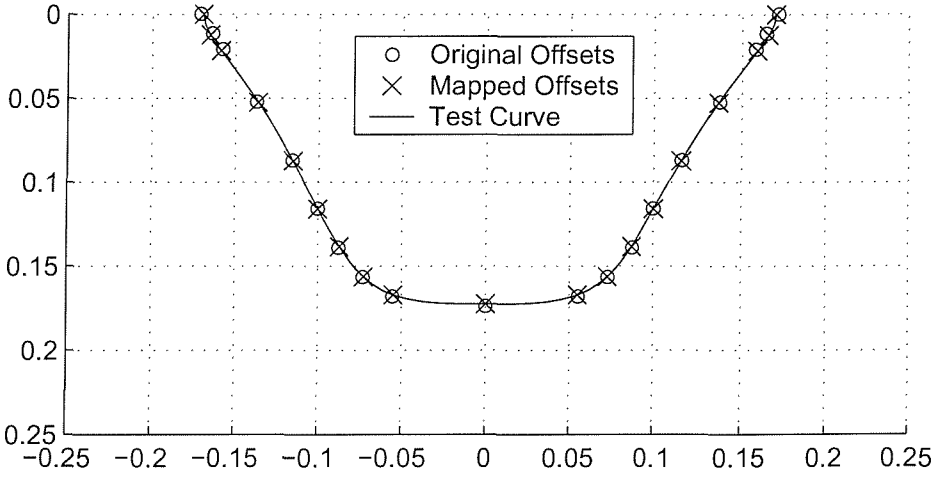

(b) Section 18

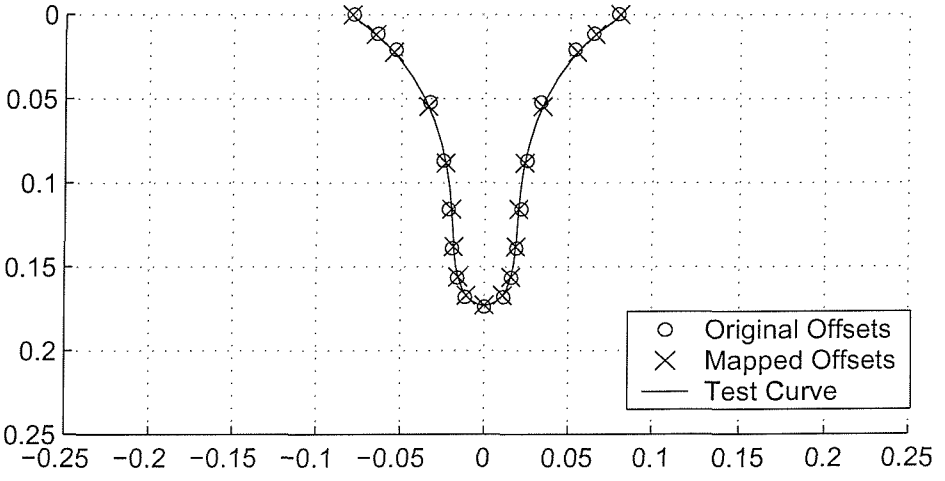

(c) Section 20

Figure 4.7: *Conformal Mapping of the Sections of Series 60 Hull Form (10 waterlines and 11 mapping coefficients).*

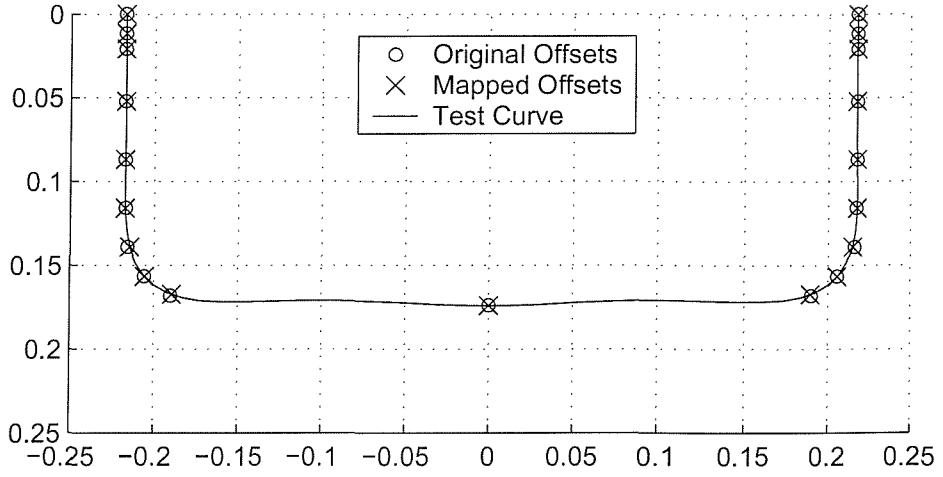

(a) Section 10

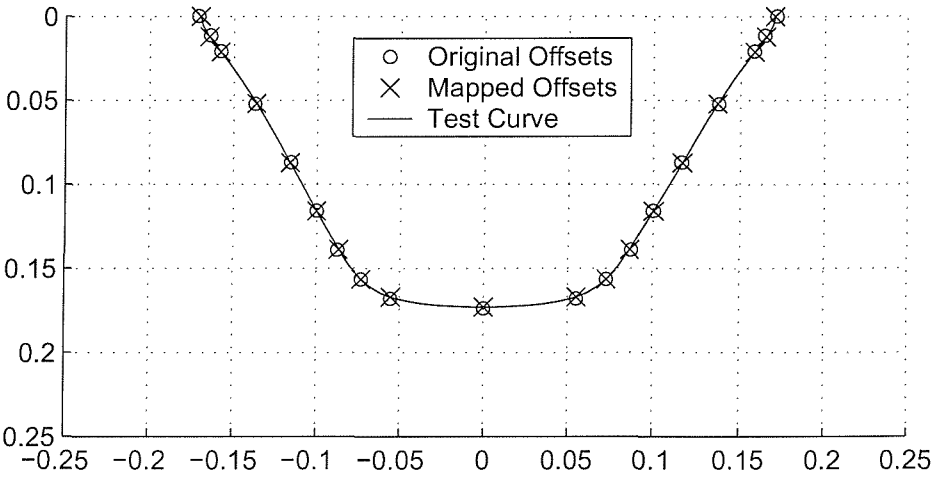

(b) Section 18

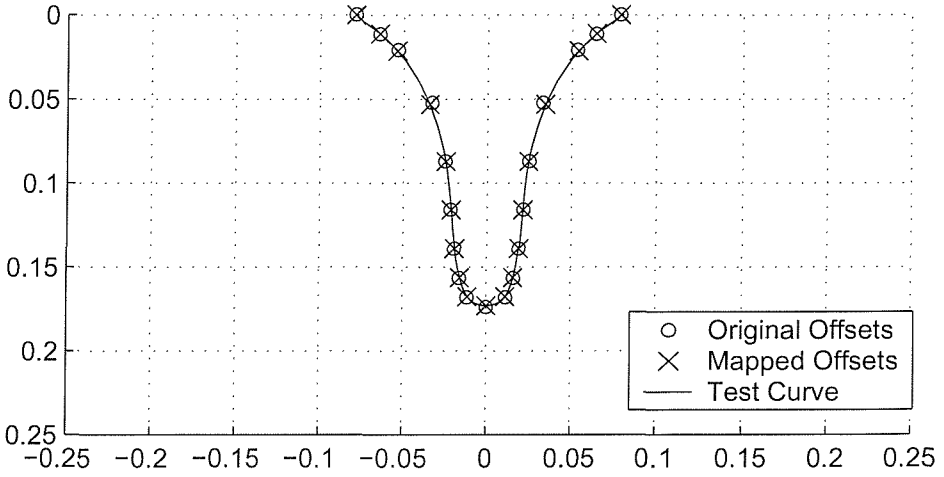

(c) Section 20

***Figure 4.8**: Conformal Mapping of the Sections of Series 60 Hull Form (10 waterlines and 14 mapping coefficients).*

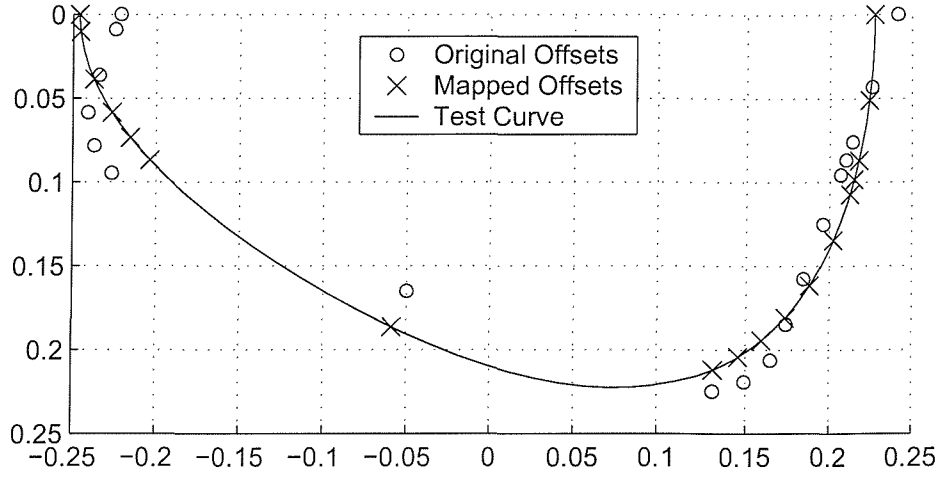

(a) Section 10

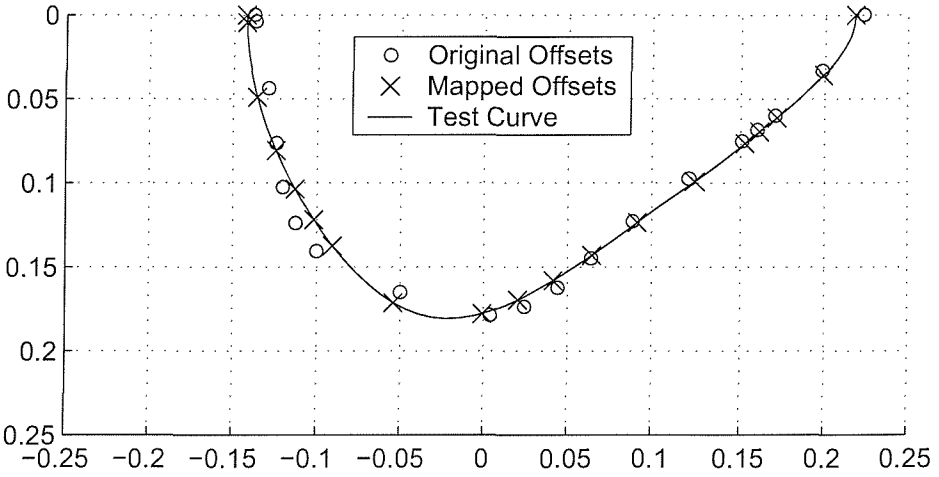

(b) Section 18

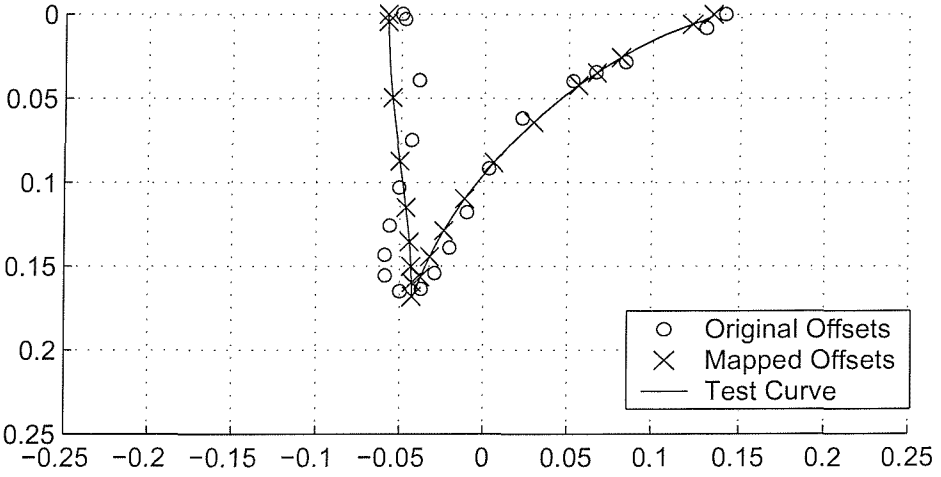

(c) Section 20

Figure 4.9: *Conformal Mapping of the Heeled Sections of Series 60 Hull Form (10 waterlines, 5 mapping coefficients and heeling angle* $20°$*).*

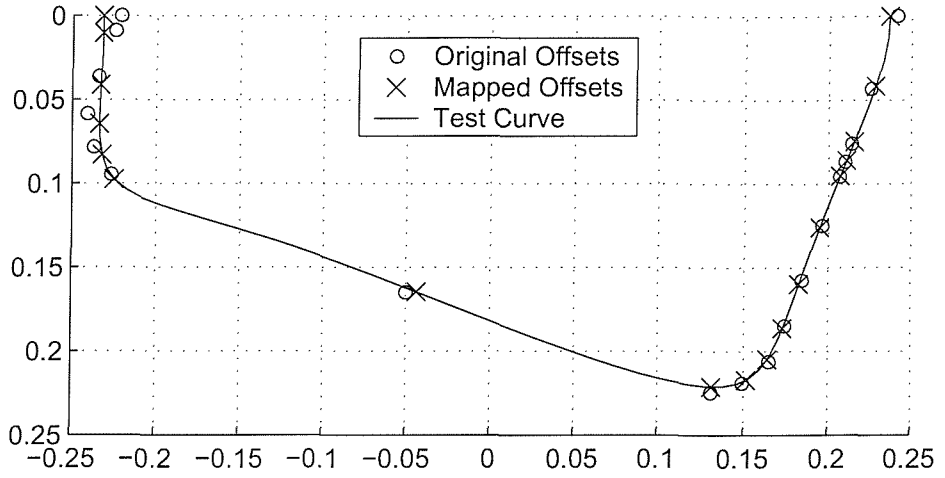

(a) Section 10

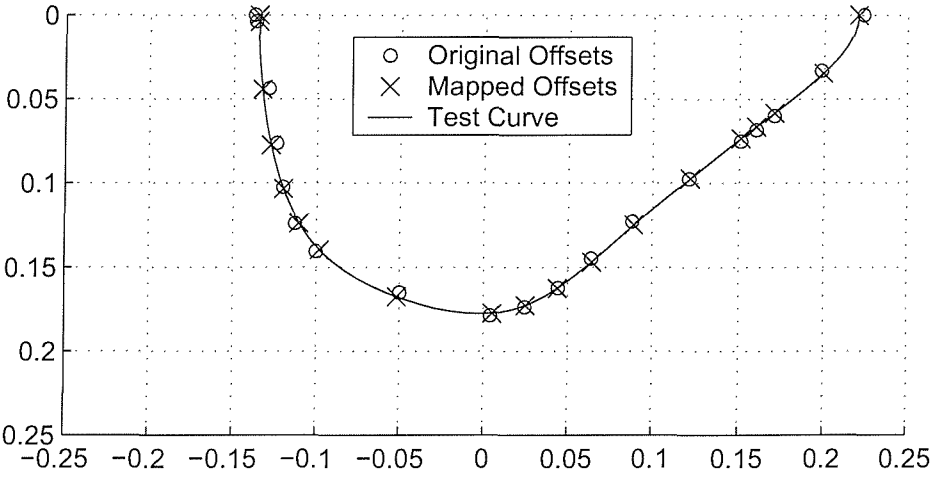

(b) Section 18

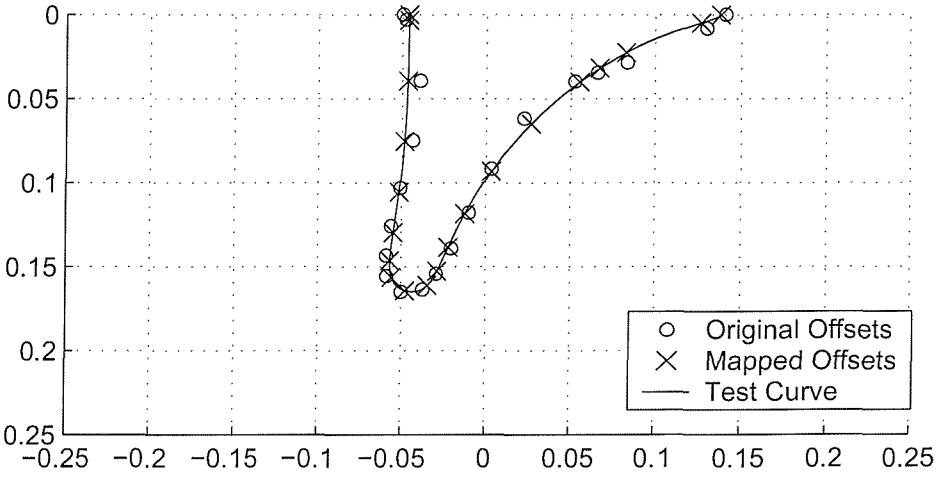

(c) Section 20

Figure 4.10: *Conformal Mapping of the Heeled Sections of Series 60 Hull Form (10 waterlines, 8 mapping coefficients and heeling angle* 20°*).*

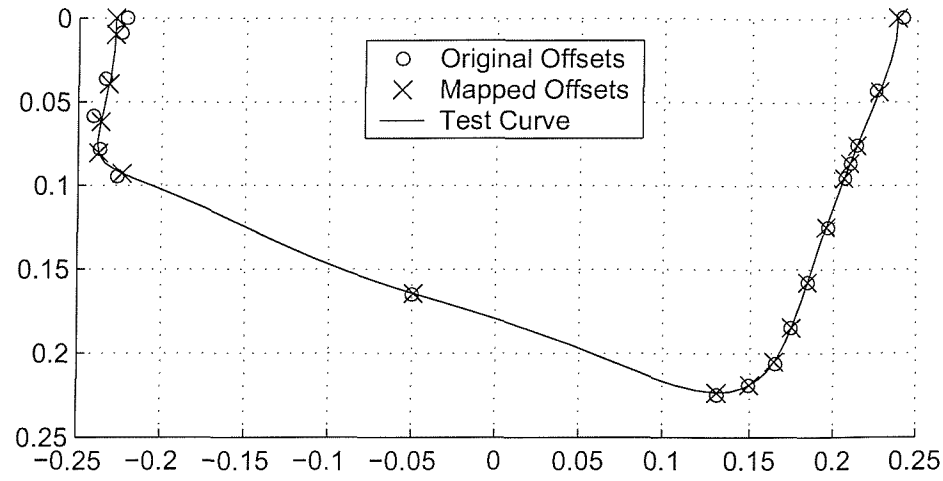

(a) Section 10

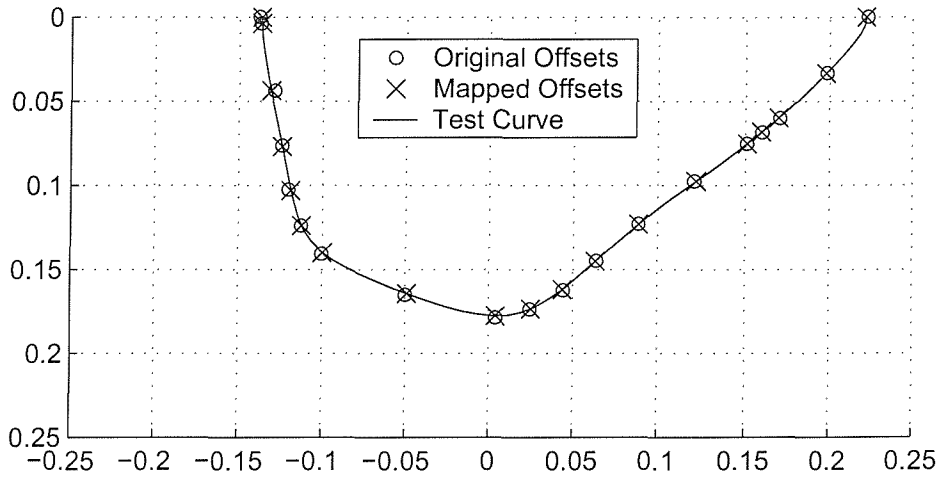

(b) Section 18

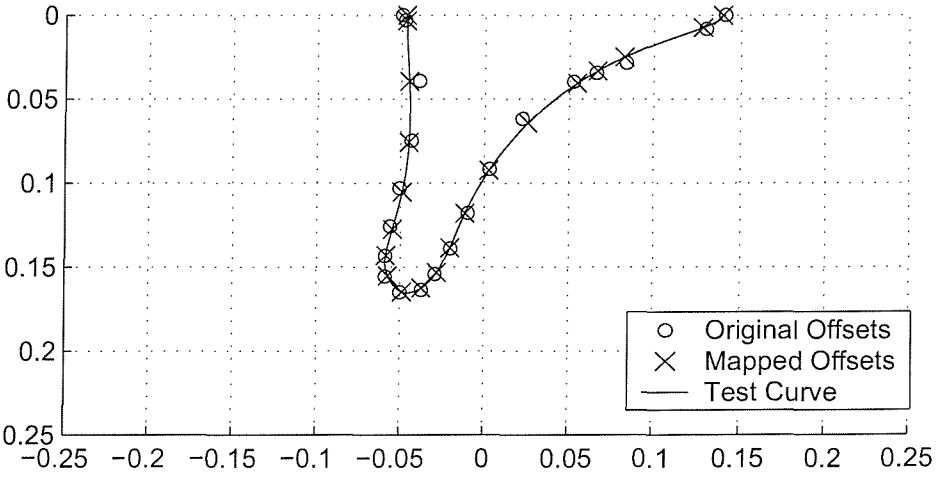

(c) Section 20

Figure 4.11: *Conformal Mapping of the Heeled Sections of Series 60 Hull Form (10 waterlines, 11 mapping coefficients and heeling angle* $20°$*).*

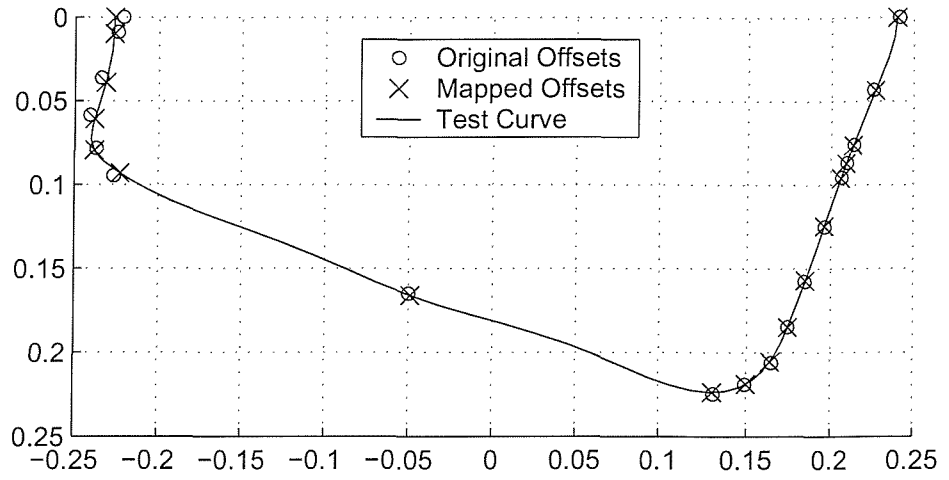

(a) Section 10

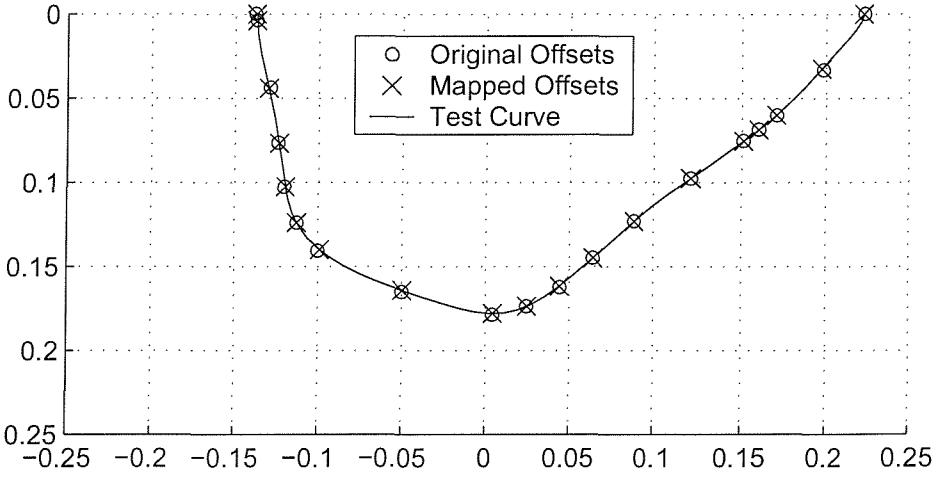

(b) Section 18

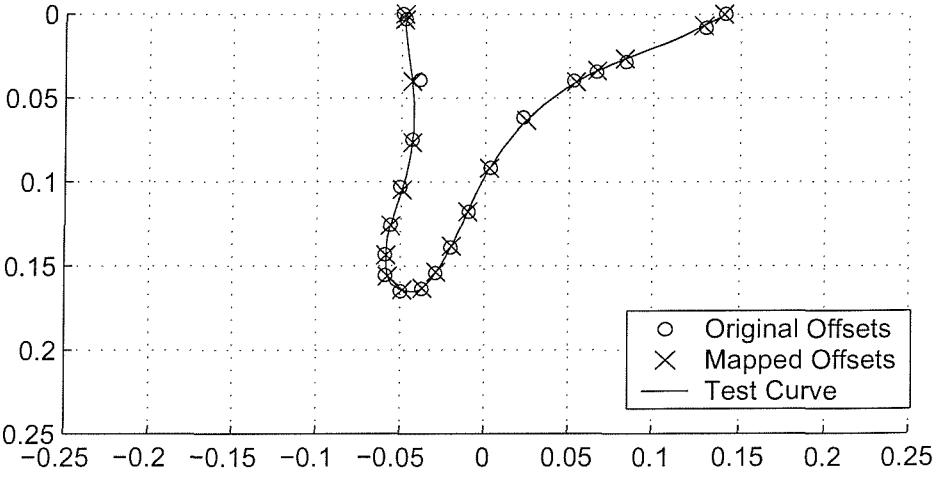

(c) Section 20

Figure 4.12: *Conformal Mapping of the Heeled Sections of Series 60 Hull Form (10 waterlines, 14 mapping coefficients and heeling angle* $20°$*).*

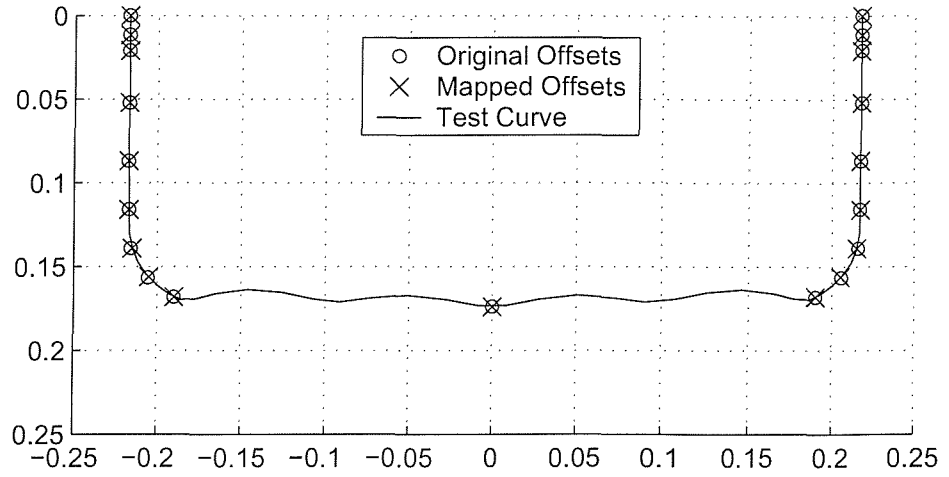

(a) 26 Mapping Coefficients

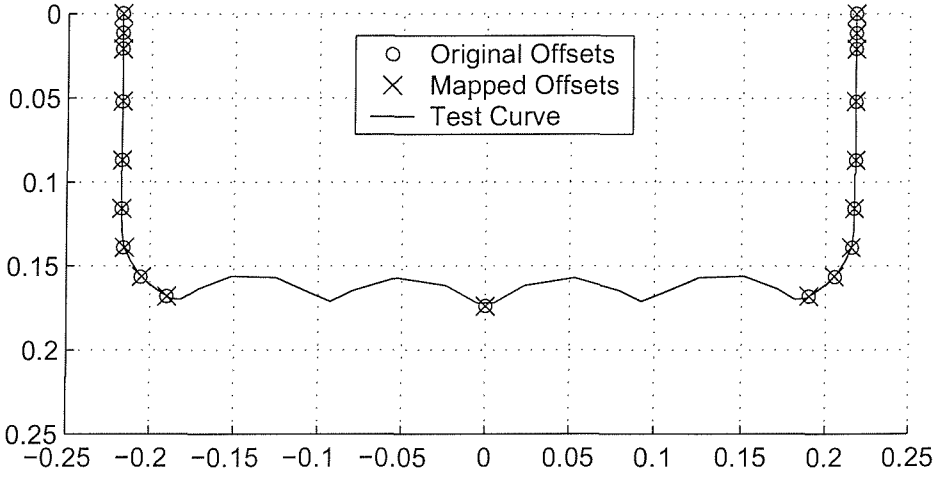

(b) 27 Mapping Coefficients

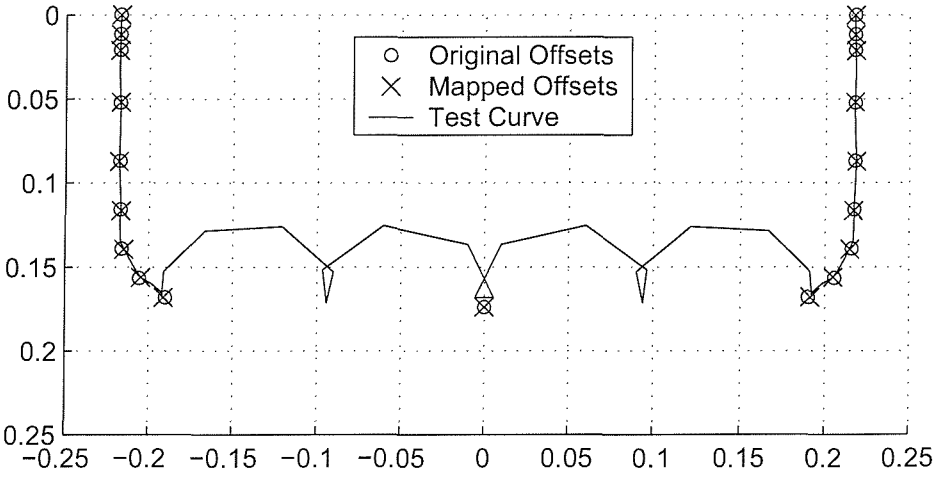

(c) 28 Mapping Coefficients

Figure 4.13: *Multi-Parameter Mapping with a Large Number of Coefficients.*

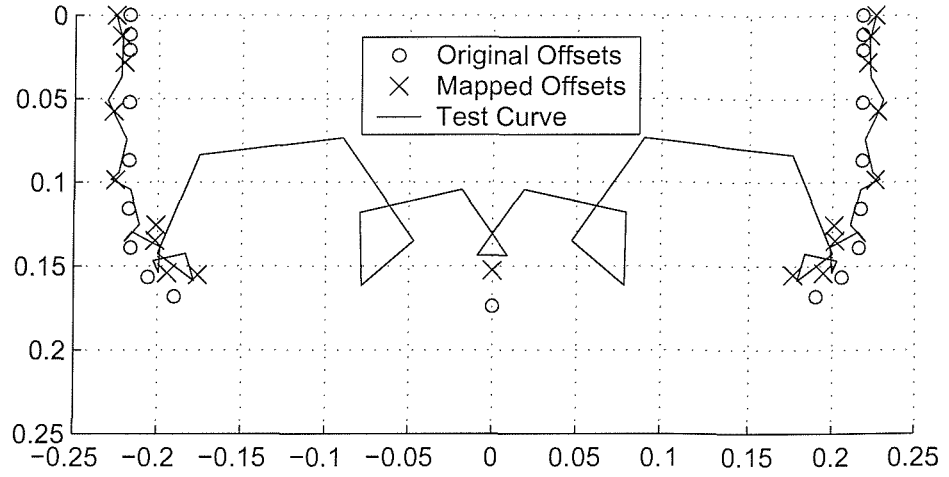

(a) Section 10

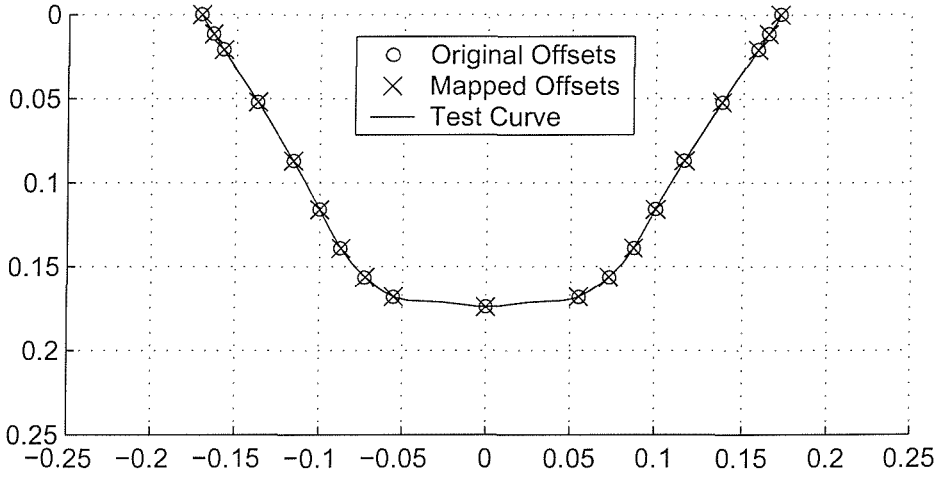

(b) Section 18

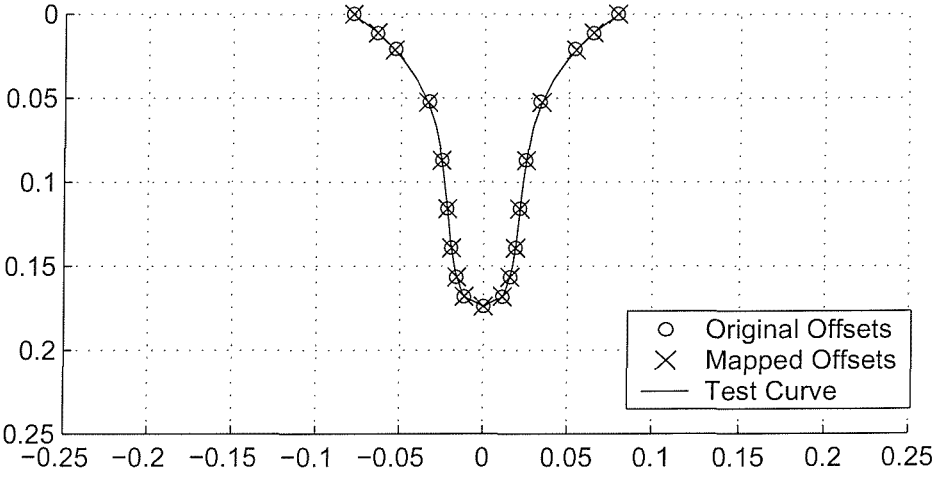

(c) Section 20

Figure 4.14: *Numerical Instability of the Multi-Parameter Conformal Mapping with a Large Number of Coefficients.*

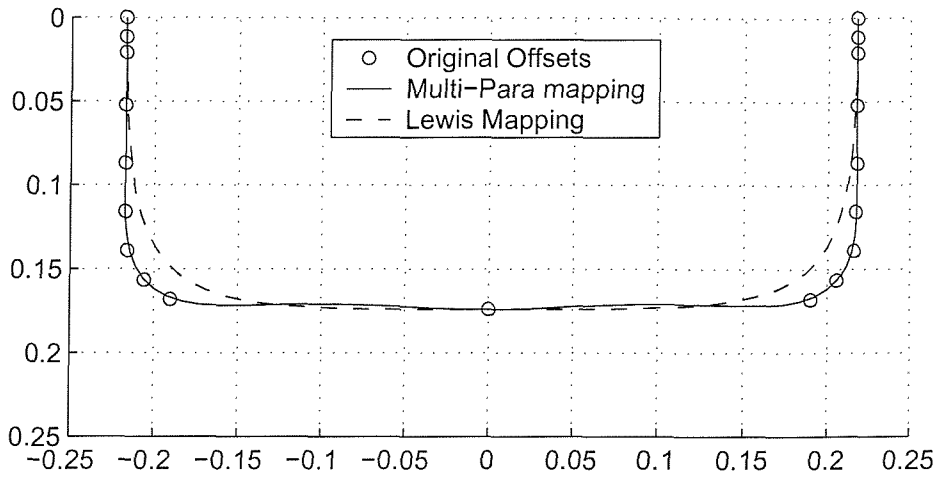

(a) Section 10 of Series 60 Hull Form

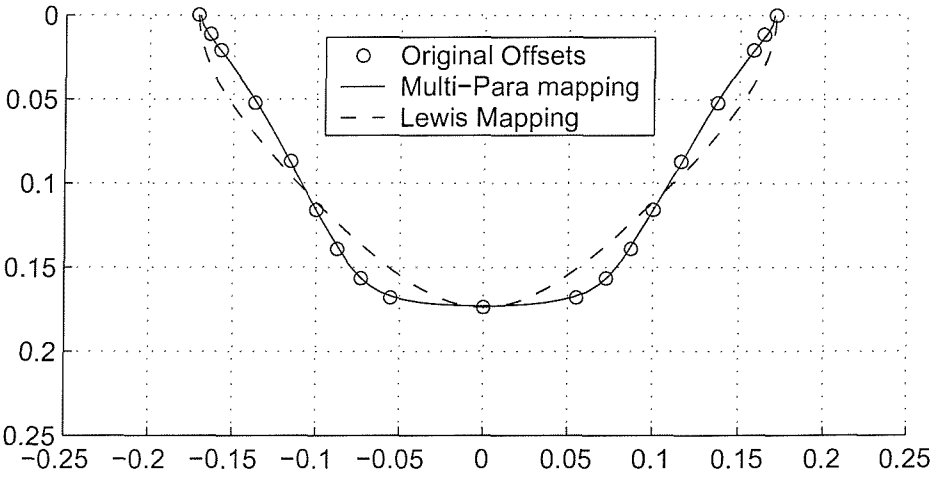

(b) Section 18 of Series 60 Hull Form

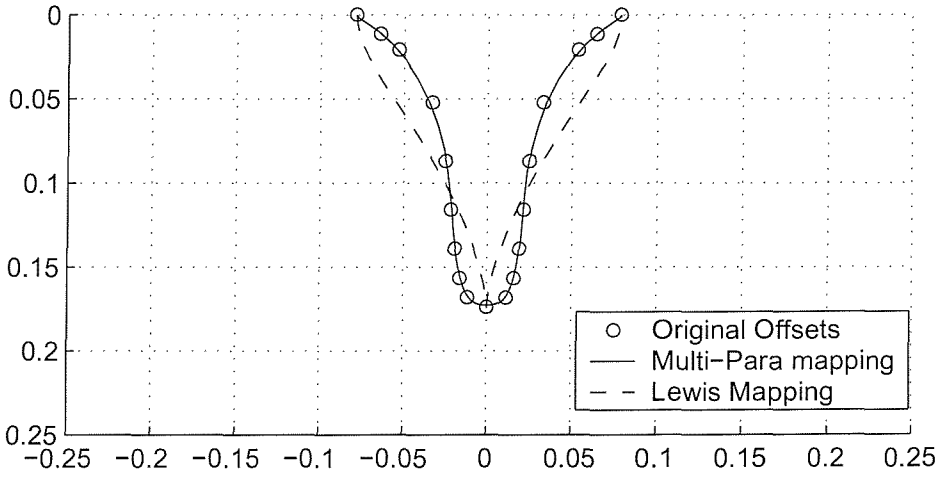

(c) Section 20 of Series 60 Hull Form

Figure 4.15: *Comparison of Two Mapping Methods for the Symmetric Sections (14 coefficients used in multi-parameter mapping).*

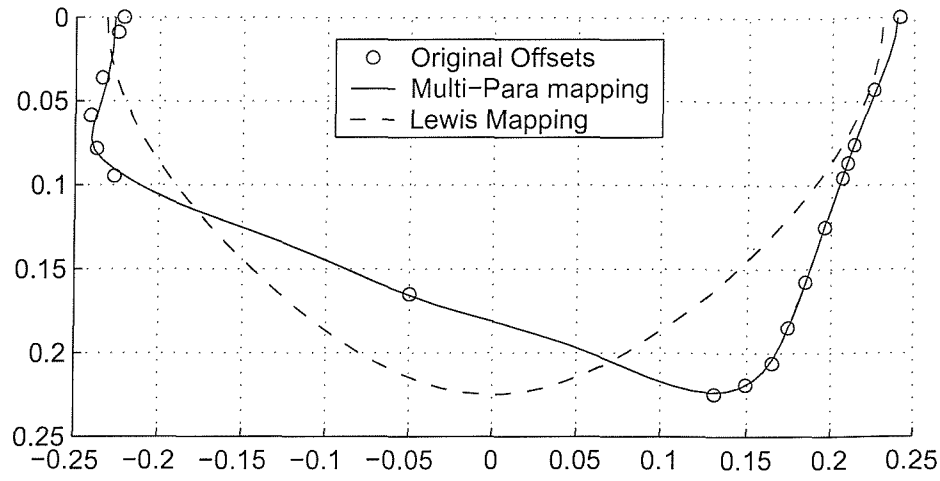

(a) Section 10 of Series 60 Hull Form

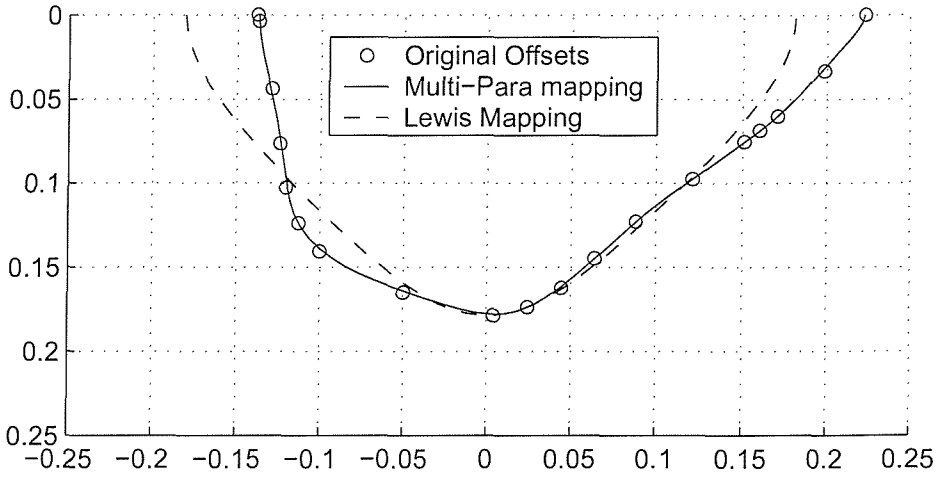

(b) Section 18 of Series 60 Hull Form

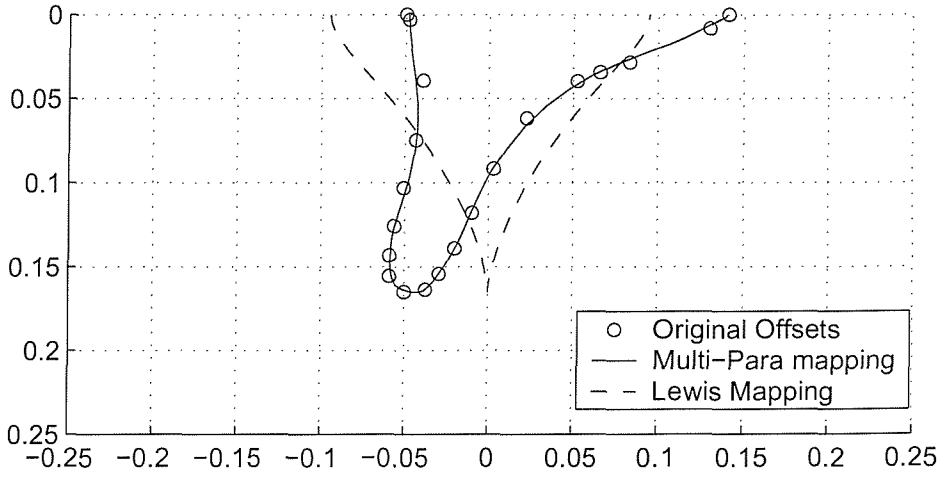

(c) Section 20 of Series 60 Hull Form

Figure 4.16: *Comparison of Two Mapping Methods for the Asymmetric Sections (14 coefficients used in multi-parameter mapping).*

4.5 Two-Dimensional Hydrodynamic Coefficients

In this section, the two-dimensional hydrodynamic coefficients $\underline{A}_{ij}$ and $\underline{B}_{ij}$, $i, j = 2, 3, 4$ of Sections 10, 18 and 20 of Series 60 hull form are presented over a wide range of frequencies. The influences of both the number of conformal mapping coefficients and the heel angles are accessed. The hydrodynamic coefficients plotted in the figures are non-dimensionalised using the factors given in Table (4.3), and denoted as a^*_{ij} and b^*_{ij} respectively. ϱ in the table is fluid density. The values of the beam B and area A of each section are given in Appendix B, Table (B.1). ω^* in the figures is the non-dimensional frequency coefficient,

$$\omega^* = \omega(B/2g)^{1/2}, \tag{4.8}$$

where ω is the wave frequency[‡].

Coefficient	Units	Dimensions	Factor
$\underline{A}_{22}$, $\underline{A}_{33}$, $\underline{A}_{23}$, $\underline{A}_{32}$	kg/m	M/L	ϱA
$\underline{B}_{22}$, $\underline{B}_{33}$, $\underline{B}_{23}$, $\underline{B}_{32}$	$kg/(m{\cdot}s)$	M/LT	$\varrho A(2g/B)^{1/2}$
$\underline{A}_{44}$	$kg{\cdot}m^2/m$	ML	ϱAB^2
$\underline{B}_{44}$	$kg{\cdot}m^2/(m{\cdot}s)$	ML/T	$\varrho AB^2(2g/B)^{1/2}$
$\underline{A}_{24}$, $\underline{A}_{42}$, $\underline{A}_{34}$, $\underline{A}_{43}$	$kg{\cdot}m/m$	M	ϱAB
$\underline{B}_{24}$, $\underline{B}_{42}$, $\underline{B}_{34}$, $\underline{B}_{43}$	$kg{\cdot}m/(m{\cdot}s)$	M/T	$\varrho AB(2g/B)^{1/2}$

Table 4.3: *Factors Used to Render the Sectional Hydrodynamic Coefficients Non-Dimensional.*

[‡]It is understood that ω should be the frequency of encounter, in the case of calculating two-dimensional hydrodynamic coefficients of sections of a ship with forward speed.

4.5.1 Effects of Mapping Coefficient Number

Bishop, *et al* [6] computed the hydrodynamic properties of a variety of symmetric sectional shapes (*e.g.* chine, bulbous bow and rectangular) for heave motion using multi-parameter conformal mapping technique, and compared the results with those of the Lewis mapping method and the Frank close-fit method, as well as with the experimental data. The hydrodynamic properties of the same symmetric sections for sway and roll motion were given by Bishop, *et al* [7]. Therefore, in this section those comparisons will not be repeated, instead the attention will be focused on the influence of the number of conformal mapping coefficients.

Figures (4.17 - 4.28) present the non-zero hydrodynamic coefficients of Sections 10, 18 and 20. Generally speaking, the mapping coefficient number has more effect on the damping coefficients than on the added-mass or added-moment of inertia, which suggests the damping coefficients are more sensitive to the shape of the under water part of the section compared with added-mass or added-moment of inertia coefficients. It is hard to find any difference between the results determined by the mapping with 11 coefficients and those determined by the mapping with 14 coefficients, except for the non-dimensional added-moment of inertia b^*_{44} of Section 18 in Figure (4.24(b)), where very little difference can be found. Meanwhile, it can also be observed that the curves determined by multi-parameter mapping method move closer to those curves determined by Lewis mapping method when the number of multi-parameter mapping coefficients decreases. These not only echo the conformal mapping results in Section §4.4, but also indicate a satisfactory convergence of the calculations.

Figures (4.17), (4.20), (4.23) and (4.26) show that the hydrodynamic properties of Section 10 calculated by Lewis mapping method closely match those calculated by multi-parameter mapping method, only minor differences exit in the damping coefficients within the frequency range, approximately, $0.5 \leq \omega^* \leq 2.0$.

This is because Section 10 can be mapped quite accurately by Lewis method compared with other two sections. It also appears that the hydrodynamic properties a_{44}^*, b_{44}^*, $a_{24}^*(a_{42}^*)$ and $b_{24}^*(b_{42}^*)$ of Section 10 are much smaller, respectively, then those of Sections 18 and 20, which may mean that the area ratio σ is a very important factor which influences the hydrodynamics properties associated with roll motion. The hydrodynamic coefficients of Section 20, as shown in Figures (4.19), (4.22), (4.25) and (4.28), vary significantly with the number of conformal mapping coefficients, which exactly reflects the conformal mapping results of this section (see Figures (4.5(c)), (4.6(c)), (4.7(c)), (4.8(c)) and (4.15(c))). It confirms that, in order to achieve the desired accuracy, many more coefficients are needed for fine, bulbous or triangular sections than those sections within the permissible range of Lewis mapping.

Sway Hydrodynamic Properties

Both the non-dimensional added-mass a_{22}^* and damping coefficient b_{22}^* of Section 10 and Section 18 computed by multi-parameter mapping method are in close agreement with those computed by Lewis mapping method, and the number of the coefficients of multi-parameter mapping has little effect on the results, shown in Figures (4.17) and (4.18). Significant discrepancies are found in both the added-mass a_{22}^* and the damping coefficient b_{22}^* of Section 20, as illustrated in Figure (4.19). The multi-parameter mapping method suggests higher added-mass and damping values compared with the Lewis conformal mapping solution. The discrepancy in added-mass a_{22}^* persists over the whole range of the non-dimensional frequencies, whereas the discrepancy in the damping b_{22}^* vanishes as b_{22}^* tends to zero in both the low and high frequency range.

Heave Hydrodynamic Properties

As shown in the Figures (4.20(a)), (4.21(a)) and (4.22(a)), the non-dimensional heave added-mass coefficients a_{33}^* of all sections obtained by multi-parameter mapping method are almost identical to those obtained by Lewis conformal mapping method respectively, confirming that the heave added-mass A_{33} is essentially the function only of section area coefficient σ and beam/draught ratio H. Small local differences in the section shape have very little influence on the results. The heave added mass is generally of the same order as the displaced mass ϱA and rises towards infinity at zero frequency. Section 10 has the largest value of a_{33}^*, since it has the largest values of H and σ. And a_{33}^* of Section 20 is smallest, because both H and σ of this section are the smallest.

In contrast to the added-mass, substantial disparities are observed between the damping coefficient results of multi-parameter mapping method and those of Lewis mapping method, shown in Figures (4.20(b)), (4.21(b)) and (4.22(b)). The number of coefficients of the multi-parameter conformal mapping has significant influence on the non-dimensional heave damping coefficients b_{33}^* of Section 18 and Section 20. The multi-parameter mapping with 14 coefficients gives a higher damping value on Section 10 and lower damping values on Sections 18 and 20, which agrees with the results presented by Bishop, *et al* [6] for a rectangular section, a fine section and a bulbous section. The disparities decrease while the b_{33}^* tends to zero at very high frequencies, which was not shown in the results of Bishop, *et al.*

Roll Hydrodynamic Properties

Figures (4.23 - 4.25) show the calculated hydrodynamic coefficients. The non-dimensional added-moments of inertia a_{44}^* of Section 10 and Section 18 are much smaller than that of Section 20. The a_{44}^* of Section 20 calculated using the multi-

parameter mapping method are greater than that found with the Lewis method, and the solution of 5 parameters mapping are much closer to the solution of Lewis mapping then that of 14 and 11 parameters mapping. The convergence of the calculations is demonstrated once again.

Great disparities are found between the damping results given by Lewis mapping method and those given by multi-parameter mapping, as well as between the damping values computed by multi-parameter mapping with difference coefficients, as shown in Figures (4.23(b)) (4.24(b)) and (4.25(b)). For Section 18, the multi-parameter mapping with 5 coefficients gives lower damping then Lewis mapping, particularly in the region near resonance frequency, where it gives the damping values as low as 50% of that given by Lewis mapping. Whereas, compared with Lewis method, the multi-paramter mapping with 8, 11 and 14 coefficients give slightly smaller damping values at the frequencies lower then resonance frequency and much higher damping values at the frequencies higher then resonamce frequency. For Section 20, in the region $\omega^* \leq 1.2$, the differences between the results produced by multi-parameter mapping with different number of coefficients are small, and they become greater when ω^* increases in the region $\omega^* \geq 1.2$. Again dramatic disparities are found between curve of Lewis mapping results and those of multi-parameter mapping results in the frequency region near the resonance.

From the discussion above, it can be concluded that the damping coefficient $\underline{B}_{44}$ is extremely sensitive to the section shape.

Sway-Roll(Roll-Sway) coupling Hydrodynamic Properties

The coupling hydrodynamic coefficients $a^*_{24}(a^*_{42})$ and $b^*_{24}(b^*_{42})$ are plotted in Figures (4.26 - 4.28). The discrepancies between the results, no matter whether they are calculated by Lewis mapping method or by multi-parameter mapping

method with different number of coefficients, follow the same pattern as that of a_{44}^* and b_{44}^*, except that the values of difference are reversed for Section 20, *e.g.* the $b_{24}^*(b_{42}^*)$ calculated using the multi-parameter mapping method are lower than that found with the Lewis method.

4.5.2 Effects of Heel Angle

The correct calculations of two-dimensional hydrodynamic coefficients are vital, since they are the foundation of calculating three-dimensional hydrodynamic coefficients. The purpose of this section therefore is to provide another check on the calculations of two-dimensional hydrodynamic coefficients and ensure that the hydrodynamic coefficients of asymmetric sections can be computed correctly as well. When a ship is heeled to a angle, sections are no longer geometrically symmetric about the x_3-axis, hence it is expected that hydrodynamic coefficients calculated by Lewis method and those calculated by multi-parameter mapping method will be much different, especially for those cross coupling coefficients. It should be noticed that the coupling between the coefficients is related to the non-symmetry of the shape of the underwater part of the section rather than just the angle of heel. For example, at zero heel angle, all cross coupling coefficients of the rectangular Section 10 between symmetric and antisymmetric motions are zero but, in general, at angles of heel the coupling coefficients are non-zero. However it is possible for this section to be heeled such that the underwater hull form returns to be symmetric (*e.g.* become a triangular shape), and the coupling coefficients are again zero. So, for avoiding confusion, only Section 20 is chosen as a sample in this section to assess the influence of heel.

Figures (4.29 - 4.32) illustrate the computed hydrodynamic coefficients of Section 20 heeled to angles $0°$, $10°$ and $20°$. Despite that the immersed sections are asymmetric about x_3-axis, the cross coupling hydrodynamic coefficients still

retain their symmetry in the sense that $a^*_{ij} = a^*_{ji}$ and $b^*_{ij} = b^*_{ji}$, $i, j = 2, 3, 4$.

It is very obvious that the hydrodynamic coefficients vary significantly with the heel angle, however the results produced by multi-parameter mapping and those produced by Lewis mapping still keep the similar trends (*e.g.* the damping coefficients b^*_{ij} tend to zero at both high and low frequencies), except a^*_{44} in Figure (4.31(a)), where the results at heel angles $10°$ and $20°$ produced by multi-parameter mapping rise sharply when the frequency is approaching zero in contrast to the corresponding Lewis mapping's results.

For those asymmetric sections the cross coupling hydrodynamic coefficients a^*_{23}/a^*_{32}, b^*_{23}/b^*_{32}, a^*_{34}/a^*_{43} and b^*_{34}/b^*_{43} should not be zero, which are shown in Figures (4.33) and (4.32). The mapped section by the Lewis conformal mapping is always symmetric, no matter what shape the original section is, therefore, the results calculated by Lewis mapping method remain zero. At larger heel angle, for example $20°$, it can be found in the figures that a^*_{23}/a^*_{32} is of the same order as a^*_{22} and a^*_{33}, a^*_{43} and b^*_{43} is even 2 - 3 times as large as a^*_{44} and b^*_{44} respectively, which means they can not be neglected, in other words, Lewis mapping can not be used with time-domain strip theory.

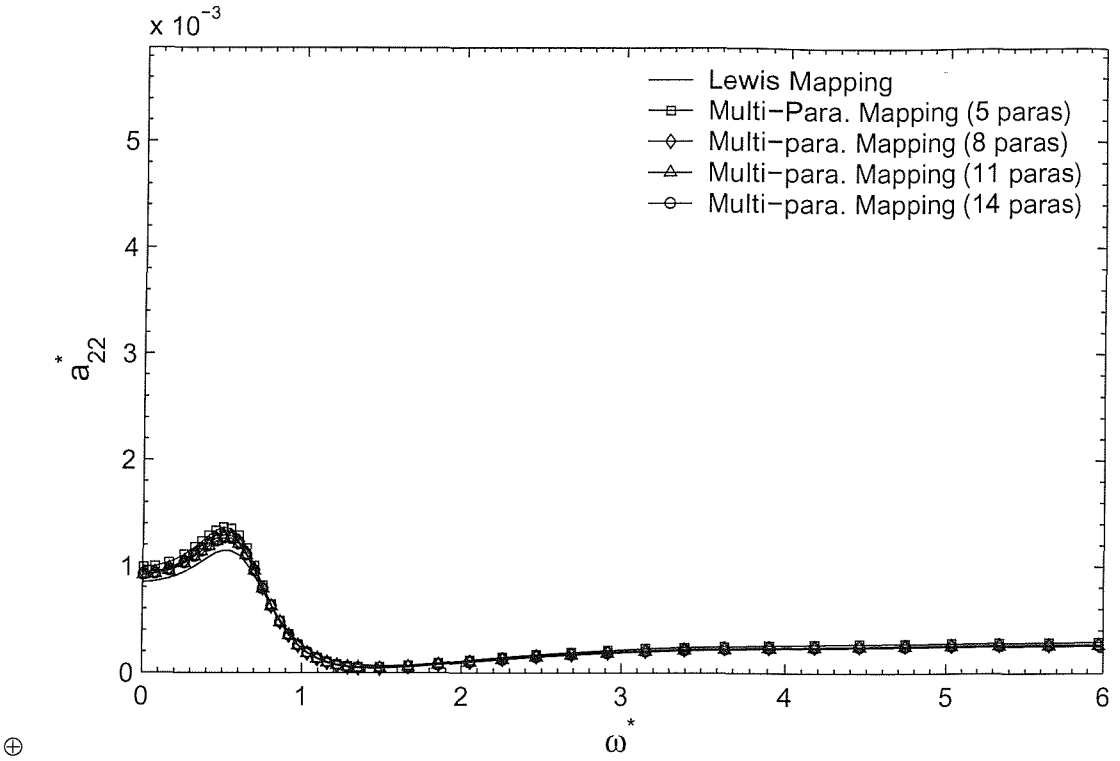

(a) Added-Mass a_{22}

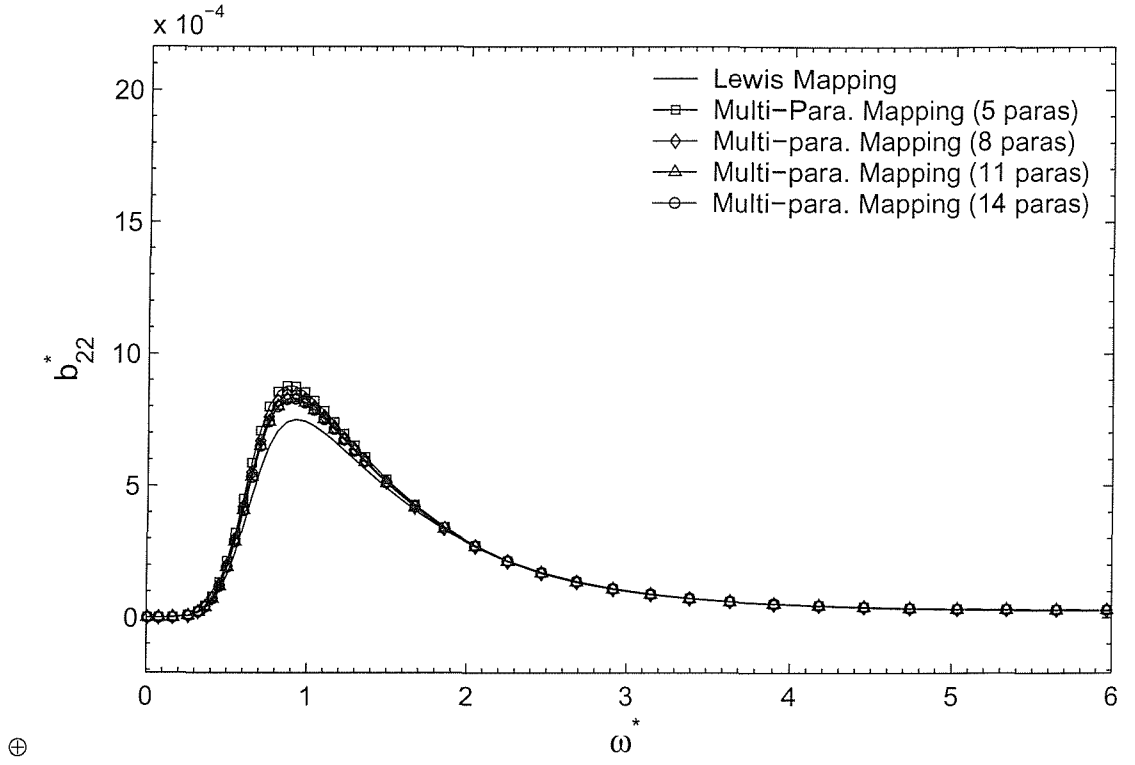

(b) Damping Coefficient b_{22}

Figure 4.17: *Sway Hydrodynamic Coefficients of Section 10 of Series 60 Hull Form without Heel Angle.*

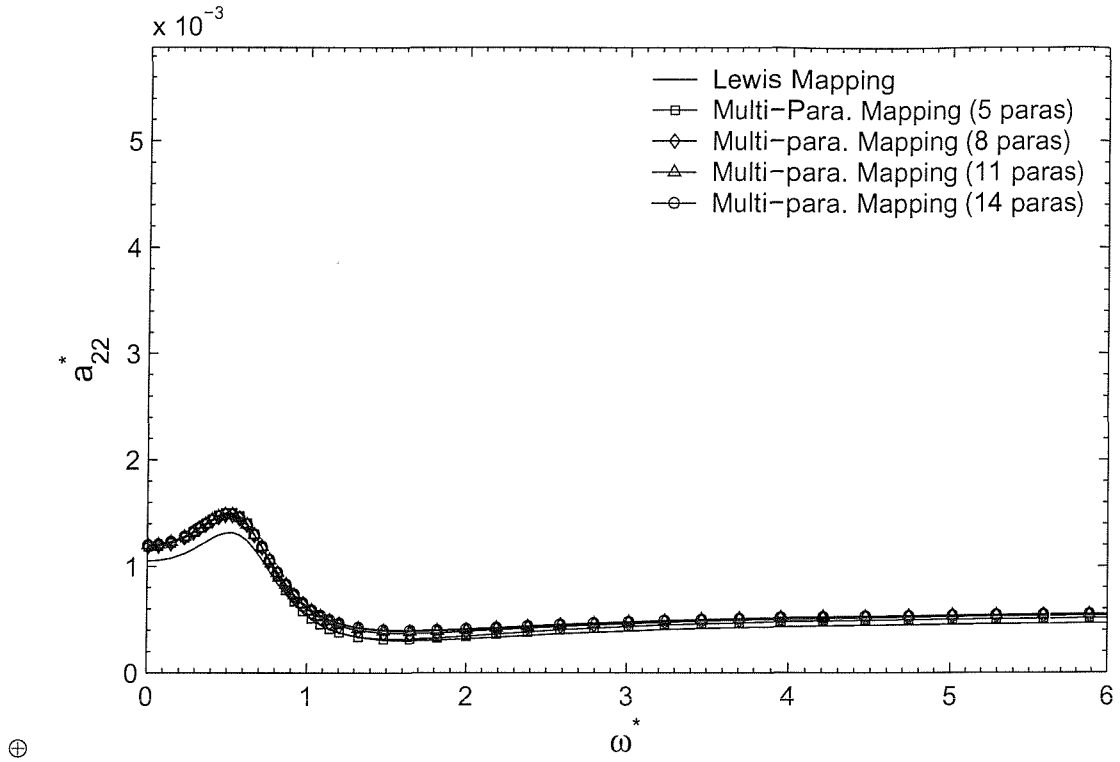

(a) Added-Mass a_{22}

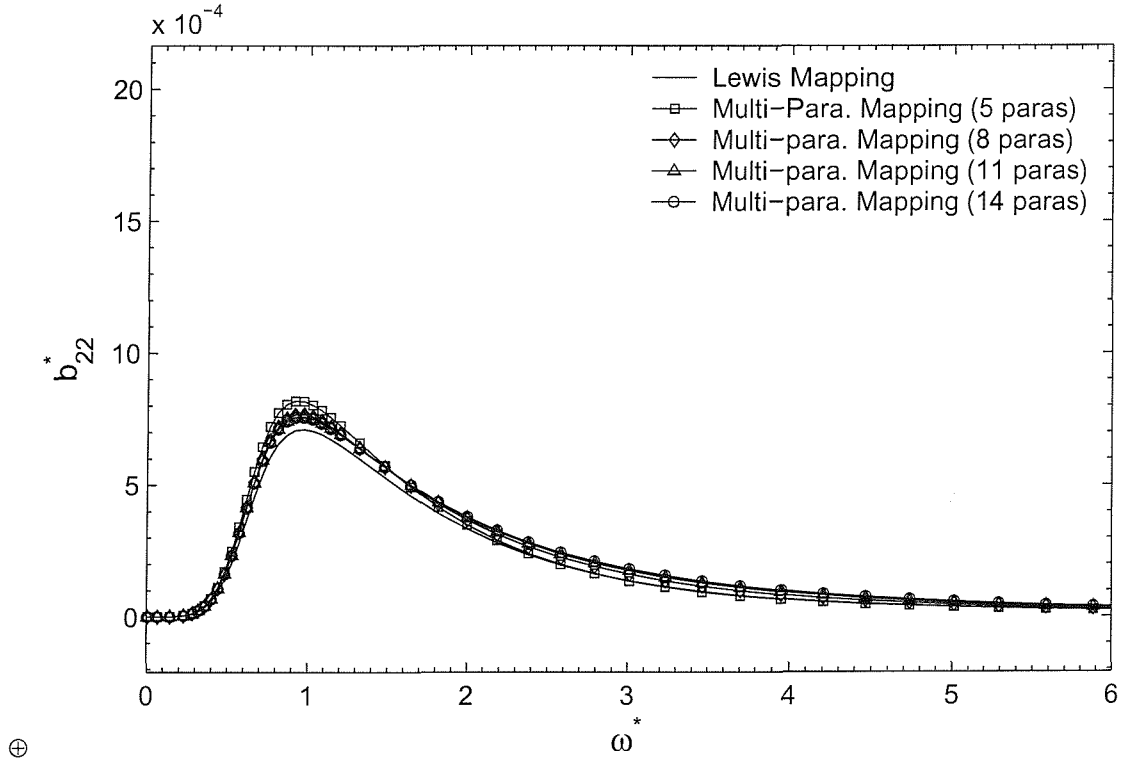

(b) Damping Coefficient b_{22}

Figure 4.18: *Sway Hydrodynamic Coefficients of Section 18 of Series 60 Hull Form without Heel Angle.*

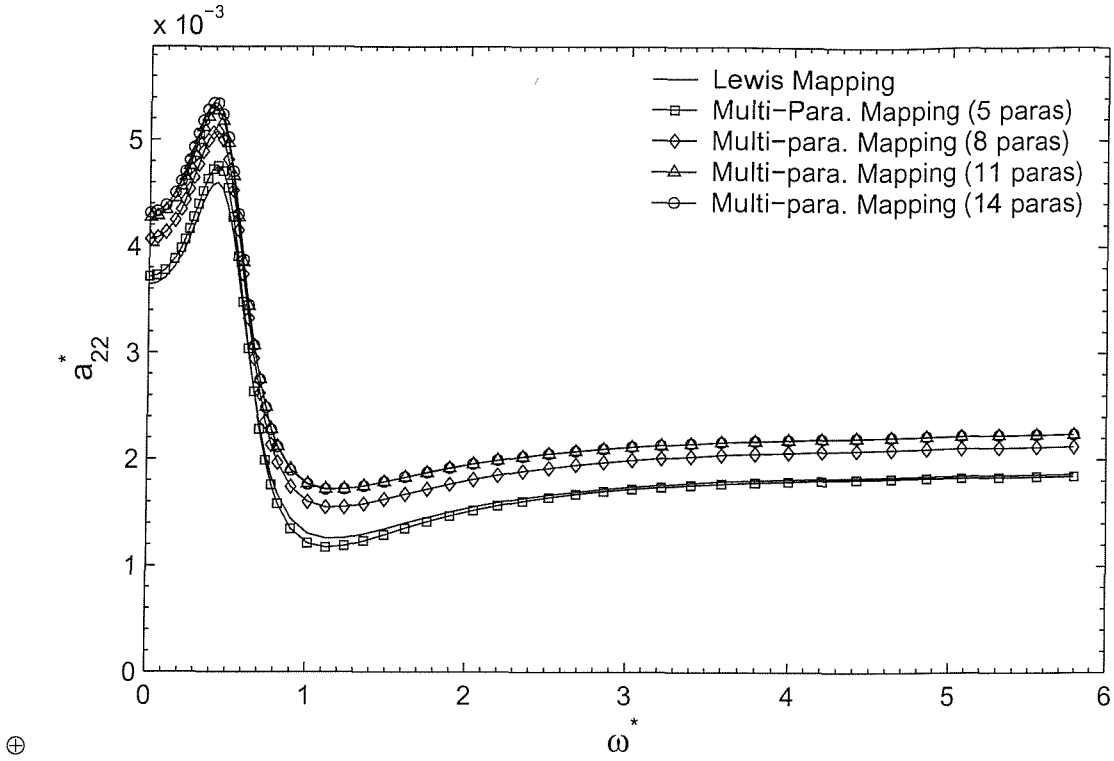

(a) Added-Mass a_{22}

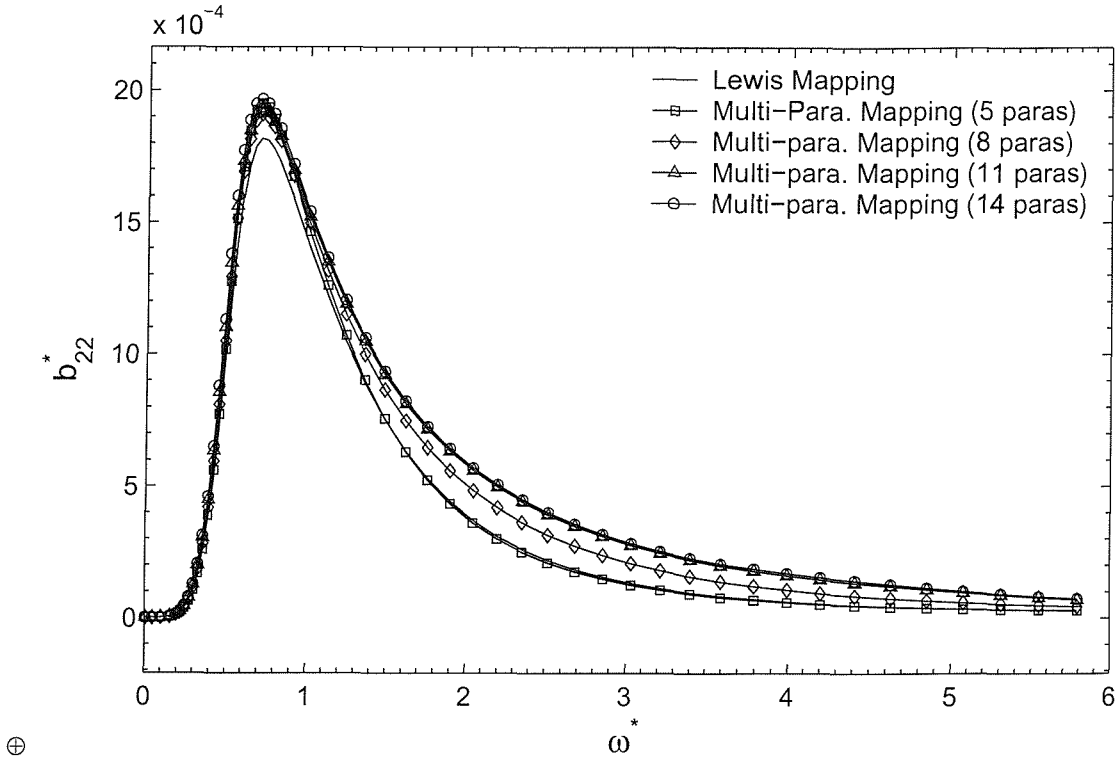

(b) Damping Coefficient b_{22}

Figure 4.19: *Sway Hydrodynamic Coefficients of Section 20 of Series 60 Hull Form without Heel Angle.*

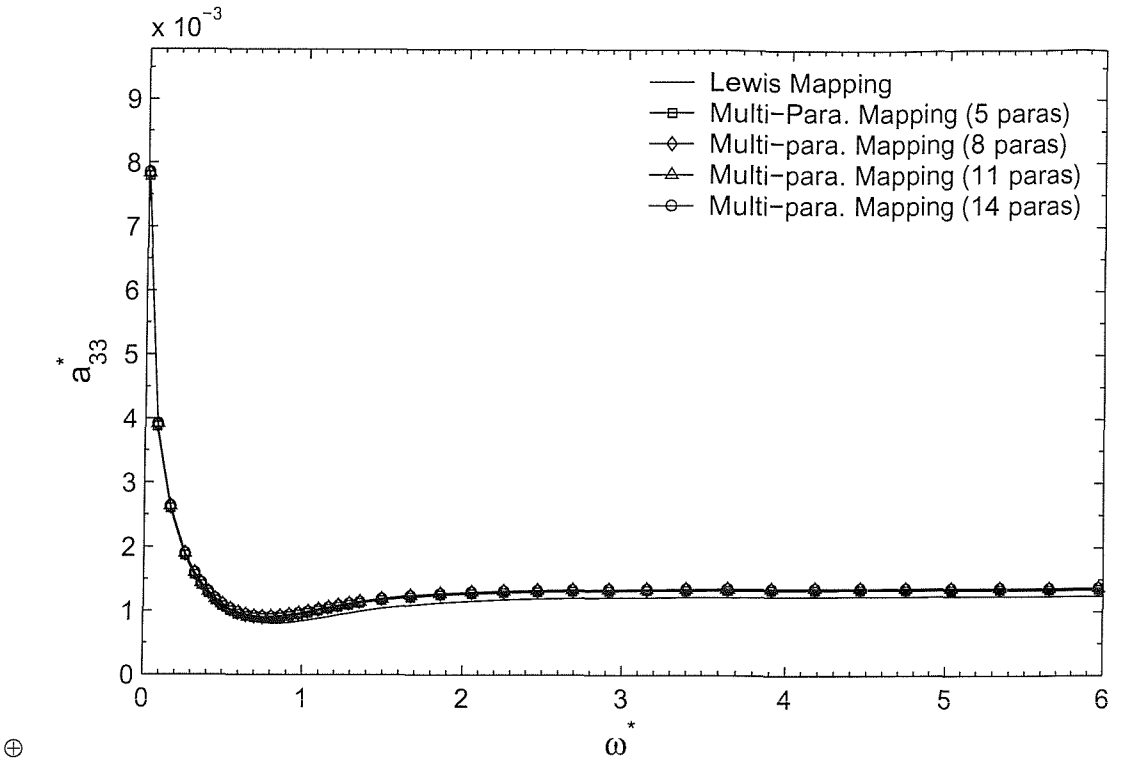

(a) Added-Mass a_{33}

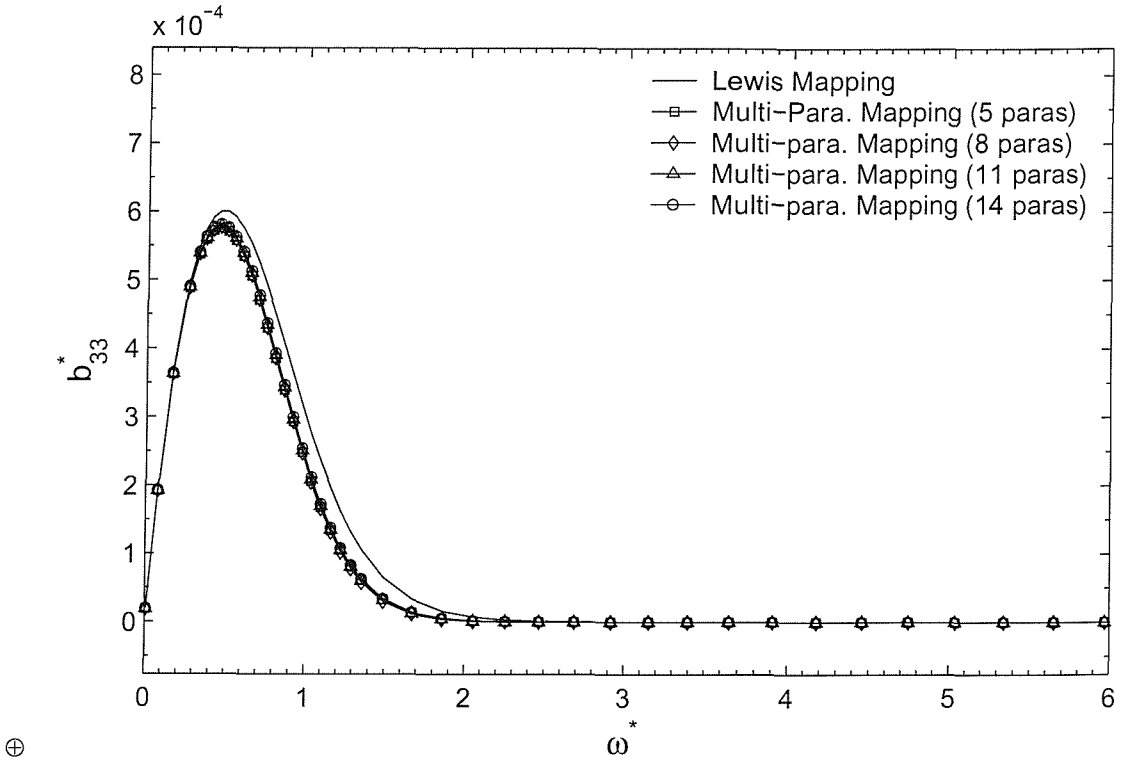

(b) Damping Coefficient b_{33}

Figure 4.20: *Heave Hydrodynamic Coefficients of Section 10 of Series 60 Hull Form without Heel Angle.*

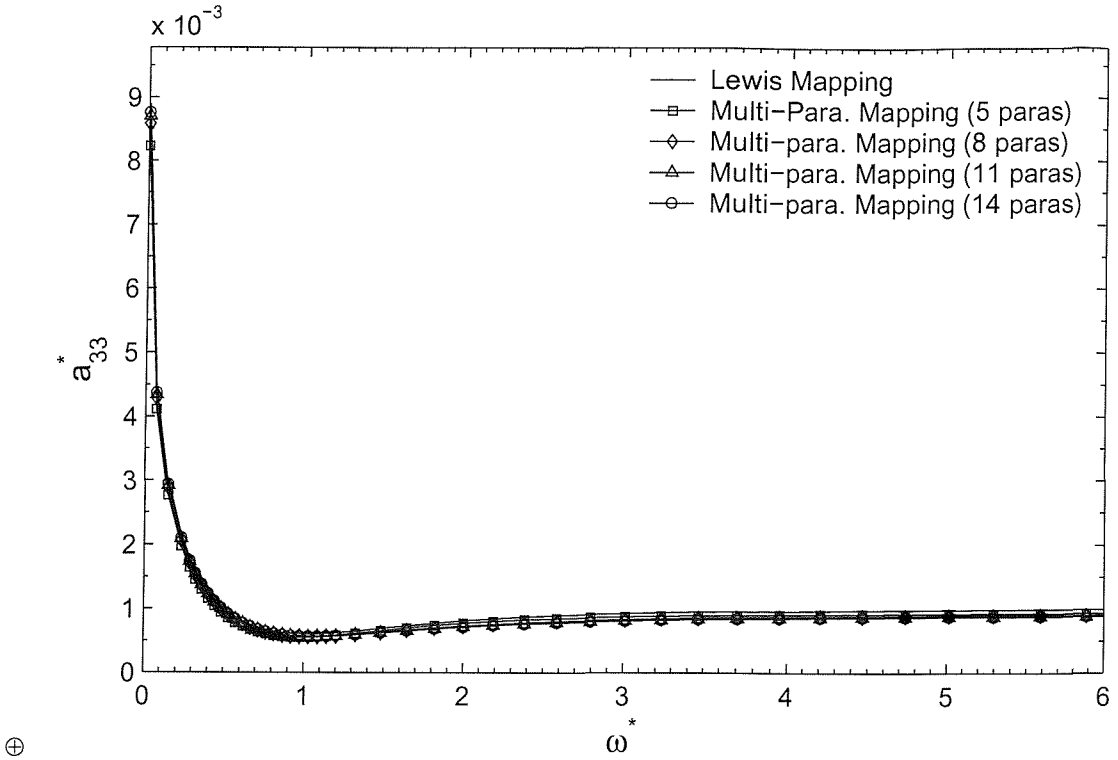

(a) Added-Mass a_{33}

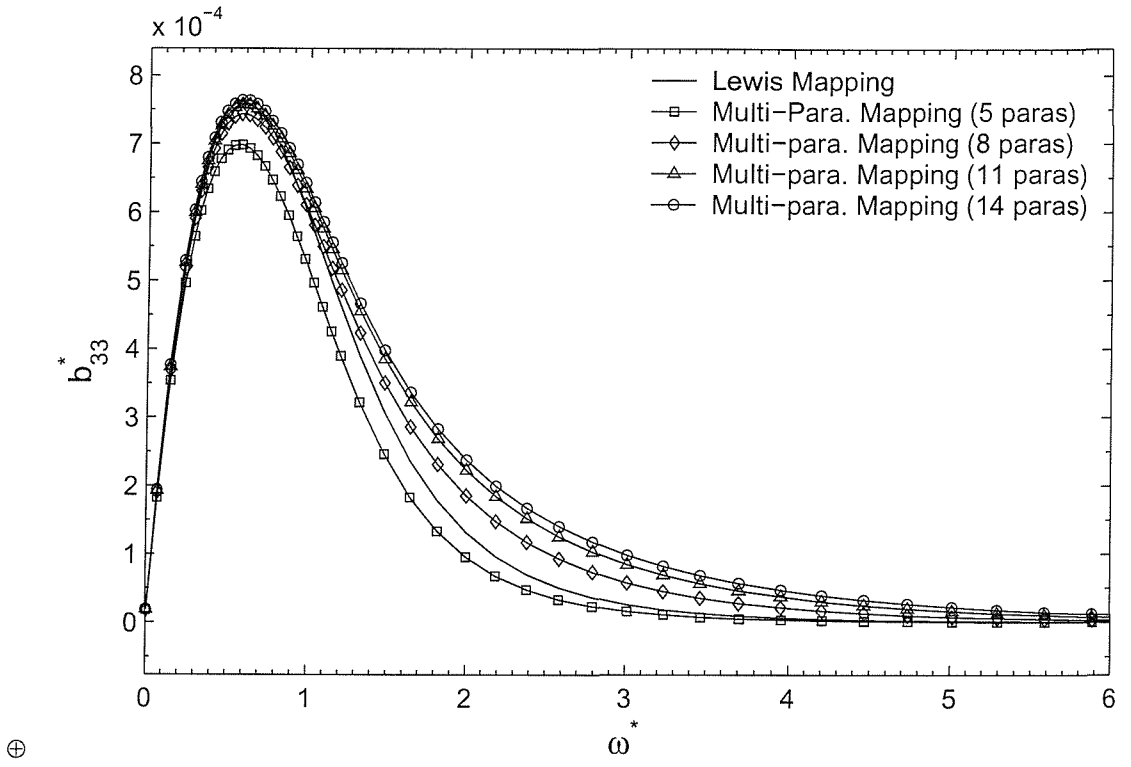

(b) Damping Coefficient b_{33}

Figure 4.21: *Heave Hydrodynamic Coefficients of Section 18 of Series 60 Hull Form without Heel Angle.*

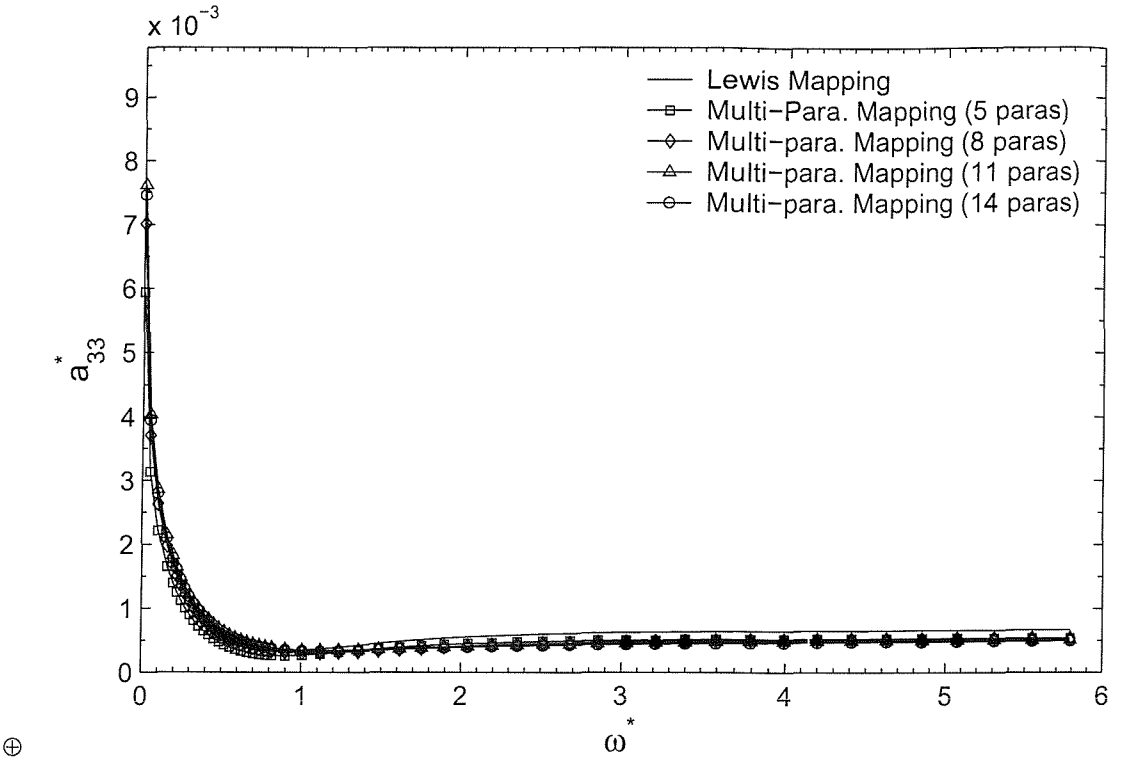

(a) Added-Mass a_{33}

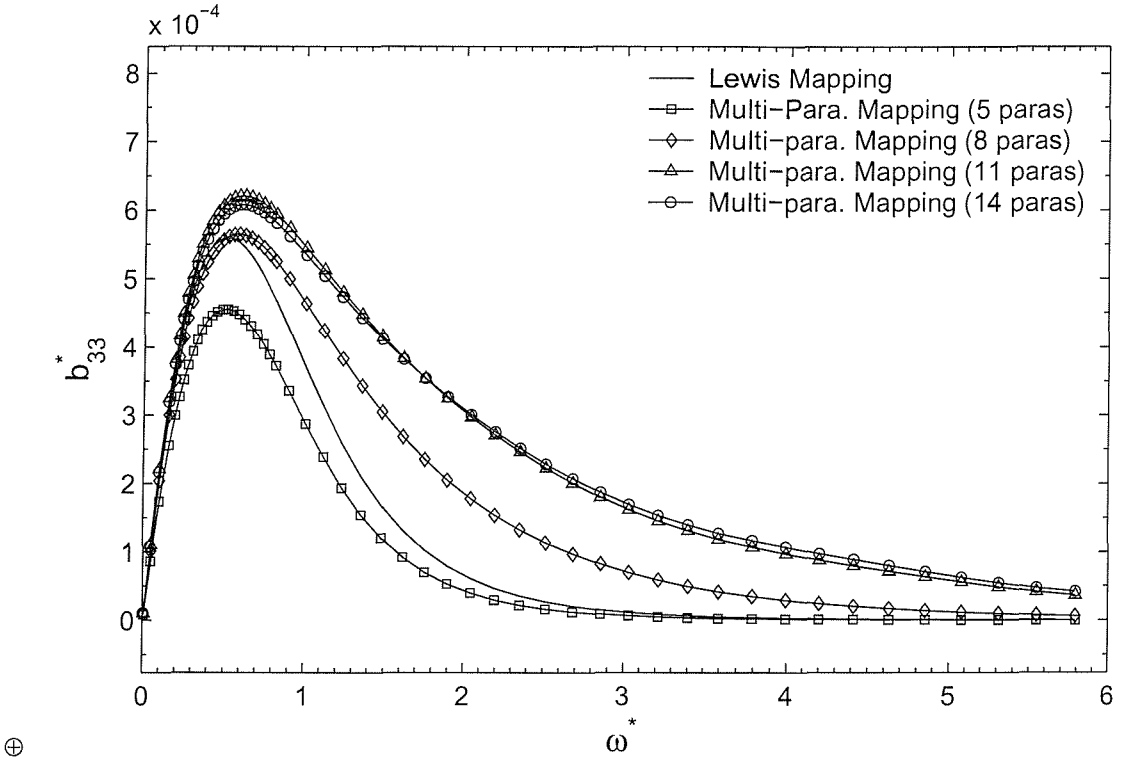

(b) Damping Coefficient b_{33}

Figure 4.22: *Heave Hydrodynamic Coefficients of Section 20 of Series 60 Hull Form without Heel Angle.*

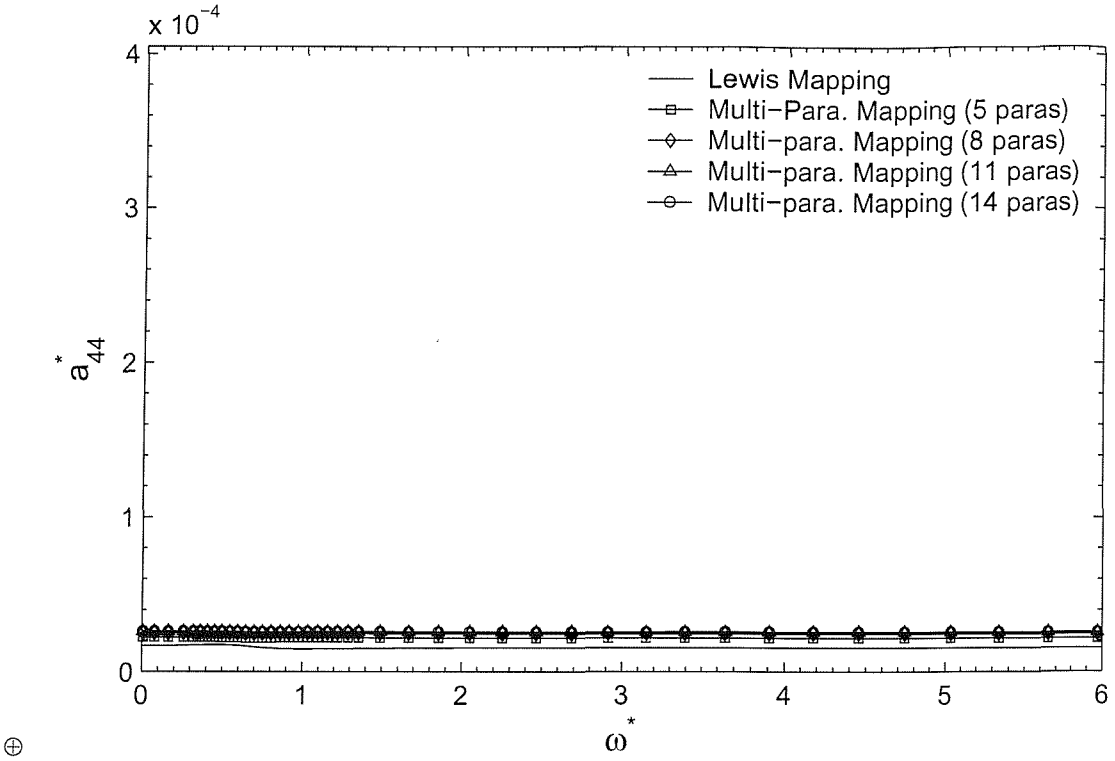

(a) Added-Moment of Inertia a_{44}

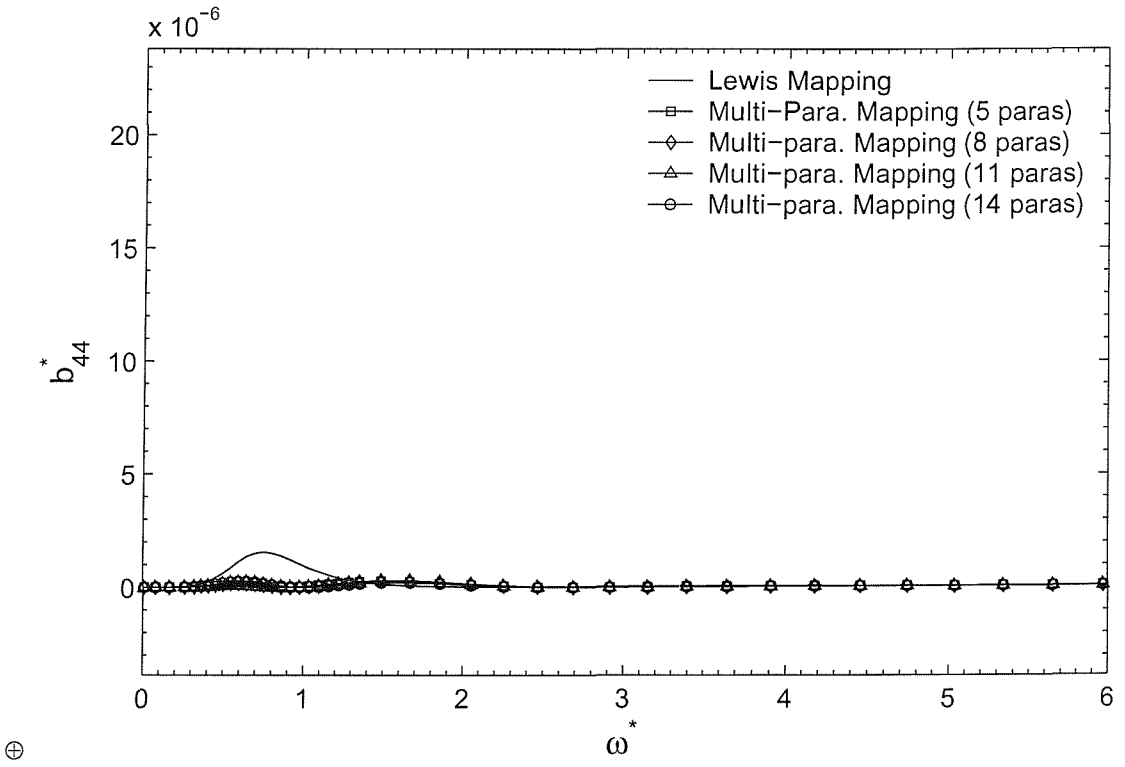

(b) Damping Coefficient b_{44}

Figure 4.23: *Roll Hydrodynamic Coefficients of Section 10 of Series 60 Hull Form without Heel Angle.*

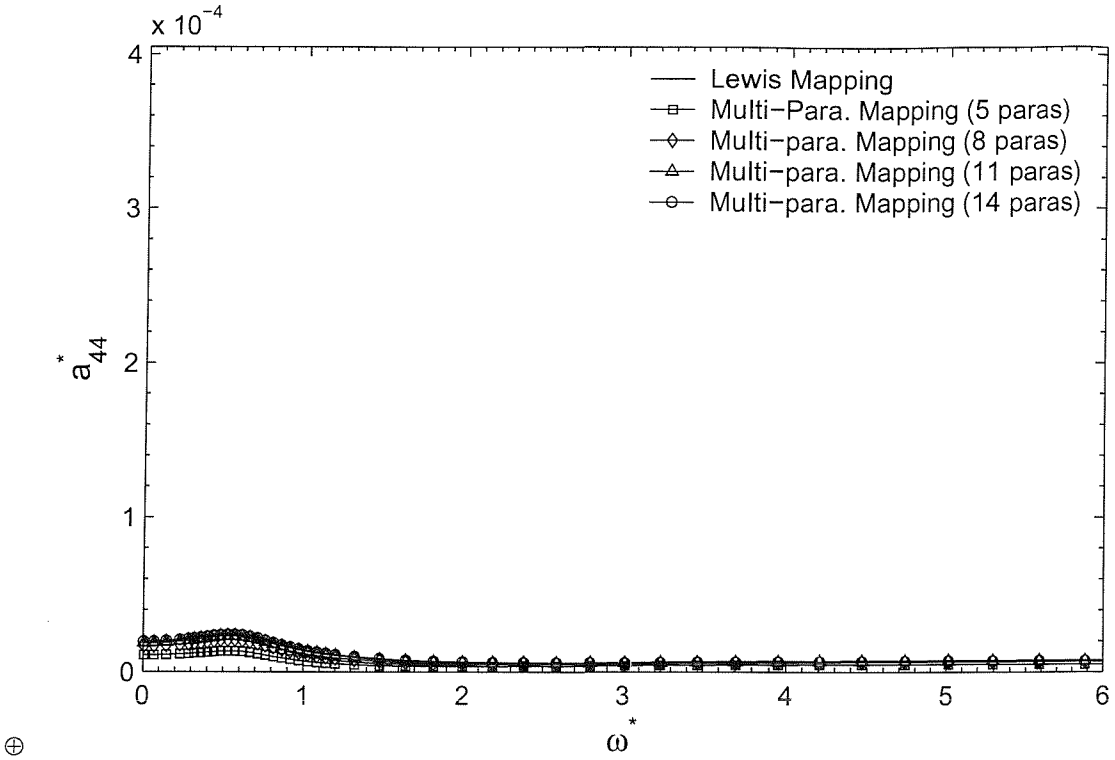

(a) Added-Moment of Inertia a_{44}

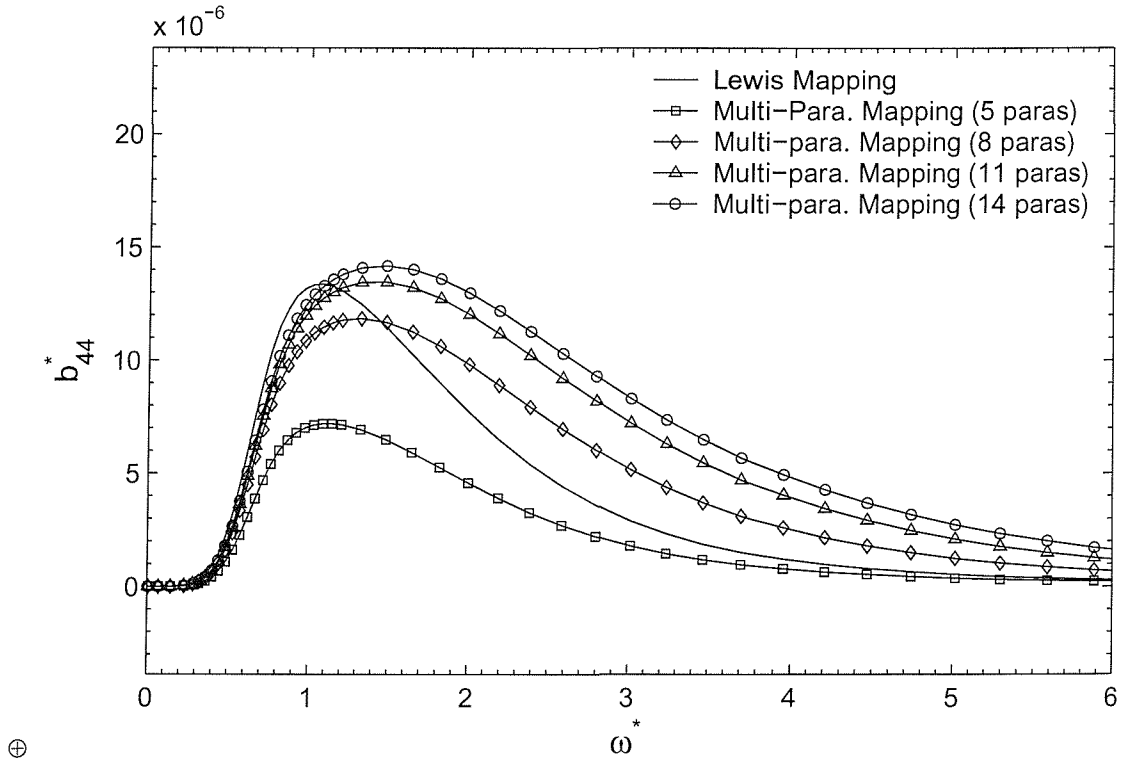

(b) Damping Coefficient b_{44}

Figure 4.24: *Roll Hydrodynamic Coefficients of Section 18 of Series 60 Hull Form without Heel Angle.*

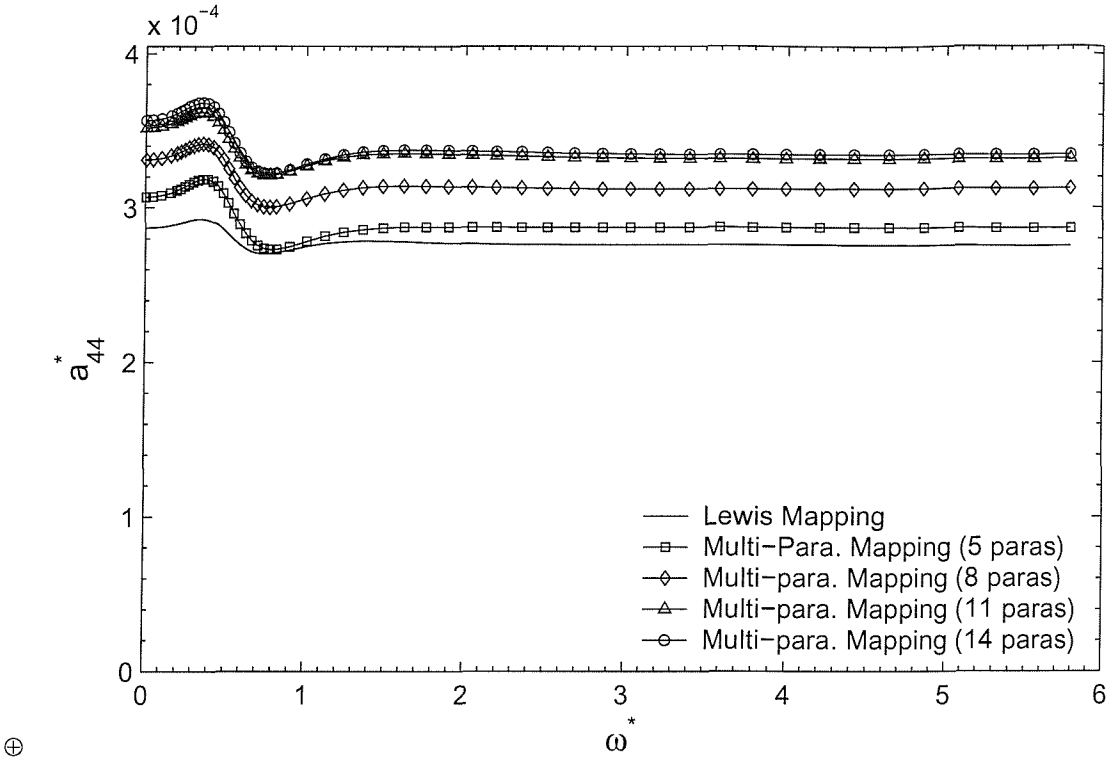

(a) Added-Moment of Inertia a_{44}

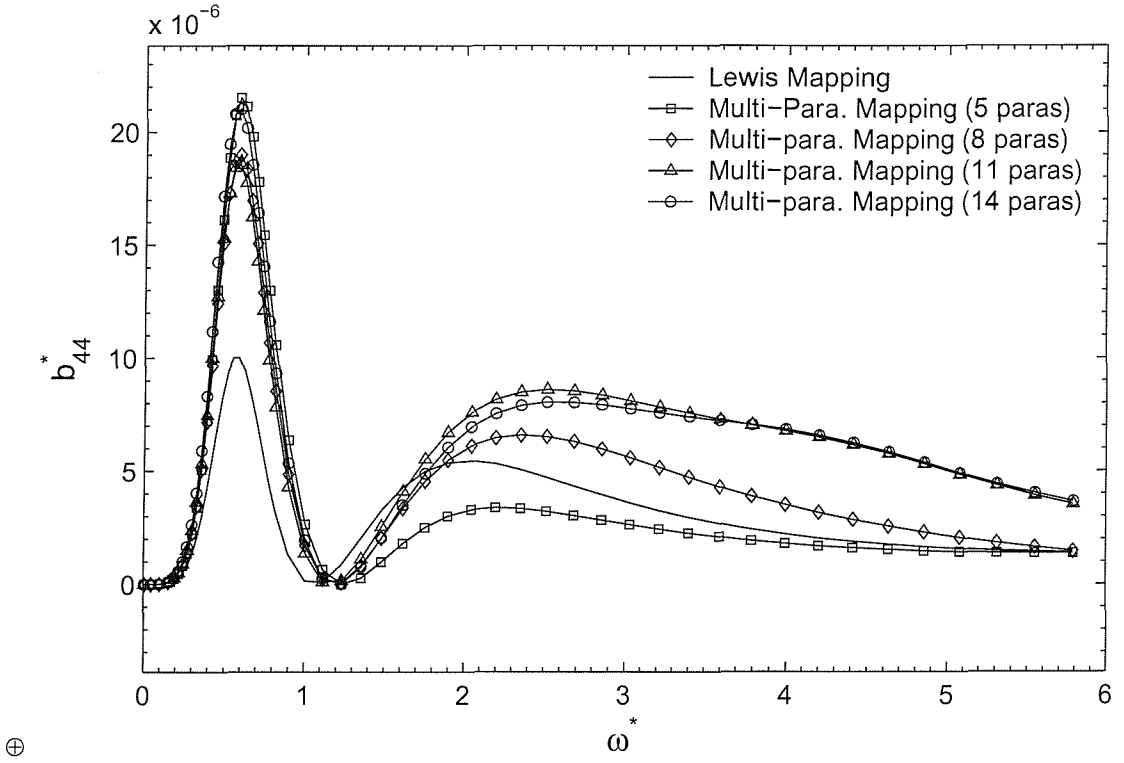

(b) Damping Coefficient b_{44}

Figure 4.25: *Roll Hydrodynamic Coefficients of Section 20 of Series 60 Hull Form without Heel Angle.*

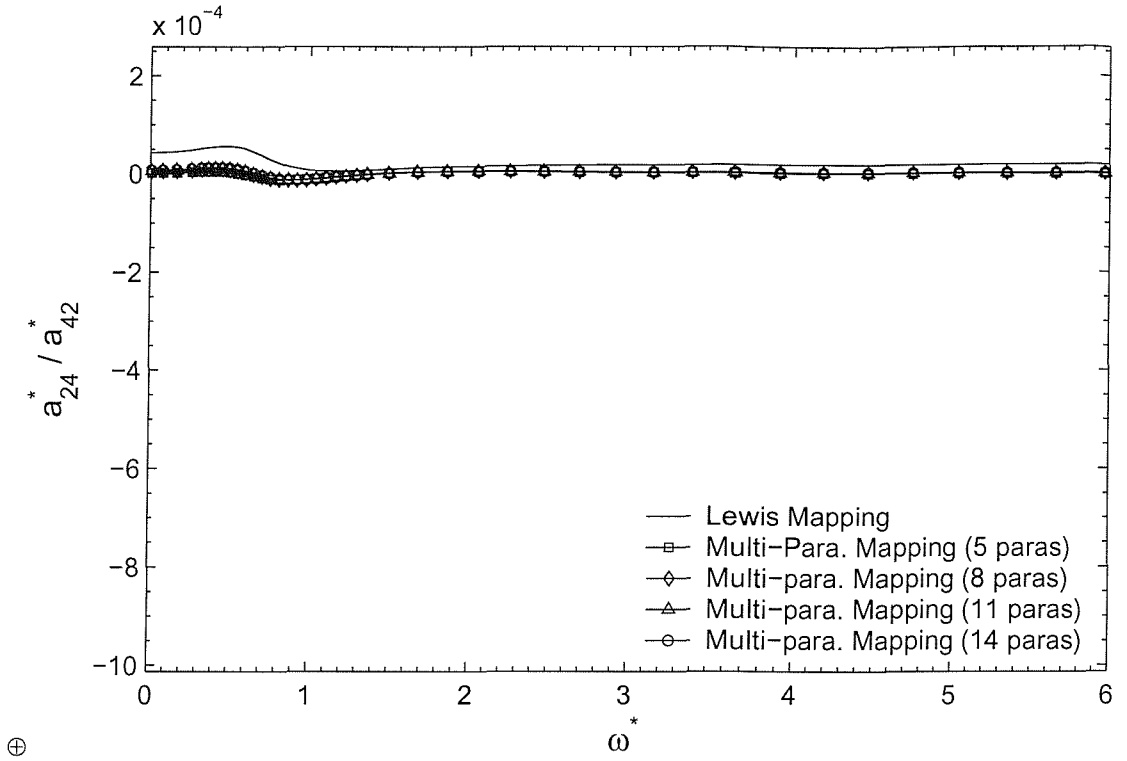

(a) Added-Mass a_{24} / Added-Moment of Inertia a_{42}

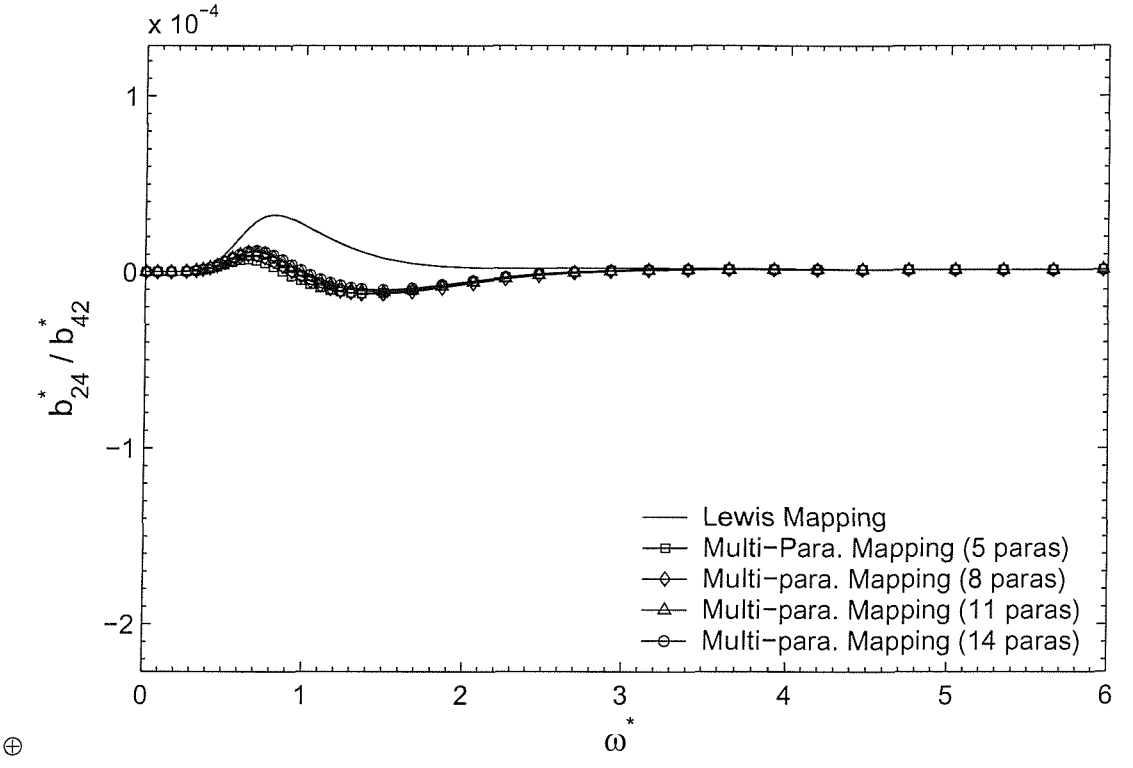

(b) Damping Coefficient b_{24}/b_{42}

Figure 4.26: *Sway-Roll and Roll-Sway Coupling Hydrodynamic Coefficients of Section 10 of Series 60 Hull Form without Heel Angle.*

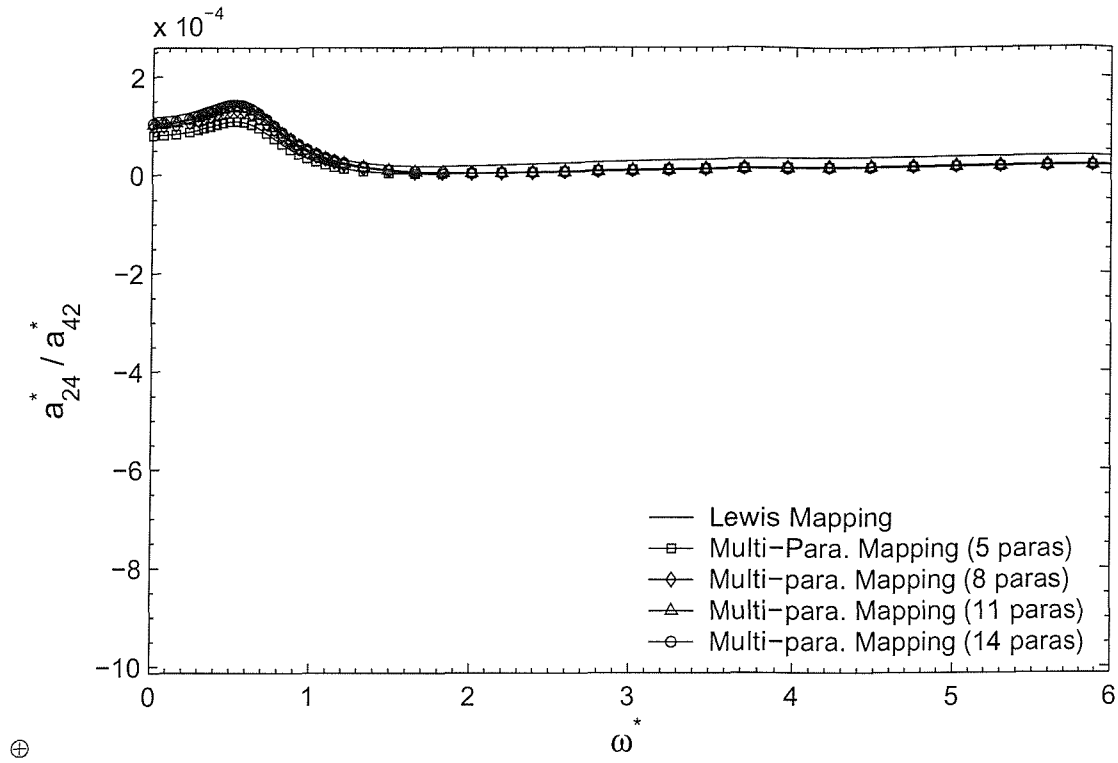

(a) Added-Mass a_{24} / Added-Moment of Inertia a_{42}

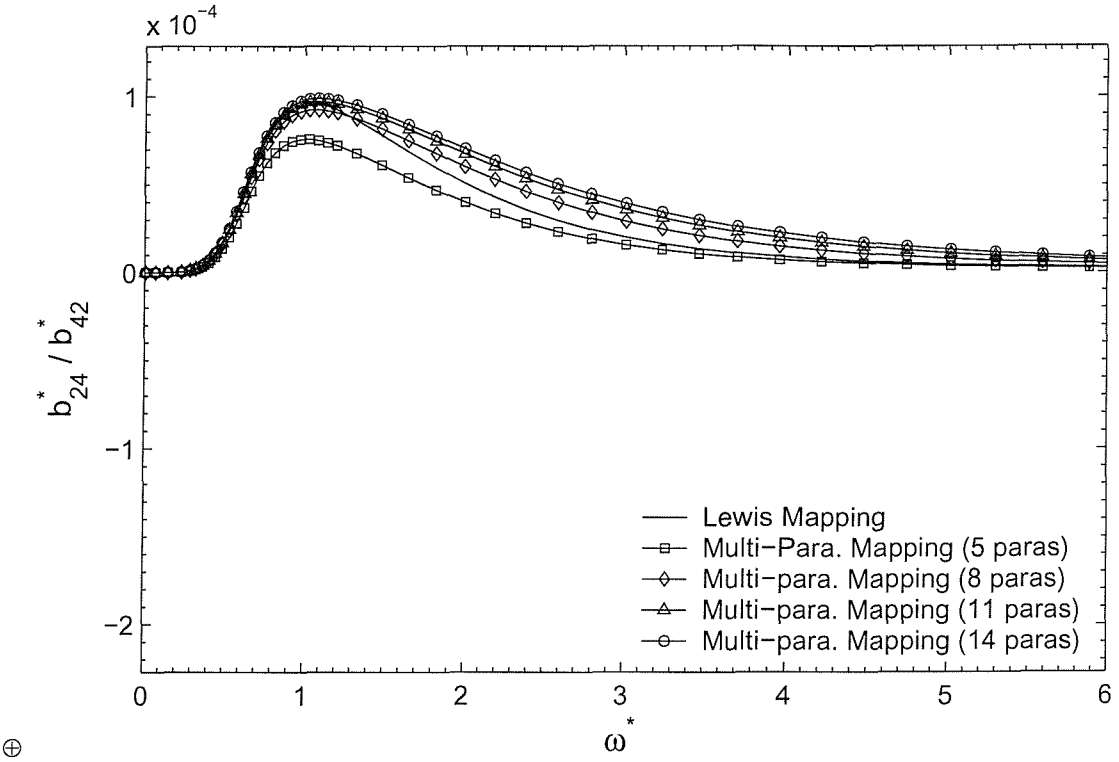

(b) Damping Coefficient b_{24}/b_{42}

Figure 4.27: *Sway-Roll and Roll-Sway Hydrodynamic Coefficients of Section 18 of Series 60 Hull Form without Heel Angle.*

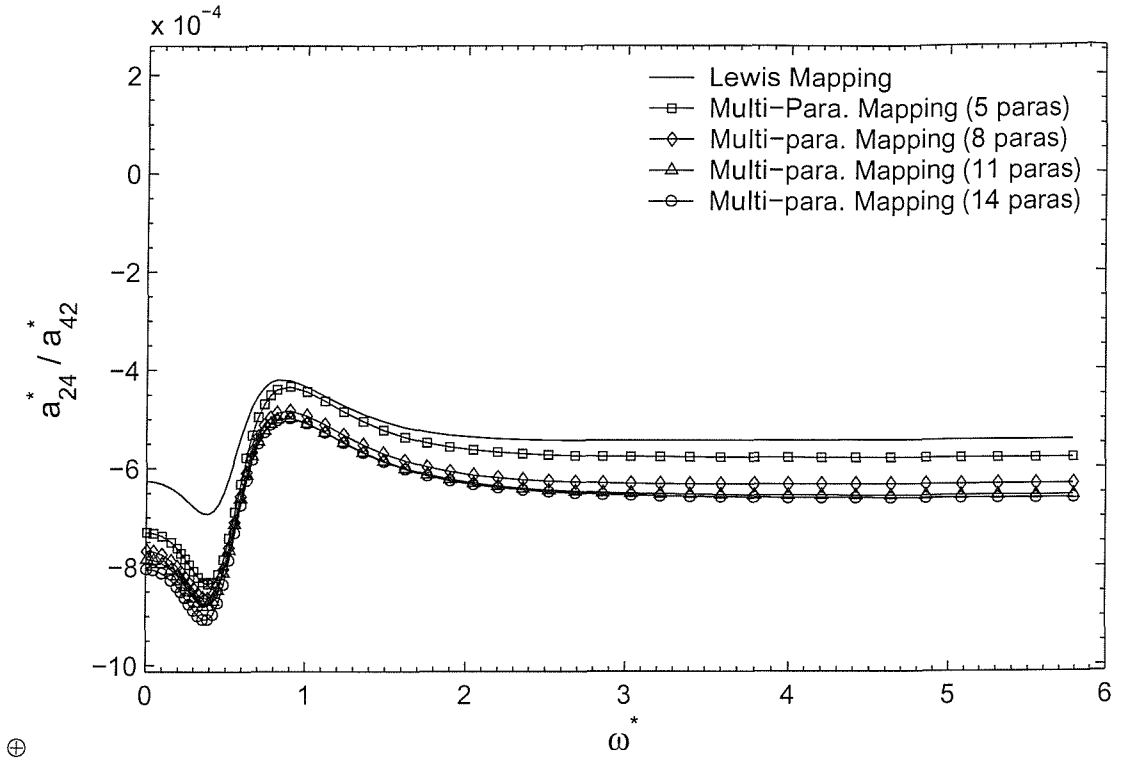

(a) Added-Mass a_{24} / Added-Moment of Inertia a_{42}

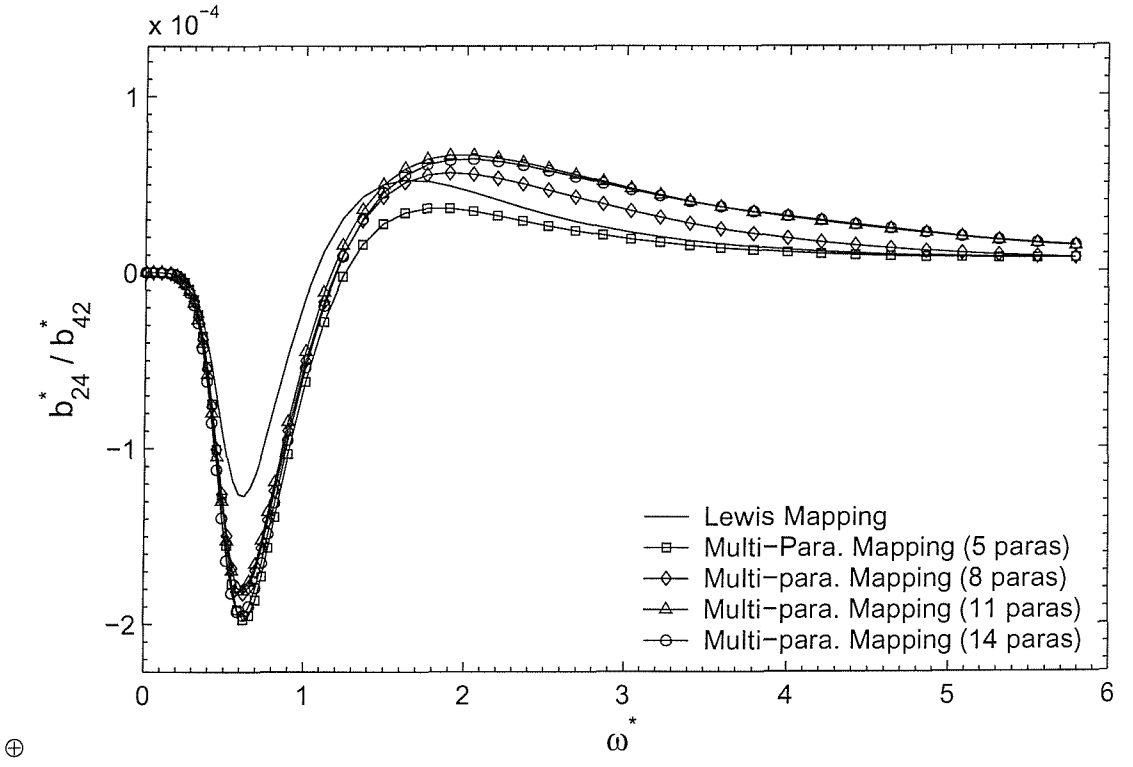

(b) Damping Coefficient b_{24}/b_{42}

Figure 4.28: *Sway-Roll and Roll-Sway Hydrodynamic Coefficients of Section 20 of Series 60 Hull Form without Heel Angle.*

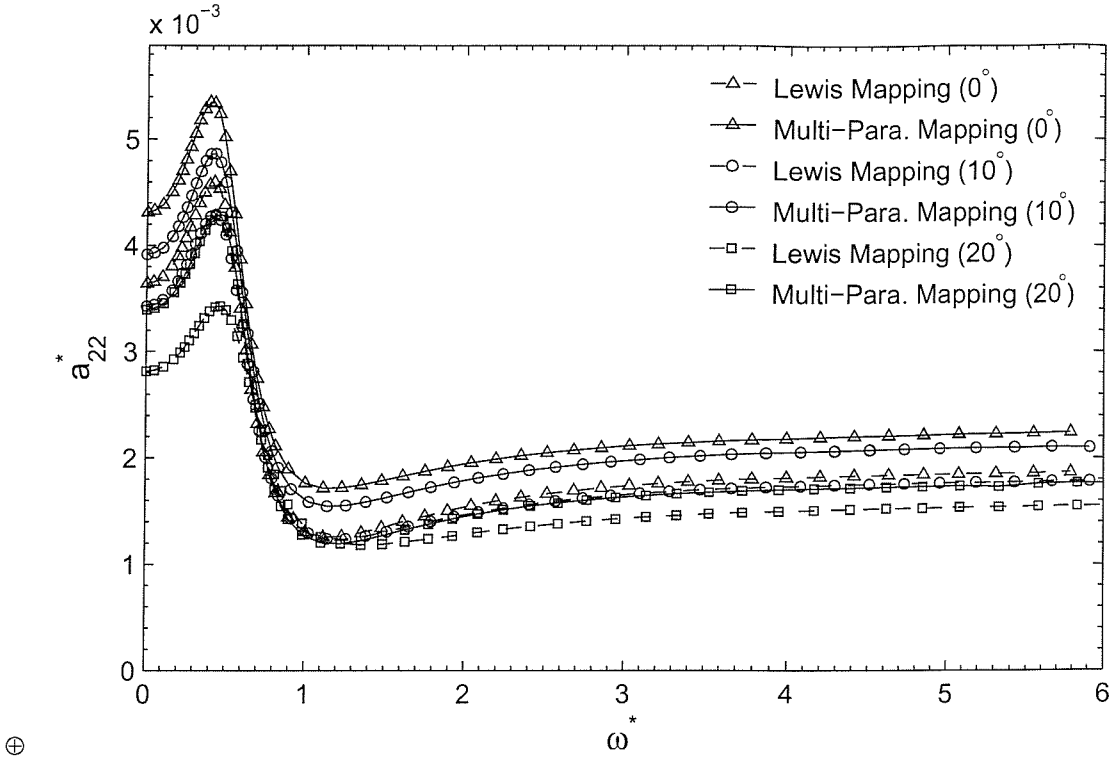

(a) Added-Mass a_{22}

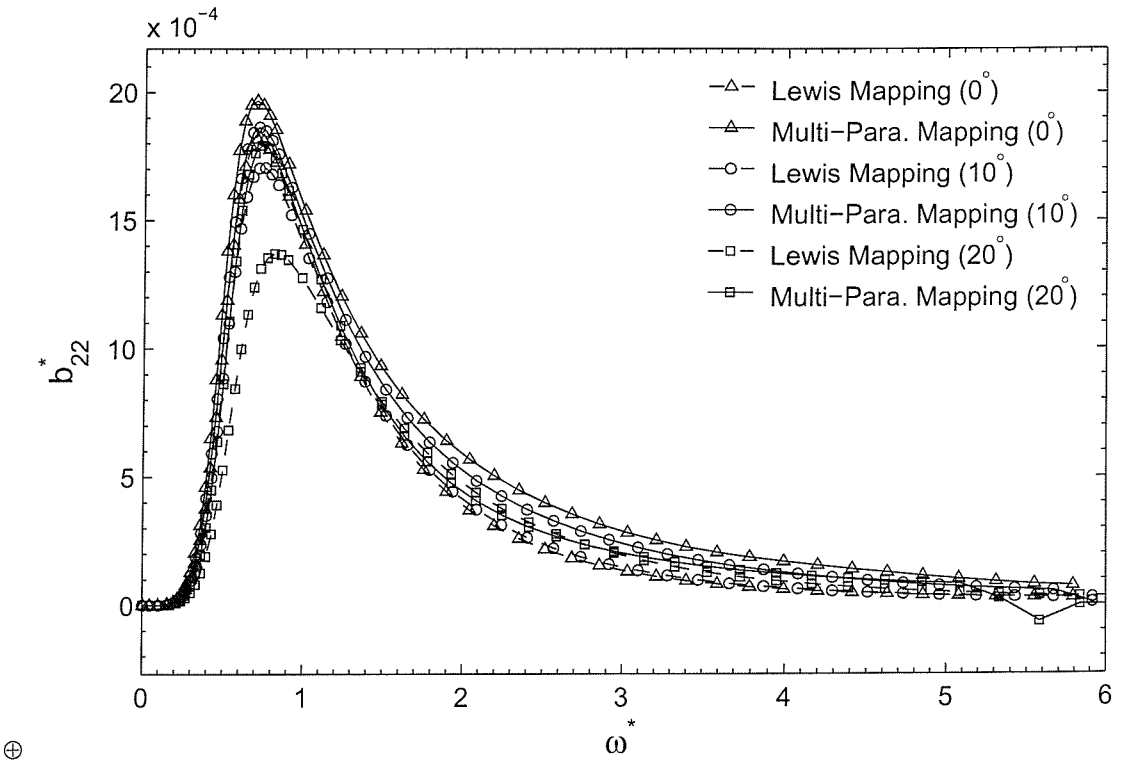

(b) Damping Coefficient b_{22}

Figure 4.29: *Sway Hydrodynamic Coefficients of Section 20 of Series 60 Hull Form with Heel Angles* $0°$, $10°$ *and* $20°$.

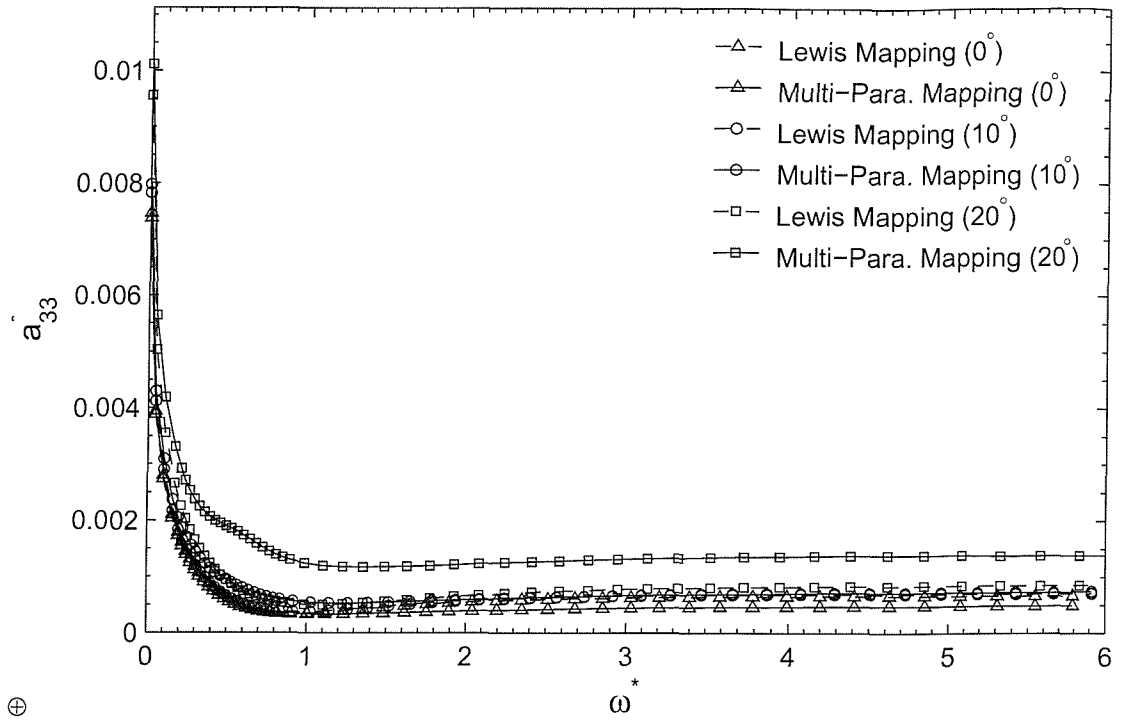

(a) Added-Mass a_{33}

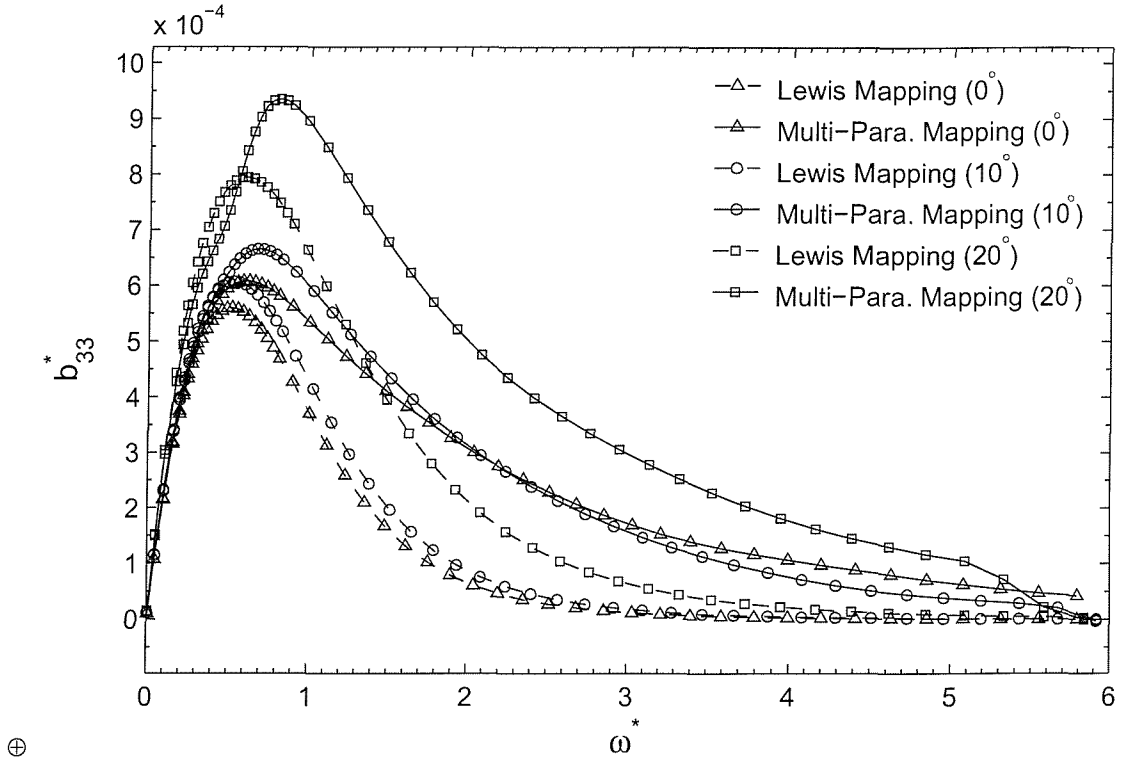

(b) Damping Coefficient b_{33}

Figure 4.30: *Heave Hydrodynamic Coefficients of Section 20 of Series 60 Hull Form with Heel Angles* 0°, 10° *and* 20°.

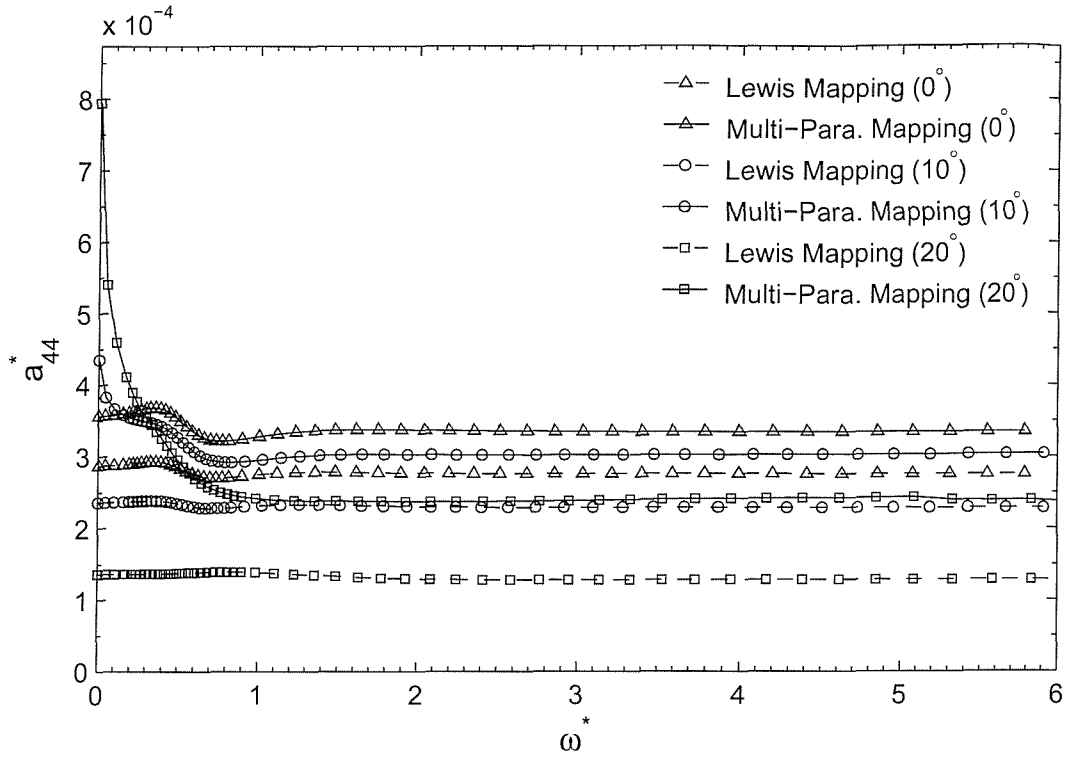

(a) Added-Moment of Inertia a_{44}

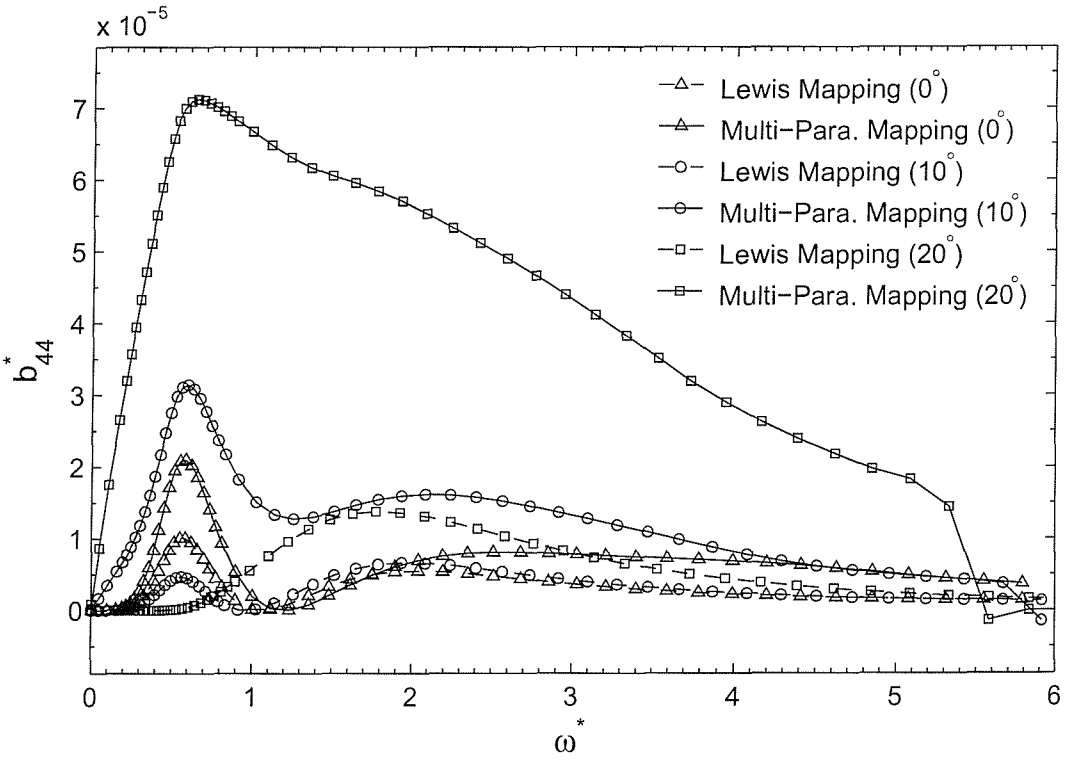

(b) Damping Coefficient b_{44}

Figure 4.31: *Roll Hydrodynamic Coefficients of Section 20 of Series 60 Hull Form with Heel Angles* $0°$, $10°$ *and* $20°$.

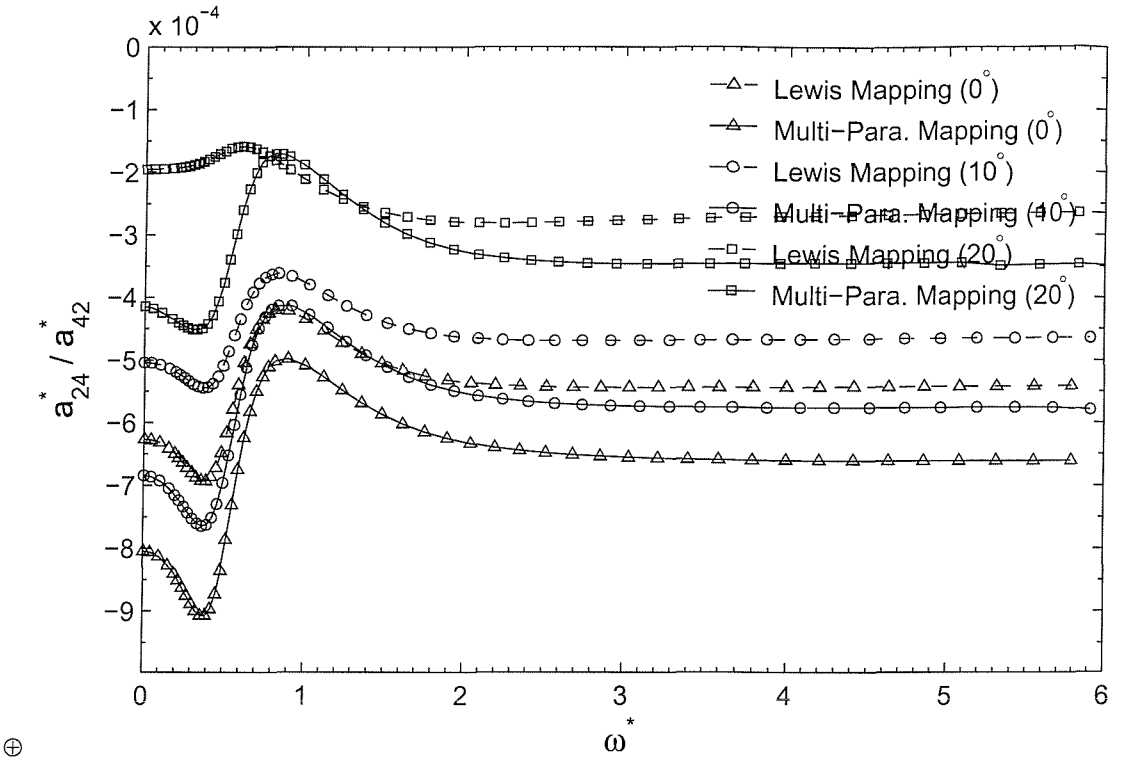

(a) Added-Mass a_{24} / Added-Moment of Inertia a_{42}

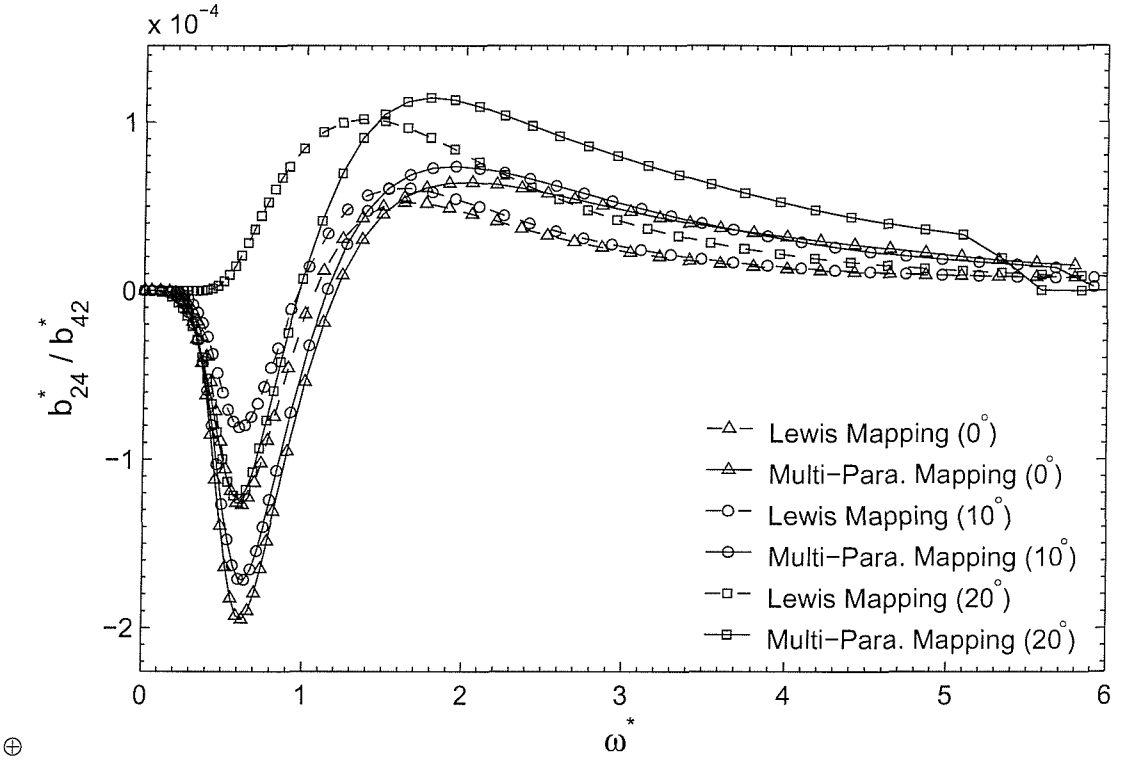

(b) Damping Coefficient b_{24}/b_{42}

Figure 4.32: *Sway-Roll and Roll-Sway Coupling Coefficients of Section 20 of Series 60 Hull Form with Heel Angles* $0°$, $10°$ *and* $20°$.

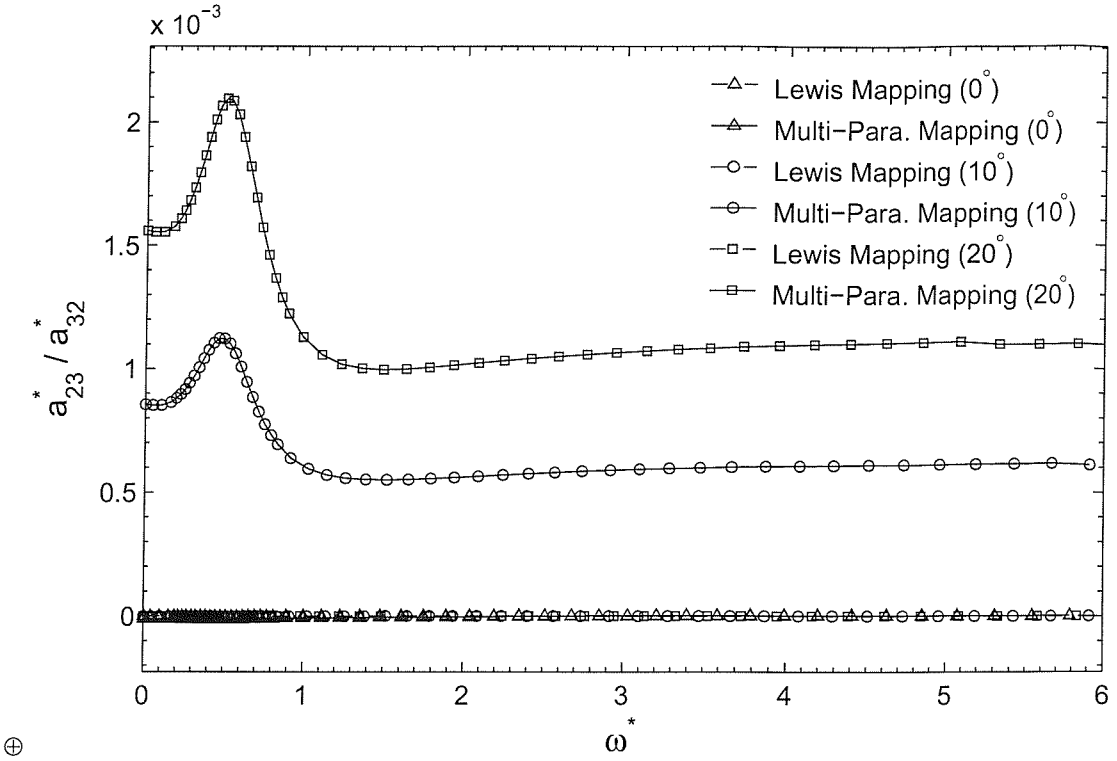

(a) Added-Mass a_{23}/a_{32}

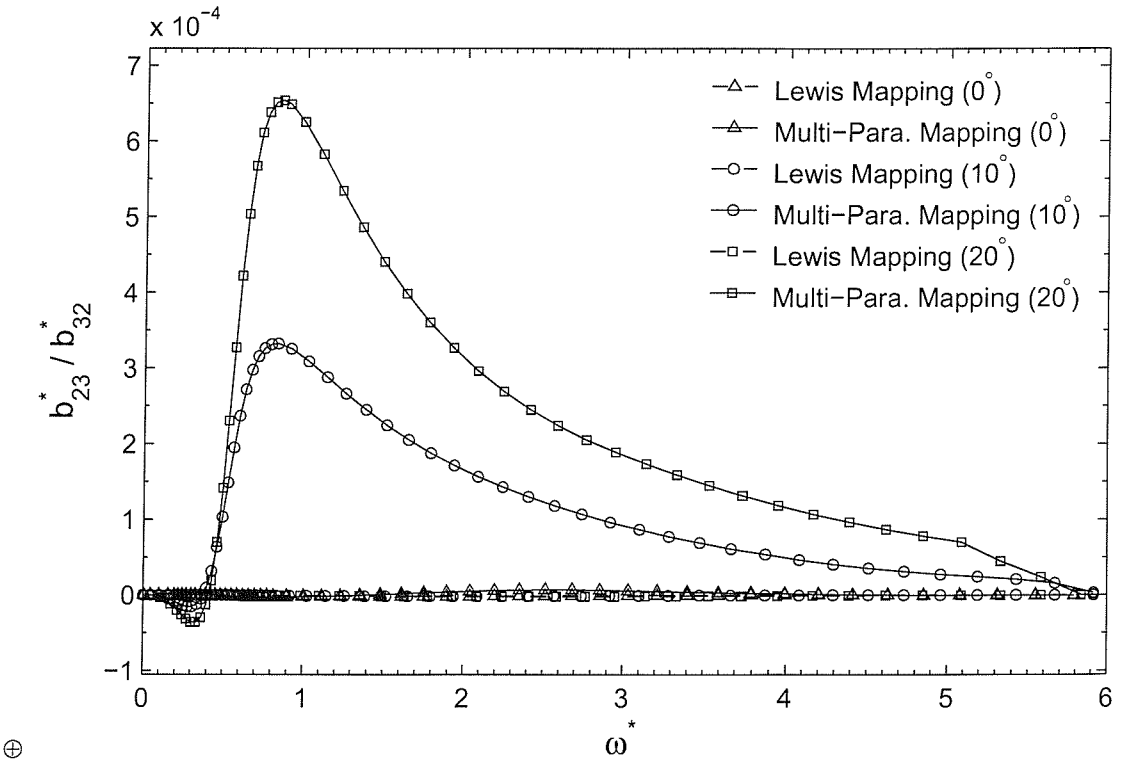

(b) Damping Coefficient b_{243}/b_{32}

Figure 4.33: *Sway-Heave and Heave-Sway Coupling Coefficients of Section 20 of Series 60 Hull Form with Heel Angles* $0°$, $10°$ *and* $20°$.

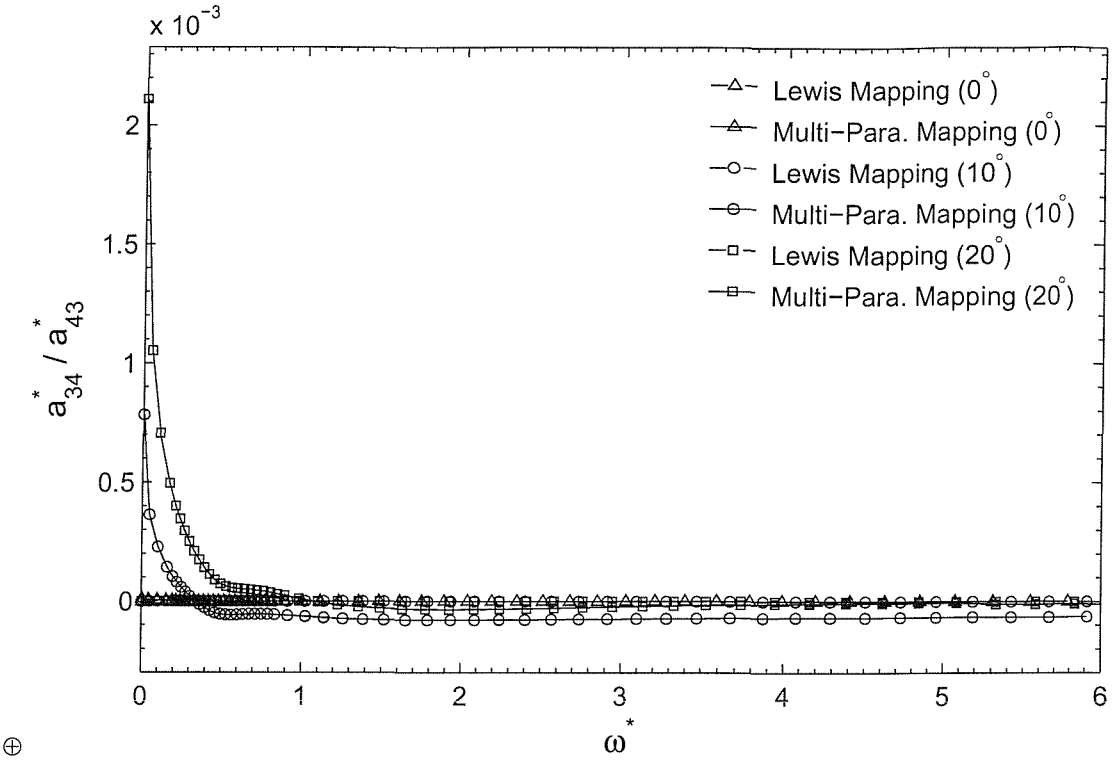

(a) Added-Mass a_{34} / Added-Moment of Inertia a_{43}

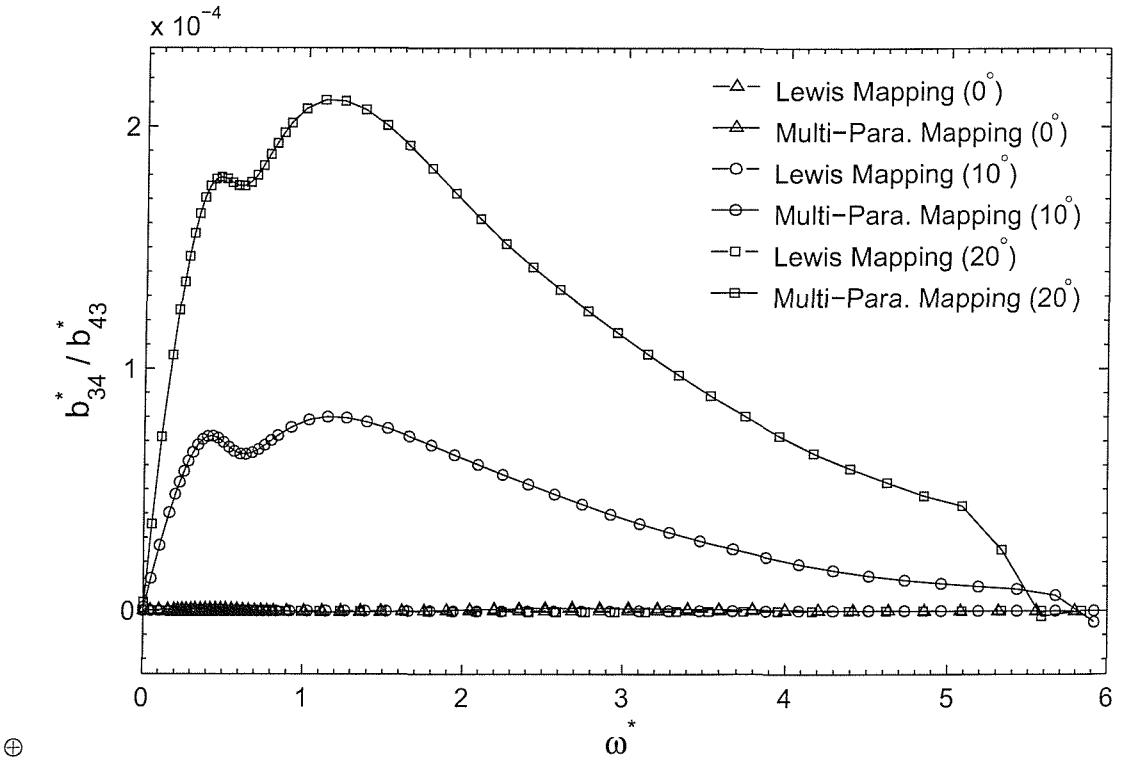

(b) Damping Coefficient b_{34}/b_{43}

Figure 4.34: *Heave-Roll and Roll-Heave Coupling Coefficients of Section 20 of Series 60 Hull Form with Heel Angles* $0°$, $10°$ *and* $20°$.

4.6 Three-Dimensional Hydrodynamic Coefficients

The three-dimensional hydrodynamics coefficients are computed by the strip theory developed by Salvesen, *et al* [56]. This strip theory has been commonly used and has been proved to be able to accurately calculate the hydrodynamics coefficients and predict ship motion and sea loads. The purpose of the section is to verify the time-domain strip theory program developed with this thesis by comparing the results with those obtained by experiment and by frequency-domain Green function method. Since the program deals with asymmetric underwater hull forms at most of the time, it is preferred to verify the program using the experimental data from those ship models with asymmetric underwater hull shape. Unfortunately no such experimental data is available. Hence only the computed hydrodynamic coefficients of a ship at equilibrium position can be compared with experimental data. The computed hydrodynamic coefficients of a ship at any other positions may be accessed qualitatively through analysing the hydrodynamic coefficients of a heeled ship.

The experimental data of the Series 60 ($C_B = 0.70$) ship model are adopted to verify the program. This hull form model has been tested by Gerritsma [19] and Gerritsma and Beukelman [20]. In addition, Chang [9], Inglis and Price [25], and Hudson [24] have given numerical results using frequency-domain Green function method. Meanwhile Liapis [28], Beck and Liapis [4], and King, *et al* [30] have presented numerical results using time-domain Green function method. Figures (4.35 - 4.42) illustrate the hydrodynamics coefficients of the Series 60 ($C_B = 0.70$) model travelling at a Froude number of 0.2. The hydrodynamic coefficients are shown in non-dimensional form as a function of non-dimensional frequency of encounter ω_e^*,

$$\omega_e^* = \omega_e \sqrt{L_{ship}/g}, \tag{4.9}$$

where ω_e is the frequency of encounter, L_{ship} is the model length between per-

pendiculars. The factors which are used to render the hydrodynamic coefficients non-dimensional are given in Table (4.4), in which ϱ is the fluid density and V_{dsp} is the model displacement.

Coefficient	Units	Dimensions	Factor
A_{22}, A_{33}	kg	M	ϱV_{dsp}
A_{44}, A_{55}, A_{66}	$kg{\cdot}m^2$	ML^2	$\varrho V_{dsp} L_{ship}^2$
A_{35}, A_{53}, A_{26}, A_{62}	$kg{\cdot}m$	ML	$\varrho V_{dsp} L_{ship}$
B_{22}, B_{33}	kg/s	M/T	$\varrho \omega_e V_{dsp}$
B_{44}, B_{55}, B_{66}	$kg{\cdot}m^2/s$	ML^2/T	$\varrho \omega_e V_{dsp} L_{ship}^2$
B_{35}, B_{53}, B_{26}, B_{62}	$kg{\cdot}m/s$	ML/T	$\varrho \omega_e V_{dsp} L_{ship}$

Table 4.4: *Factors Used to Render the Hydrodynamic Coefficients of the Series 60 ($C_B = 0.70$) Model Non-Dimensional.*

4.6.1 Symmetric Hydrodynamic Coefficients

Figures (4.35 - 4.38) show the symmetric hydrodynamics coefficients. Four sets of data are presented. The black diamond markers represent the experimental results of Gerritsma and Beukelman[20] for a Froude number of 0.2. The curves with circle markers are the results computed using strip theory and Lewis conformal mapping to solve two-dimensional problem. The curves with triangle markers are the results calculated using strip theory and multi-parameter conformal mapping to solve two-dimensional problem. The results computed by frequency-domain Green function method are shown as curves with square markers. The program of frequency-domain Green function method was provided by Dr. D. A. Hudson in School of Engineering Sciences, University of Southampton.

It is very obvious that the strip theory indeed gives much smoother results than the frequency-domain Green function method over the whole range of fre-

quency. It also appears that strip theory results are in much better agreement with experimental data, especially the coefficients A^*_{33}, A^*_{55}, B^*_{33}, B^*_{35} and B^*_{53} match the experimental results very well. This is the reason that strip theory is still the most commonly used method in engineering design, although Green function methods or Rankine panel methods appear mathematically more consistent. Two sets of data computed by strip theory are very much close, only a minor discrepancy of added-mass A^*_{33} is found in the high frequency range, $\omega^*_e > 2.5$. In Section §4.5.1, it has been shown that for sectional added-mass coefficient a^*_{33} Lewis mapping method and multi-parameter mapping method indeed give very similar predictions. Although great disparities are found among the damping coefficients b^*_{33} of sections near bow and stern, the overall symmetric hydrodynamic coefficients of the model are not affected, since they are dominated by mid body sections (*e.g.* Section 10), where damping coefficients computed by Lewis method and multi-parameter method are similar.

4.6.2 Anti-Symmetric Hydrodynamic Coefficients

Figures (4.39 - 4.43) show the anti-symmetric hydrodynamics coefficients. Same as symmetric hydrodynamics coefficients, four sets of data are presented, except that the experimental results were measured by van Leeuwen [67] for the Series 60 ($C_B = 0.70$) ship model at a Froude number of 0.2 with a rudder attached (but without a propeller). The original data were measured with respect to the body-fixed coordinate system, but can be transformed to equilibrium coordinate system by means of the transforms provided by Bailey, *et al* [1]. The transformed data are used to plot the figures here.

Again strip theory always gives smoother results than the Green function method does. Agreement between the computed sway hydrodynamic coefficients A^*_{22}, B^*_{22} and the experiment data are fairly good. Strip theory gives better

prediction of A_{22}^* in the high frequency range, $\omega_e^* > 3.5$, whereas Green function method performances better in the frequency range near resonance, $1.5 < \omega_e^* < 3.5$, where A_{22}^* is over-predicted by strip theory. In the case of B_{22}^*, strip theory has better performance over the entire frequency range. Oscillation appears in the results of Green function method in the high frequency range. Green function method also tends to under-predict B_{22}^* in the frequency range $2.5 < \omega_e^* < 5.0$, particularly at the frequency of resonance. Results computed by two strip theories are very much close, minor differences exist only at the frequencies very near resonance.

Hydrodynamic coefficients of yaw motion are illustrated in Figures (4.40) and (4.41). Added-mass coefficient A_{66}^* predicted by Green function method appears in better agreement with the experimental results that those computed by strip theory, particularly in the frequency range $1.5 < \omega_e^* < 3.5$. At the high frequencies, $\omega_e^* > 4.0$, B_{66}^* are well predicted by strip theory, while at other frequencies, both Green function method and strip theory fail to give good enough predictions.

Among the cross coupling coefficients of sway and yaw motions, B_{26}^* are accurately predicted by both strip theory and Green function method, as shown in Figure (4.41(b)). However, for the rest of the coefficients, only the same qualitative trends as the experiments are achieved by both methods. The discrepancies, however are not significant, between the results computed by two strip theories can be seen in all the cross coupling coefficients.

The hydrodynamic coefficients associated with the pure roll motion of Series 60 ($C_B = 0.70$) ship model are shown in Figure (4.43). Great disparities can be seen in both added-mass coefficient A_{44}^* and damping coefficient B_{44}^*. The values of A_{44}^* given by strip theories are much higher then those given by Green function method. Due to lack of experimental results, it is difficult to justify

which are more accurate. Results computed by two strip theories follow the same trends, though the difference is substantial. Figures (4.23 - 4.25) show that the hydrodynamic coefficients associated with roll are dominated by the sections near bow and stern (*e.g.* Section 20), where the results of sectional A_{44} computed by multi-parameter mapping are higher then those given by Lewis mapping. Therefore, it is not surprising to see that the three-dimensional added-mass A^*_{44} in Figure (4.43(a)) predicted by strip theory using multi-parameter conformal mapping are higher then that predicted by strip theory using Lewis conformal mapping method.

For the roll damping coefficient B^*_{44}, the experimental data by Vugts [68] are included[§]. Figure (4.43(b)) shows that Green function method substantially under-estimates the roll damping, which can be explained as a consequence of the potential flow assumptions. It seems that no good reason to explain why strip theory gives such higher damping values, compared with Green function method, which is worth further investigation. Meanwhile, it has to be pointed out that the accuracy of experimental data is somewhat doubtful, since contradictions are found in the two figures of B_{44} provided by Hudson[24], where the experimental data was taken from.

4.6.3 Hydrodynamic Coefficients of a Heeled Series 60 ($C_B = 0.70$) Model

Figures (4.44 - 4.47) show the hydrodynamic coefficients associated with vertical plan motions of the Series 60 ($C_B = 0.70$) ship model. The results suggest that the heel has limited influence on the total hydrodynamic coefficient values, especially for the heave pitch cross coupling coefficients. No matter what the method is used to compute sectional hydrodynamic coefficients and no matter what the

[§]This was taken from Hudson [24].

heel angle is, the results are quite close to each other, except for those A^*_{33} computed by strip theory with Lewis conformal mapping in Figure (4.35(a)), which are influenced by heel angle in the high frequency range, but the results follow exact same trend.

Same conclusion can be drawn from the results of the hydrodynamic coefficients associated with lateral plane motions, as shown in the Figures (4.48 - 4.51). A^*_{22} and A^*_{62} are more likely influenced by heel angle. The magnitude of A^*_{62} computed by multi-parameter mapping are larger then that computed by Lewis mapping method, however they follow that same trend when the heel angle increases. In the case of A^*_{22}, disparities are shown at the high frequencies. For other coefficients, minor influences only appear near the frequency range of resonance.

Figures (4.52 - 4.55) show that heel angle has strong influence on the hydrodynamic coefficients associated with roll motion, which is expected since in Section §4.5.2, it has been shown that the sectional hydrodynamic coefficients associated roll motion are strongly influenced by heel angle. Compared with A^*_{22}, A^*_{26}, and B^*_{22}, B^*_{26} respectively, A^*_{24} and B^*_{24} clearly are of small order, even at larger heel angles, and the same is true for A^*_{64} and B^*_{64}, which indicates that heel angle may not have strong influence on ship motion of sway and yaw mode. However, Figures (4.52), (4.53) and (4.54) show that the hydrodynamic coefficients contributing to ship roll motion computed by multi-parameter mapping method are of same order, particularly at large heel angles, and they are very strongly affected by the heel angle in the low frequency range. Therefore the roll motions predicted by traditional strip theory and by time-domain strip theory may be of significant difference. All the curves in Figures (4.52 - 4.55) are very smooth and curves of each coefficient for the different heel angles follow the same trends. This indicates that the results produced by the program are reliable.

Figures (4.56-4.64) present those hydrodynamic coefficients which are zero

when ship is in up right position. Obviously, only the strip theory with multi-parameter are able to be predict them when the model is heeled. The magnitudes of the coefficients increase with the heel angle and curves are smooth. Once again it indicates the program is trustworthy.

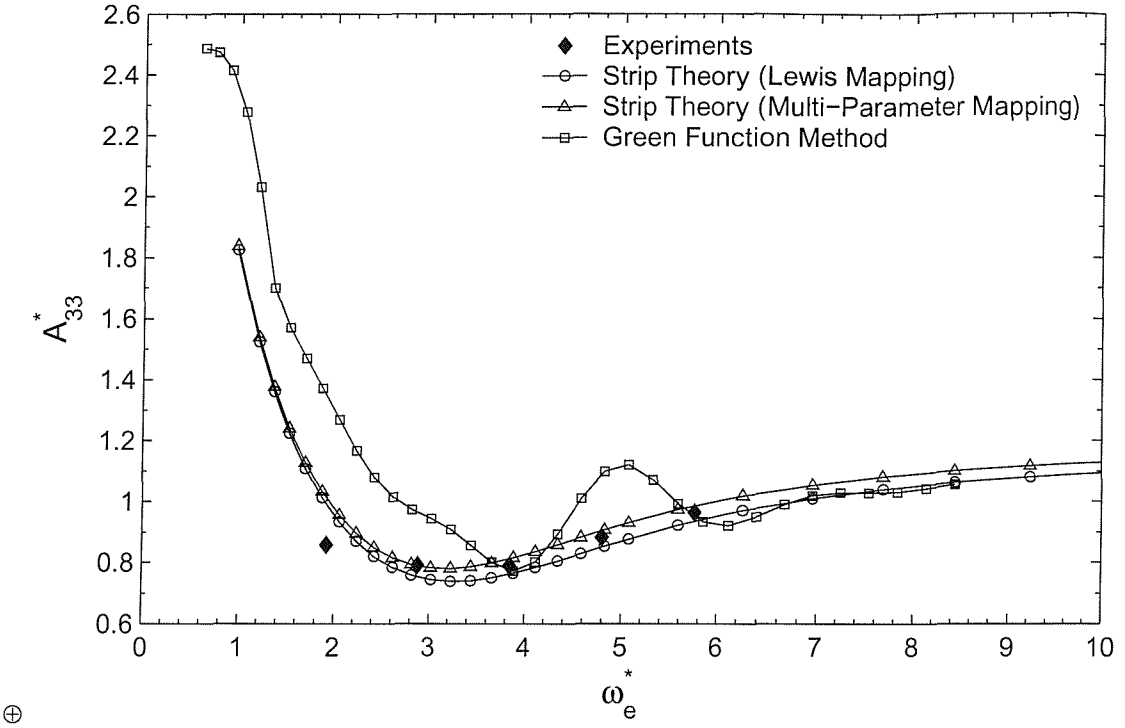

(a) Added-Mass A_{33}

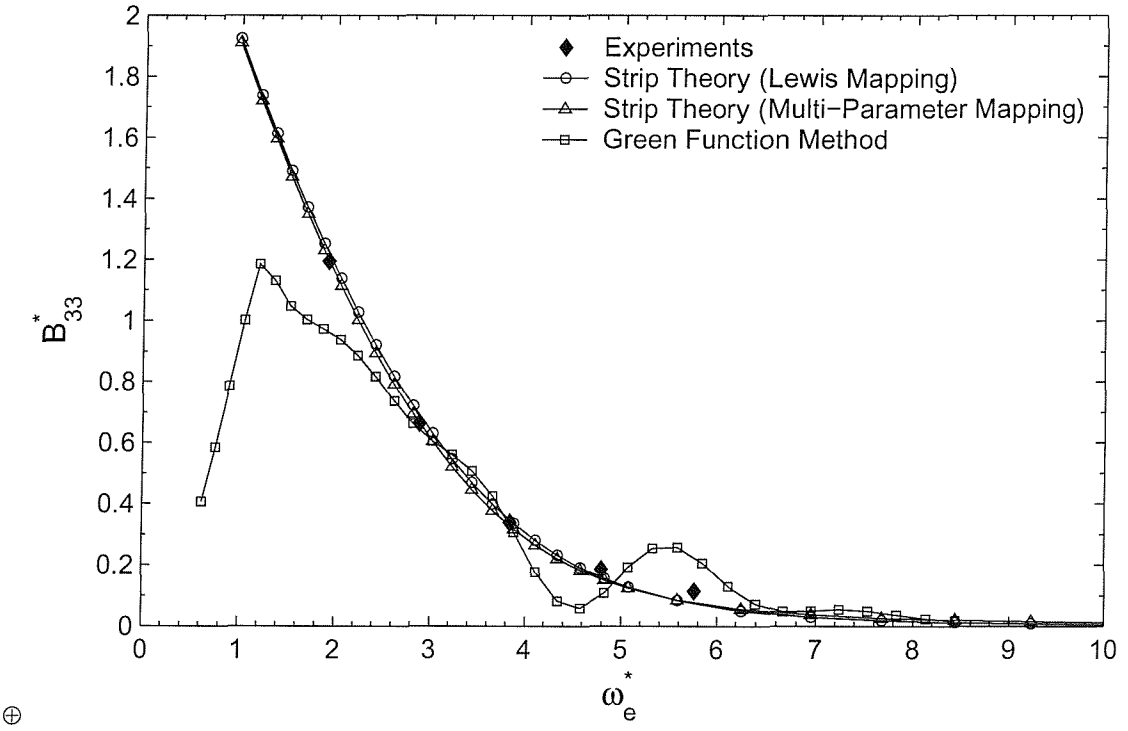

(b) Damping Coefficient B_{33}

Figure 4.35: *Comparison of the Predicted and Measured Heave Hydrodynamic Coefficients of Series 60 Ship Model.*

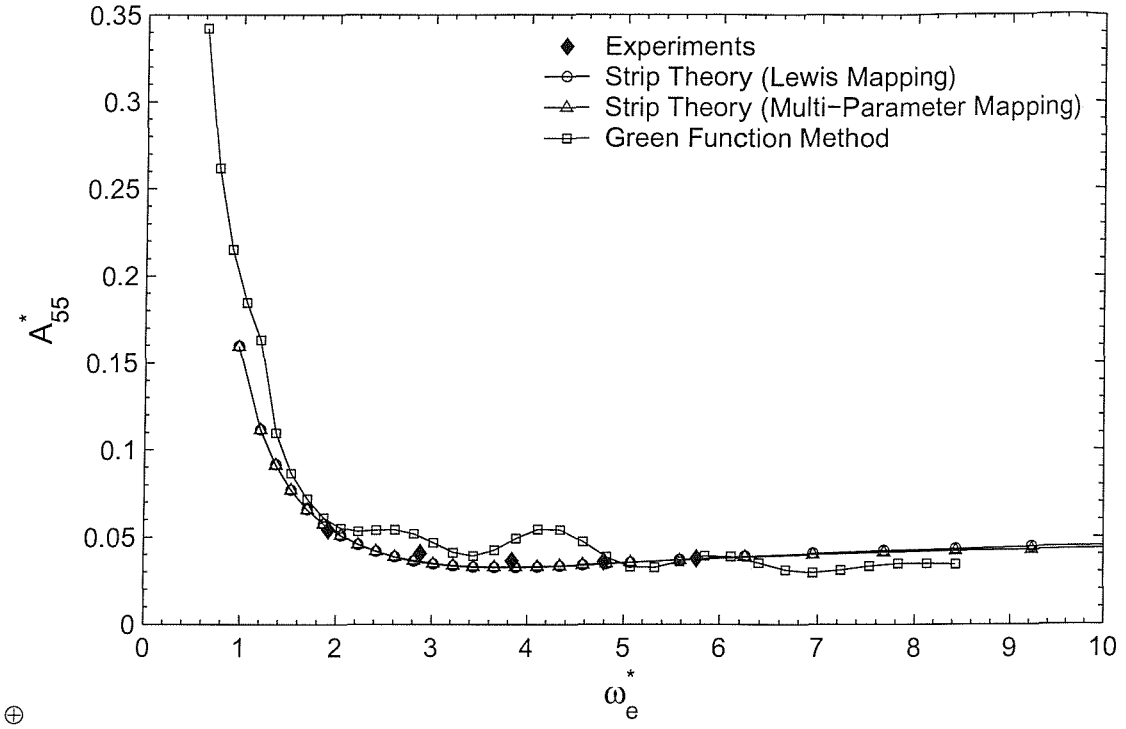

(a) Added-Moment of Inertia A_{55}

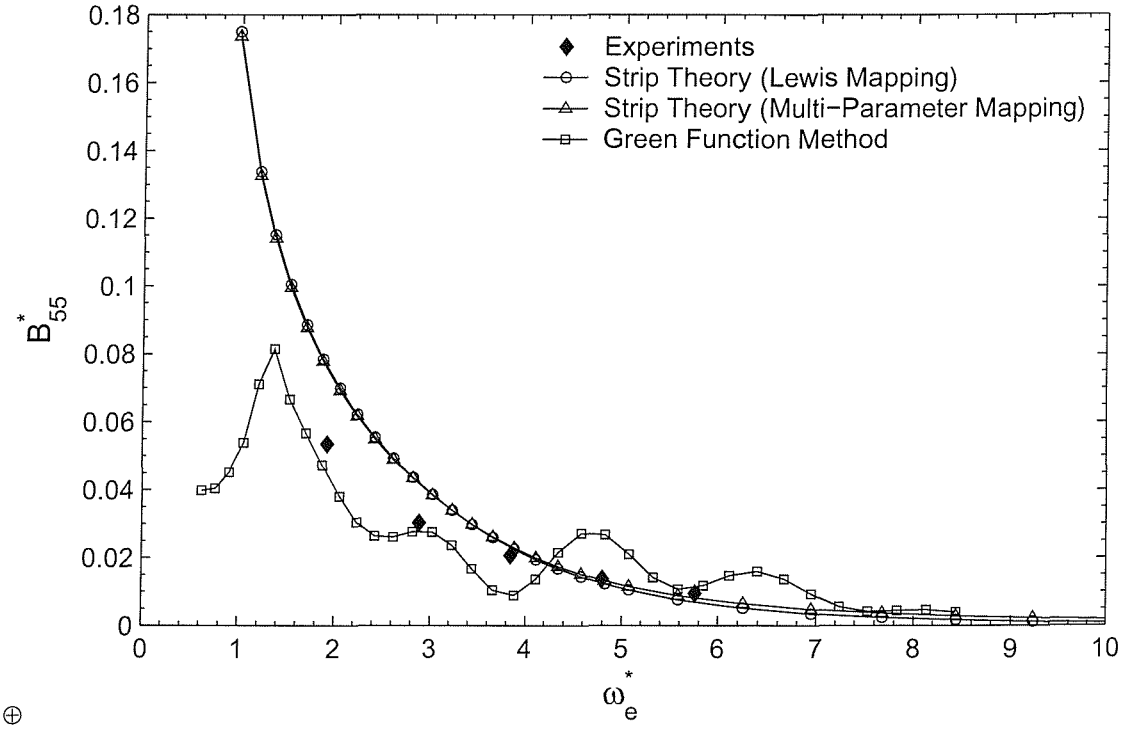

(b) Damping Coefficient B_{55}

Figure 4.36: *Comparison of the Predicted and Measured Pitch Hydrodynamic Coefficients of Series 60 Ship Model.*

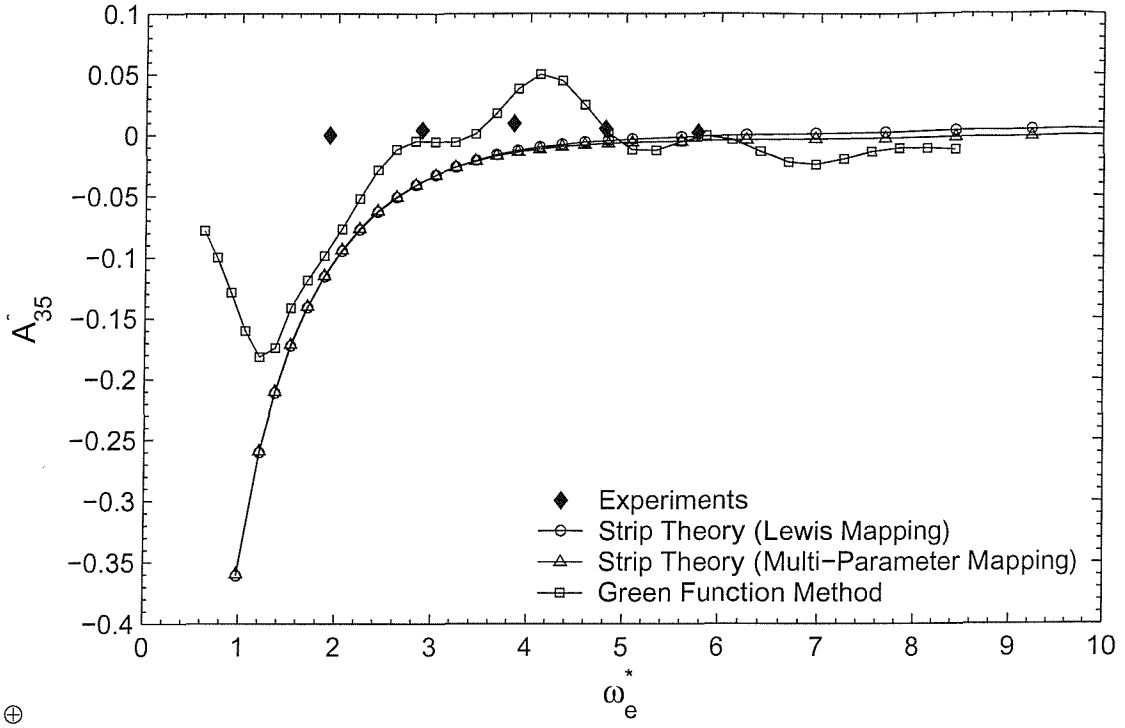

(a) Added-Mass A_{35}

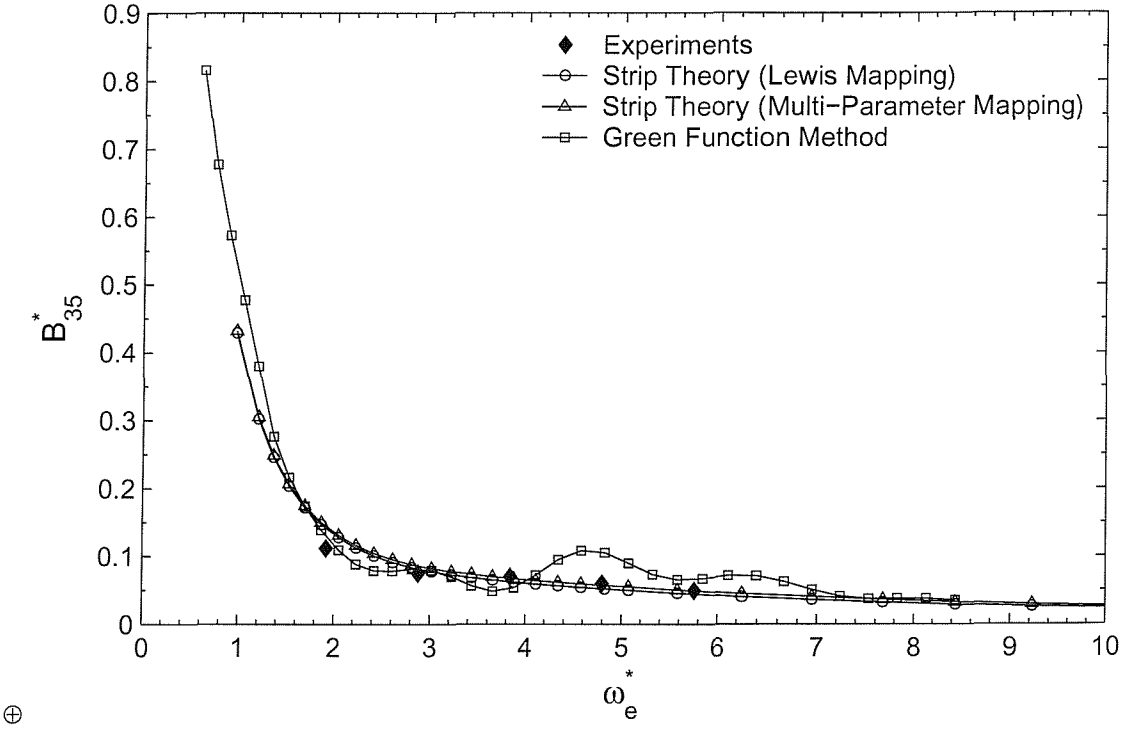

(b) Damping Coefficient B_{35}

Figure 4.37: *Comparison of the Predicted and Measured Heave-Pitch Coupling Hydrodynamic Coefficients of Series 60 Ship Model.*

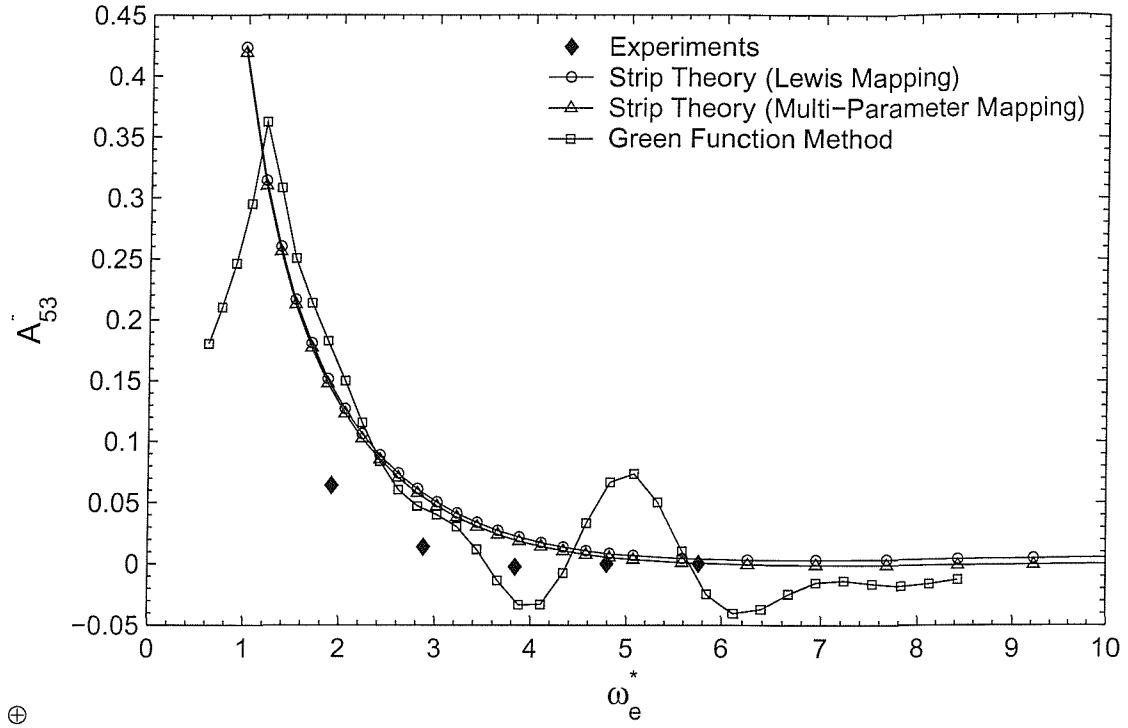

(a) Added-Moment of Inertia A_{53}

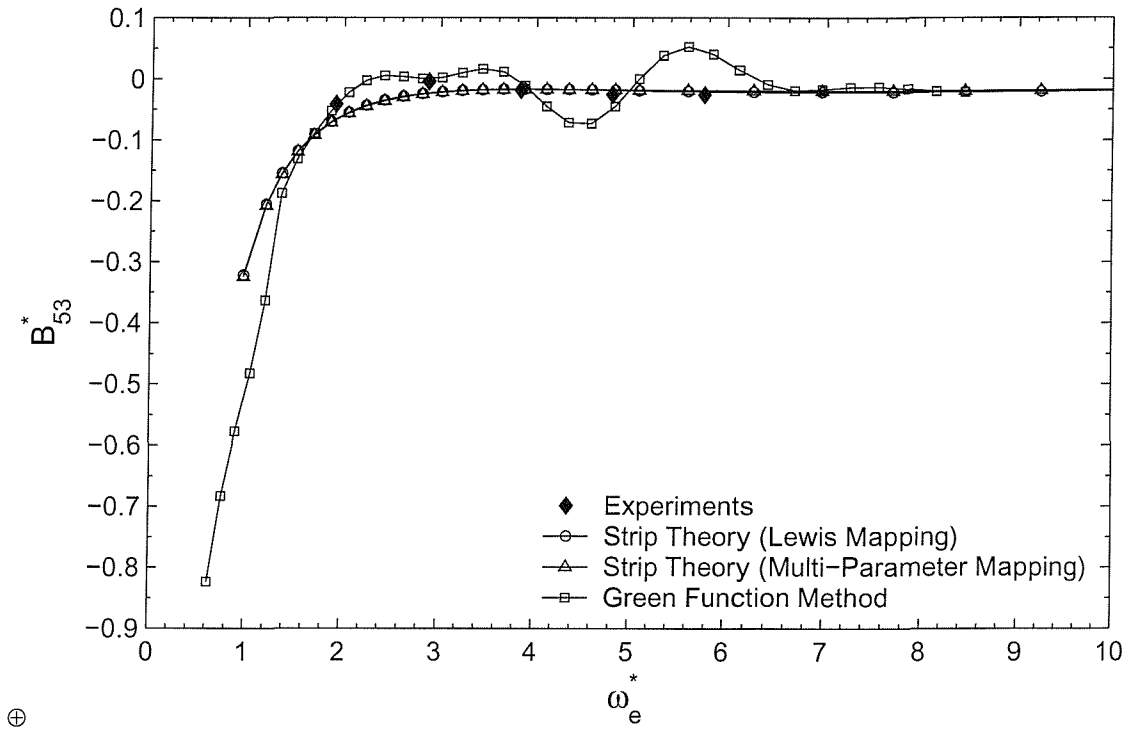

(b) Damping Coefficient B_{53}

Figure 4.38: *Comparison of the Predicted and Measured Pitch-Heave Coupling Hydrodynamic Coefficients of Series 60 Ship Model.*

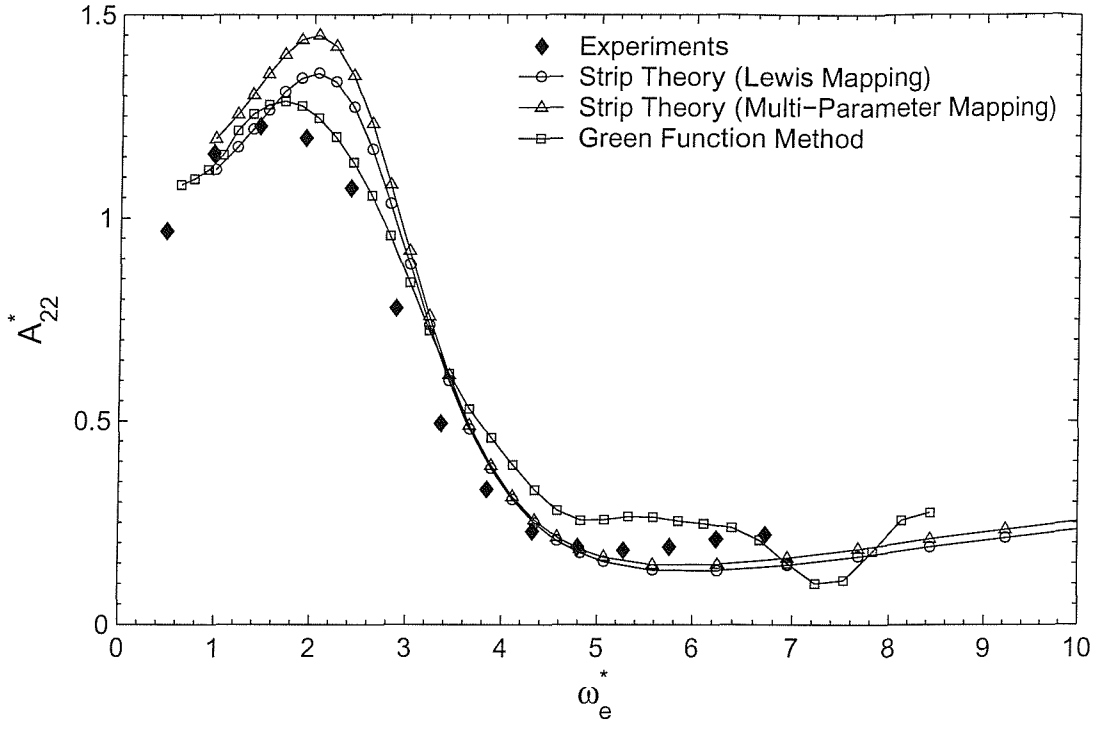

(a) Added-Mass A_{22}

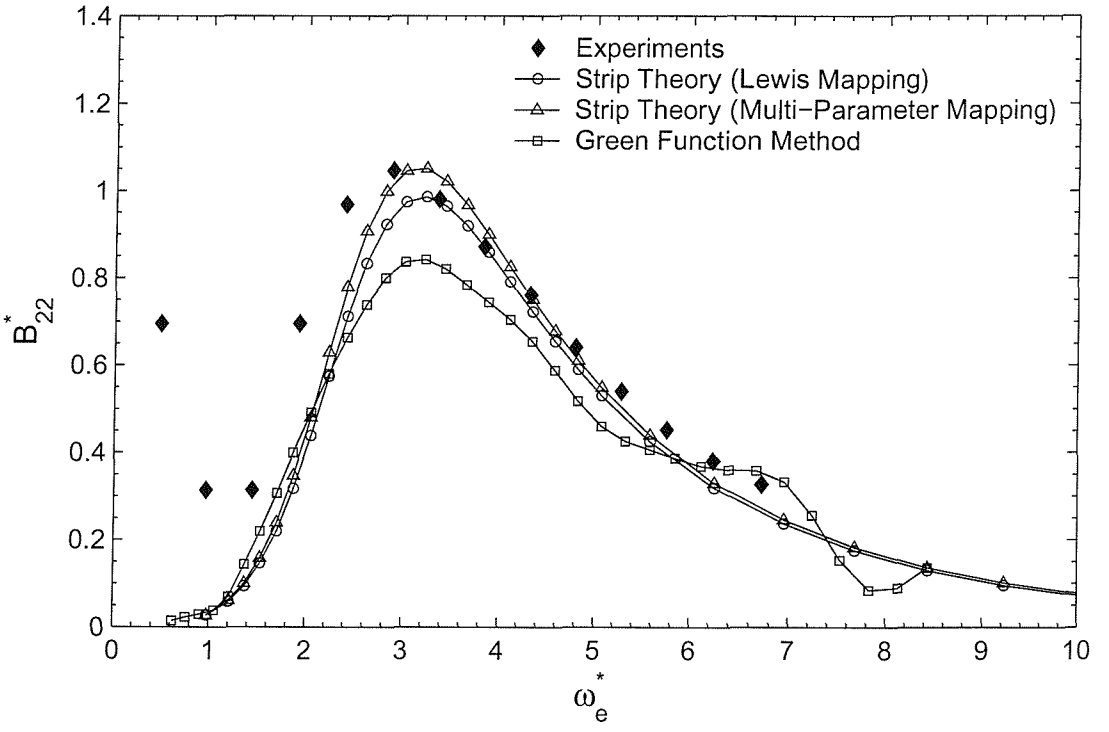

(b) Damping Coefficient B_{22}

Figure 4.39: *Comparison of the Predicted and Measured Sway Hydrodynamic Coefficients of Series 60 Ship Ship Model.*

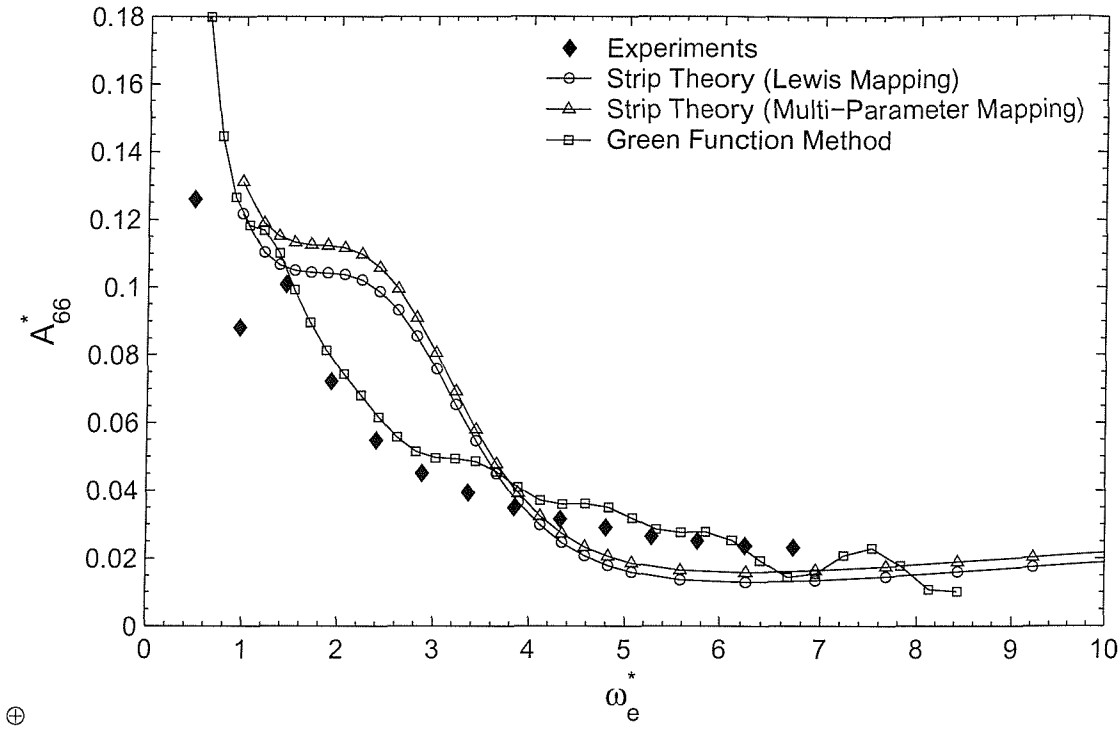

(a) Added-Moment of Inertia A_{66}

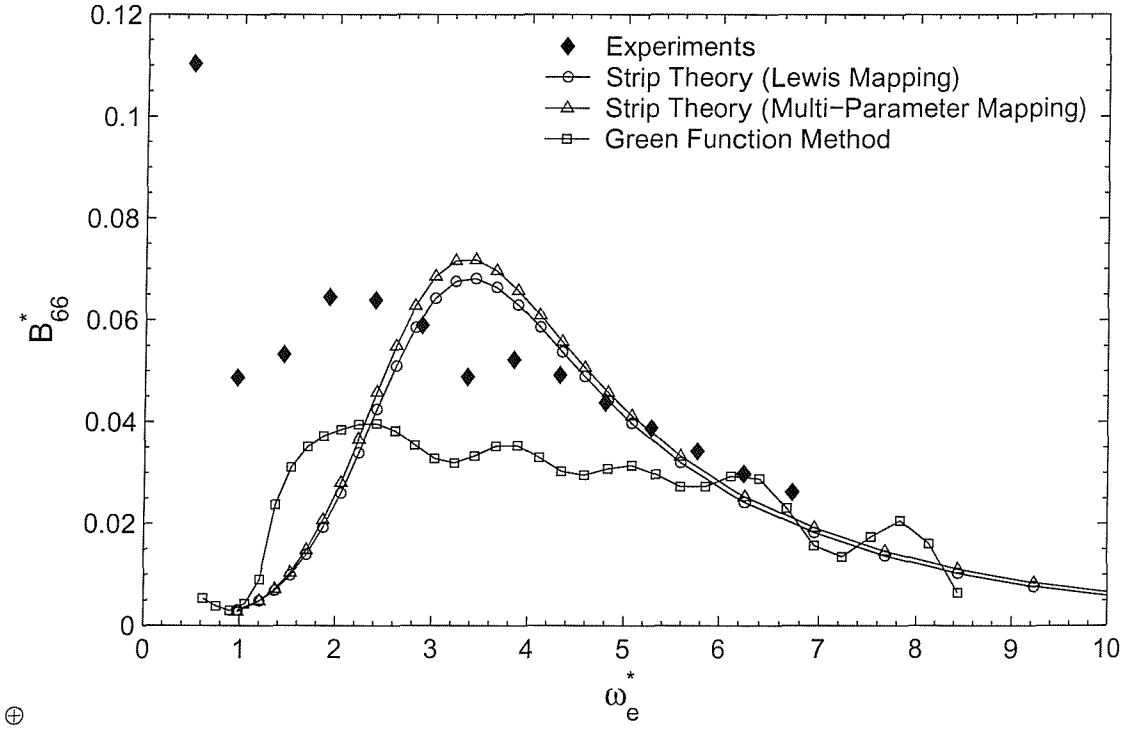

(b) Damping Coefficient B_{66}

Figure 4.40: *Comparison of the Predicted and Measured Yaw Hydrodynamic Coefficients of Series 60 Ship Model.*

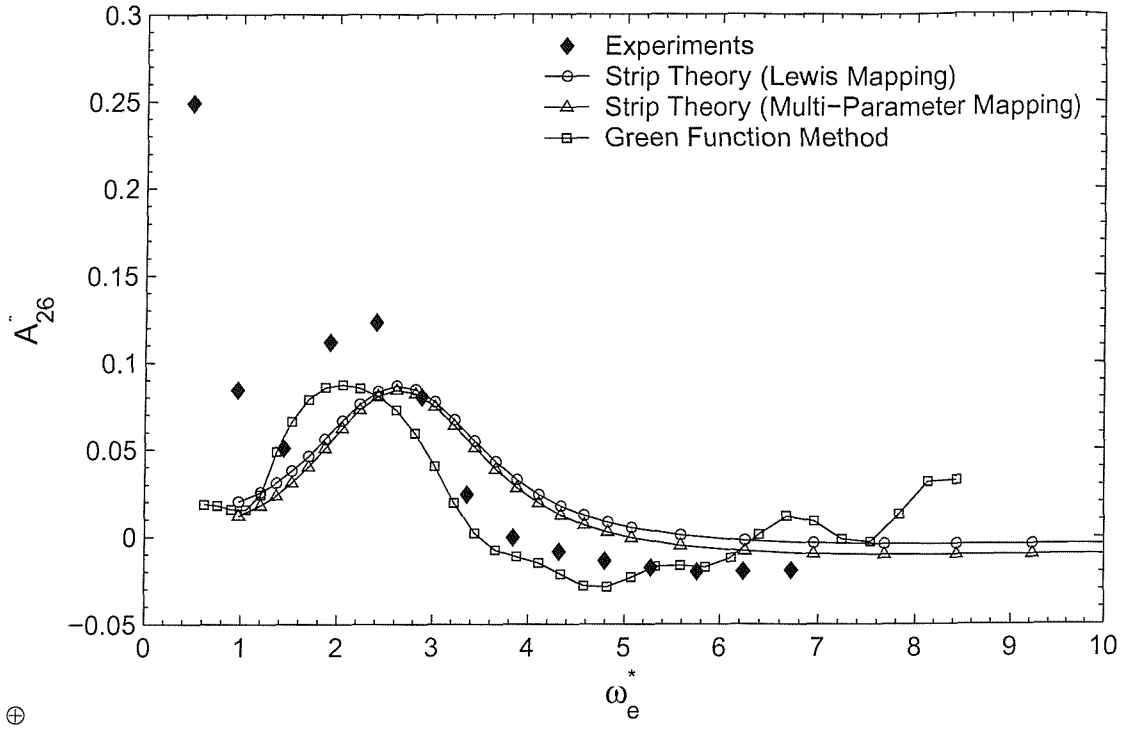

(a) Added-Mass A_{26}

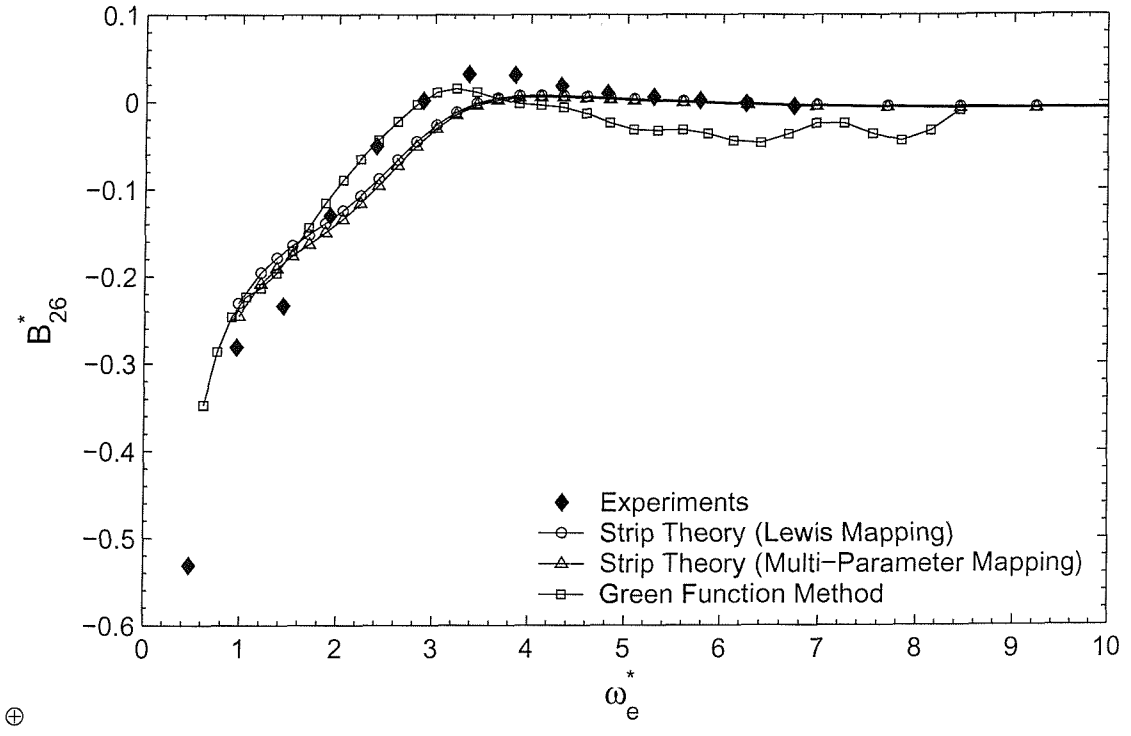

(b) Damping Coefficient B_{26}

Figure 4.41: *Comparison of the Predicted and Measured Sway-Yaw Coupling Hydrodynamic Coefficients of Series 60 Ship Model.*

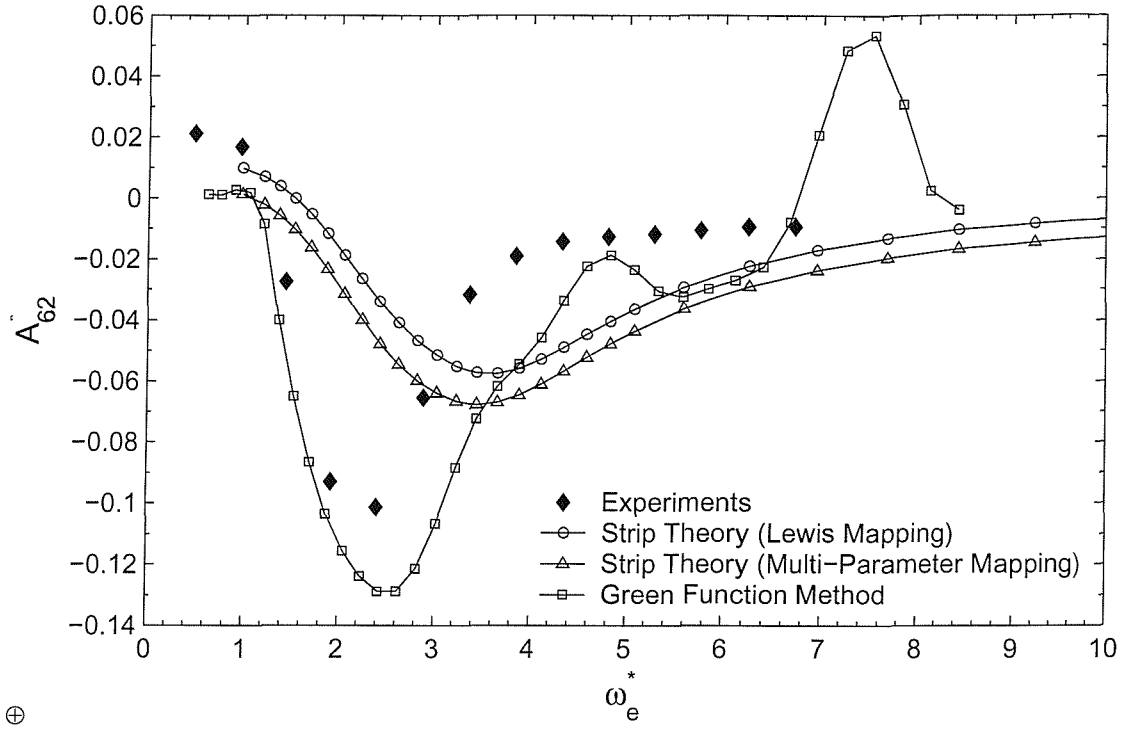

(a) Added-Moment of Inertia A_{62}

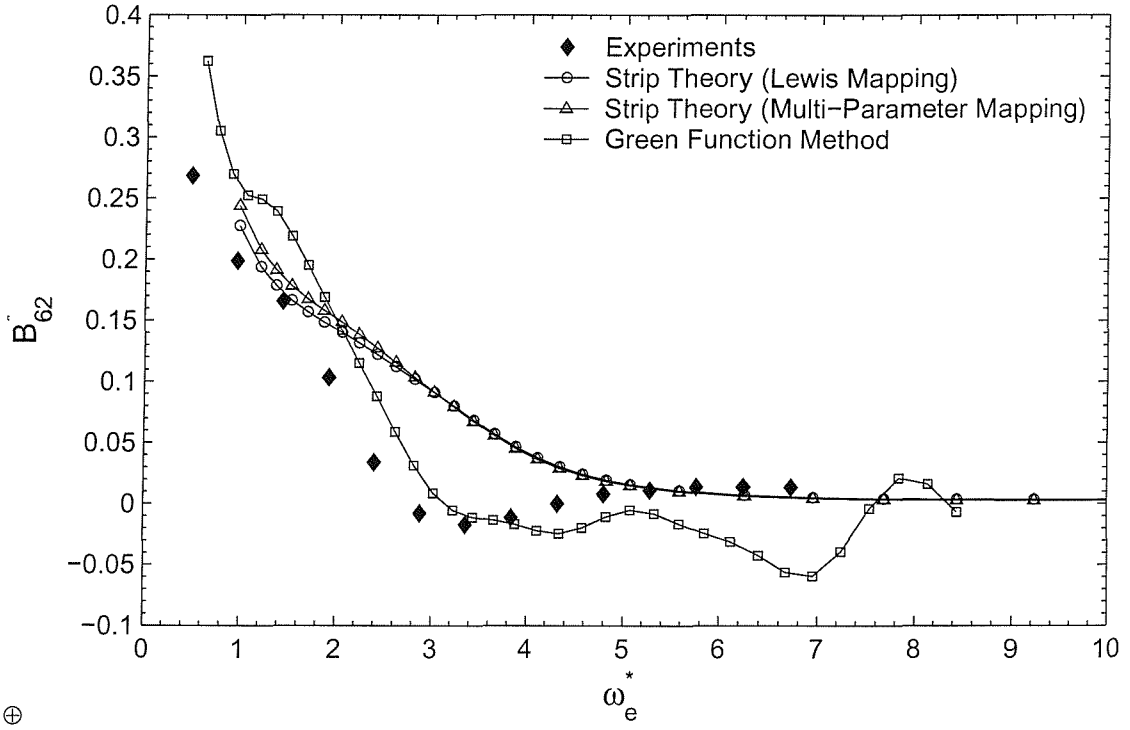

(b) Damping Coefficient B_{62}

Figure 4.42: *Comparison of the Predicted and Measured Yaw-Sway Coupling Hydrodynamic Coefficients of Series 60 Ship Model.*

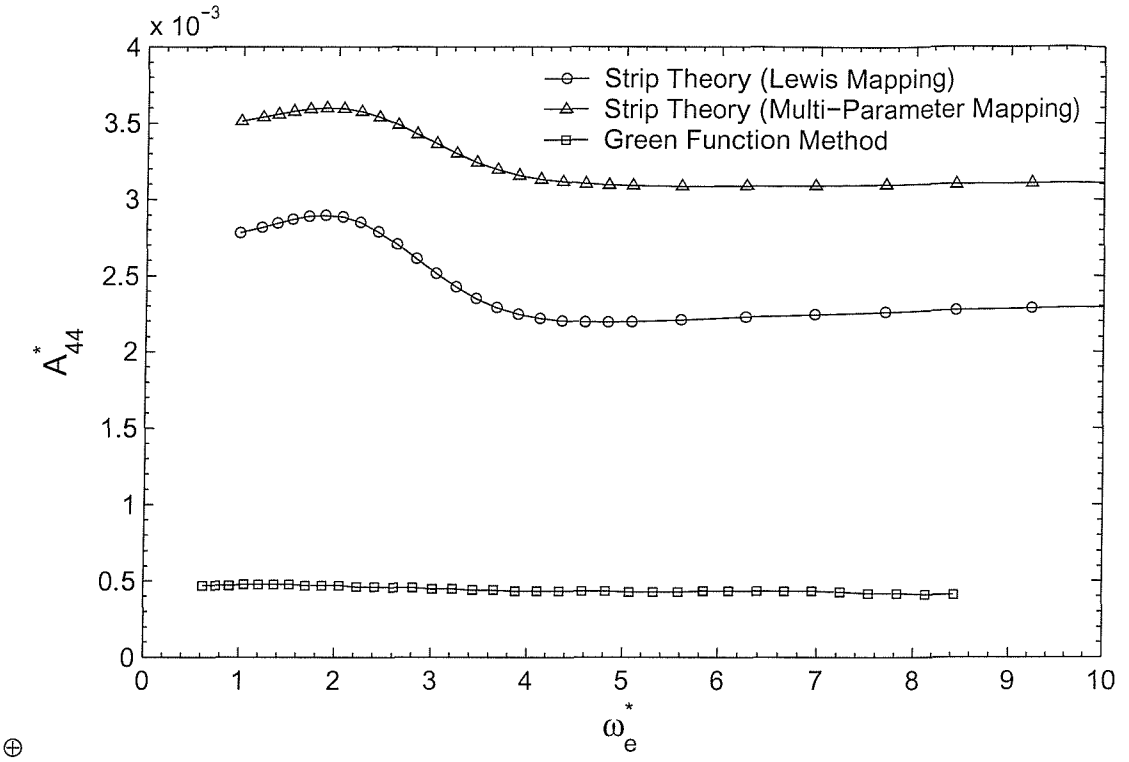

(a) Added-Moment of Inertia A_{44}

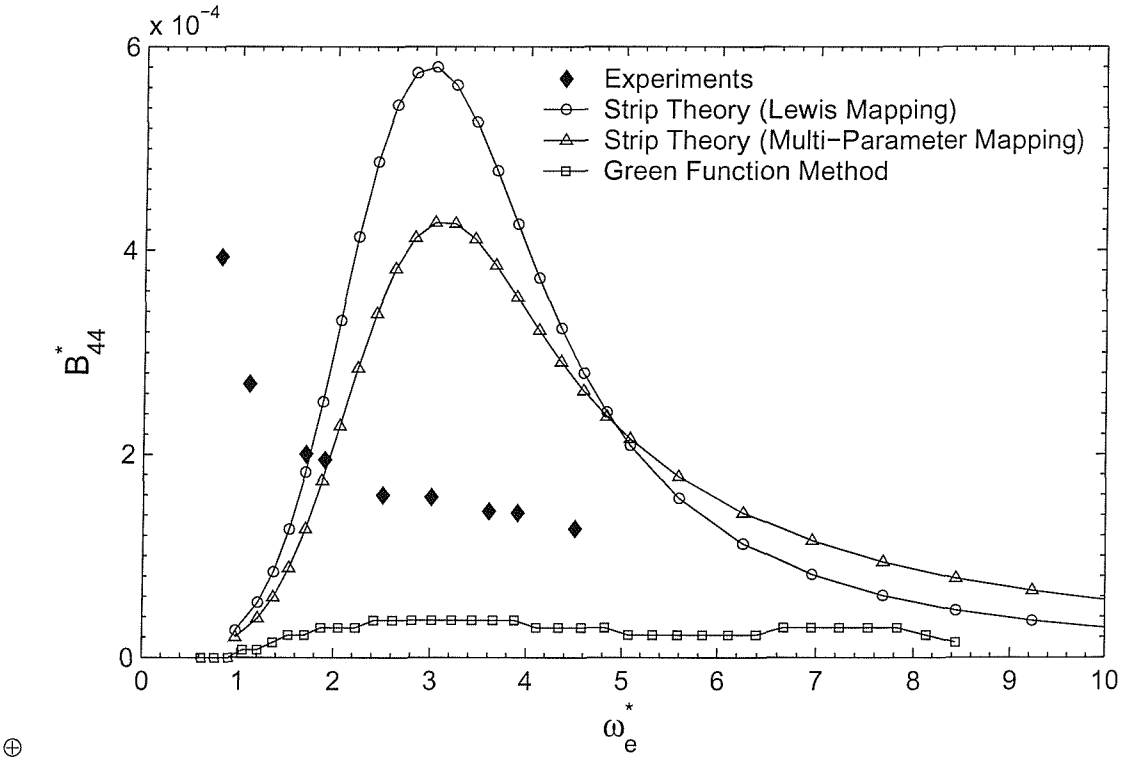

(b) Damping Coefficient B_{44}

Figure 4.43: *Comparison of the Predicted and Measured Roll Hydrodynamic Coefficients of Series 60 Ship Model.*

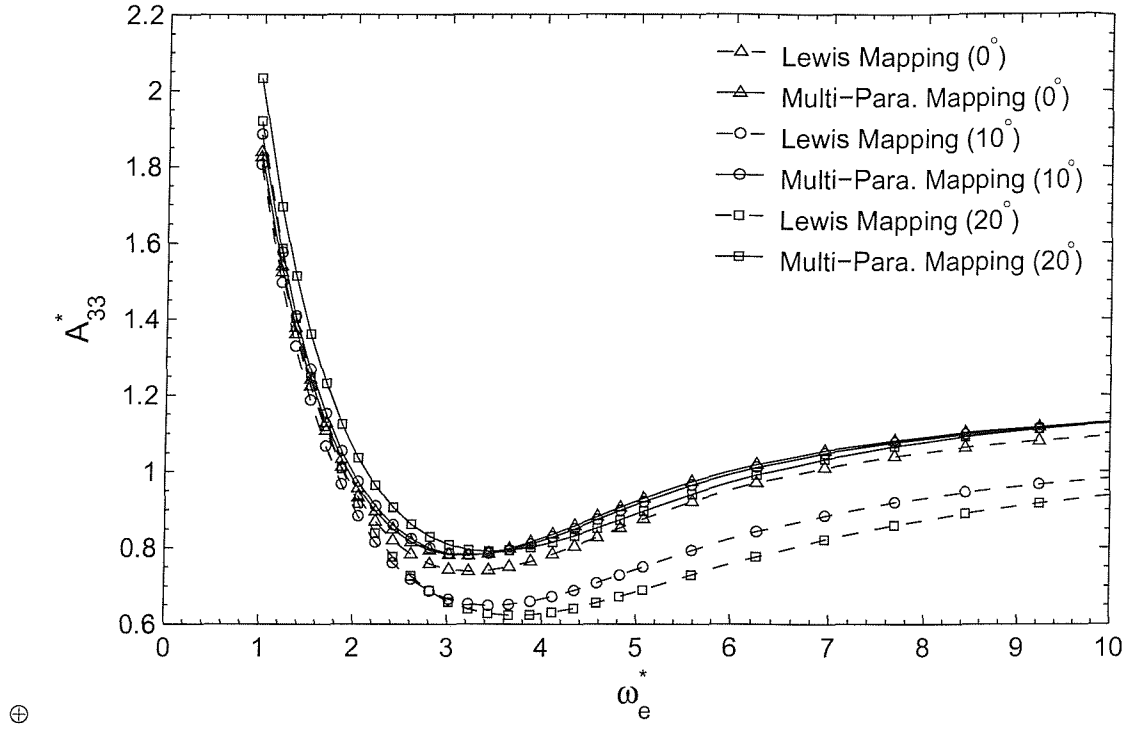

(a) Added-Mass A_{33}

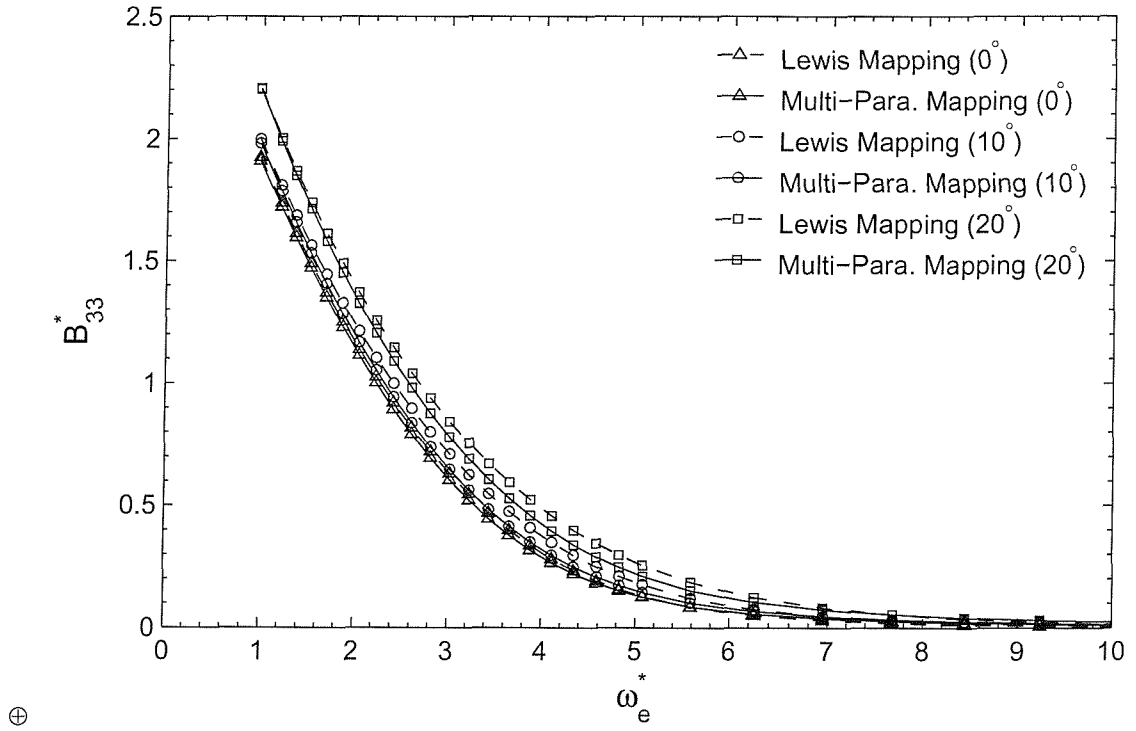

(b) Damping Coefficient B_{33}

Figure 4.44: *Comparison of Heave Coefficients of Series 60 Ship Model at Heel Angles* $0°$, $10°$ *and* $20°$.

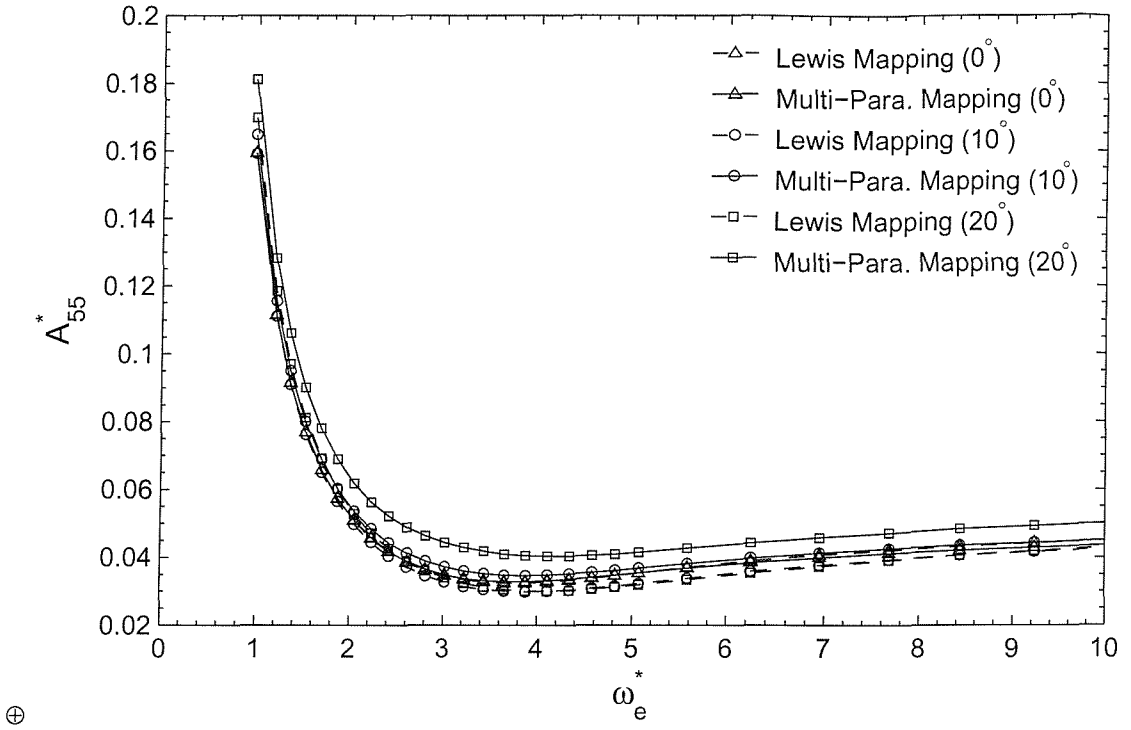

(a) Added-Moment of Inertia A_{55}

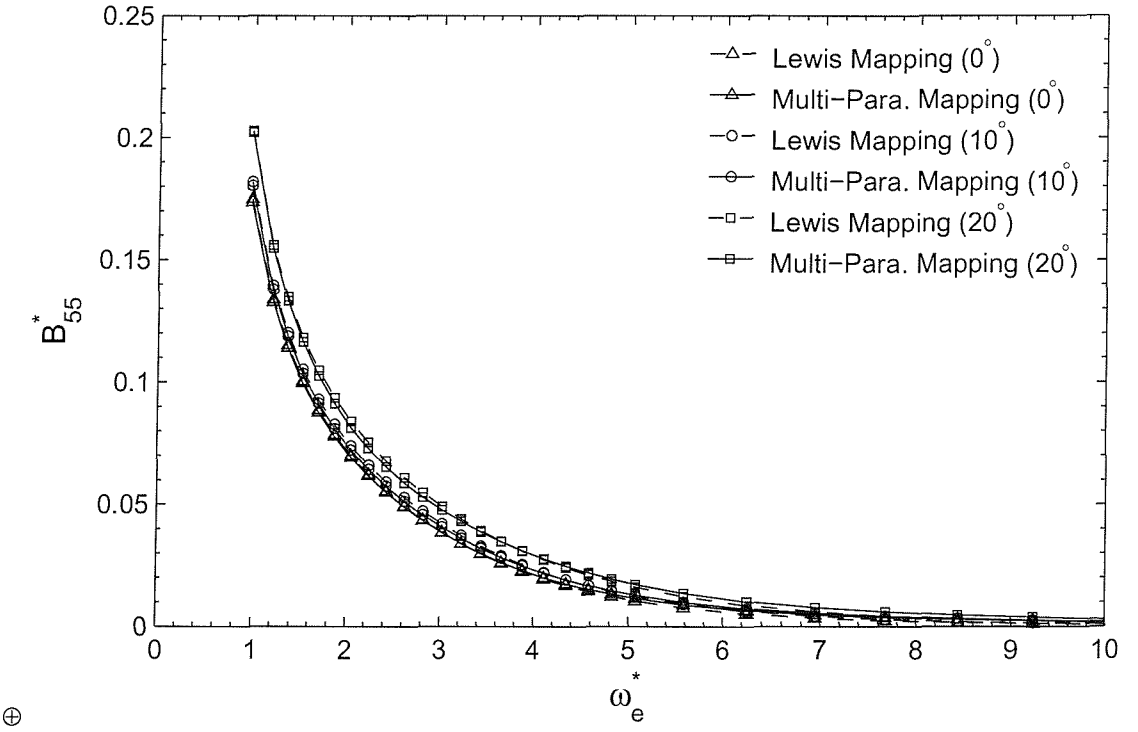

(b) Damping Coefficient B_{55}

Figure 4.45: *Comparison of Pitch Coefficients of Series 60 Ship Model at Heel Angles* 0°, 10° *and* 20°.

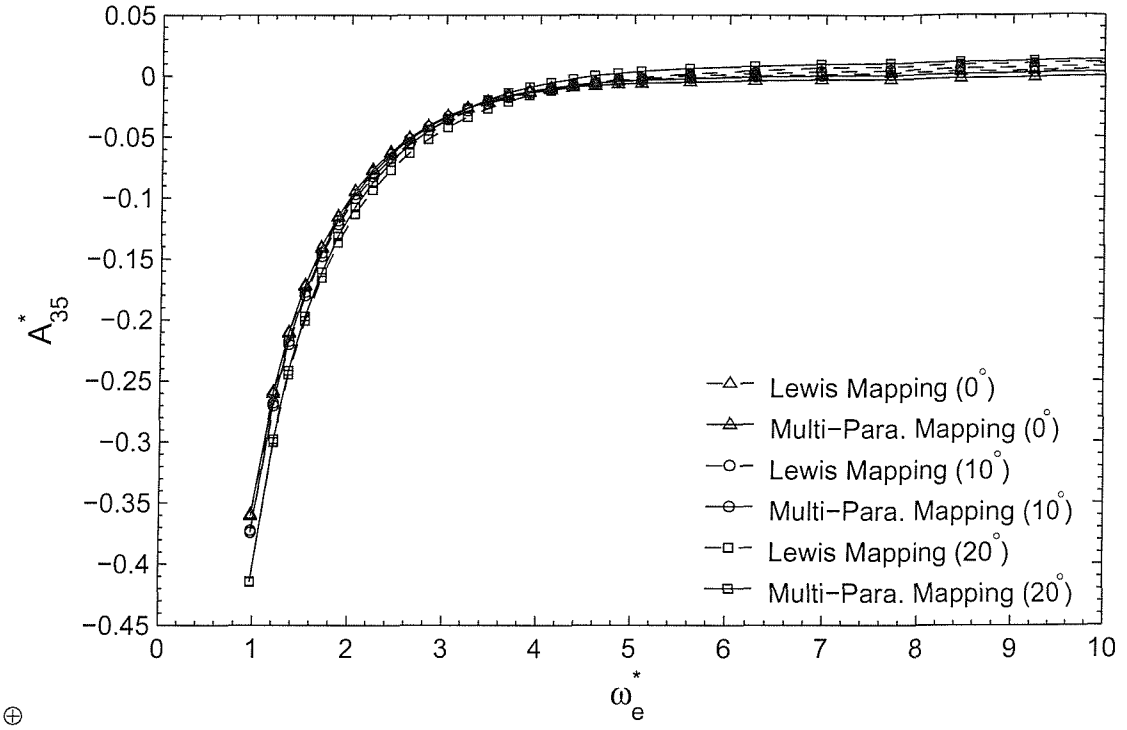

(a) Added-Mass A_{35}

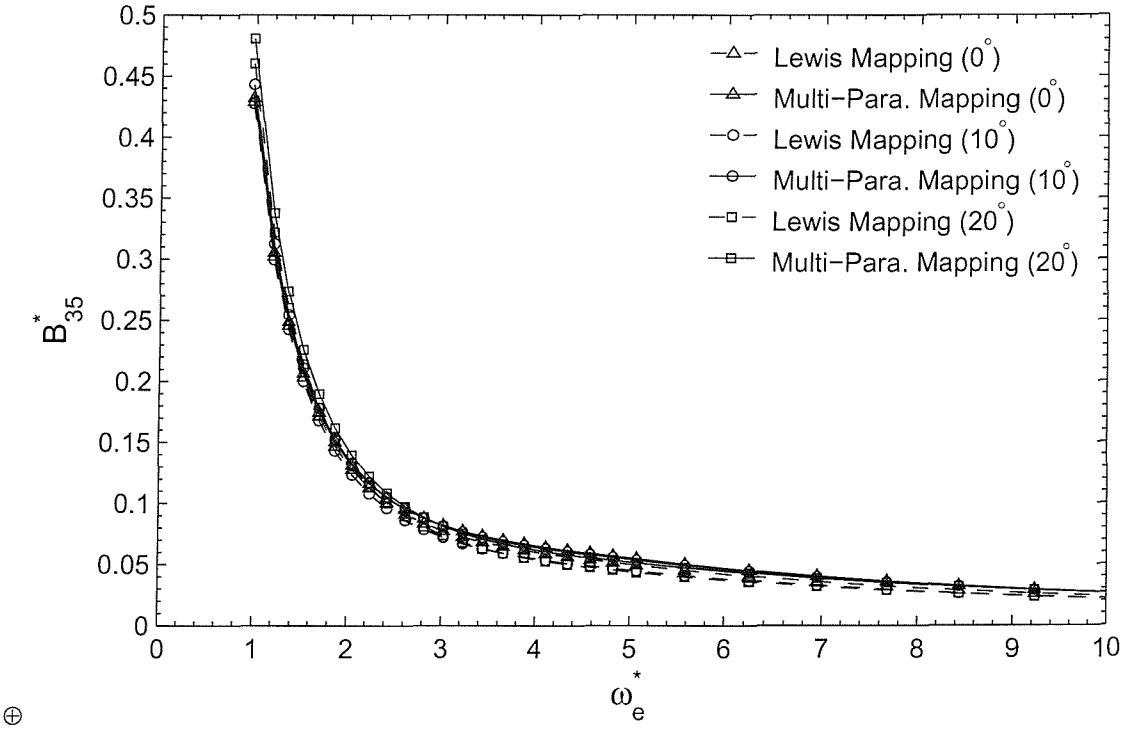

(b) Damping Coefficient B_{35}

Figure 4.46: *Comparison of Pitch-Heave Coupling Coefficients of Series 60 Ship Model at Heel Angles* 0°, 10° *and* 20°.

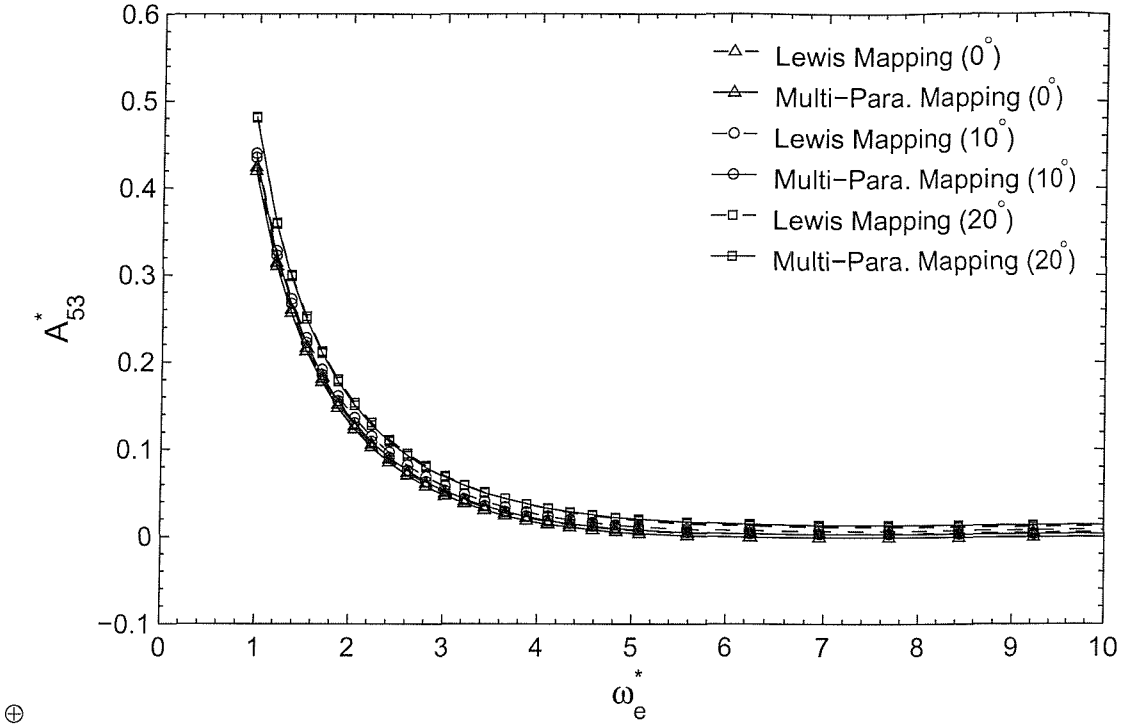

(a) Added-Moment of Inertia A_{53}

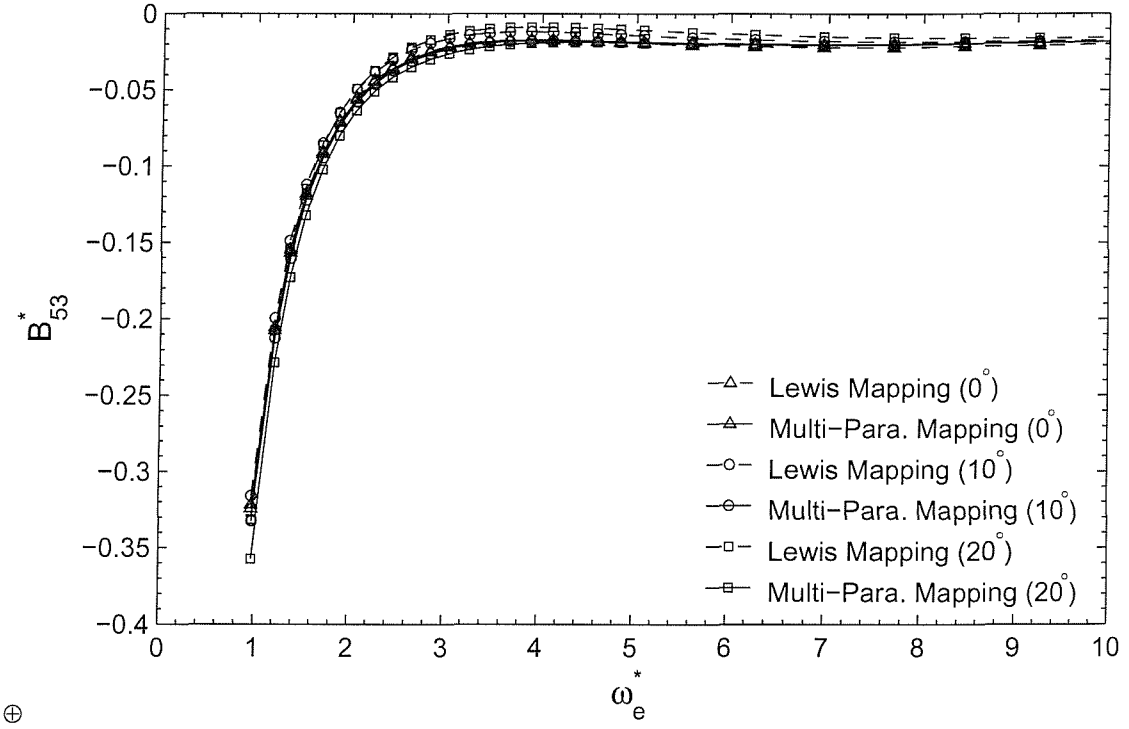

(b) Damping Coefficient B_{53}

Figure 4.47: *Comparison of Heave-Pitch Coupling Coefficients of Series 60 Ship Model at Heel Angles* 0°, 10° *and* 20°.

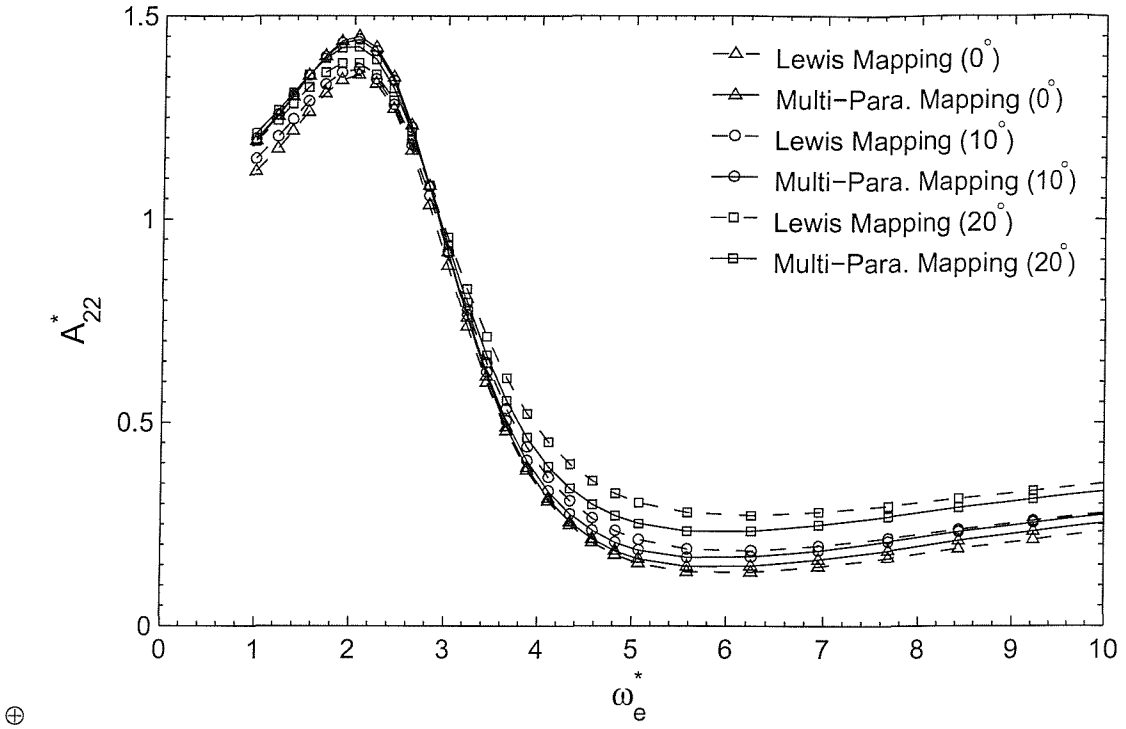

(a) Added-Mass A_{22}

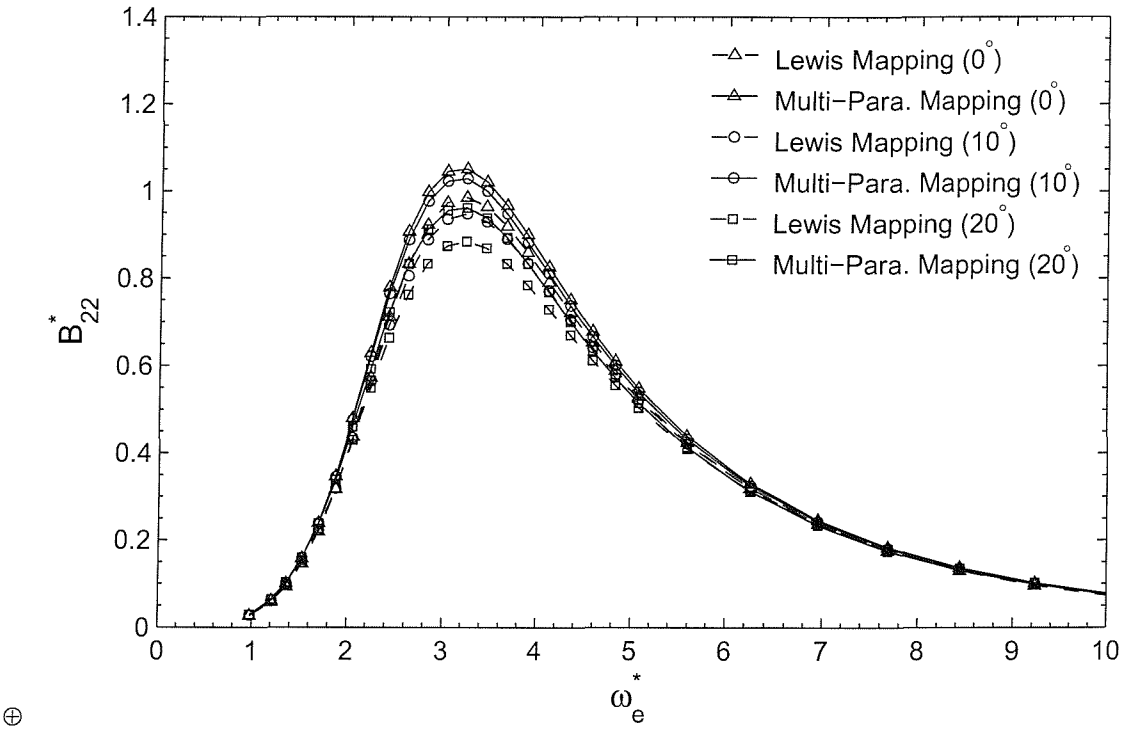

(b) Damping Coefficient B_{22}

Figure 4.48: *Comparison of Sway Coefficients of Series 60 Ship Model at Heel Angles* 0°, 10° *and* 20°.

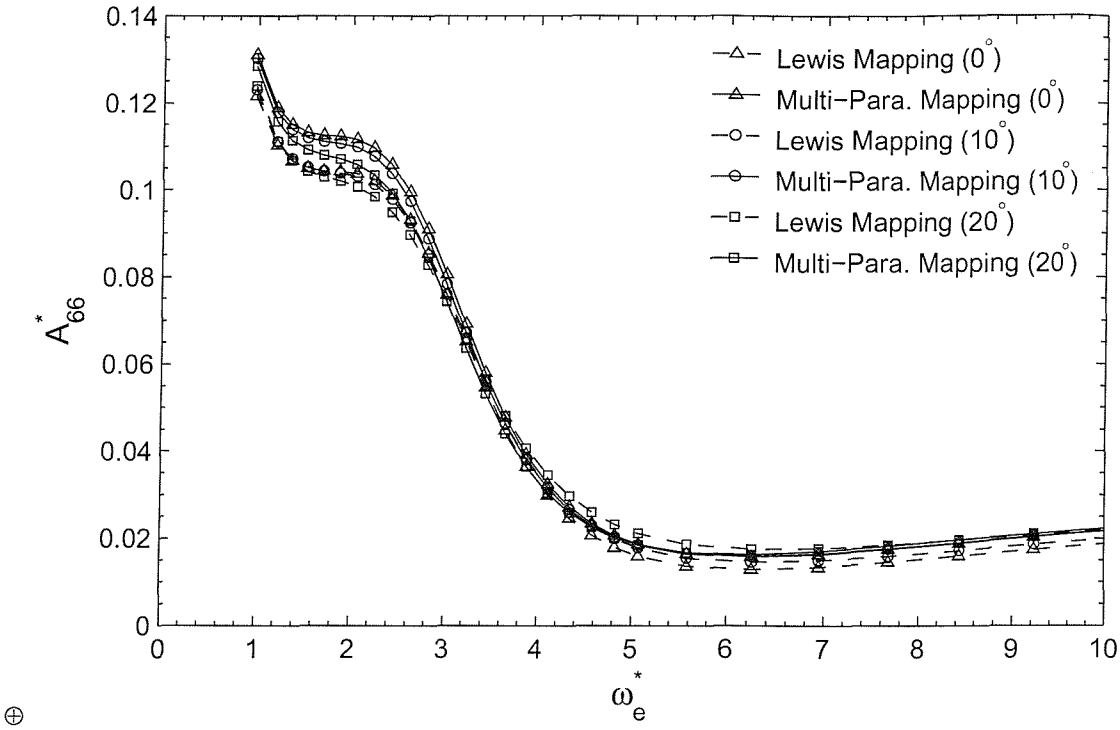

(a) Added-Moment of Inertia A_{66}

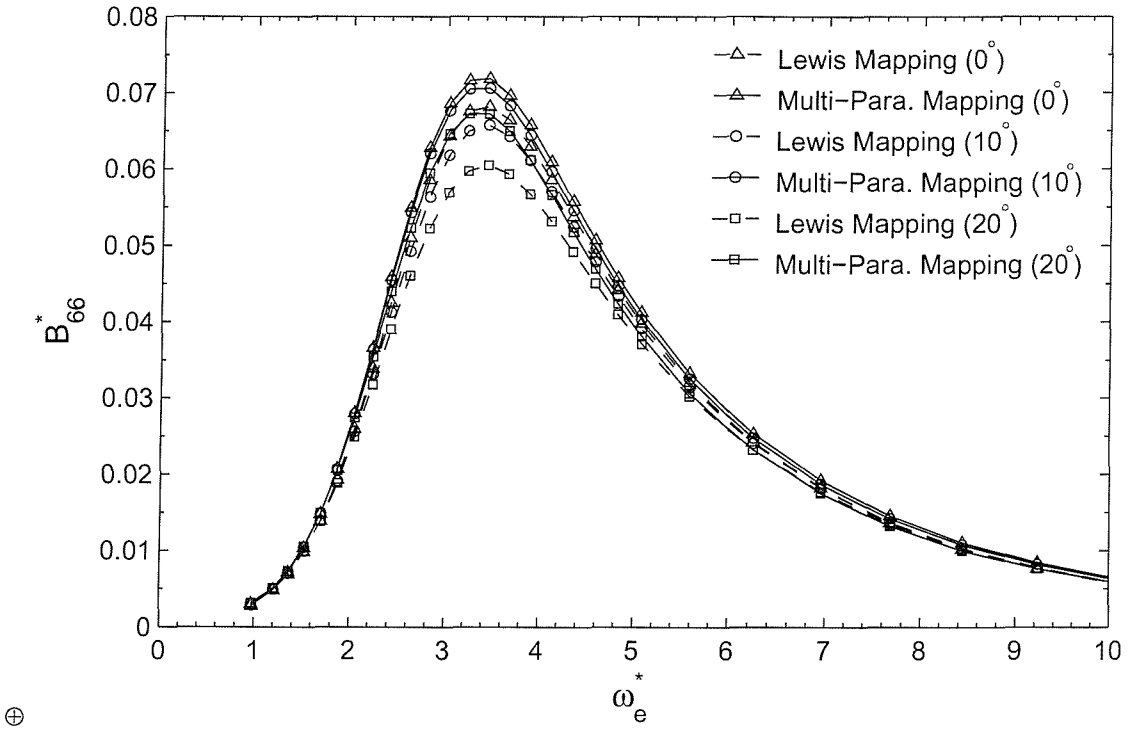

(b) Damping Coefficient B_{66}

Figure 4.49: *Comparison of Yaw Coefficients of Series 60 Ship Model at Heel Angles* 0°, 10° *and* 20°.

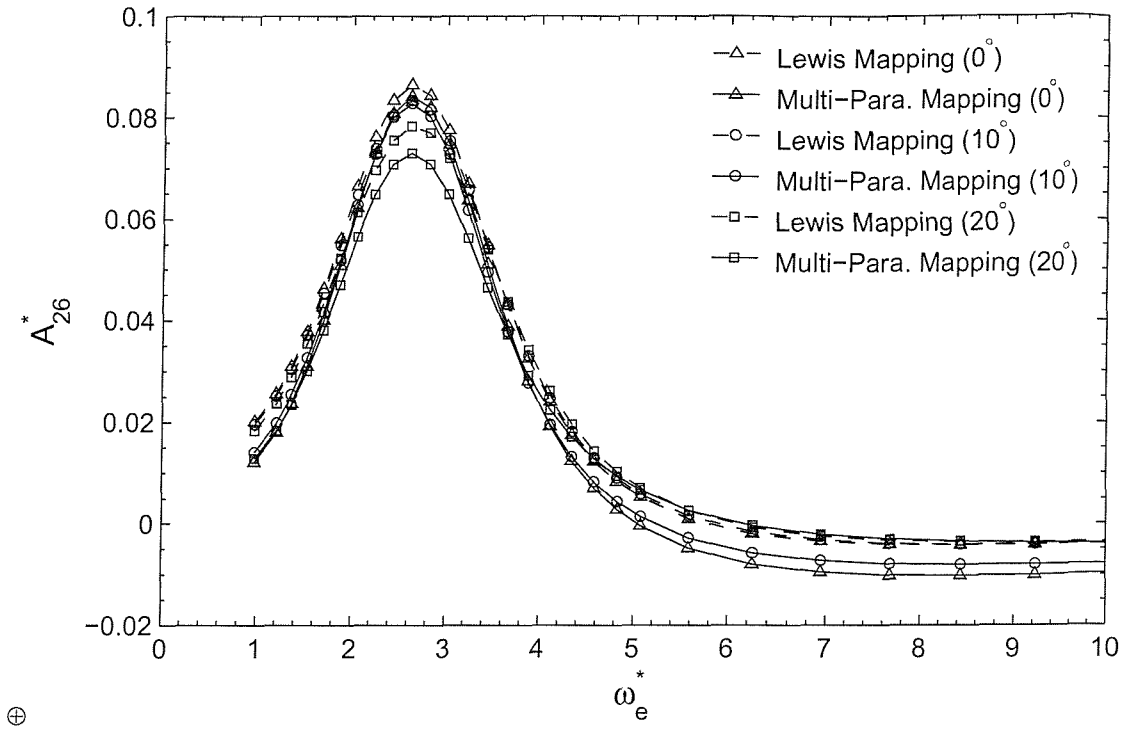

(a) Added-Mass A_{26}

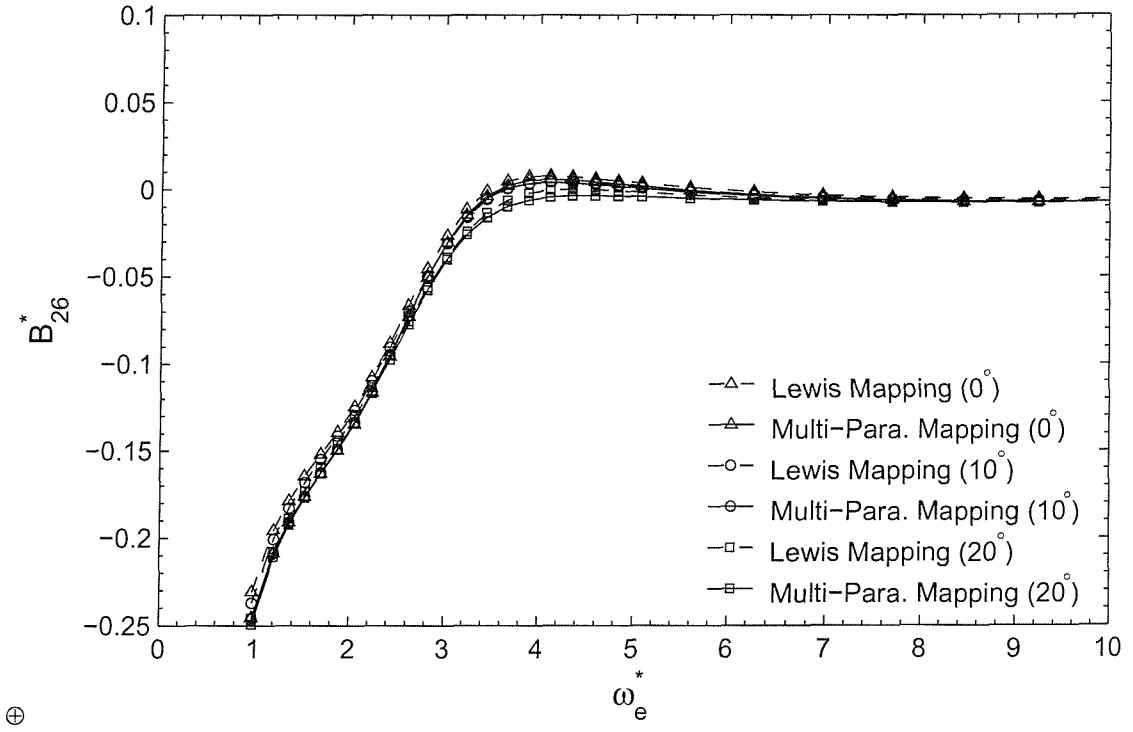

(b) Damping Coefficient B_{26}

Figure 4.50: *Comparison of Sway-Yaw Coupling Coefficients of Series 60 Ship Model at Heel Angles* $0°$, $10°$ *and* $20°$.

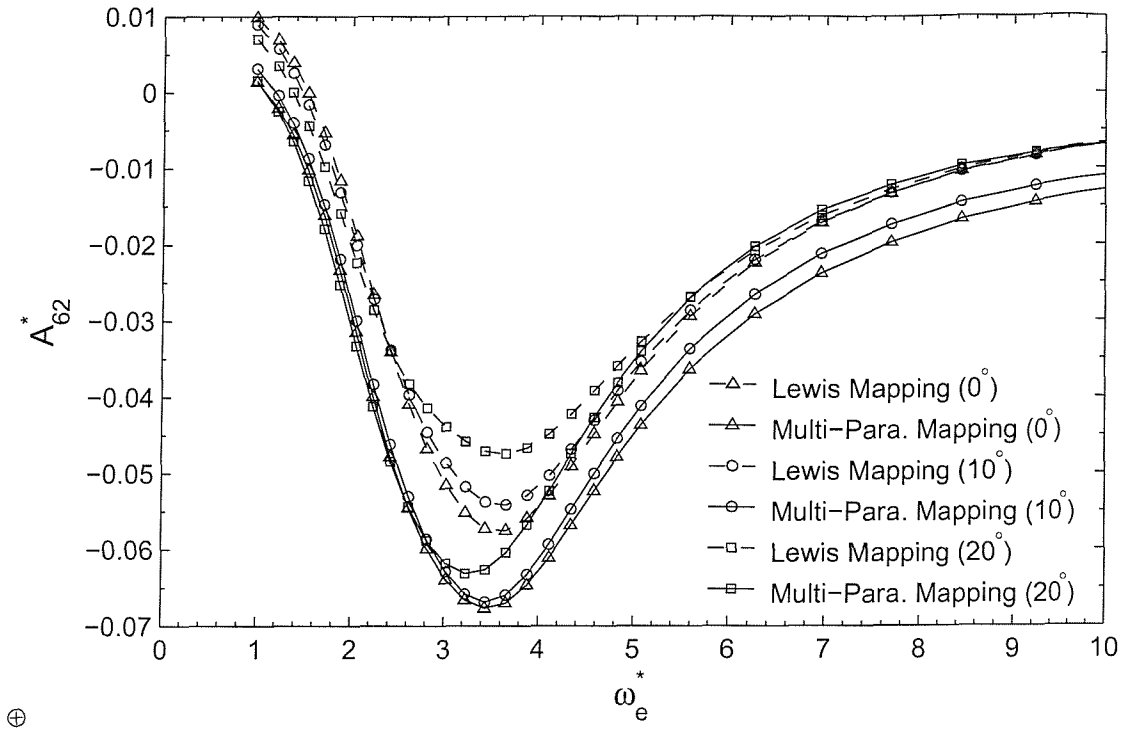

(a) Added-Moment of Inertia A_{62}

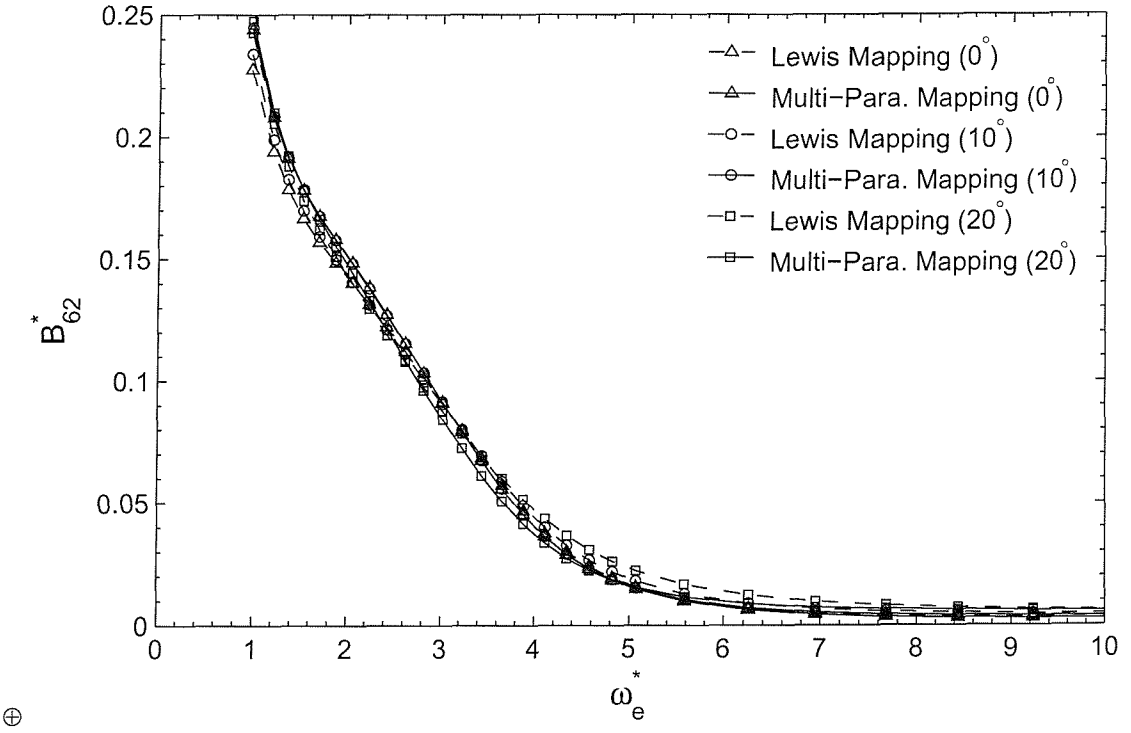

(b) Damping Coefficient B_{62}

Figure 4.51: *Comparison of Yaw-Sway Coupling Coefficients of Series 60 Ship Model at Heel Angles* $0°$, $10°$ *and* $20°$.

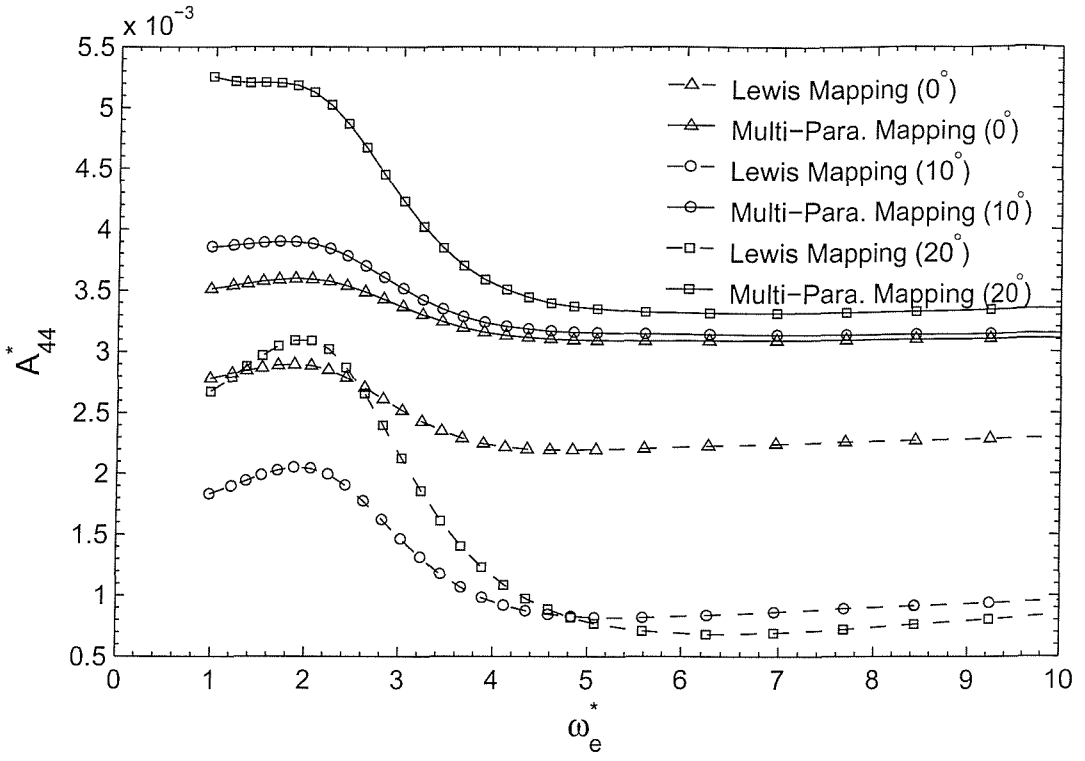

(a) Added-Moment of Inertia A_{44}

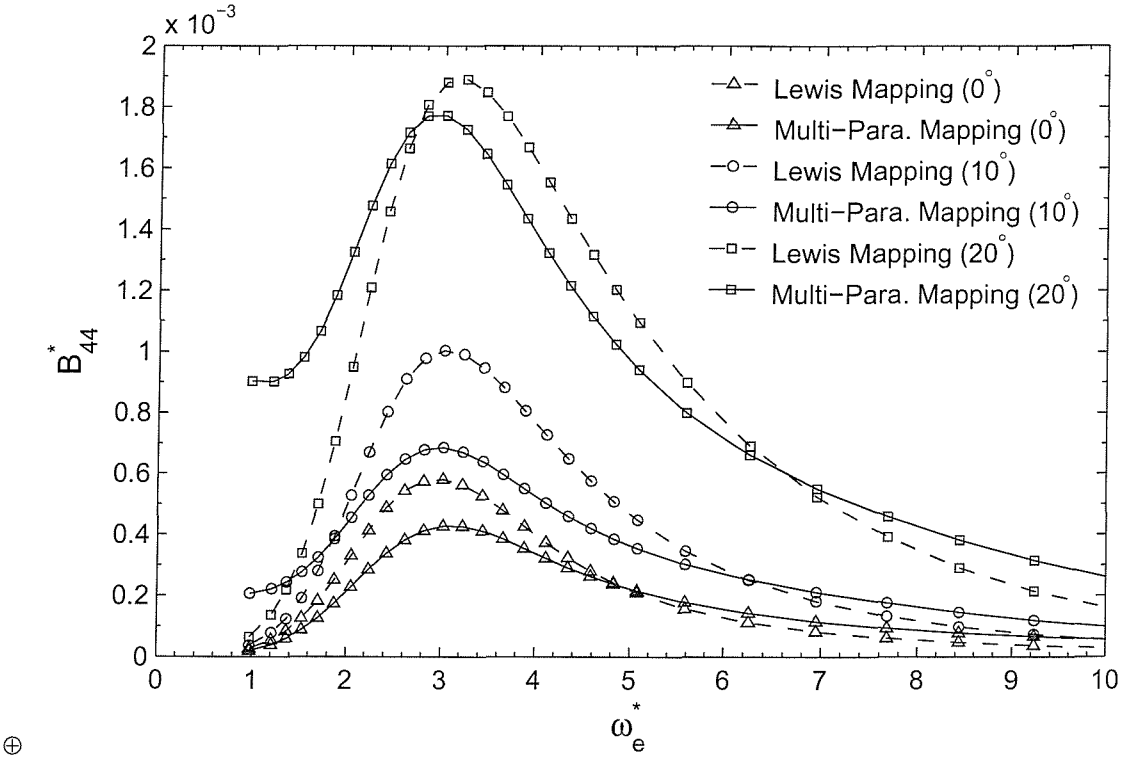

(b) Damping Coefficient B_{44}

Figure 4.52: *Comparison of Roll Coefficients of Series 60 Ship Model at Heel Angles* 0°, 10° *and* 20°.

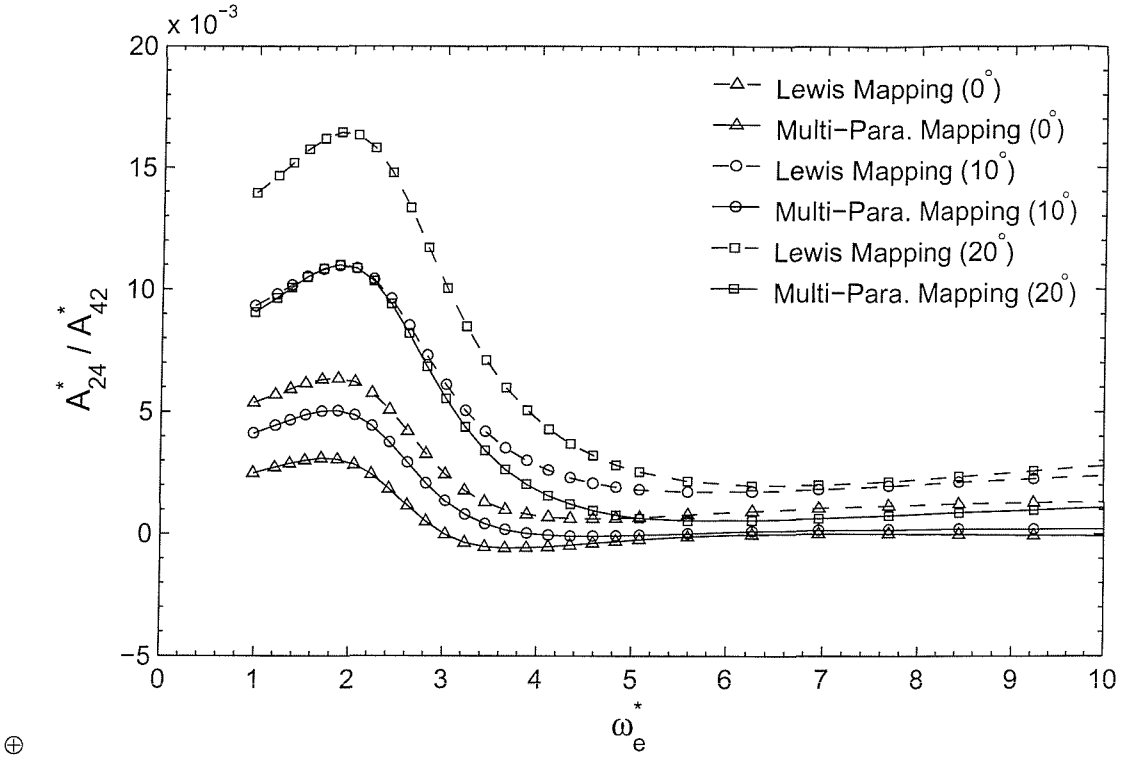

(a) Added-Mass A_{24} / Added-Moment of Inertia A_{42}

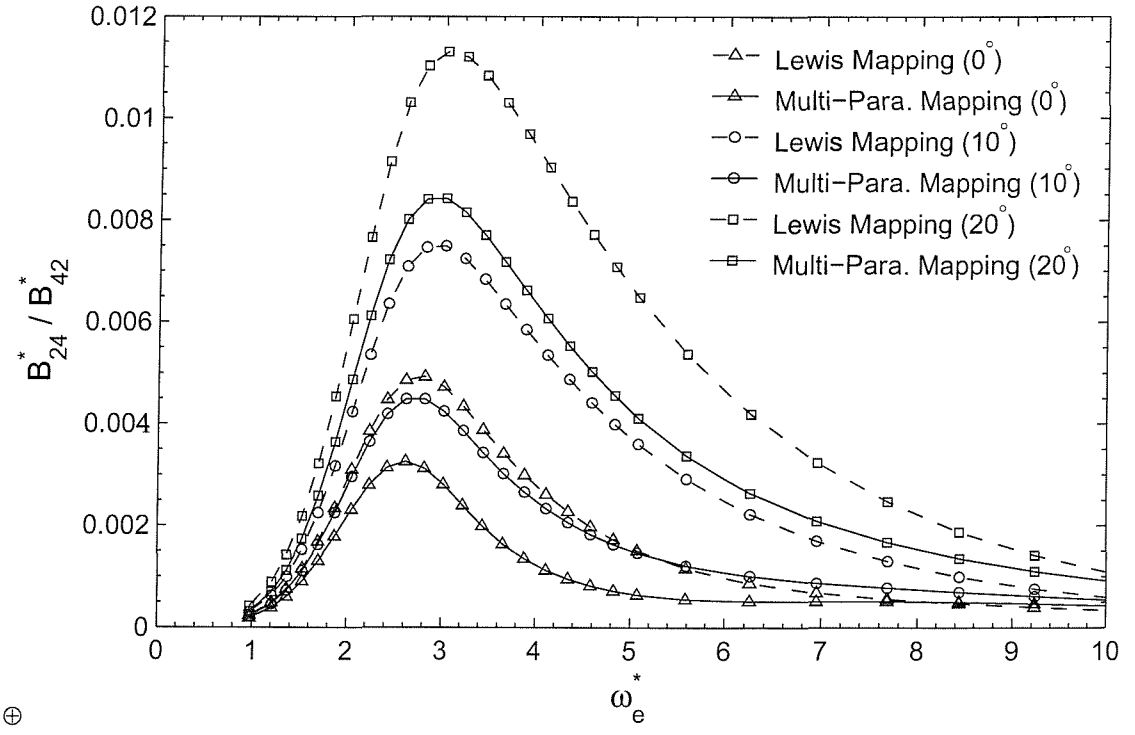

(b) Damping Coefficient B_{24}/B_{42}

Figure 4.53: *Comparison of Sway-Roll/Roll-Away Coupling Coefficients of Series 60 Ship Model at Heel Angles* $0°$, $10°$ *and* $20°$.

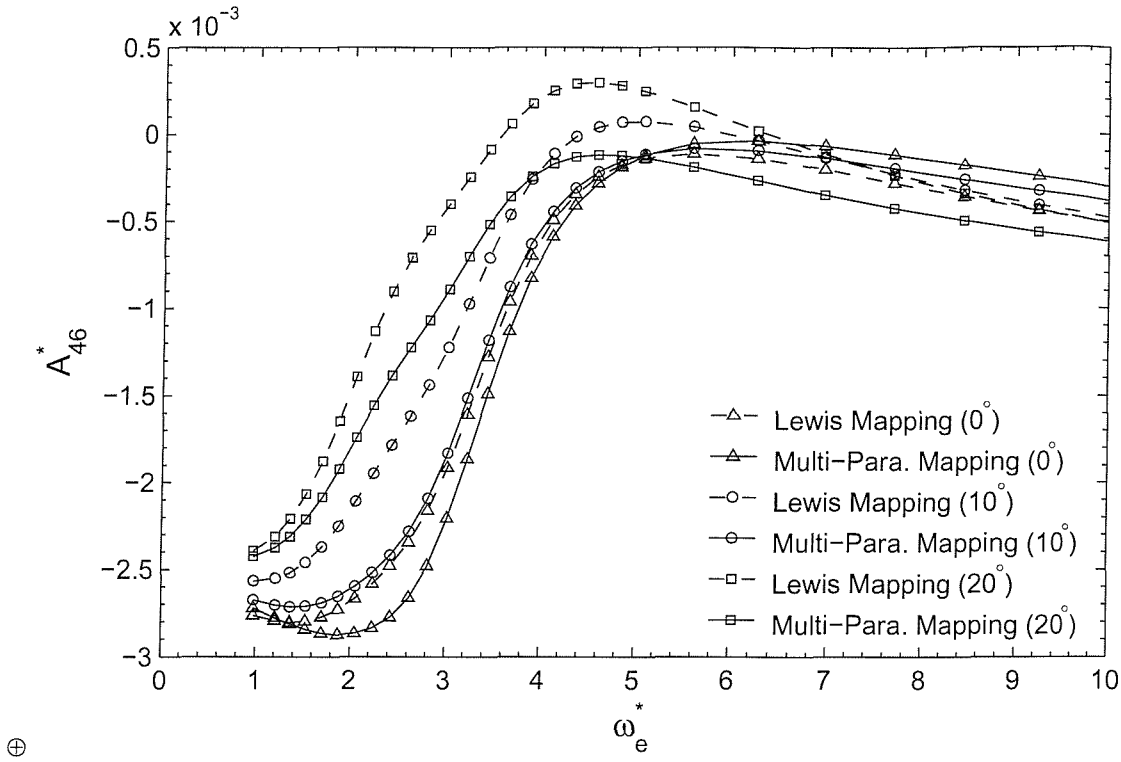

(a) Added-Moment of Inertia A_{46}

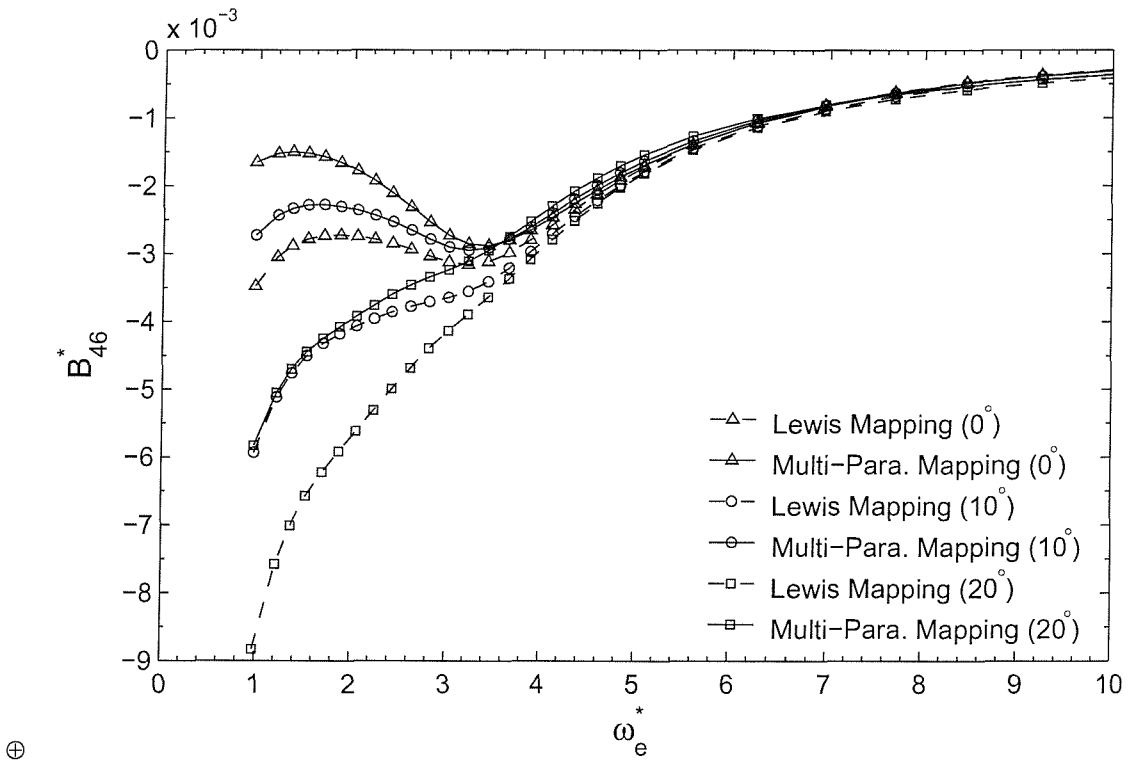

(b) Damping Coefficient B_{46}

Figure 4.54: *Comparison of Roll-Yaw Coupling Coefficients of Series 60 Ship Model at Heel Angles* $0°$, $10°$ *and* $20°$.

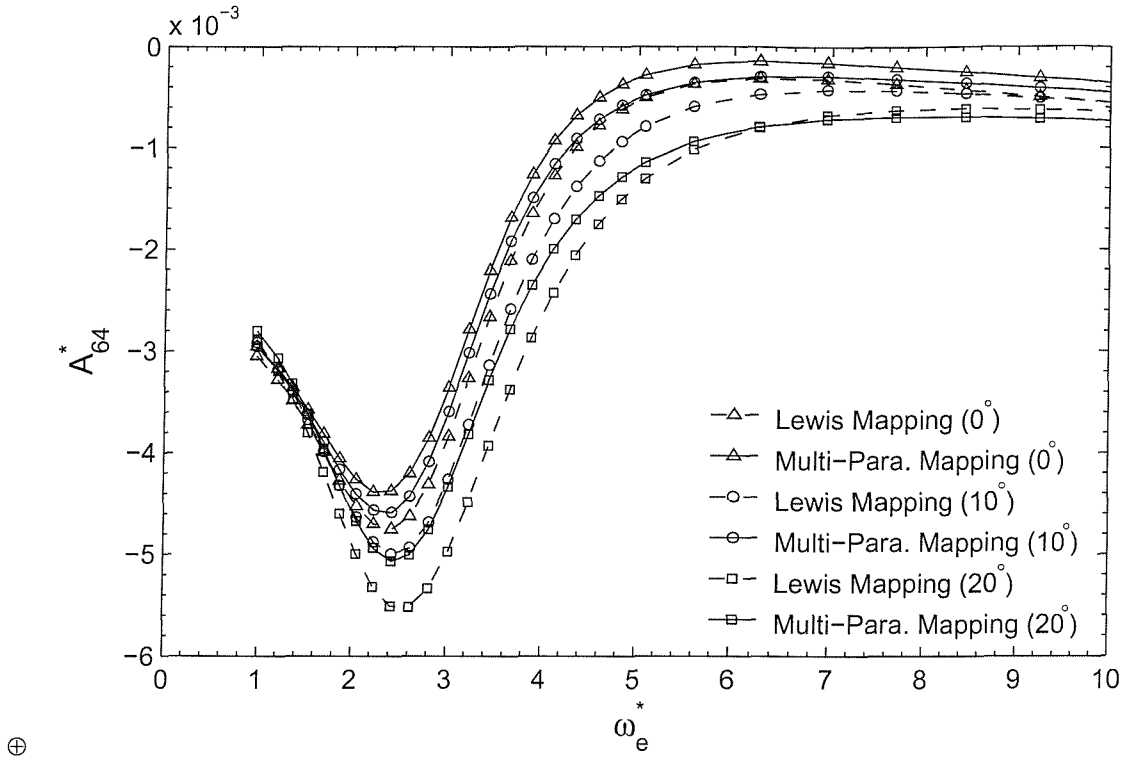

(a) Added-Moment of Inertia A_{64}

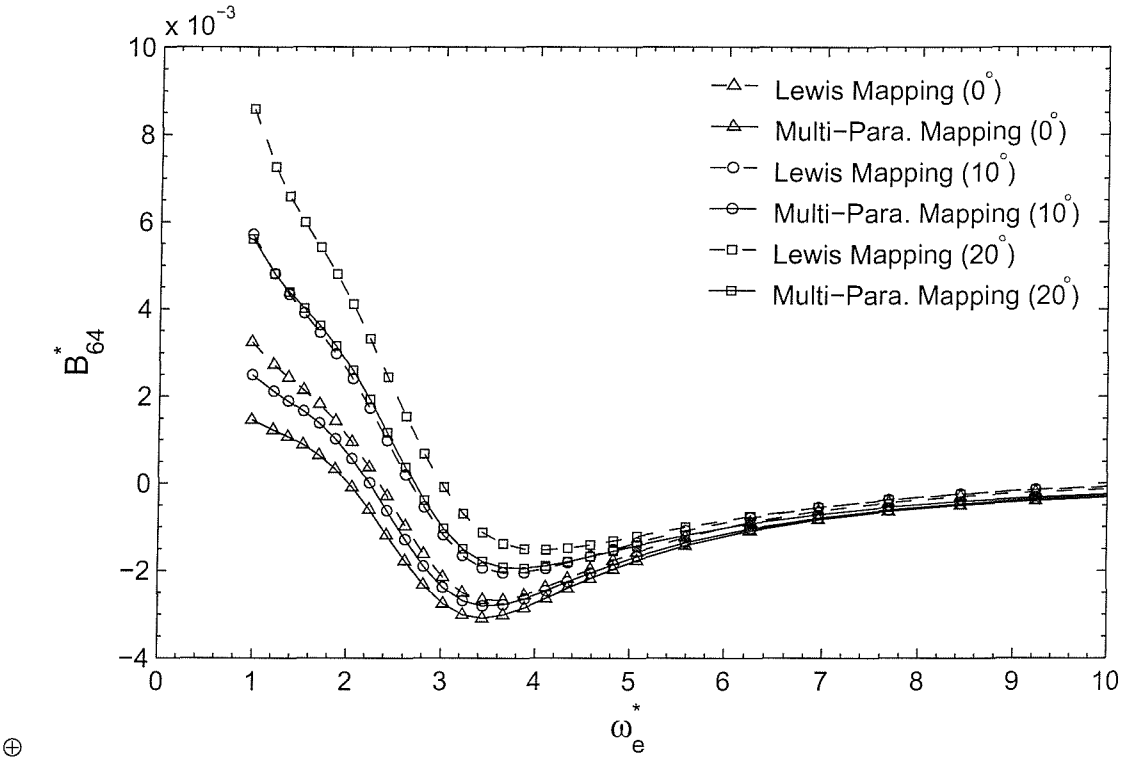

(b) Damping Coefficient B_{64}

Figure 4.55: *Comparison of Yaw-Roll Coupling Coefficients of Series 60 Ship Model at Heel Angles* $0°$, $10°$ *and* $20°$.

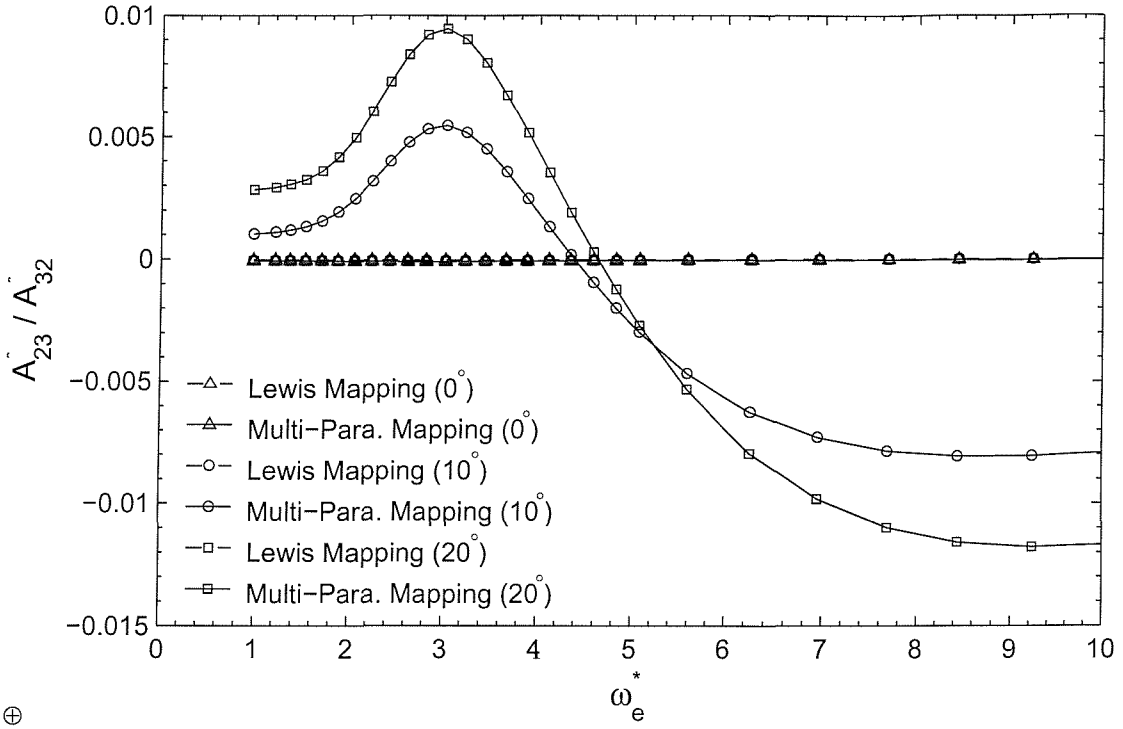

(a) Added-Mass A_{23}/A_{32}

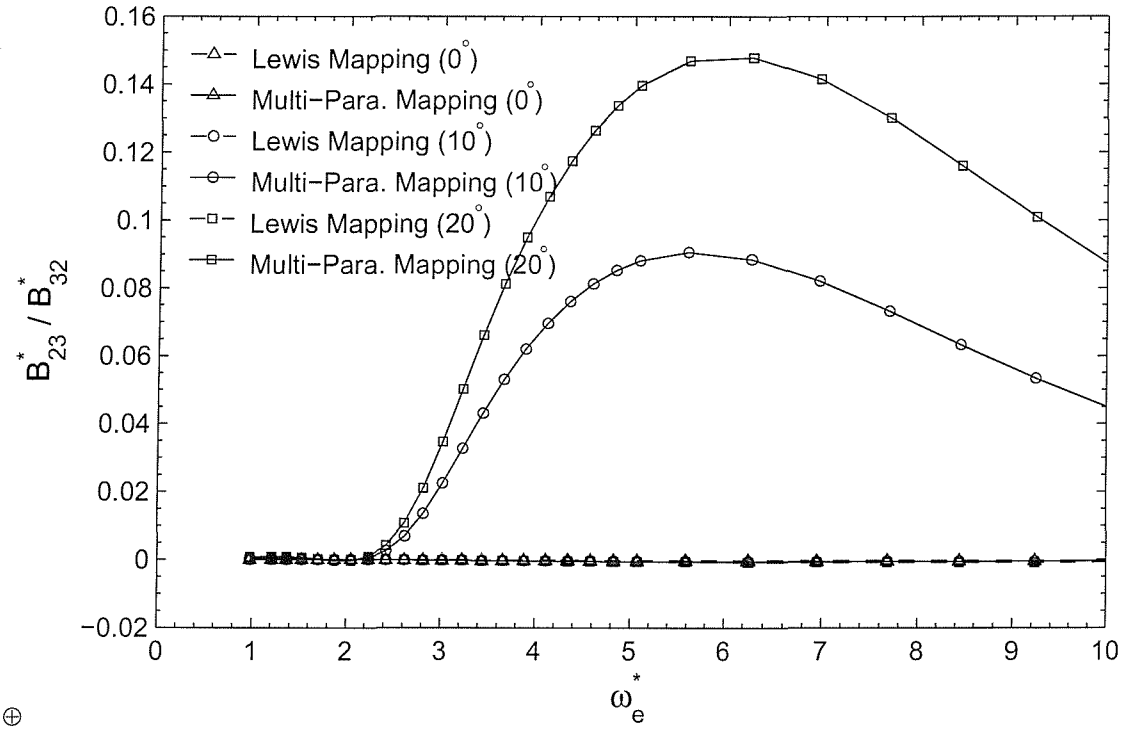

(b) Damping Coefficient B_{23}/B_{32}

Figure 4.56: *Comparison of Sway-Pitch/Pitch-Sway Coupling Coefficients of Series 60 Ship Model at Heel Angles* 0°, 10° *and* 20°.

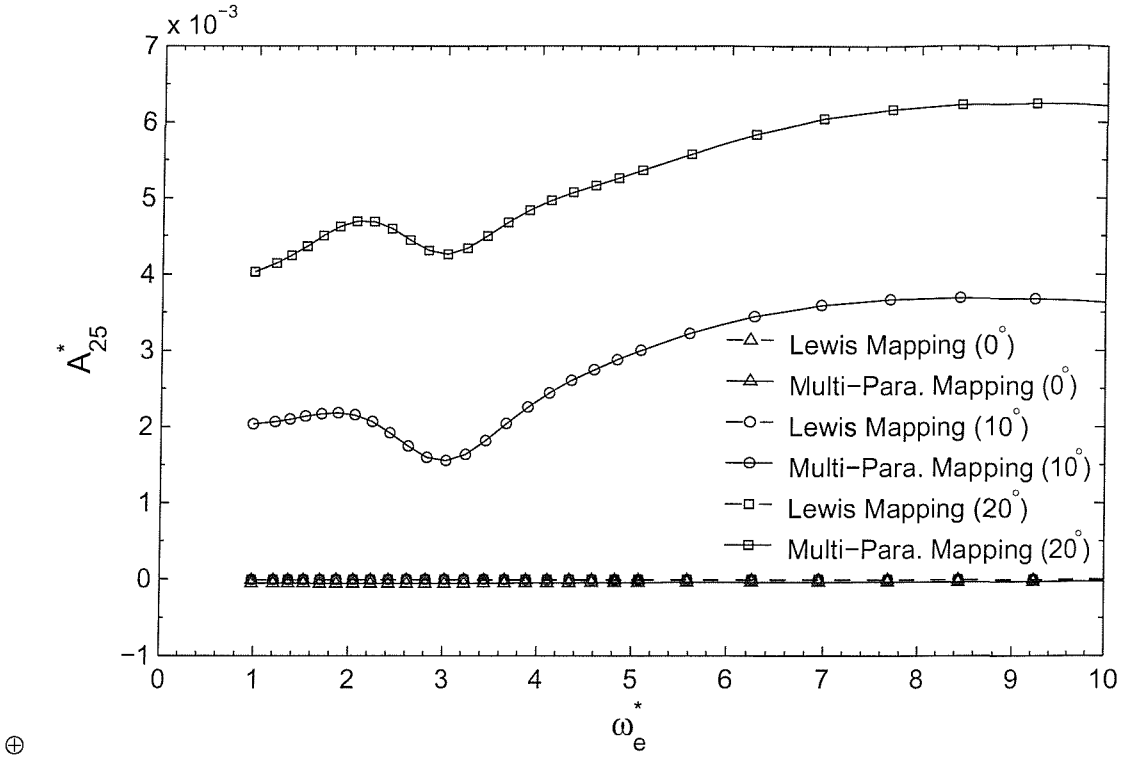

(a) Added-Mass A_{25}

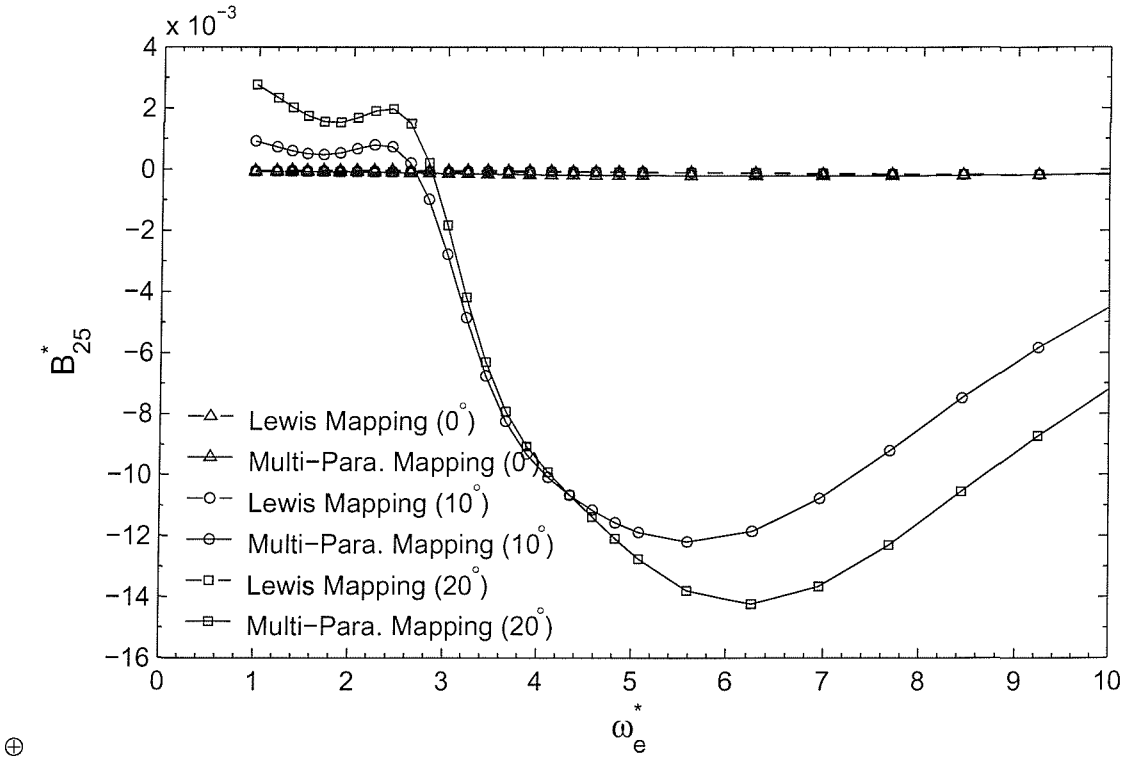

(b) Damping Coefficient B_{25}

Figure 4.57: *Comparison of Sway-Pitch Coupling Coefficients of Series 60 Ship Model at Heel Angles* $0°$, $10°$ *and* $20°$.

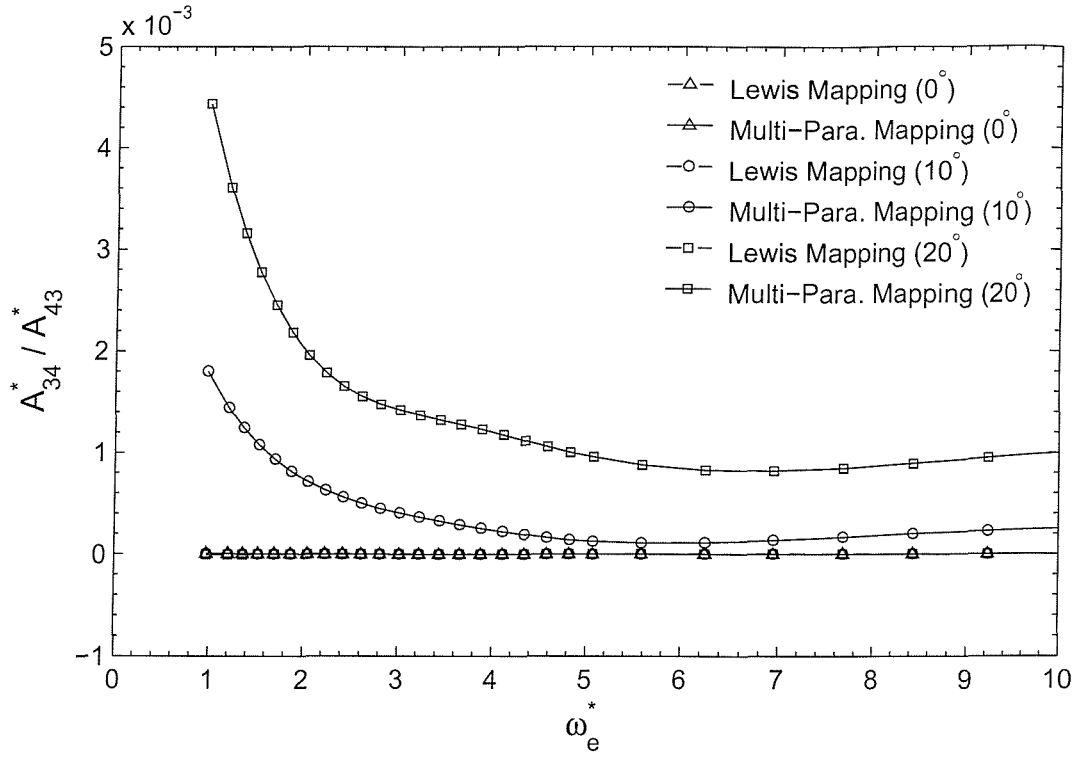

(a) Added-Mass A_{34} / Added-Moment of Inertia A_{43}

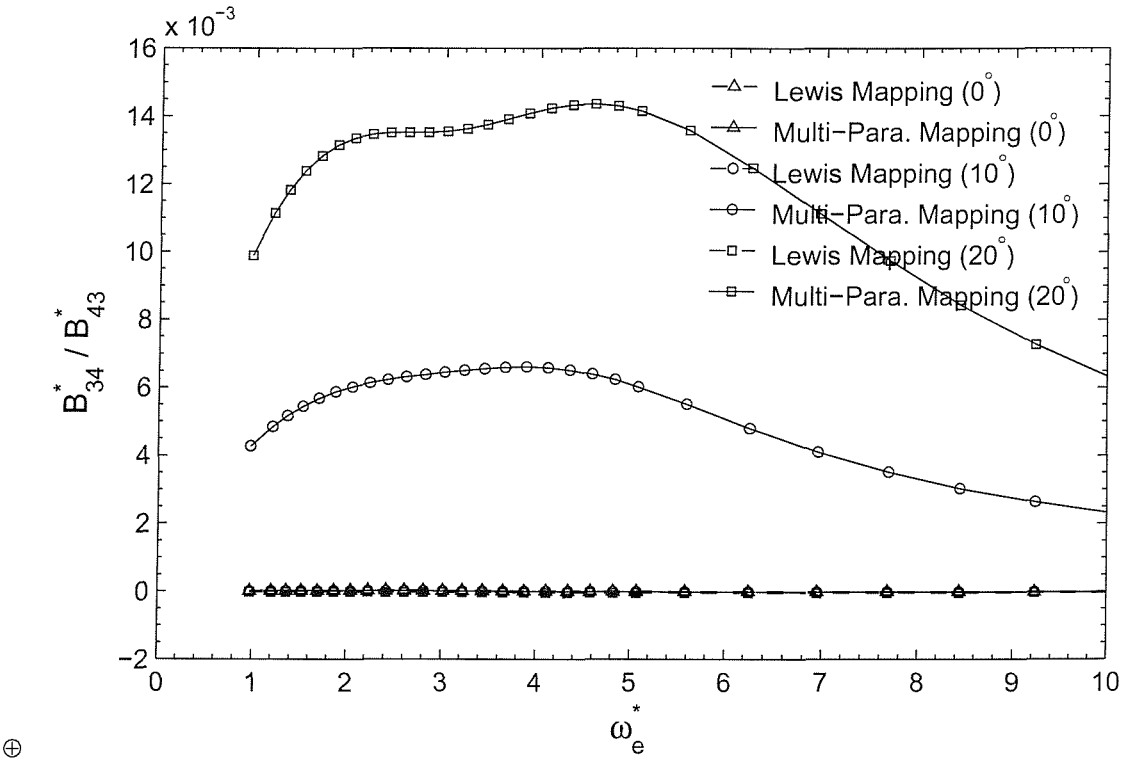

(b) Damping Coefficient B_{34}/B_{43}

Figure 4.58: *Comparison of Heave-Roll/Roll-Heave Coupling Coefficients of Series 60 Ship Model at Heel Angles* $0°$, $10°$ *and* $20°$.

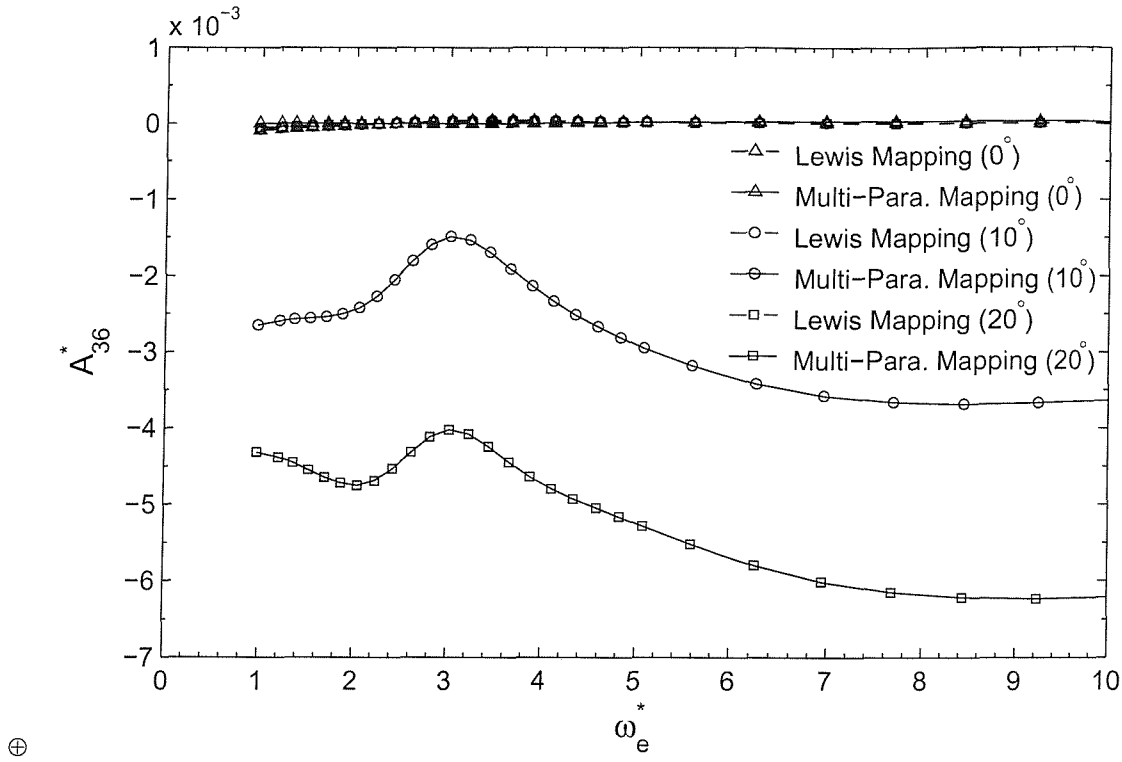

(a) Added-Mass A_{36}

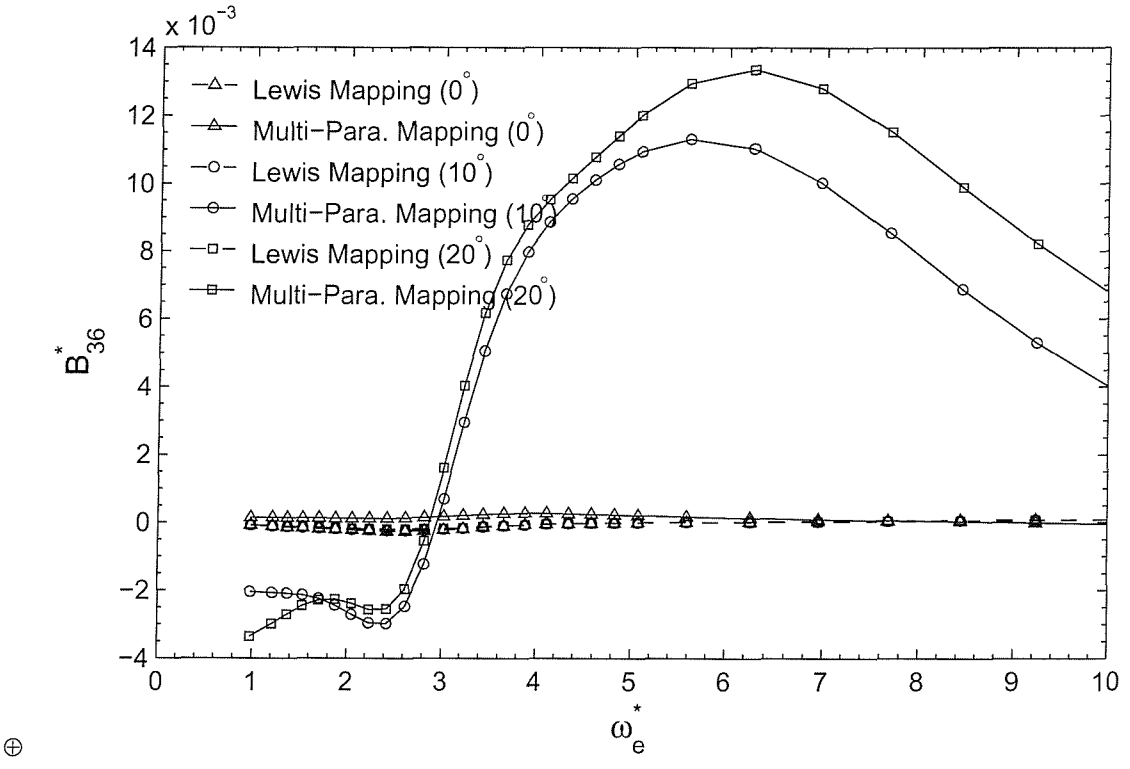

(b) Damping Coefficient B_{36}

Figure 4.59: *Comparison of Heave-Yaw Coupling Coefficients of Series 60 Ship Model at Heel Angles* $0°$, $10°$ *and* $20°$.

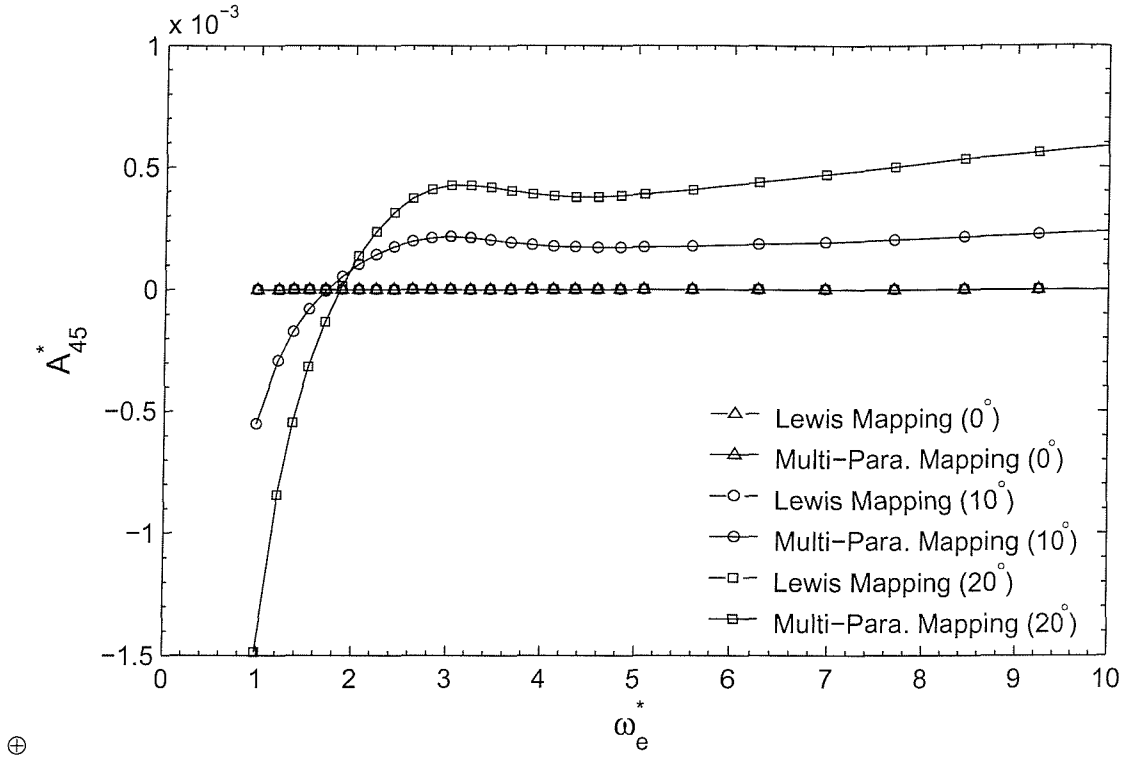

(a) Added-Moment of Inertia A_{45}

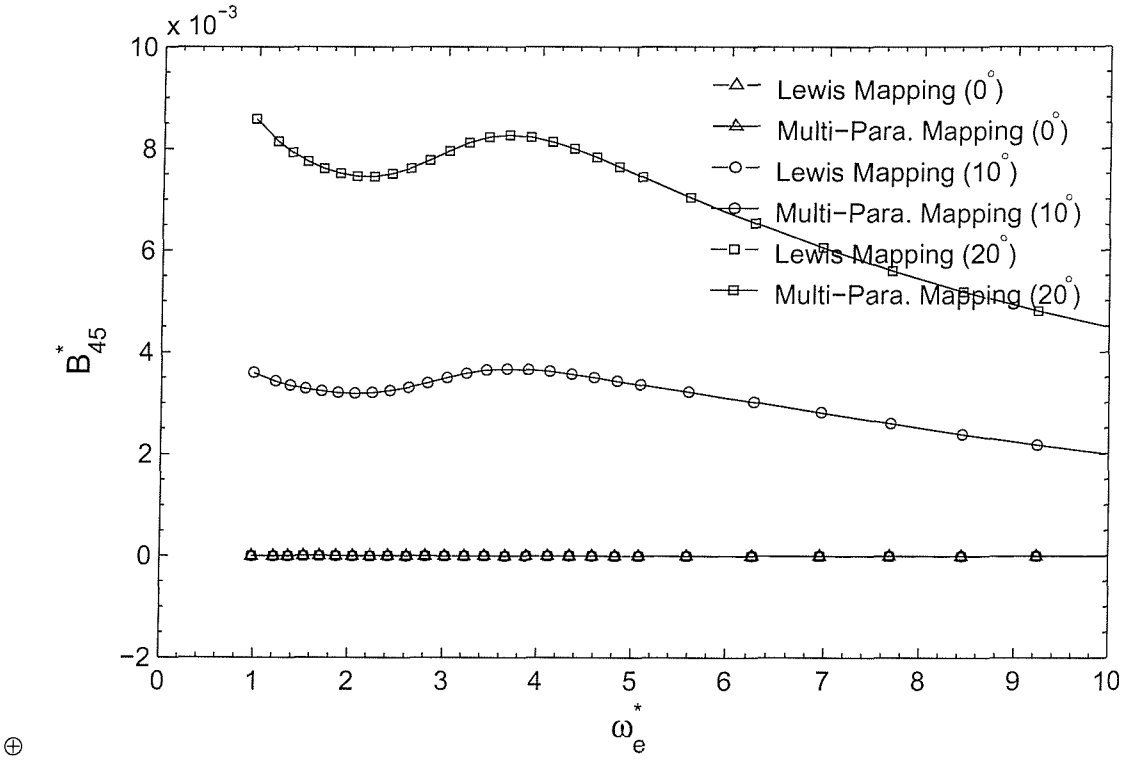

(b) Damping Coefficient B_{45}

Figure 4.60: *Comparison of Roll-Pitch Coupling Coefficients of Series 60 Ship Model at Heel Angles* $0°$, $10°$ *and* $20°$.

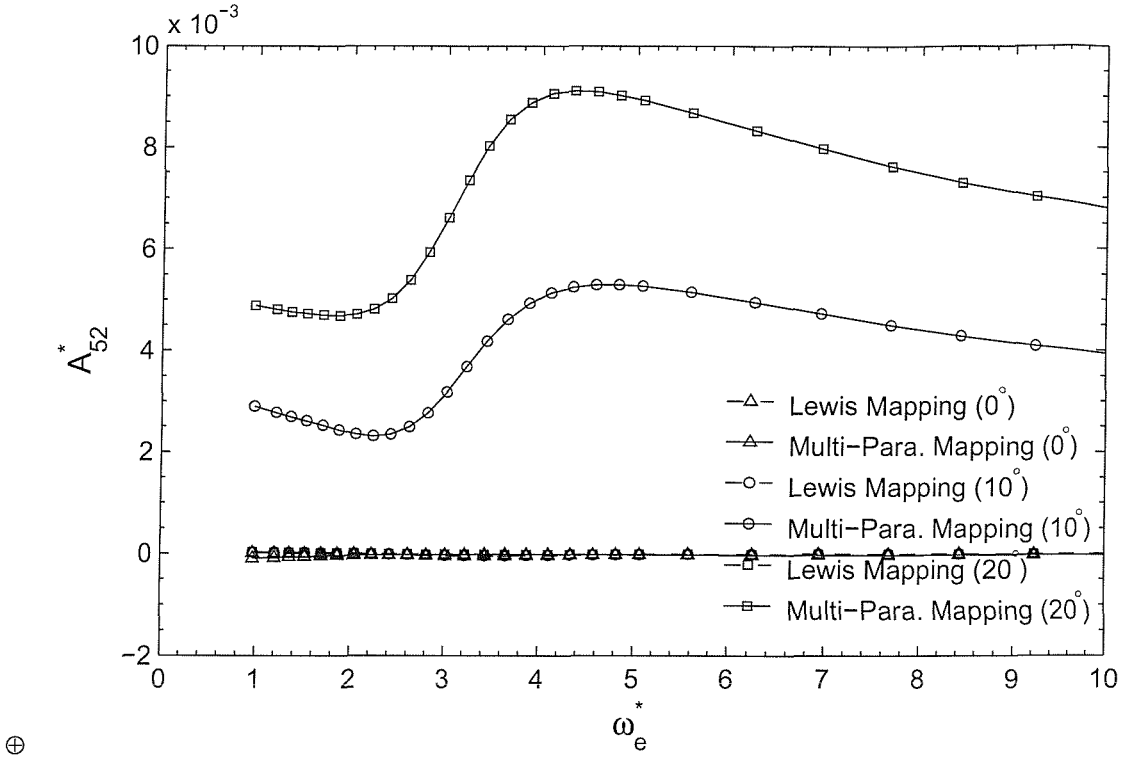

(a) Added-Moment of Inertia A_{52}

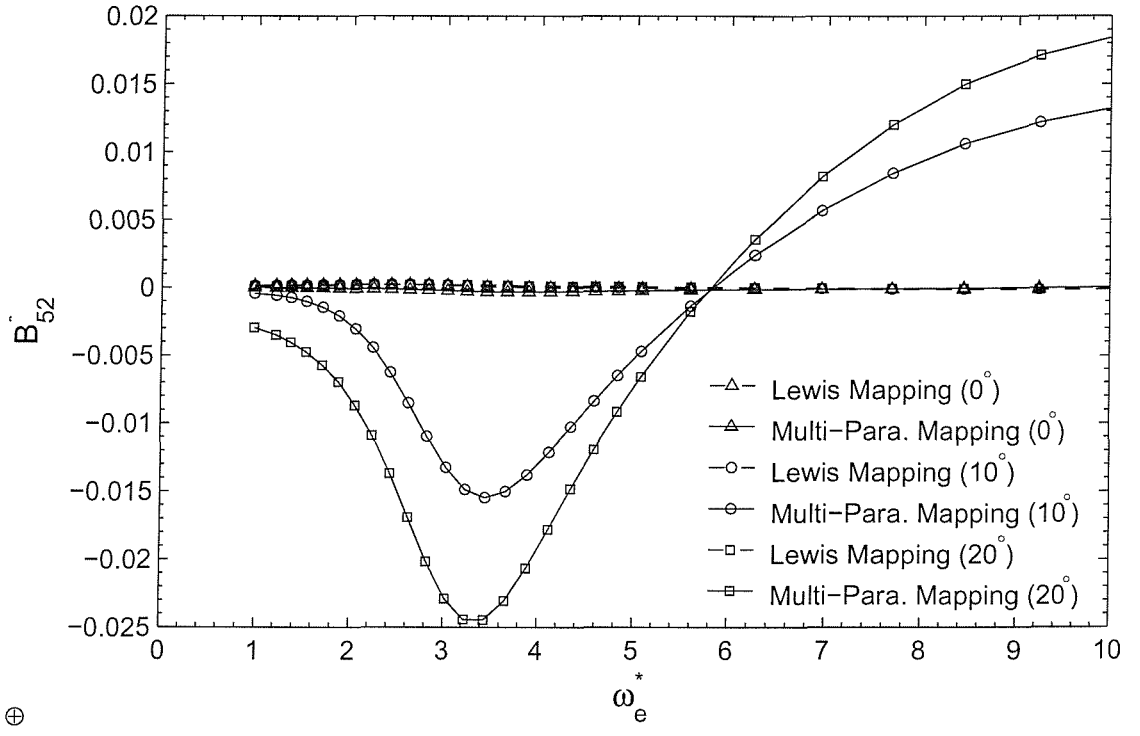

(b) Damping Coefficient B_{52}

Figure 4.61: *Comparison of Pitch-Sway Coupling Coefficients of Series 60 Ship Model at Heel Angles* $0°$, $10°$ *and* $20°$.

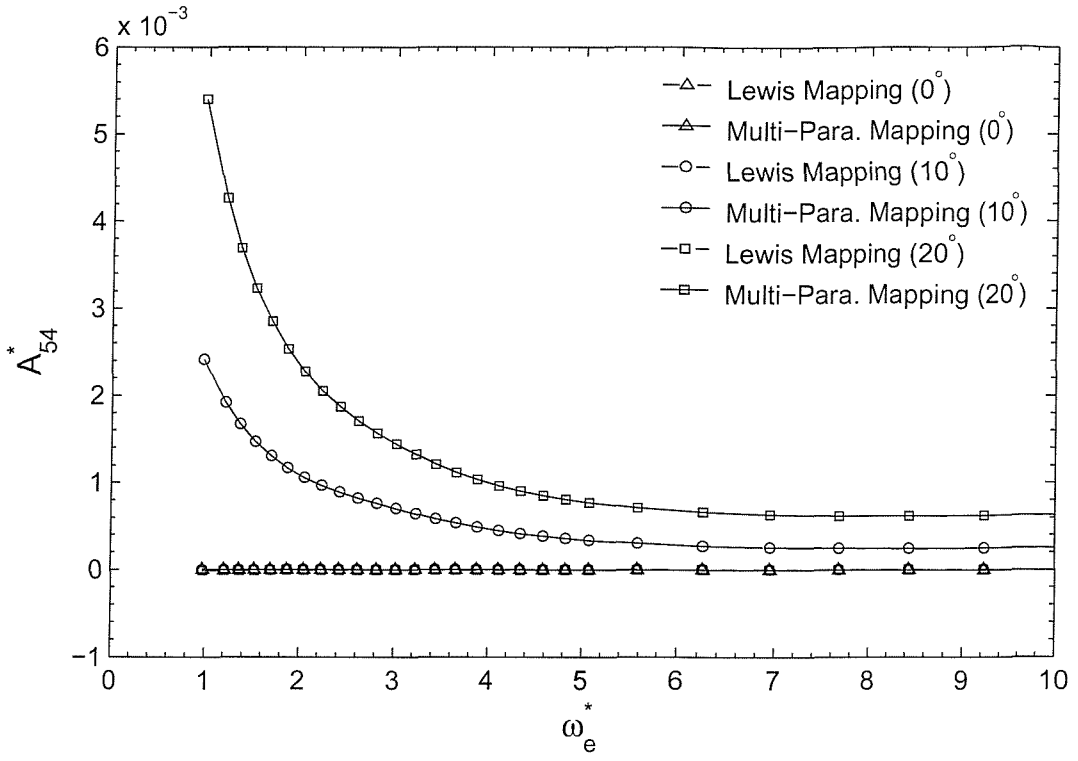

(a) Added-Moment of Inertia A_{54}

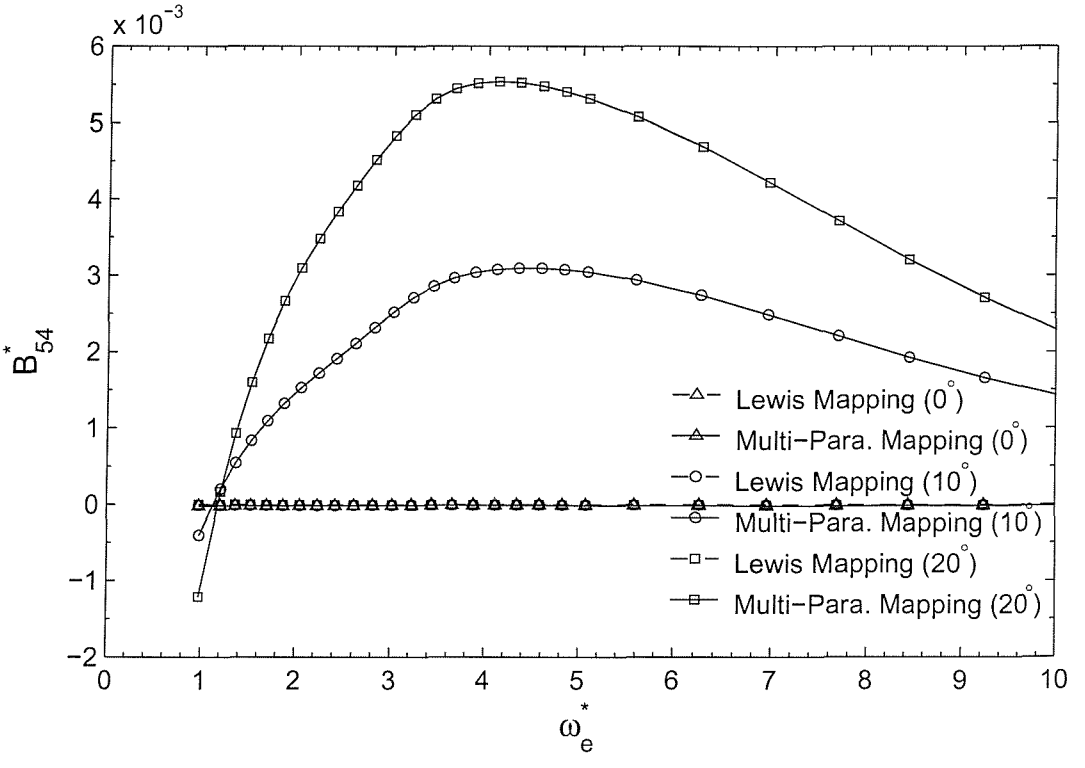

(b) Damping Coefficient B_{54}

Figure 4.62: *Pitch-Roll Coupling Coefficients of Series 60 Ship Model at Heel Angles* $0°$, $10°$ *and* $20°$.

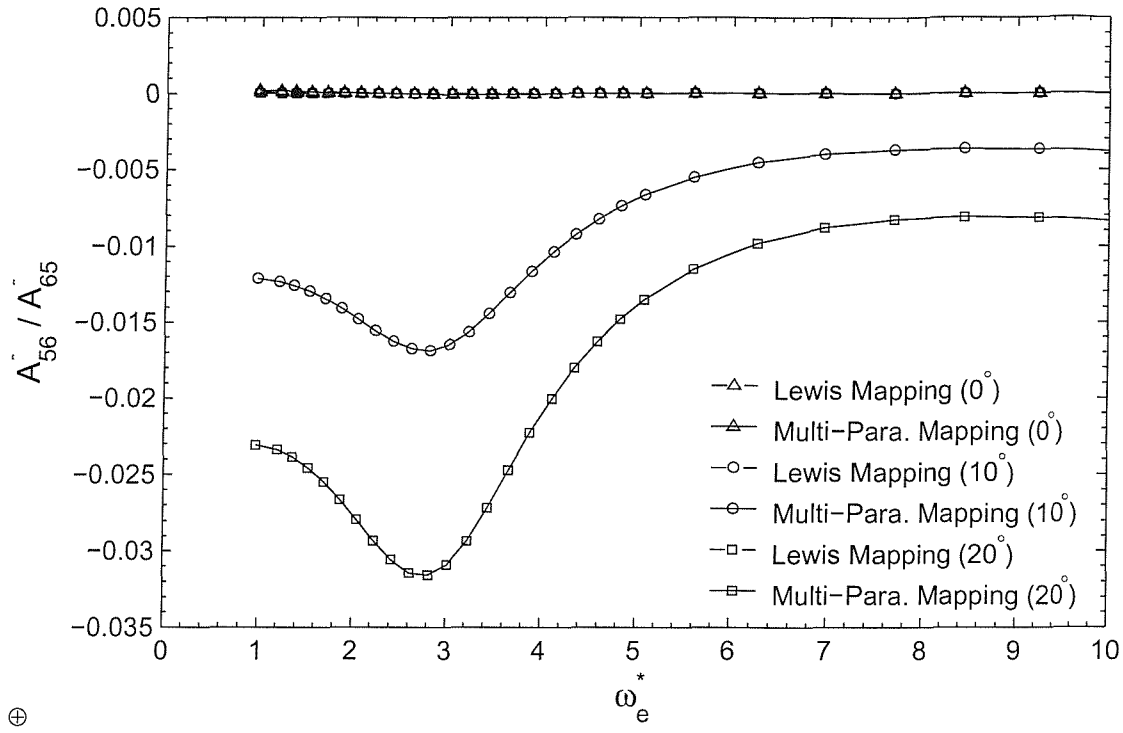

(a) Added-Moment of Inertia A_{56}/A_{65}

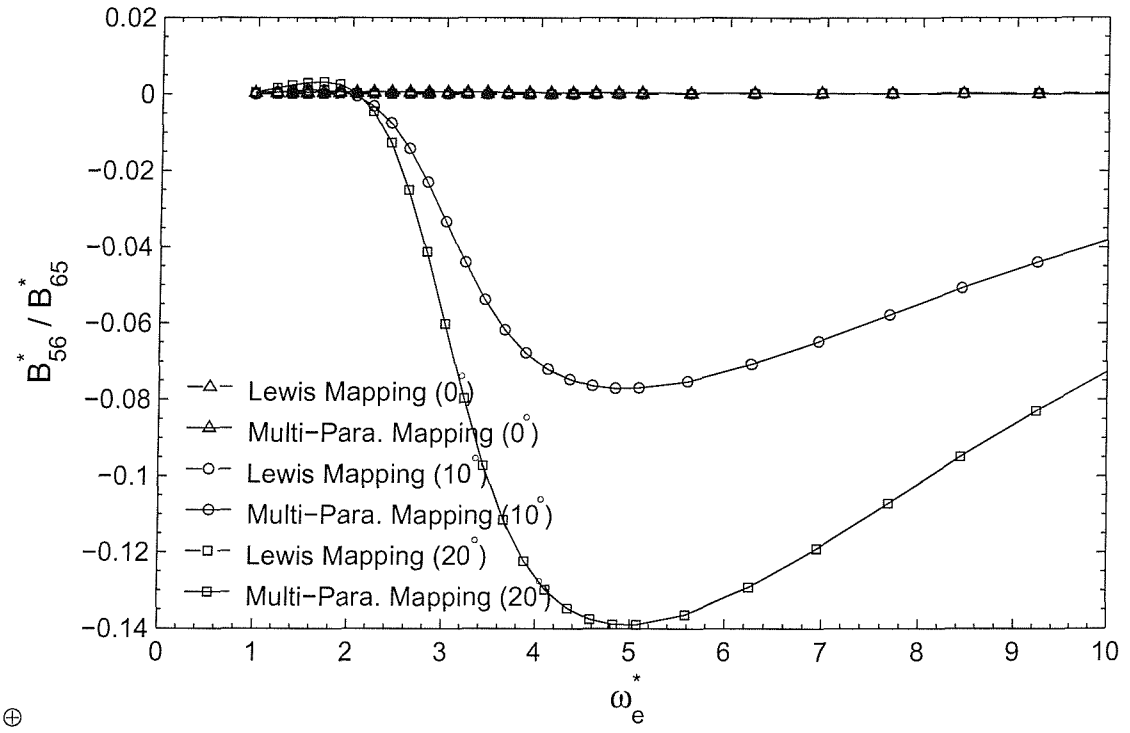

(b) Damping Coefficient B_{56}/B_{65}

Figure 4.63: *Comparison of Pitch-Yaw/Yaw-Pitch Coupling Coefficients of Series 60 Ship Model at Heel Angles* $0°$, $10°$ *and* $20°$.

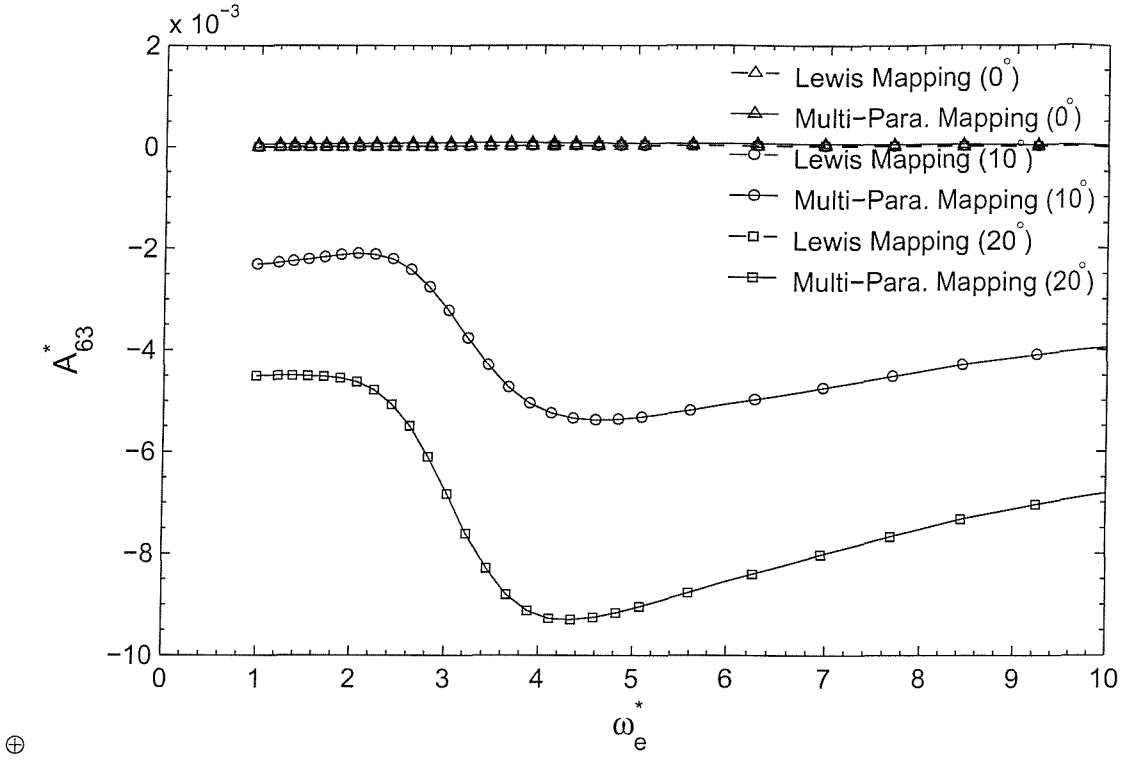

(a) Added-Moment of Inertia A_{63}

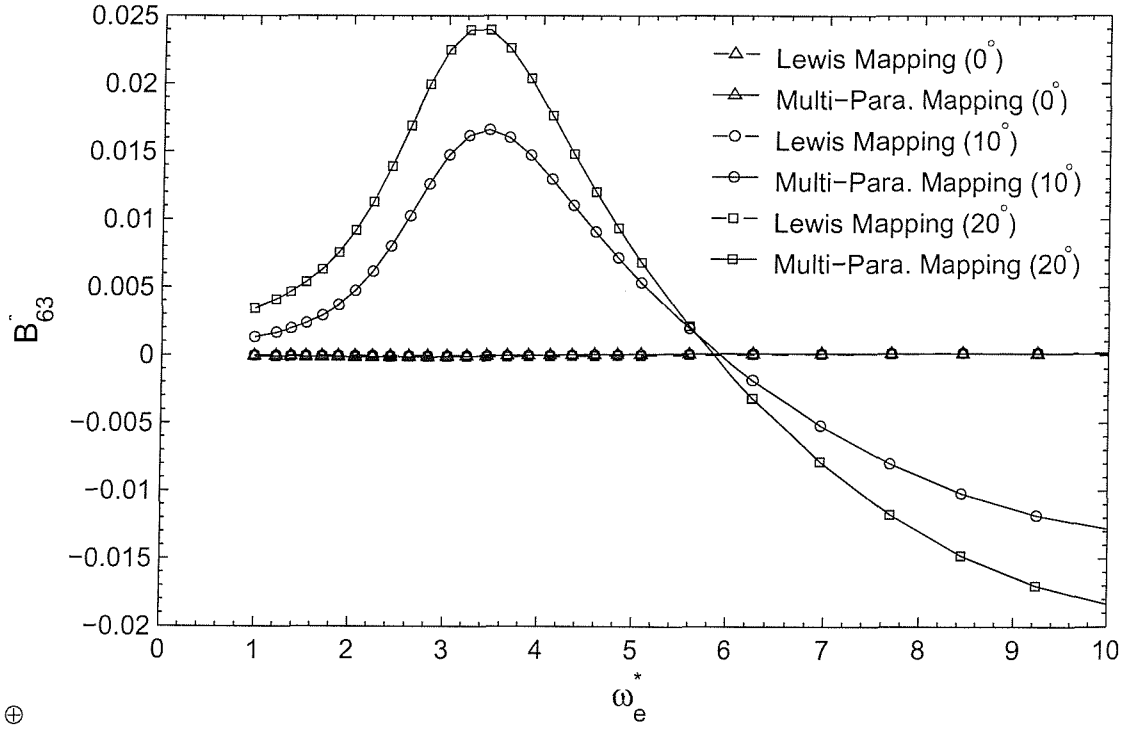

(b) Damping Coefficient B_{63}

Figure 4.64: *Comparison of Yaw-Heave Coupling Coefficients of Series 60 Ship Model at Heel Angles* $0°$, $10°$ *and* $20°$.

Chapter 5

Motion Prediction in Regular Seaways

5.1 Introduction

This chapter focuses on the prediction of ship motions in regular sea waves. In the forgoing chapters, ship motion equations (3.194) are derived and the methods of calculating hydrodynamic coefficients are discussed. This chapter, therefore, discusses the excitation forces and the solution of those five coupled equations*. The numerical method adopted in this chapter to solve the equations is Newmark β direct integration method, which is widely used in structural dynamics analysis [2, 8]. In general, Newmark method is applied to the system of linear differential equations of second order with constant coefficients. However, in time-domain strip theory method the coefficients of ship motion equations (3.194) are not constants, rather time-varying. The generalized mass matrix M_{ji}, added-mass coefficients A_{ji}, damping coefficients B_{ji} and hydrostatic restoring coefficients C_{ji} all vary at each time step. In order to ensure numerical stability, the unconditionally

*The surge motion is usually ignored.

stable parameters are used in Newmark method.

The Series 60 hull form with a block coefficient $C_B = 0.7$ is one of a systematic series of hull forms that represent traditional cruiser-stern commercial ships. It has been tested extensively in towing tanks, so that it is chosen again as a test case. Both predicted forces and motions are compared with experimental data and the results of other calculations.

5.2 Froude-Kriloff Forces

Froude-Kriloff forces are computed using Equations (3.175) and (3.176). Since the incident wave potential ϕ_0 is explicitly known with respect to the coordinate system $o(x_1, x_2, x_3)$, the sectional Froude-Kriloff forces (3.176) can be computed directly as follows,

$$\underline{F}_j^I = g e^{-\imath K_0 x_1 \cos\mu} e^{K_0 h_G} \sum_{i=1}^{N_{pt}-2} \left\{ e^{K_0\left[\imath x_{2i}^m \sin\mu - x_{3i}^m\right]} \widetilde{\underline{n}}_{ji} + e^{K_0\left[\imath x_{2(i+1)}^m \sin\mu - x_{3(i+1)}^m\right]} \widetilde{\underline{n}}_{j(i+1)} \right\} \Delta\ell_i \qquad j = 2, 3, 4, \quad (5.1)$$

where

$$x_{2i}^m = \frac{x_{2i} + x_{2(i+1)}}{2} \quad (5.2)$$

$$x_{3i}^m = \frac{x_{3i} + x_{3(i+1)}}{2} \quad (5.3)$$

$$\Delta x_{2i} = x_{2(i+1)} - x_{2i}, \quad (5.4)$$

$$\Delta x_{3i} = x_{3(i+1)} - x_{3i}, \quad (5.5)$$

$$\widetilde{\underline{n}}_{2i} = \frac{\Delta x_{3i}}{\sqrt{(\Delta x_{2i})^2 + (\Delta x_{3i})^2}}, \quad (5.6)$$

$$\widetilde{\underline{n}}_{3i} = \frac{-\Delta x_{2i}}{\sqrt{(\Delta x_{2i})^2 + (\Delta x_{3i})^2}}, \quad (5.7)$$

$$\widetilde{\underline{n}}_{4i} = (x_{2i}^m - X_2^G)\widetilde{\underline{n}}_{3i} - (x_{3i}^m - X_3^G)\widetilde{\underline{n}}_{2i}, \quad (5.8)$$

$$\Delta\ell_i = \sqrt{(x^m_{2(i+1)} - x^m_{2i})^2 + (x^m_{3(i+1)} - x^m_{3i})^2}. \tag{5.9}$$

(x_{2i}, x_{3i}), $i = 1, 2, \ldots, N_{pt}$, are section definition points, which have to be in the order such that $x_{2(i+1)} \geq x_{2i}$. X^G_i is the coordinate of the centre of the gravity of the ship in the coordinate system $o(x_1, x_2, x_3)$, which is considered as the rotating centre of each section. It could be understood that the distance $\Delta\ell_i$ between two consecutive section definition points must be small enough in order to achieve the desired integration accuracy. However, this could not always be guaranteed by the hull rationalization method introduced in Section §4.2 for those ships without or with just a little floor rise, *e.g.* Section 10 of Series 60 ($C_B = 0.7$) model shown in Figures (4.5(a) - 4.8(a)), where the distances between the points next to the keel are too large to be acceptable. The numerical accuracy is poor unless extra points are interpolated.

Alternatively, by using the conformal mapping Equations (3.92) and (3.93), the integration in Equation (3.176) can be performed with respect to variable ϑ,

$$\underline{F}^I_2 = g e^{-\imath K_0 x_1 \cos\mu} \int_{-\frac{\pi}{2}}^{+\frac{\pi}{2}} e^{K_0(\imath \boldsymbol{x}_2 \sin\mu - \boldsymbol{x}_3 + h_G)} \frac{\partial \boldsymbol{x}_3}{\partial \vartheta}\Big|_{r=1} d\vartheta, \tag{5.10}$$

$$\underline{F}^I_3 = -g e^{-\imath K_0 x_1 \cos\mu} \int_{-\frac{\pi}{2}}^{+\frac{\pi}{2}} e^{K_0(\imath \boldsymbol{x}_2 \sin\mu - \boldsymbol{x}_3 + h_G)} \frac{\partial \boldsymbol{x}_2}{\partial \vartheta}\Big|_{r=1} d\vartheta, \tag{5.11}$$

$$\begin{aligned} \underline{F}^I_4 = -g e^{-\imath K_0 x_1 \cos\mu} \int_{-\frac{\pi}{2}}^{+\frac{\pi}{2}} e^{K_0(\imath \boldsymbol{x}_2 \sin\mu - \boldsymbol{x}_3 + h_G)} \Big[(\boldsymbol{x}_2 - X^G_2) \frac{\partial \boldsymbol{x}_2}{\partial \vartheta} \\ + (\boldsymbol{x}_3 - X^G_3) \frac{\partial \boldsymbol{x}_3}{\partial \vartheta} \Big]_{r=1} d\vartheta. \end{aligned} \tag{5.12}$$

This method generally gives much better results, provided that the conformal mapping is accurate. Unlike the distribution of section definition points (x_{2i}, x_{3i}) on the section contour, which is subject to the rationalisation process, ϑ can be distributed evenly and for an arbitrary number of values over range $[-\pi/2, \pi/2]$.

Figure (5.1) shows the amplitude of the heave and pitch Froude-Kriloff forces of a Series 60 ($C_B = 0.7$) model travelling with forward speed $F_n = 0.2$ in sinusoidal head waves. F_3^{I*} and F_5^{I*} are non-dimensional forces, ω_e^* is the non-dimensional frequency of encounter,

$$F_3^{I*} = \frac{|F_3^I| L_{ship}}{\varrho g \eta_0 V_{dsp}}, \tag{5.13}$$

$$F_5^{I*} = \frac{|F_5^I|}{\varrho g \eta_0 V_{dsp}}, \tag{5.14}$$

$$\omega_e^* = \omega_e \sqrt{L_{ship}/g}, \tag{5.15}$$

where η_0 is the amplitude of the incident wave, L_{ship} is the model length between perpendiculars, ϱ is the fluid density, and V_{dsp} is the model displacement. Figure (5.2) provides the corresponding phase angles of the heave and pitch forces.

Surprisingly, not only the amplitude of the forces but also the phase angles predicted by strip theory are extremely close to those computed using frequency-domain Green function method, even though much less information of the hull is required in strip theory compared with Green function method.

5.3 Diffraction Forces

Equations (3.177), (3.178) and (3.179) are used to compute the diffraction forces. It has to resort to the conformal mapping equations to compute the sectional diffraction forces (3.179), since the potentials $\underline{\Phi}_j$ is unknown in the coordinate system $o(x_1, x_2, x_3)$. After applying the conformal mapping Equations (3.92) and (3.93), $\underline{\Phi}_j$ can be replaced by $\underset{\sim}{\Phi}_j$, Equation (3.179) becomes

$$\underline{F}_j^D = -\omega_0 e^{-\imath x_1 K_0 \cos\mu} \int_{-\frac{\pi}{2}}^{+\frac{\pi}{2}} e^{K_0(\imath x_2 \sin\mu - x_3 + h_G)} \left(\imath \frac{\partial x_2}{\partial \vartheta} \Big|_{r=1} \right.$$

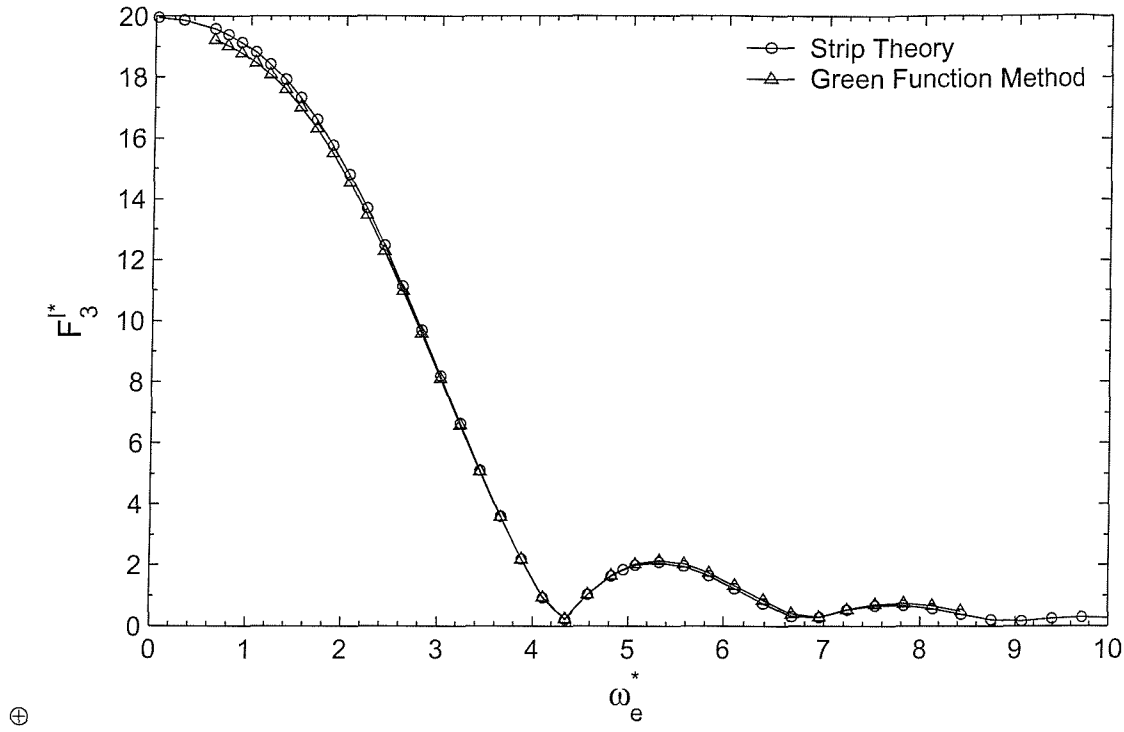

(a) Heave

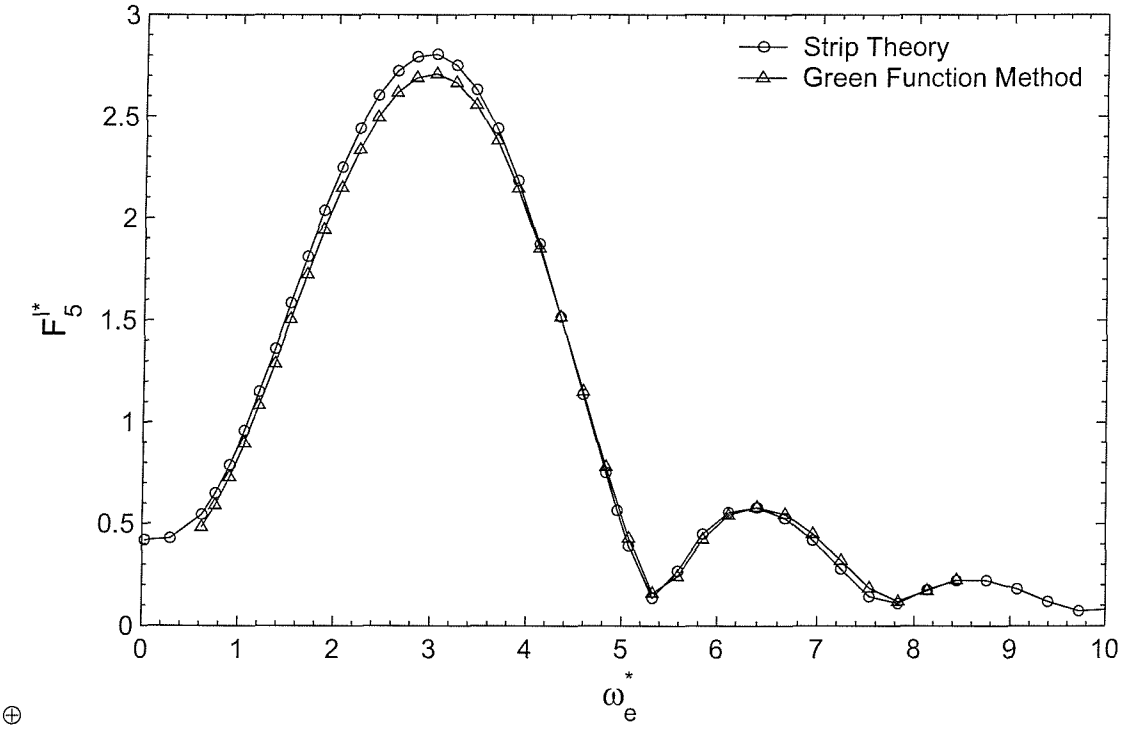

(b) Pitch

Figure 5.1: *Froude-Kriloff Forces of a Series 60 ($C_B = 0.7$) Model Travelling with Forward Speed $F_n = 0.2$.*

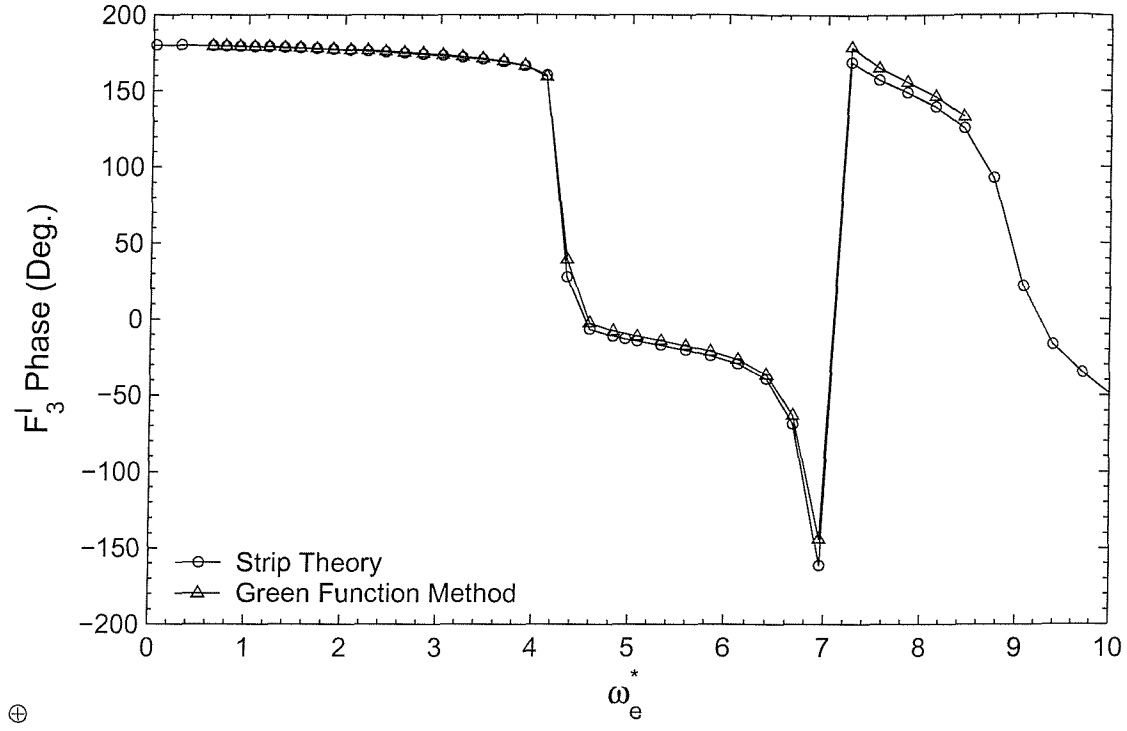

(a) Heave

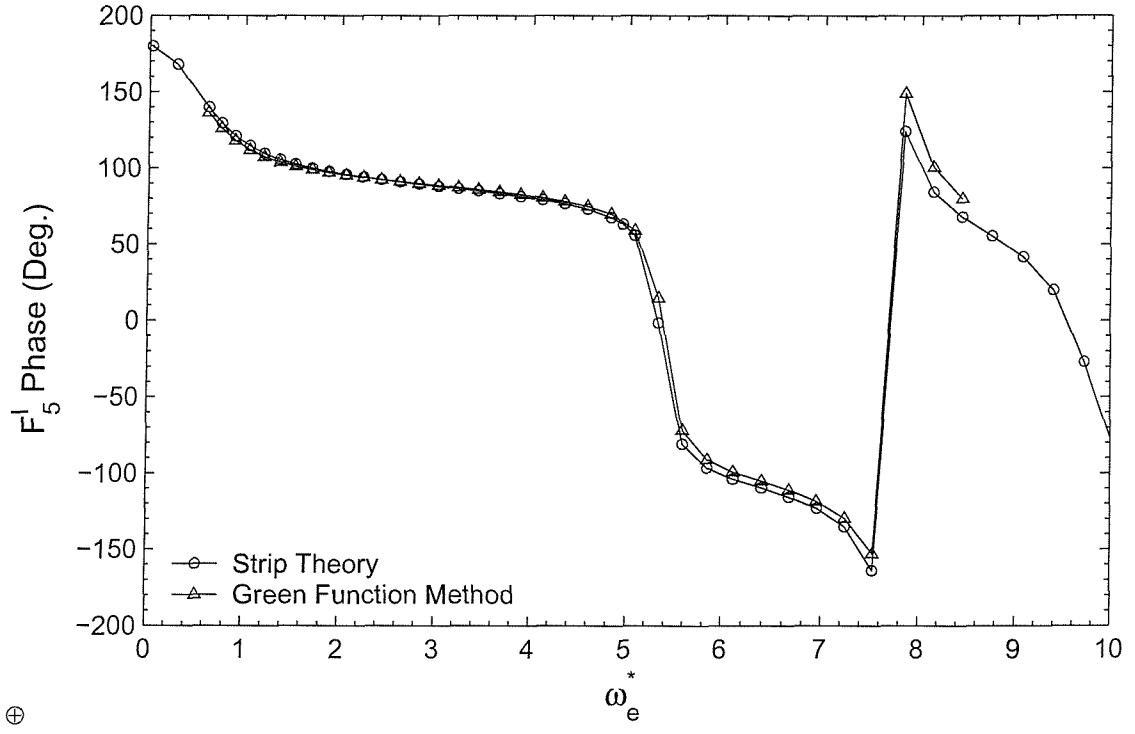

(b) Pitch

Figure 5.2: *Phases of Froude-Kriloff Forces of a Series 60 ($C_B = 0.7$) Model Travelling with Forward Speed $F_n = 0.2$.*

$$+ \frac{\partial \boldsymbol{x}_3}{\partial \vartheta}\Big|_{r=1} \sin\mu\Big) \underset{\sim}{\Phi}_j^0 d\vartheta, \qquad j = 2,3,4. \quad (5.16)$$

Figure (5.3) depicts the amplitude of the heave and pitch diffraction forces, the corresponding phase angles are illustrated in Figure (5.4). Diffraction forces are shown in the same non-dimensional form as the Froude-Kriloff forces,

$$F_3^{D*} = \frac{|F_3^D| L_{ship}}{\varrho g \eta_0 V_{dsp}}, \quad (5.17)$$

$$F_5^{D*} = \frac{|F_5^D|}{\varrho g \eta_0 V_{dsp}}. \quad (5.18)$$

Presently neither the diffraction forces measured by experiment nor the results computed by other seakeeping programs are available for comparison, in the Figures (5.3) and (5.4) only the diffraction forces predicted by time-domain strip theory are presented. However, comparing the total forces computed by time-domain strip theory with those computed by Green function method indicates that the significant differences exist between the diffraction forces calculated by these two methods. Figure (5.5) illustrates the amplitude of the total heave and pitch exciting forces, where the experimental results were measured by Gerritsma [18] on the Series 60 ($C_B = 0.7$), ship model travelling in regular sinusoidal head waves with a Froude number of 0.20. The non-dimensional exciting forces are obtained by

$$F_3^* = \frac{|F_3^D + F_3^I| L_{ship}}{\varrho g \eta_0 V_{dsp}}, \quad (5.19)$$

$$F_5^* = \frac{|F_5^D + F_5^I|}{\varrho g \eta_0 V_{dsp}}. \quad (5.20)$$

The heave exciting forces predicted by the strip theory and the Green function method are in fairly close agreement, except in the frequency range $4.2 \leq \omega_e^* \leq 5.6$, where strip theory seems to give slightly better prediction. Signifi-

cant discrepancies between the pitch exciting forces can be seen clearly in Figure (5.5(b)), however, the result given by strip theory and that given by Green function method follow the same trend. Since just a few experimental results are available over a limited frequency range, it is quite difficult to obtain a fair judgement. Compared with experimental data, strip theory gives a little bit better prediction then Green function method on the resonance frequency. In the frequency range near the resonance, the results of strip theory are higher then the experimental data, while the results given by Green function method are lower then the experimental data.

Figure (5.6) illustrates the phase angles of heave and pitch exciting forces. Since no experimental results are available at present, it is impossible to judge which method, strip theory or Green function method, gives more accurate prediction of phase angles. Apparently strip theory and Green function method give quite different predictions in the high frequency range, $\omega_e^* \geq 3.0$ for heave exciting force, and $\omega_e^* \geq 4.0$ for pitch exciting force. However, those high frequencies are not of importance in practical ship design.

5.4 Newmark-β Direct Integration Method

There are many methods for advancing the solution of (3.194) in time, *e.g.* the Central Difference Method and the Implicit Linear Acceleration Method [2, 8]. The method considered here is Newmark-β Direct Integration Method which is proposed by Newmark [49] for the solution of structural dynamic problems. During the past decades it has been applied to the dynamic analysis of many practical engineering structures. In addition, it has been modified and improved by many other researchers.

The Newmark method can be derived in a number of ways, and can be found

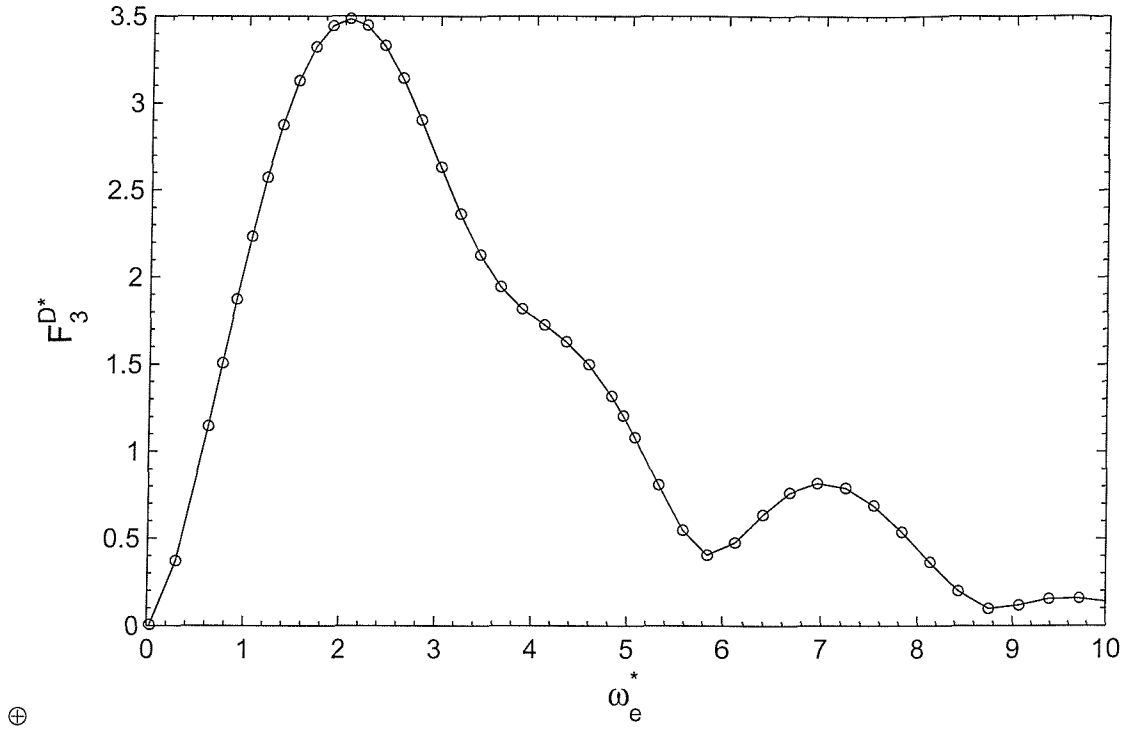

(a) Heave

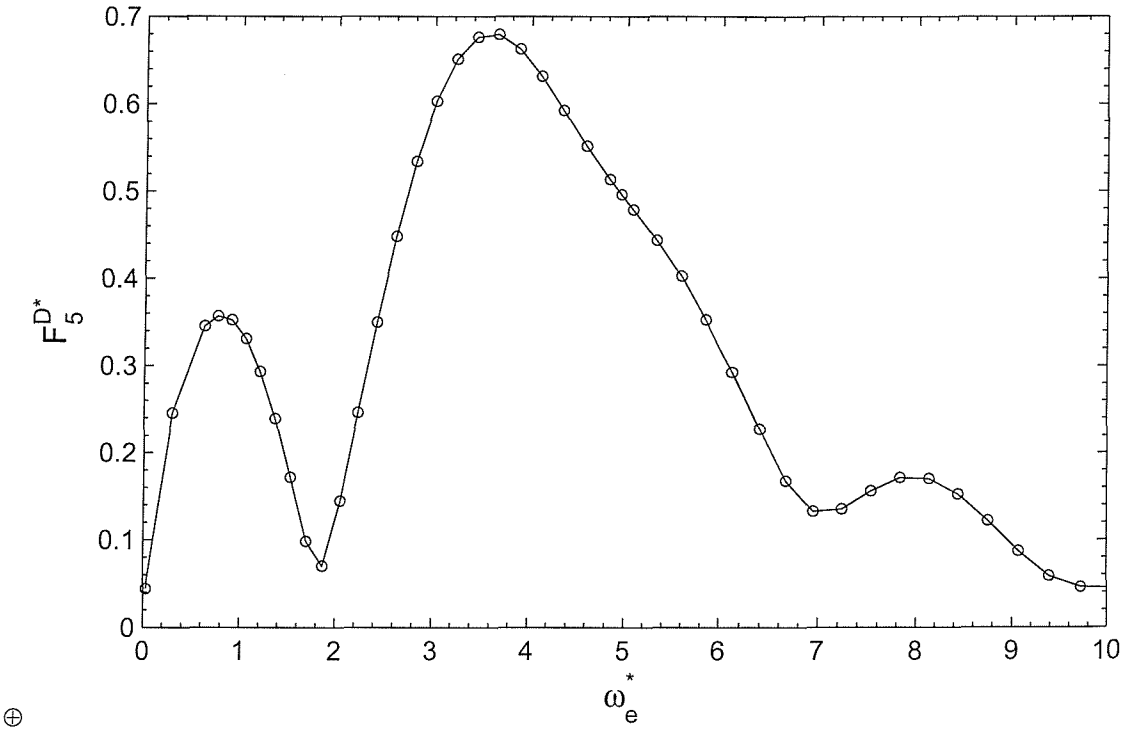

(b) Pitch

Figure 5.3: *Diffraction Forces of a Series 60 ($C_B = 0.7$) Model Travelling with Forward Speed $F_n = 0.2$.*

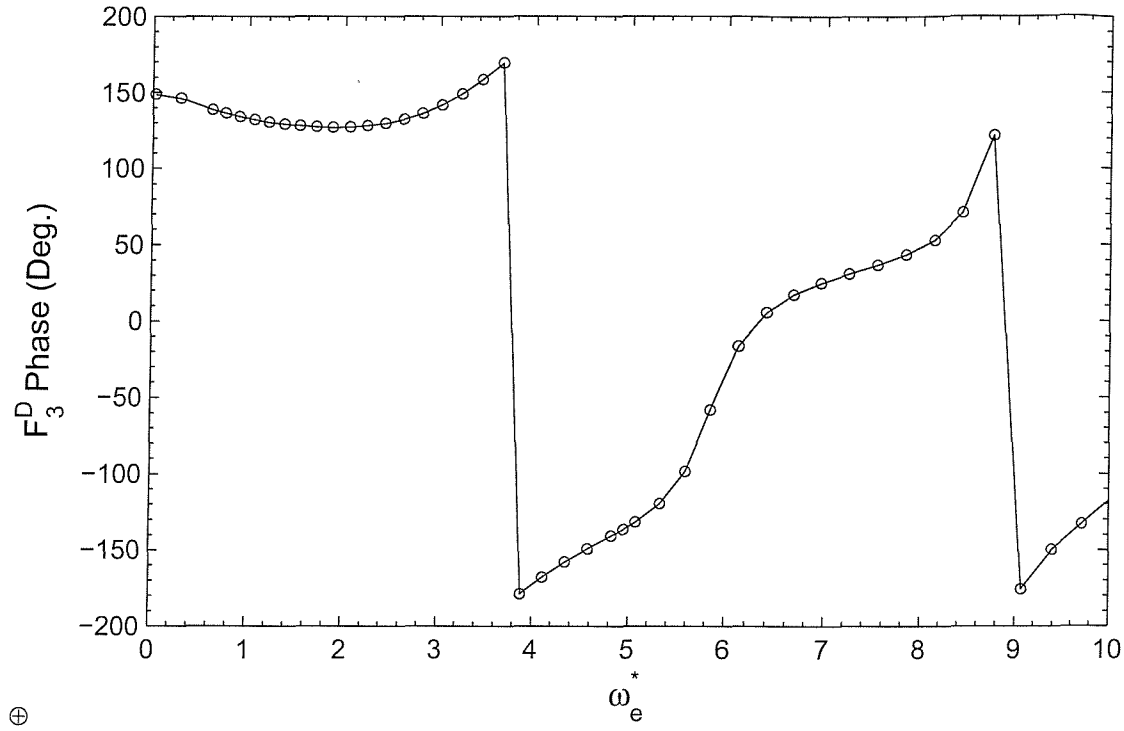

(a) Heave

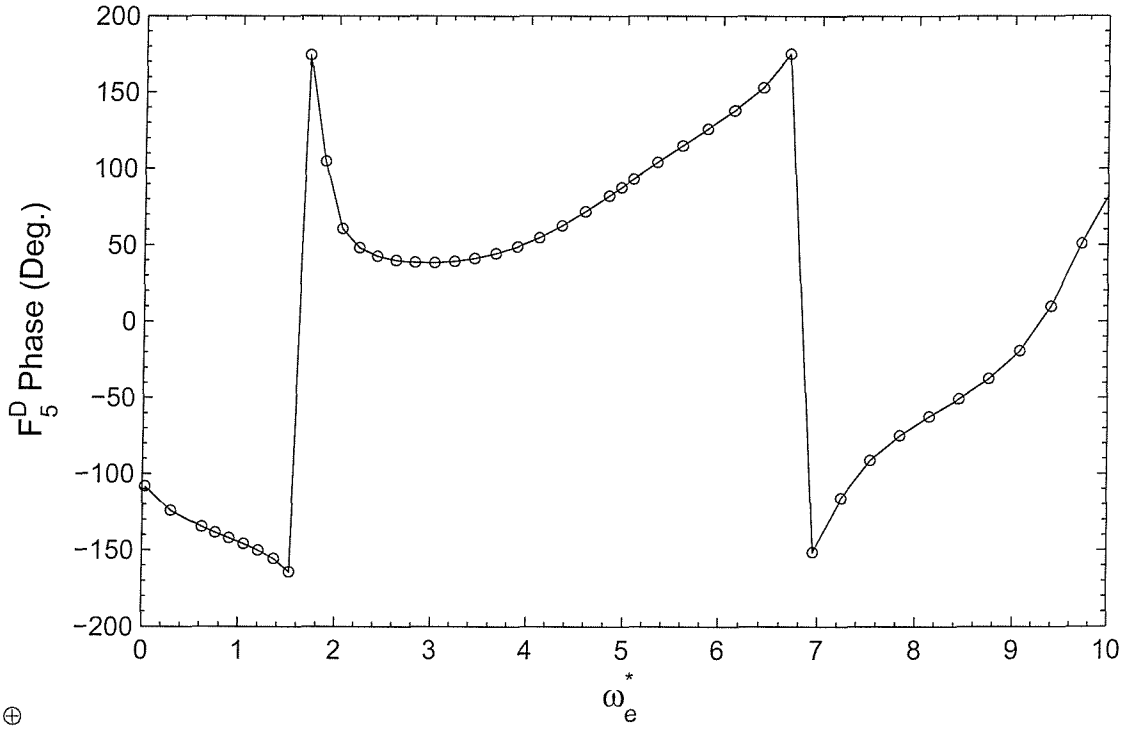

(b) Pitch

Figure 5.4: *Phases of Diffraction Forces of a Series 60 ($C_B = 0.7$) Model Travelling with Forward Speed $F_n = 0.2$.*

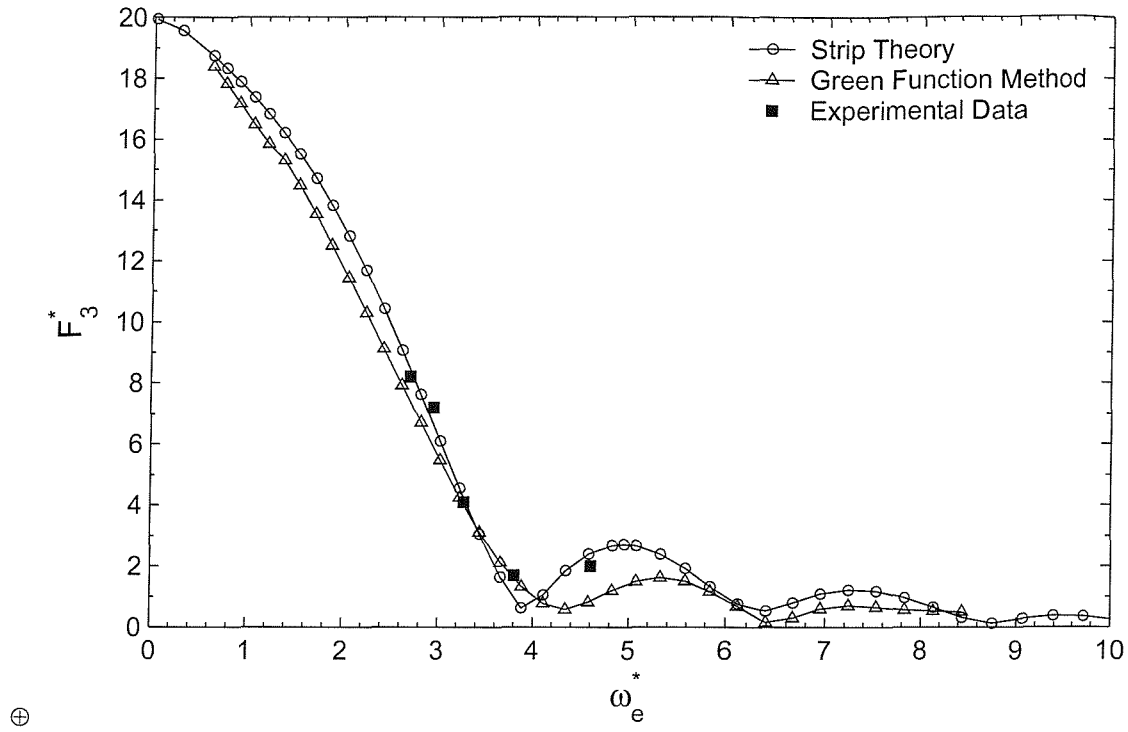

(a) Heave

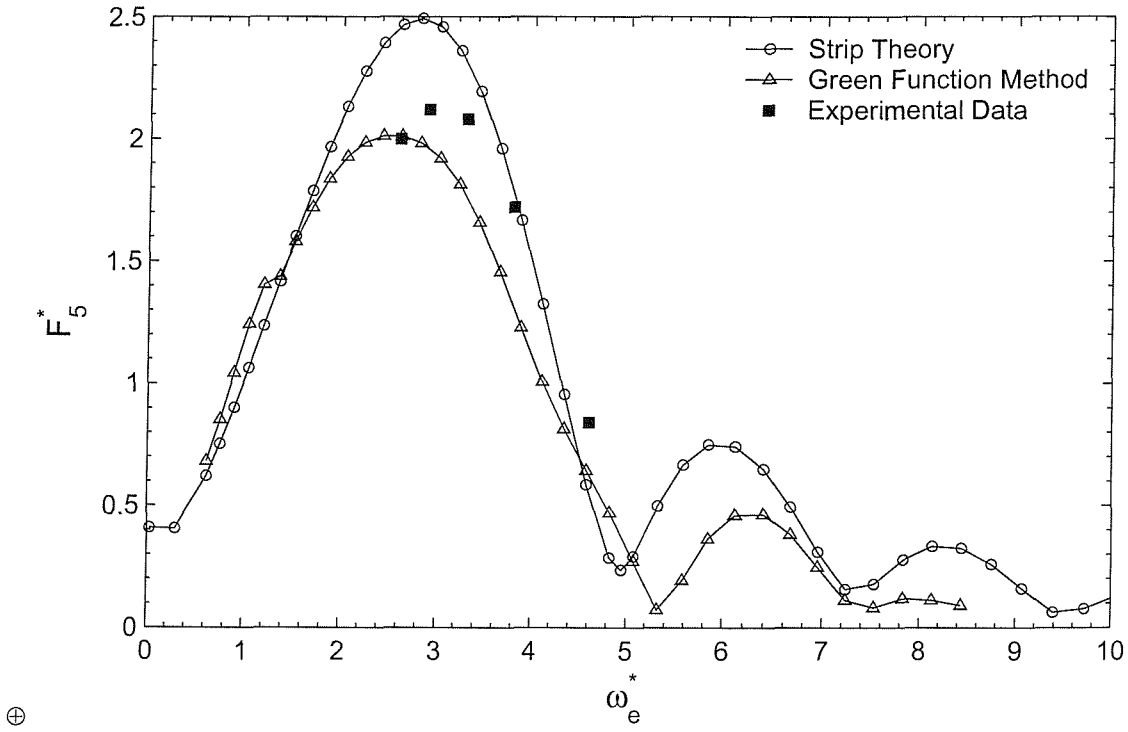

(b) Pitch

Figure 5.5: *Total Exciting Forces of a Series 60 ($C_B = 0.7$) Model Travelling with Forward Speed $F_n = 0.2$.*

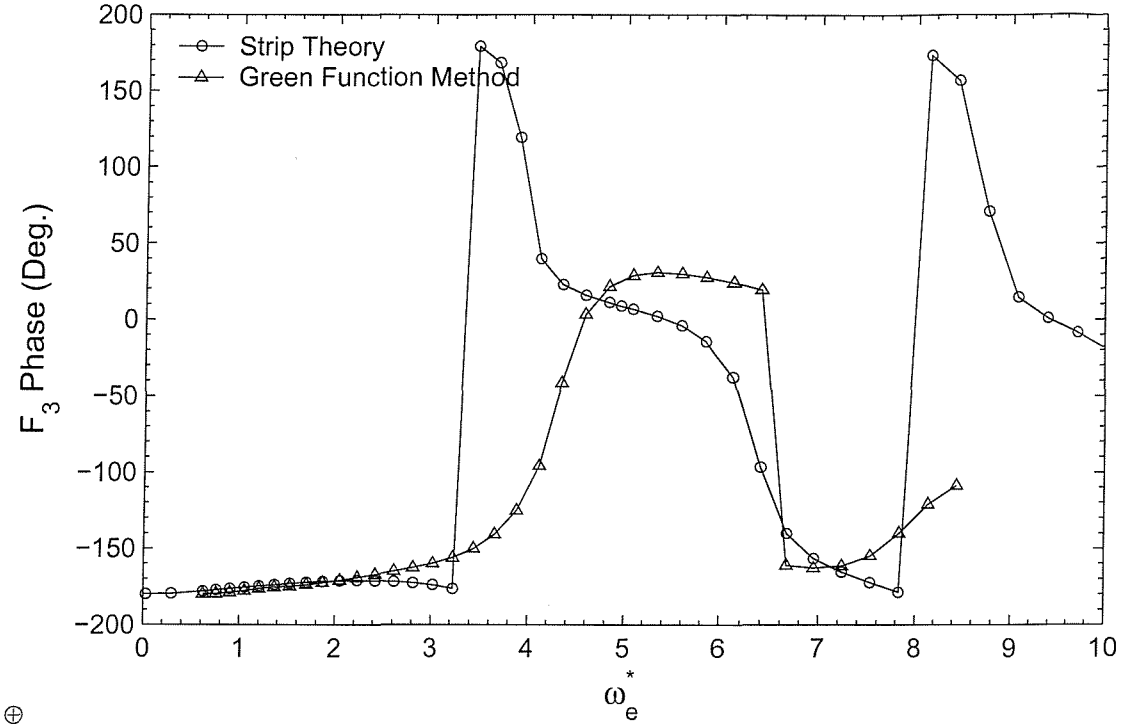

(a) Heave

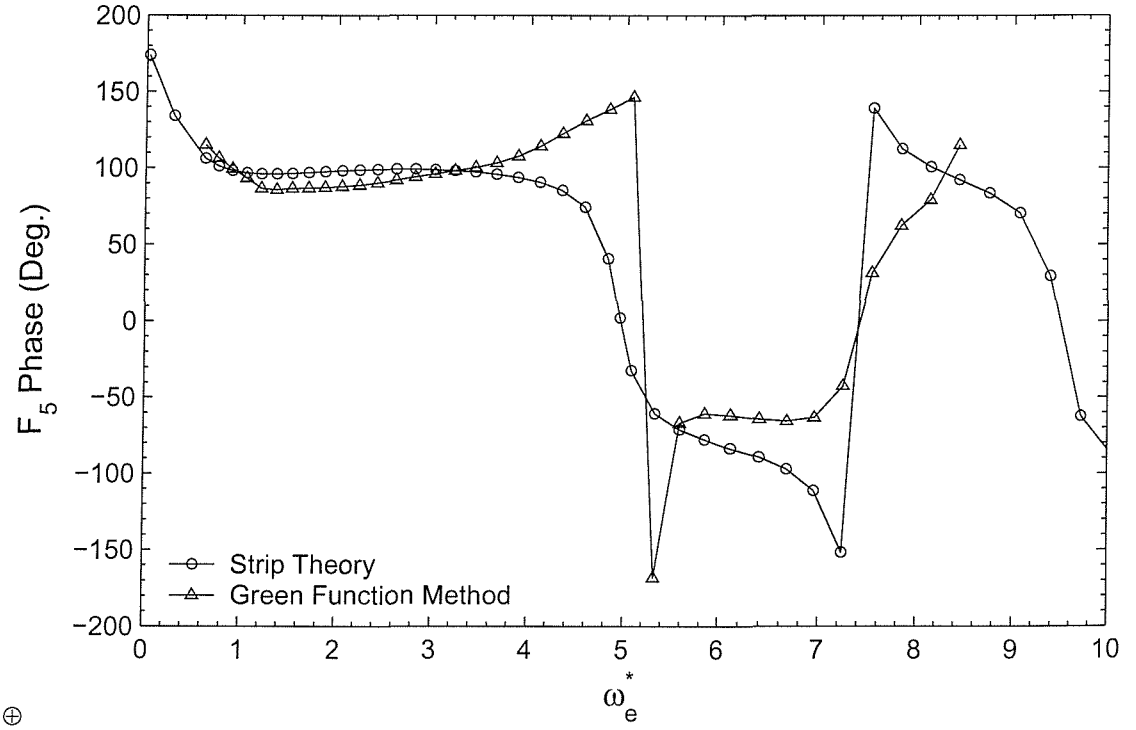

(b) Pitch

Figure 5.6: *Phases of Total Exciting Forces of a Series 60 ($C_B = 0.7$) Model Travelling with Forward Speed $F_n = 0.2$.*

in many texts. The time dimension is represented by a set of discrete points each a time increment Δt apart. The system is solved at each of these points in time using as data the solution at a previous time. The value of a function ξ at time t and $t + \Delta t$ will be denoted by $\xi(t) = \xi^{(t)}$ and $\xi(t + \Delta t) = \xi^{(t+\Delta t)}$ respectively. The standard forms of Newmark's equations for problem (3.194) are

$$\xi_i^{(t+\Delta t)} = \xi_i^{(t)} + \Delta t \dot{\xi}_i^{(t)} + (\frac{1}{2} - \beta)\Delta t^2 \ddot{\xi}_i^{(t)} + \beta \Delta t^2 \ddot{\xi}_i^{(t+\Delta t)}, \tag{5.21}$$

$$\dot{\xi}_i^{(t+\Delta t)} = \dot{\xi}_i^{(t)} + (1 - \epsilon)\Delta t \ddot{\xi}_i^{(t)} + \epsilon \Delta t \ddot{\xi}_i^{(t+\Delta t)}. \tag{5.22}$$

where ϵ and β are parameters that can be determined to obtain integration accuracy and stability. When $\epsilon = 1/2$ and $\beta = 1/6$, relations (5.21) and (5.22) correspond to the linear acceleration method.

In addition to (5.21) and (5.22), for solution of the displacement, velocities and accelerations at time $t + \Delta t$, the ship motion equations (3.194) at time $t + \Delta t$ are also considered,

$$\left[M_{ji}^{(t+\Delta t)} + A_{ji}^{(t+\Delta t)}\right]\ddot{\xi}_i^{(t+\Delta t)} + B_{ji}^{(t+\Delta t)}\dot{\xi}_i^{(t+\Delta t)} + C_{ji}\xi_i^{(t+\Delta t)} = F_j^{E(t+\Delta t)}, \tag{5.23}$$

where $F_j^{E(t+\Delta t)}$ are the exciting forces,

$$F_j^{E(t+\Delta t)} = \Re\left[F_j^{I(t+\Delta t)} + F_j^{D(t+\Delta t)}\right]. \tag{5.24}$$

Solving Equation (5.21) for $\ddot{\xi}_i^{(t+\Delta t)}$ in terms of $\xi_i^{(t+\Delta t)}$, and then substituting for $\ddot{\xi}_i^{(t+\Delta t)}$ into (5.22) gives

$$\dot{\xi}_i^{(t+\Delta t)} = \frac{\epsilon}{\beta \Delta t}\xi_i^{(t+\Delta t)} - \frac{\epsilon}{\beta \Delta t}\xi_i^{(t)} + \left(1 - \frac{\epsilon}{\beta}\right)\dot{\xi}_i^{(t)} + \left(1 - \frac{\epsilon}{2\beta}\right)\Delta t \ddot{\xi}_i^{(t)}. \tag{5.25}$$

The substation of Equations (5.21) and (5.25) into the Equation (5.23) provides an

expression from which the displacement at the time $t + \Delta t$ can be determined,

$$\left[\frac{M_{ji}^{(t)} + A_{ji}^{(t)}}{\beta \Delta t^2} + \frac{\epsilon B_{ji}^{(t)}}{\beta \Delta t} + C_{ji}\right] \xi_i^{(t+\Delta t)} = F_j^{E(t+\Delta t)} + \left[\frac{M_{ji}^{(t)} + A_{ji}^{(t)}}{\beta \Delta t^2} + \frac{\epsilon B_{ji}^{(t)}}{\beta \Delta t}\right] \xi_i^{(t)} + \left[\frac{M_{ji}^{(t)} + A_{ji}^{(t)}}{\beta \Delta t} + \frac{(\epsilon - \beta) B_{ji}^{(t)}}{\beta}\right] \dot{\xi}_i^{(t)} + \left[\frac{(1 - 2\beta)(M_{ji}^{(t)} + A_{ji}^{(t)})}{2\beta} + \frac{(\epsilon - 2\beta) \Delta t B_{ji}^{(t)}}{2\beta}\right] \ddot{\xi}_i^{(t)}. \quad (5.26)$$

Since $M_{ji}^{(t+\Delta t)}$, $A_{ji}^{(t+\Delta t)}$ and $B_{ji}^{(t+\Delta t)}$ in Equation (5.23) are unknown at the time $t + \Delta t$, they are replaced by $M_{ji}^{(t)}$, $A_{ji}^{(t)}$ and $B_{ji}^{(t)}$ respectively when deriving the Equation (5.26). $\ddot{\xi}_i^{(t+\Delta t)}$ and $\dot{\xi}_i^{(t+\Delta t)}$ can also be calculated using Equations (5.21) and (5.22), after obtaining $\xi_i^{(t+\Delta t)}$.

The Newmark method is second order accurate and depends on two real parameters ϵ and β. The parameter values are directly linked to accuracy and stability of Newmark integration method (Figure (5.7)). The classical values are given by Bathe [2] and Burnett [8]:

i. $\beta = 0$, $\epsilon = 1/2$: Newmark method is identical to the central difference method (conditionally stable);

ii. $\beta = 1/4$, $\epsilon = 1/2$: This choice of parameters corresponds to a trapezoidal rule (unconditionally stable method in linear analyses). It leads to a constant average acceleration;

iii. $\beta = 1/6$, $\epsilon = 1/2$: Newmark method is identical to the linear acceleration method (conditionally stable);

iv. $\beta = 1/12$, $\epsilon = 1/2$: Newmark method is identical to Fox-Goodwin method, which is fourth order accurate (conditionally stable).

The stability of an integration method is determined by examining the behaviour of the numerical solution for arbitrary initial conditions. An integration

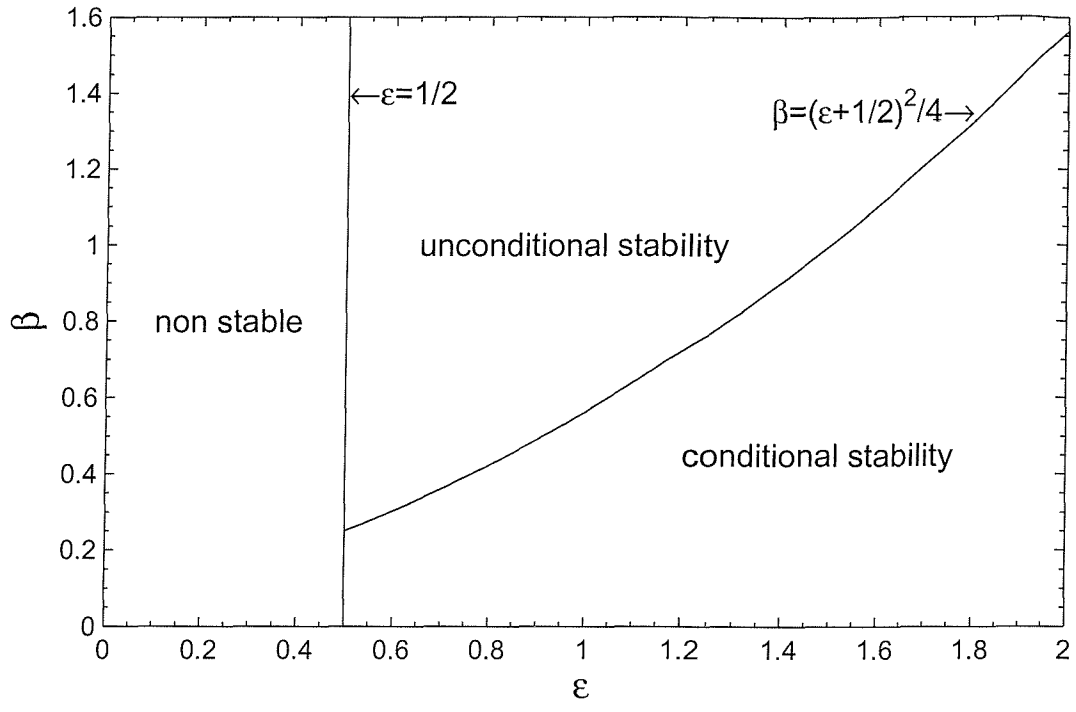

Figure 5.7: *Stability of Newmark Direct Integration Method.*

method is unconditionally stable if the solution for any initial conditions does not grow without bound for any time step Δt. The method is only conditionally stable if the above only holds provided that Δt is smaller than a certain value, usually called the stability critical time step Δt_{cr}. As mentioned before, the coefficients of the ship motion equations (3.194) are not constants and therefore it is difficult to determine the critical time step Δt_{cr} in advance. Therefore, to ensure the numerical stability, parameters $\beta = 1/4$, $\epsilon = 1/2$ are used. Bathe and Wilson [2] also proved that the method corresponding to $\beta = 1/4$, $\epsilon = 1/2$ has the most desired accuracy characteristics.

If conditionally stable parameters such as $\beta = 1/6$, $\epsilon = 1/2$ are employed, the time step size Δt, and hence the number of time steps for a given time range considered, is determined by the critical time step Δt_{cr}, and not much choice is available. However, using unconditionally stable parameters, the time step Δt has to be chosen to yield an accurate and effective solution. The errors in the

integration can be measured in terms of period elongation and amplitude decay. The relationships between the errors and the the time step Δt are obtained by comparing the exact solution with the numerical solutions. However, only for some simple problems, can the exact solutions be found. Therefore, the unforced heave and pitch motion equations (5.27) and (5.28) are considered here,

$$(m + A_{33})\ddot{\xi}_3 + B_{33}\dot{\xi}_3 + C_{33}\xi_3 + A_{35}\ddot{\xi}_5 + B_{35}\dot{\xi}_5 + C_{35}\xi_5 = 0, \tag{5.27}$$

$$(I_{22} + A_{55})\ddot{\xi}_5 + B_{55}\dot{\xi}_5 + C_{55}\xi_5 + A_{53}\ddot{\xi}_3 + B_{53}\dot{\xi}_3 + C_{53}\xi_3 = 0. \tag{5.28}$$

For a Series 60 ($C_B = 0.7$) ship model advancing in a head wave with a speed $F_n = 0.2$, the values of the coefficients in the Equations (5.27) and (5.28) are shown in Table (5.1). The wave frequency is chosen as $\omega_0 = 5.2\ rad/s$.

Coefficient	Value	Coefficient	Value
m	1.6564e-01	I_{22}	8.5001e-02
A_{33}	1.4308e-01	A_{55}	5.1314e-02
B_{33}	2.4269e-01	B_{55}	1.8727e-01
C_{33}	1.0413e+01	C_{55}	5.4837e+00
A_{35}	−3.9861e-03	A_{53}	3.8454e-03
B_{35}	2.4093e-01	B_{53}	−7.2330e-02
C_{35}	6.4735e-01	C_{53}	6.4735e-01

Table 5.1: *Values of the Coefficients of the Heave and Pitch Motion Equations.*

The exact solutions for the ordinary differential equations (5.27) and (5.28)

are not difficult to be found as

$$\begin{aligned}
\xi_3 =& C_1^3 e^{-0.37272t}[-0.010407\cos(5.5641t) + 0.15536\sin(5.5641t)] + \\
& C_2^3 e^{-0.37272t}[-0.010407\sin(5.5641t) - 0.15536\cos(5.5641t)] + \\
& C_1^3 e^{-0.69242t}[0.046407\cos(6.5434t) + 0.057606\sin(6.5434t)] + \\
& C_2^3 e^{-0.69242t}[0.046407\sin(6.5434t) - 0.057606\cos(6.5434t)],
\end{aligned} \tag{5.29}$$

$$\begin{aligned}
\xi_5 =& C_1^5 e^{-0.37272t}[0.073579\cos(5.5641t) - 0.038696\sin(5.5641t)] + \\
& C_2^5 e^{-0.37272t}[0.073579\sin(5.5641t) + 0.038696\cos(5.5641t)] + \\
& C_1^5 e^{-0.69242t}[-0.013762\cos(6.5434t) + 0.13005\sin(6.5434t)] + \\
& C_2^5 e^{-0.69242t}[-0.013762\sin(6.5434t) - 0.13005\cos(6.5434t)],
\end{aligned} \tag{5.30}$$

where C_1^3, C_2^3, C_1^5 and C_2^5 are constants determined by initial conditions. The exact and numerical solutions with initial conditions $\xi_3 = 0.1$, $\dot{\xi}_3 = 0$, $\xi_5 = 0$, $\dot{\xi}_5 = 0$ are drawn in Figure (5.8). The period elongation and amplitude decay increase with the integration time step Δt. In order to achieve the desired accuracy Δt has to be as small as $0.01s$, in the other words, $\Delta t \leq T/100$ (T is the period), which is used as a criteria for setting the integration time step in the time-domain motion program.

5.5 Motion Prediction in Head Seas

For ship with lateral symmetry hull form advancing in regular head waves, roll, sway and yaw are absent and the motions are confined to surge, heave and pitch. Surge motion is independent of all the other motions and therefore usually ignored in seakeeping calculations. The heave and pitch equations are coupled,

$$(m + A_{33})\ddot{\xi}_3 + B_{33}\dot{\xi}_3 + C_{33}\xi_3 + A_{35}\ddot{\xi}_5 + B_{35}\dot{\xi}_5 + C_{35}\xi_5 = \Re(F_3^I + F_3^D), \tag{5.31}$$

$$(I_{22} + A_{55})\ddot{\xi}_5 + B_{55}\dot{\xi}_5 + C_{55}\xi_5 + A_{53}\ddot{\xi}_3 + B_{53}\dot{\xi}_3 + C_{53}\xi_3 = \Re(F_5^I + F_5^D), \tag{5.32}$$

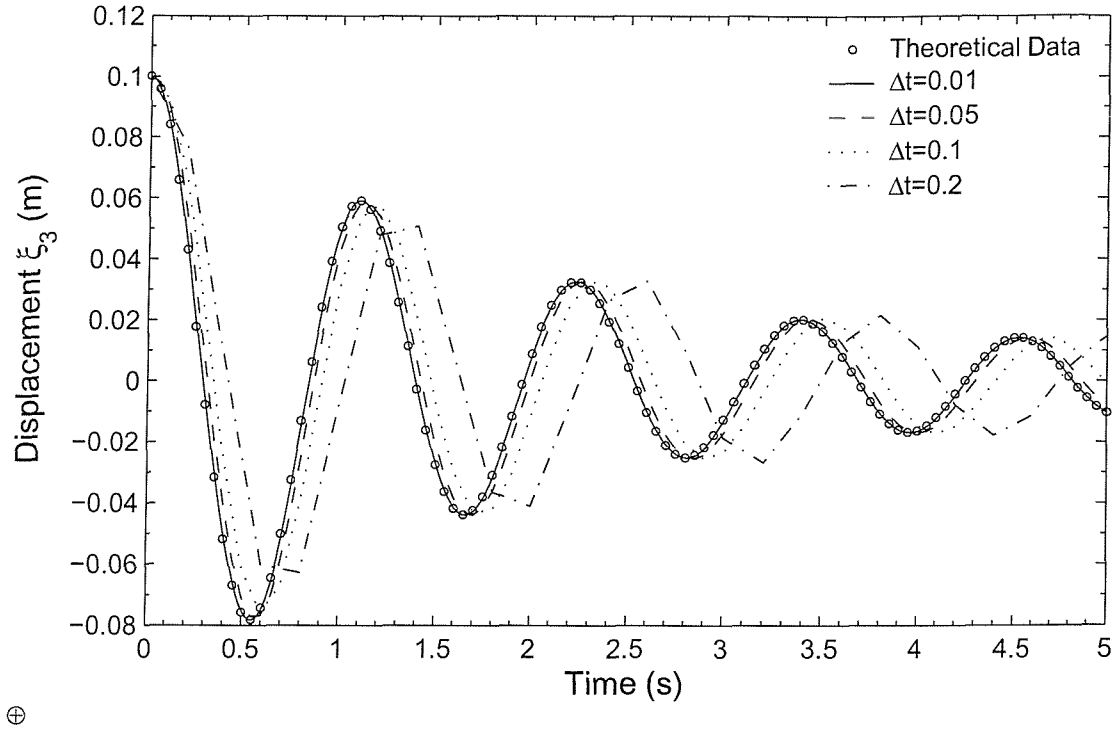

(a) Heave

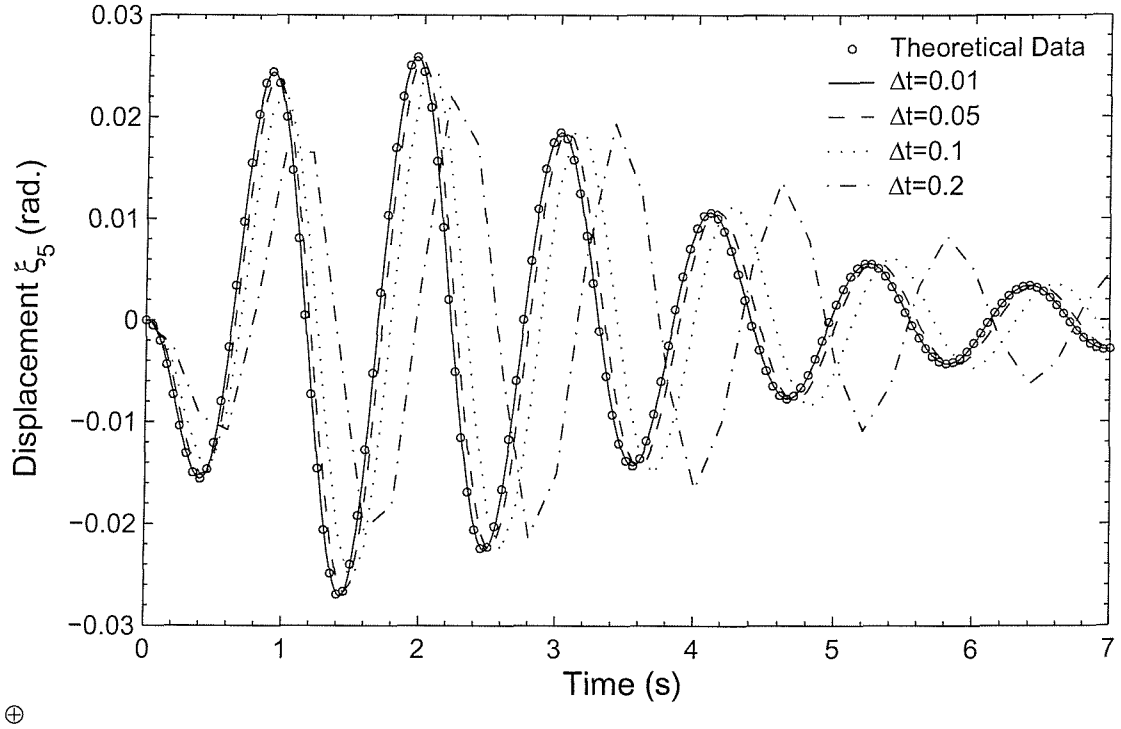

(b) Pitch

Figure 5.8: *Solutions of Unforced Motions.*

so that heave motions are influenced by pitch and vice versa.

The outputs of the time-domain strip theory program are the history (time series) of displacement, velocity and acceleration of each motion. Figure (5.9) shows the examples of displacement histories of heave and pitch motion of a Series 60 ($C_B = 0.7$) model travelling with forward speed $F_n = 0.2$ in a head wave ($\omega_0 = 4.0\ rad/s$). The model is at rest ($\xi_3 = 0$, $\dot{\xi}_3 = 0$, $\xi_5 = 0$, $\dot{\xi}_5 = 0$) at $t = 0$. It is clear that both heave and motion are sinusoidal in time and reach steady oscillatory state roughly after 4 cycles. The transient period is short, which may be because the time convolution term is omitted in the equations of motions, so that the initial condition can not effectively affect the motions afterwords. The results are very stable so that their amplitudes and phases can be found by being fitted with sinusoidal functions.

5.5.1 Curve Fitting with Sinusoidal Function

In this section the cosine function,

$$y(t) = A + B\cos(\omega_e t + \vartheta), \tag{5.33}$$

is fitted to the displacement, velocity and acceleration history of each motion. Since the ship motions are of the same frequency as the exciting forces, the angular frequency in the cosine function (5.33) is always the frequency of encounter ω_e. A is the height from abscissa to mean value, B is the amplitude, and ϑ is phase shift – distance in radians from $t = 0$ to starting point of the function new cycle. The phase shift can be removed by using trigonometric identity,

$$y(t) = A + C\cos(\omega_e t) + D\cos(\omega_e t), \tag{5.34}$$

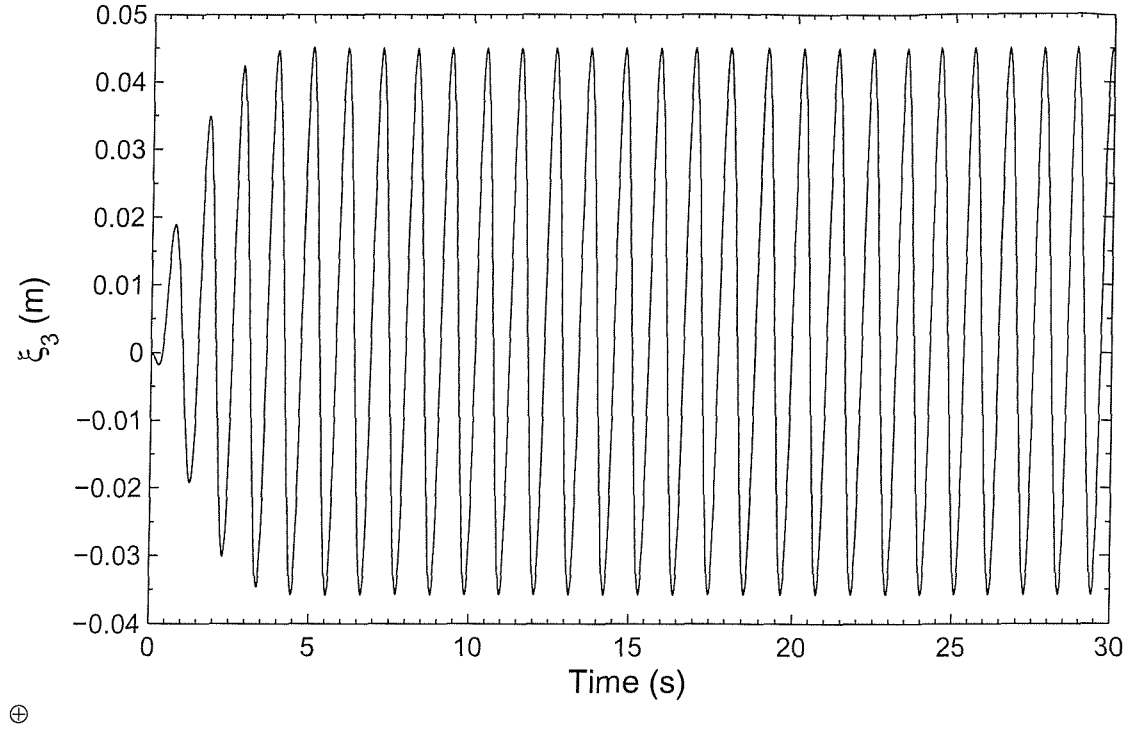

(a) Heave Displacement History

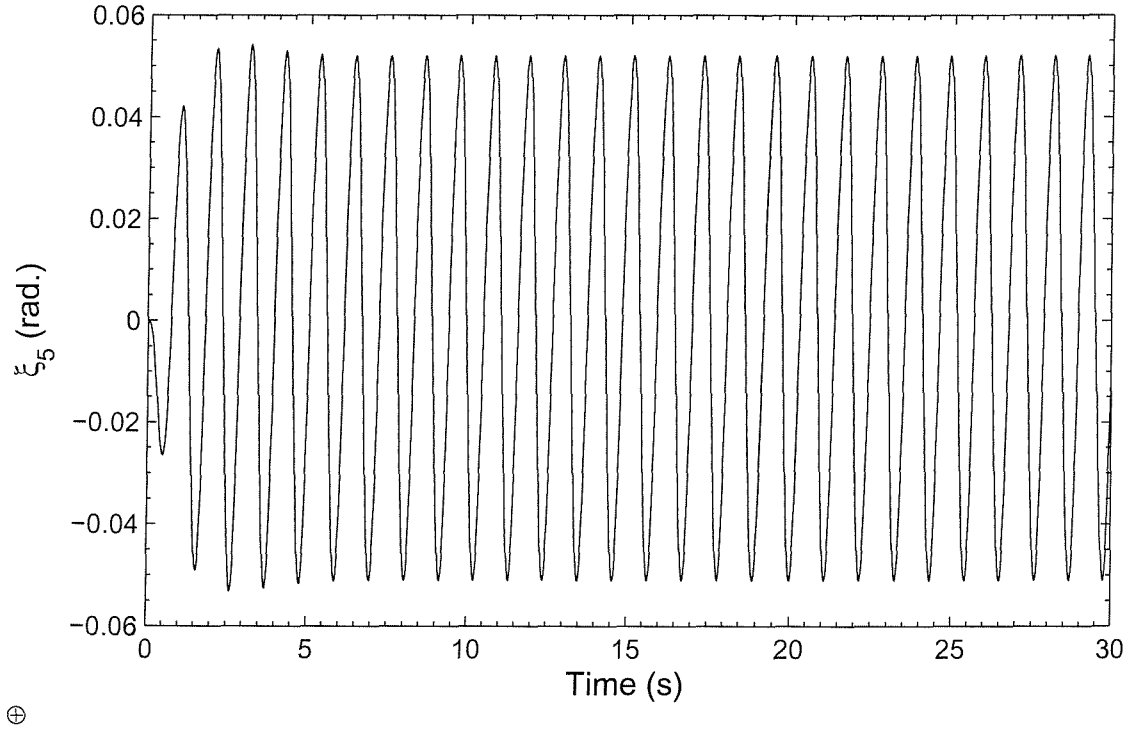

(b) Pitch Displacement History

Figure 5.9: *Motion Histories of a Series 60 ($C_B = 0.7$) Model Travelling with Forward Speed $F_n = 0.2$ in Head Waves ($\omega_0 = 4.0\ rad/s$).*

where

$$C = B\cos\vartheta, \tag{5.35}$$

$$D = -B\sin\vartheta, \tag{5.36}$$

$$\vartheta = \arctan(-D/C), \tag{5.37}$$

$$B = \sqrt{C^2 + D^2}. \tag{5.38}$$

Let $(\hat{y}_i, t_i)$, $i = 1, 2, \ldots, N_{th}$ be N_{th} data points in a given motion history (displacement, velocity or acceleration), the coefficients A, C and D of the fitted curve for this motion history are determined such that the total sum of the squares of the residuals,

$$S_r = \sum_{i=1}^{N_{th}} (y_i - \hat{y}_i)^2 = \sum_{i=1}^{N_{th}} [A + C\cos(\omega_e t_i) + D\cos(\omega_e t_i) - \hat{y}_i]^2, \tag{5.39}$$

is minimized. Taking partial derivative of S_r with respect to each of the unknown coefficients, and setting each resulting equation to zero gives three normal equations to solve for coefficient A, C and D,

$$\begin{pmatrix} N_{th} & \sum_{i=1}^{N_{th}} \cos(\omega_e t_i) & \sum_{i=1}^{N_{th}} \sin(\omega_e t_i) \\ \sum_{i=1}^{N_{th}} \cos(\omega_e t_i) & \sum_{i=1}^{N_{th}} \cos^2(\omega_e t_i) & \sum_{i=1}^{N_{th}} \cos(\omega_e t_i)\sin(\omega_e t_i) \\ \sum_{i=1}^{N_{th}} \sin(\omega_e t_i) & \sum_{i=1}^{N_{th}} \cos(\omega_e t_i)\sin(\omega_e t_i) & \sum_{i=1}^{N_{th}} \sin^2(\omega_e t_i) \end{pmatrix} \begin{pmatrix} A \\ C \\ D \end{pmatrix}$$
$$= \begin{pmatrix} \sum_{i=1}^{N_{th}} \hat{y}_i \\ \sum_{i=1}^{N_{th}} \hat{y}_i \cos(\omega_e t_i) \\ \sum_{i=1}^{N_{th}} \hat{y}_i \sin(\omega_e t_i) \end{pmatrix}. \tag{5.40}$$

This is known as the *least squares* technique.

However, if the N_{th} data points are equispaced at intervals of Δt and with

the total time length of $T = (N_{th} - 1)\Delta t = 2\pi/\omega_e$, it has

$$\frac{1}{N_{th}} \sum_{i=1}^{N_{th}} \sin(\omega_e t_i) = 0, \tag{5.41}$$

$$\frac{1}{N_{th}} \sum_{i=1}^{N_{th}} \cos(\omega_e t_i) = 0, \tag{5.42}$$

$$\frac{1}{N_{th}} \sum_{i=1}^{N_{th}} \sin^2(\omega_e t_i) = \frac{1}{2}, \tag{5.43}$$

$$\frac{1}{N_{th}} \sum_{i=1}^{N_{th}} \cos^2(\omega_e t_i) = \frac{1}{2}, \tag{5.44}$$

$$\frac{1}{N_{th}} \sum_{i=1}^{N_{th}} \sin(\omega_e t_i) \cos(\omega_e t_i) = 0. \tag{5.45}$$

Thus for equispaced data points Equation (5.40) becomes

$$\begin{pmatrix} N_{th} & 0 & 0 \\ 0 & N_{th}/2 & 0 \\ 0 & 0 & N_{th}/2 \end{pmatrix} \begin{pmatrix} A \\ C \\ D \end{pmatrix} = \begin{pmatrix} \sum_{i=1}^{N_{th}} \hat{y}_i \\ \sum_{i=1}^{N_{th}} \hat{y}_i \cos(\omega_e t_i) \\ \sum_{i=1}^{N_{th}} \hat{y}_i \sin(\omega_e t_i) \end{pmatrix}, \tag{5.46}$$

and coefficients A, C and D are easily solved.

Figure (5.10) shows the displacement histories of heave and pitch motion and the corresponding fitted cosine curves for a Series 60 ($C_B = 0.7$) model moving with forward speed $F_n = 0.2$ in a head wave. The frequency of encounter $\omega_e = 5.78401\ rad/s$. The values of the coefficients A, B and ϑ are listed in Table (5.2). Since only the amplitude and the phase angle of steady state oscillation are of importance, the transient process is excluded from curving fitting, *e.g.* the first 4 cycles in Figure (5.10(a)). It can be seen that equilibrium positions of both heave and pitch motion are not at 0, this is because the ship model is not perfectly balanced in calm water with the initial data given in the input file (*e.g.* draught, weight and centre of gravity). However it brings no error into the final results of amplitude and phase angle.

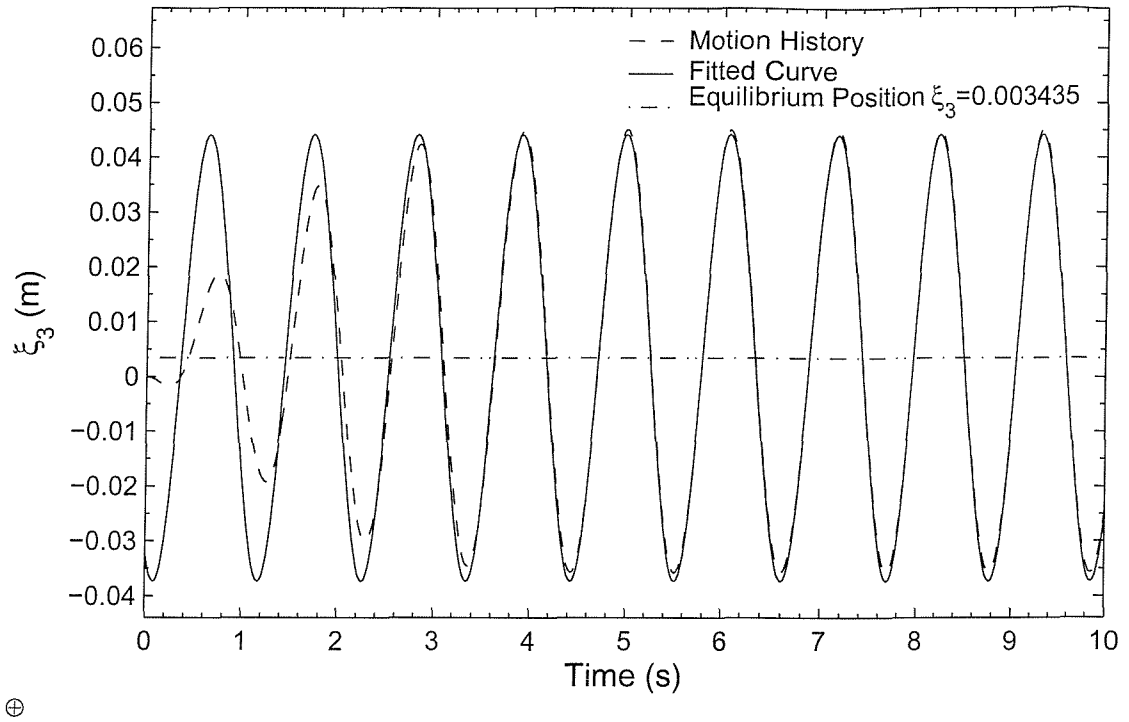

(a) Heave Displacement History

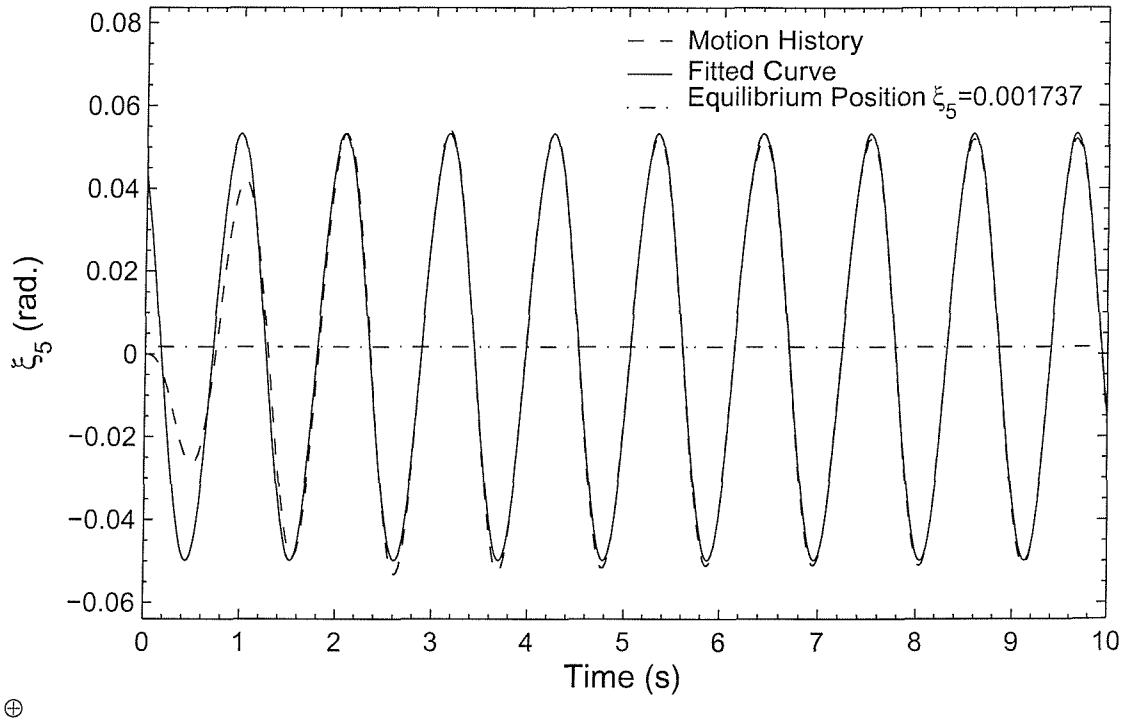

(b) Pitch Displacement History

Figure 5.10: *Displacement Histories and Corresponding Fitted Curves of a Series 60 ($C_B = 0.7$) Model Travelling with Forward Speed $F_n = 0.2$ in Head Waves ($\omega_0 = 4.0\ rad/s$).*

Motion	A	B	ϑ (rad.)
Heave Displacement	0.3435e-02	0.4077e-01	0.2637e+01
Pitch Displacement	0.1737e-02	0.5160e-01	0.6281e+00

Table 5.2: *Values of the Coefficients of the Fitted Curves of the Motion Histories of the Series 60 ($C_B = 0.7$) Model Travelling with Forward Speed $F_n = 0.2$ in Head Waves ($\omega_0 = 4.0\ rad/s$).*

5.5.2 Phasing of Displacement, Velocity and Acceleration

Phasing of displacement, velocity and acceleration may be used as a criteria to access the quality of predicted ship motions. Figure (5.11) shows displacement, velocity and acceleration history of predicted heave and pitch motion of a Series 60 ($C_B = 0.7$) model in a head wave ($\omega_0 = 4.0\ rad/s$). The forward speed is $2.1232\ knots$ ($F_n = 0.2$). The displacement results are scaled up by a factor of 5, whilst the acceleration results are scaled down by a factor of 5, so that they can be readily compared with the velocity results. Table (5.3) shows the values of the phase angles, where ϑ_ξ, $\vartheta_{\dot{\xi}}$ and $\vartheta_{\ddot{\xi}}$ represent the phase angles of displacement, velocity and acceleration respectively.

Phase Angle (rad.)		ϑ_ξ	$\vartheta_{\dot{\xi}}$	$\vartheta_{\ddot{\xi}}$	$\vartheta_\xi - \vartheta_{\dot{\xi}}$	$\vartheta_{\ddot{\xi}} - \vartheta_{\dot{\xi}}$
$F_n = 0.2$	Heave	2.637	4.183	-0.493	-1.546	-4.676
	Pitch	0.628	2.238	3.786	-1.610	1.548
$F_n = 0.3$	Heave	1.530	3.099	4.679	-1.569	1.580
	Pitch	0.081	1.667	3.223	-1.586	1.556

Table 5.3: *Phase Angles of the Motions of the Series 60 ($C_B = 0.7$) Model Travelling with Forward Speed $F_n = 0.2$ in Head Waves ($\omega_0 = 4.0\ rad/s$).*

The results demonstrate that the correct phasing of each motion is achieved. The acceleration always leads the velocity by about $\pi/2$, whilst the displacement

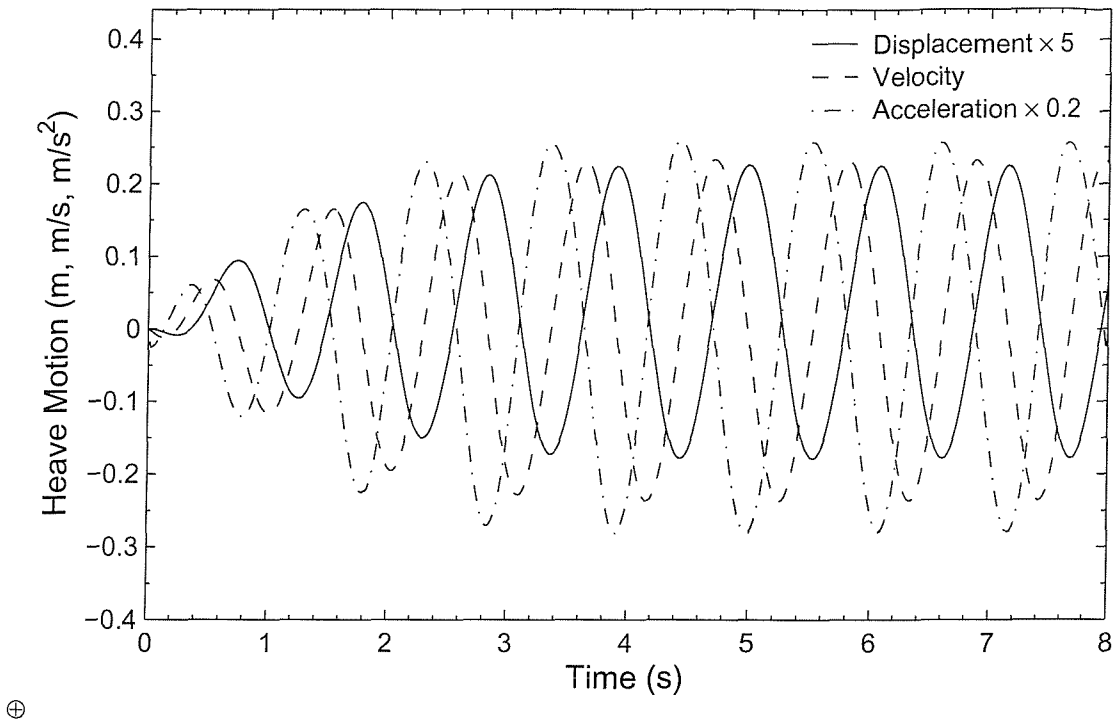

(a) Heave Motion Histories

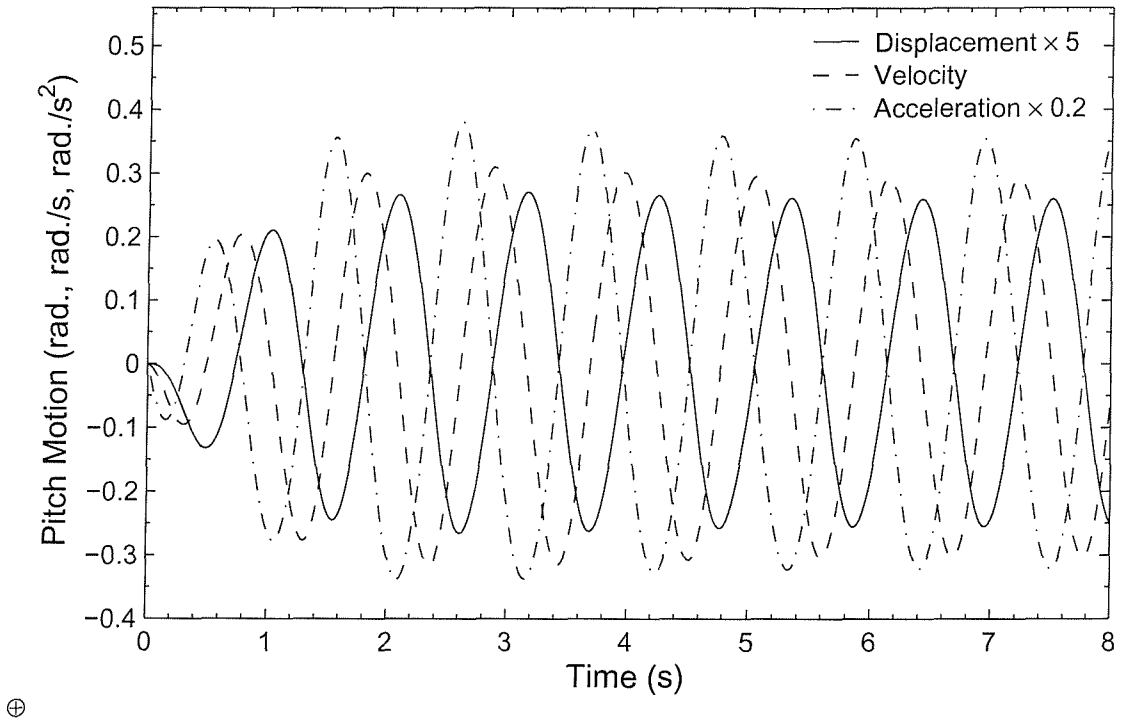

(b) Pitch Motion Histories

Figure 5.11: *Phasing of the Predicted Motions of a Series 60 ($C_B = 0.7$) Model Travelling with Forward Speed $F_n = 0.2$ in Head Waves ($\omega_0 = 4.0$ rad/s).*

lags the velocity by about $\pi/2$. This also further proves that the time stepping scheme (Newmark-β integration method) is accurate.

5.5.3 Comparisons with Experimental Data

Here the experimental data of a Series 60 ($C_B = 0.70$) ship model is chosen to validate this time-domain strip theory method, because Series 60 hull form has been extensively studied numerically and experimentally and a large amount of data is available. Figure (5.12) shows the comparisons of pitch and heave motion of a Series 60 ($C_B = 0.70$) ship model travelling at a Froude number of 0.2 in regular head waves. The experimental data measured for two different wave amplitudes ($\eta_0 = L_{ship}/100$ and $\eta_0 = L_{ship}/80$) were given by Gerritsma and Beukelman [21]. The numerical results with legend "Calculation of Gerritsma" are also taken from the work of Gerritsma and Beukelman [21]. Three-dimensional numerical results are presented with legend "Green Function Method", which are produced by frequency-domain Green function method [24] using 510 panels. Incident wave amplitude η_0 is set to be $L_{ship}/100$ in the computation using time-domain strip theory. ξ_3^* and ξ_5^* are non-dimensional heave and pitch motion, ω_e^* is the non-dimensional frequency of encounter,

$$\xi_3^* = \xi_3/\eta_0, \tag{5.47}$$

$$\xi_5^* = \xi_5/(\eta_0 K_0), \tag{5.48}$$

$$\omega_e^* = \omega_e\sqrt{L_{ship}/g}, \tag{5.49}$$

where L_{ship} is the ship length between perpendiculars, η_0 is the amplitude of the incident wave, and K_0 is wave number.

For the heave motion shown in Figure (5.12(a)), predictions given by time-domain strip theory are extremely close to the experimental data over whole fre-

quency range, and slightly better than the results of Gerritsma and Beukelman in the low frequency range, *i.e.* $\omega_e^* \leq 3.5$. Three-dimensional Green function method gives much worse predictions in the frequency range near resonance.

Figure (5.12(b)) shows time-domain strip theory does not give as good predictions for pitch motion as those for heave motion. It tends to under-predict around the resonant frequency, whilst Green function method very much over-predicts. This may be due to the difference in predictions of damping coefficient B_{55}. Figure (4.36(b)) shows that in the low frequency range ($\omega_e^* \leq 4.0$) the damping coefficients B_{55} given by time-domain strip theory are always higher than experimental data, while those given by Green function method are lower than experimental data.

At a Froude number of 0.3, time-domain strip theory still gives excellent predictions of heave motion as shown in Figure (5.13(a)). In the low frequency range, time-domain strip theory obviously performs much better then the strip theory used by Gerritsma and Beukelman. Figure (5.13(b)) shows that theoretical results and experimental data of pitch motion are in reasonable close agreement. Resonance can be found near the frequency $\omega_e^* \approx 3.5 - 3.7$.

Generally speaking, the predictions of pitch motion given by time-domain strip theory are not as good as the predictions of heave motion at both speeds. However, in the high frequency range the predictions are excellent, which confirms that strip theory indeed is a short wave length theory. The reason can be found in §3.4.4, where in order to simplify the calculation of radiation wave potential the frequency of encounter ω_e is assumed to be hight, $\omega_e \gg U(\partial/\partial x)$.

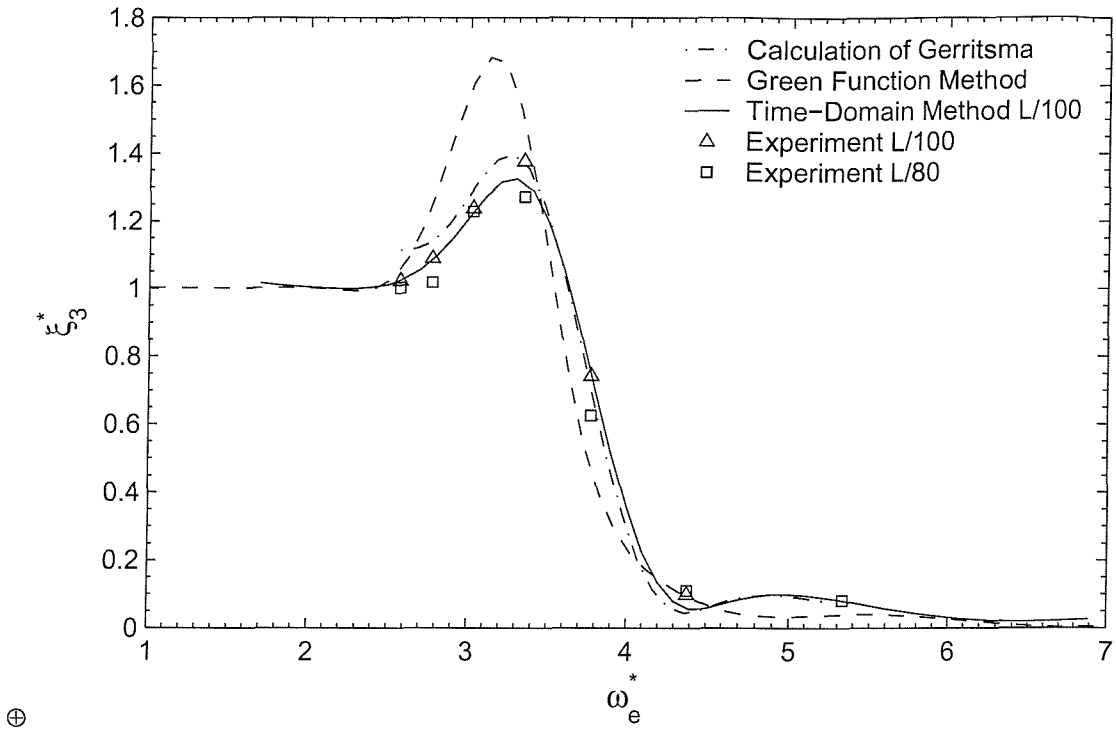

(a) Heave

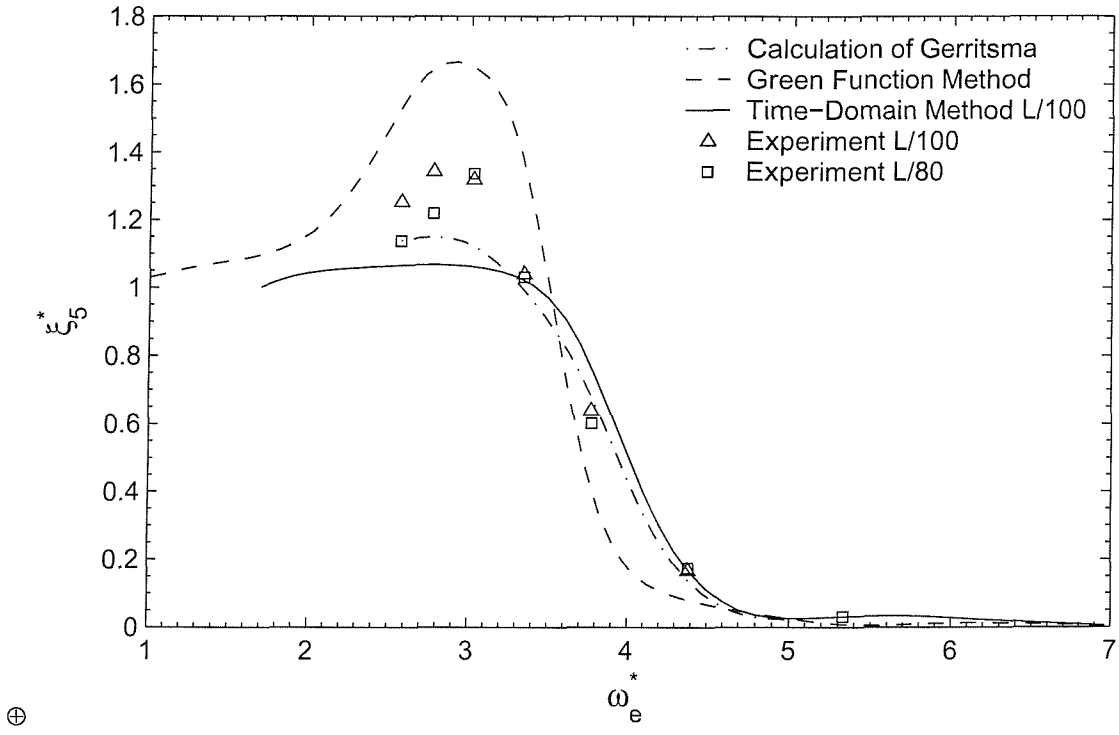

(b) Pitch

Figure 5.12: *Comparison of the Motions of a Series 60 ($C_B = 0.7$) Model Travelling with Forward Speed $F_n = 0.2$ in Head Waves.*

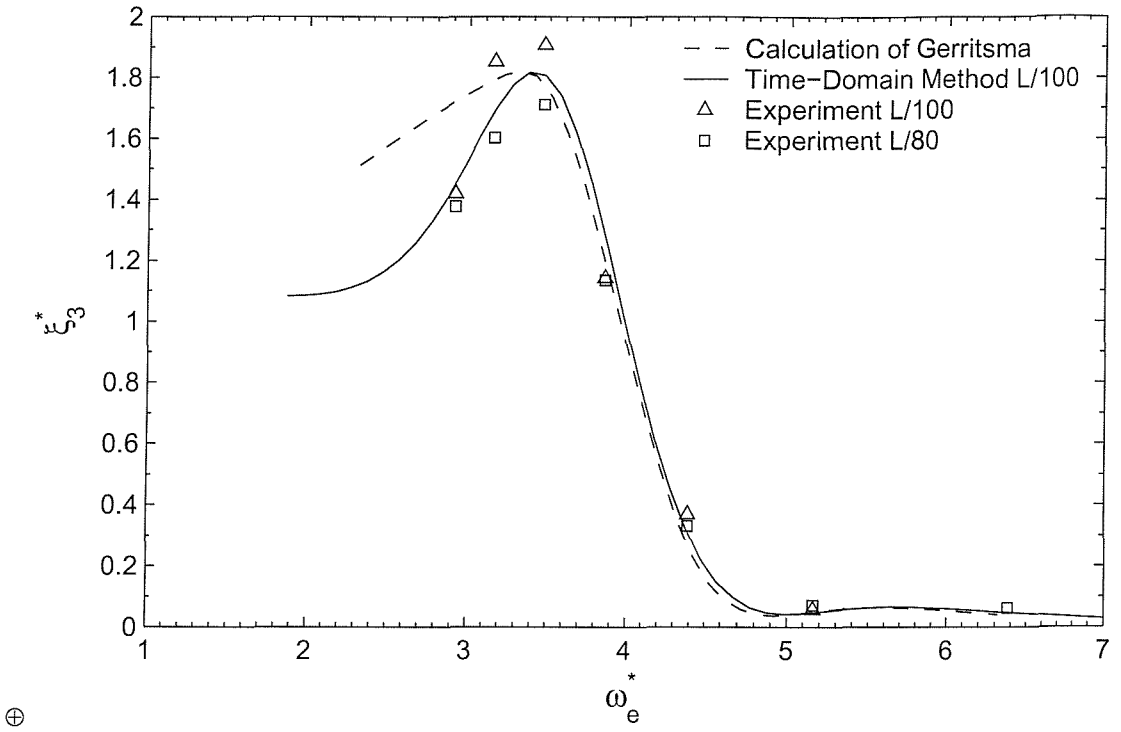

(a) Heave

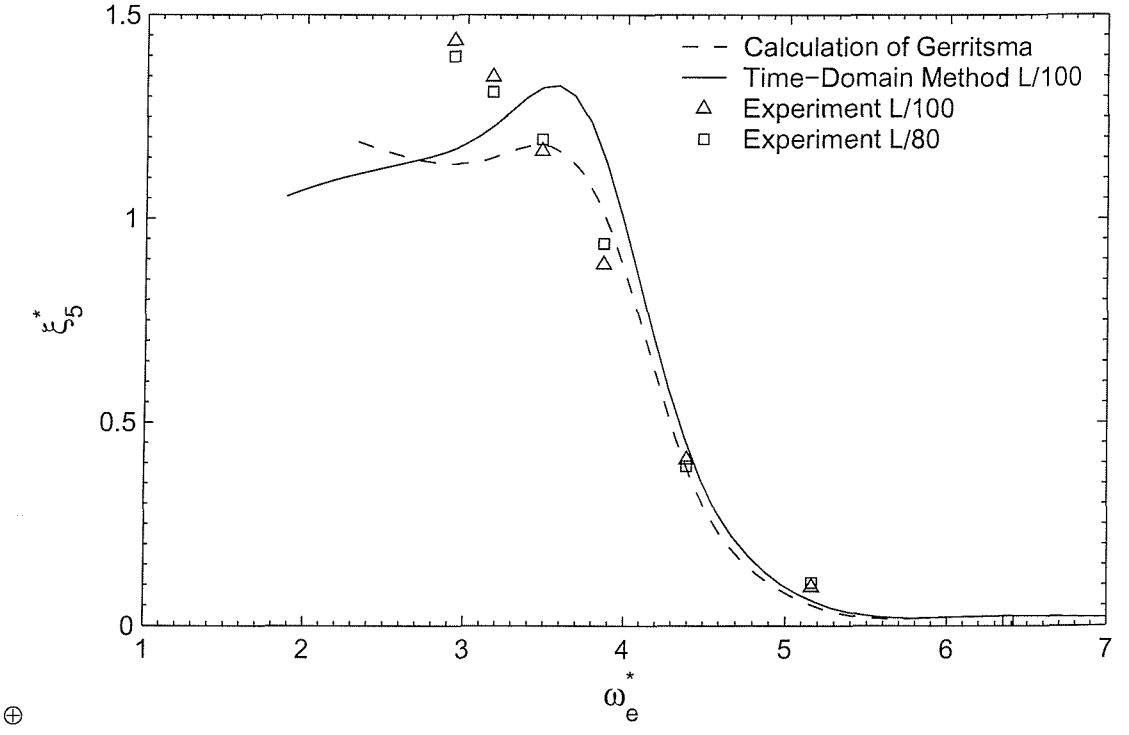

(b) Pitch

Figure 5.13: *Comparison of the Motions of a Series 60 ($C_B = 0.7$) Model Travelling with Forward Speed $F_n = 0.3$ in Head Waves.*

5.5.4 Effect of the Incident Wave Amplitude

The essential objective of this thesis is to extend the traditional linear strip theory to deal with large-amplitude motions by encompassing the changing shape of the wetted hull. Therefore RAOs of ship motions are expected to vary with the incident wave amplitude.

Figures (5.14) and (5.15) show heave and pitch RAOs of a Series 60 ship model moving in head waves with forward speed $F_n = 0.2$ and $F_n = 0.3$, respectively. Non-linearities, although not very prominent, can be found in both heave and pitch motions, particularly in the resonant frequency range.

5.6 Motion Prediction in Oblique Seas

In oblique waves the ship motions are no longer confined to the vertical plane. Roll, sway and yaw motions also occur. However, the vertical plane equations of motion for the symmetrical ship are independent of those for the lateral plane. So the lateral plane motions in oblique waves of small amplitude will have no effect on the vertical plane motions and these may therefore be considered in isolation. Suppressing roll, sway and yaw motions, heave and pitch motions predicted by time-domain strip theory, together with the experimental data, are shown in Figure (5.16). The incident wave amplitude $\eta_0 = L_{ship}/100$, and the heading angle $\mu = 135°$.

The predictions of lateral plane motions in the time domain seem quite problematic. One of the important reasons is the lack of restoring forces for the sway and yaw motions. Small perturbations in these motions will result in the ship being deviated from its original course. If there are no means to correct this false action, the program eventually will malfunction. For a Series 60 ($C_B = 0.7$) ship

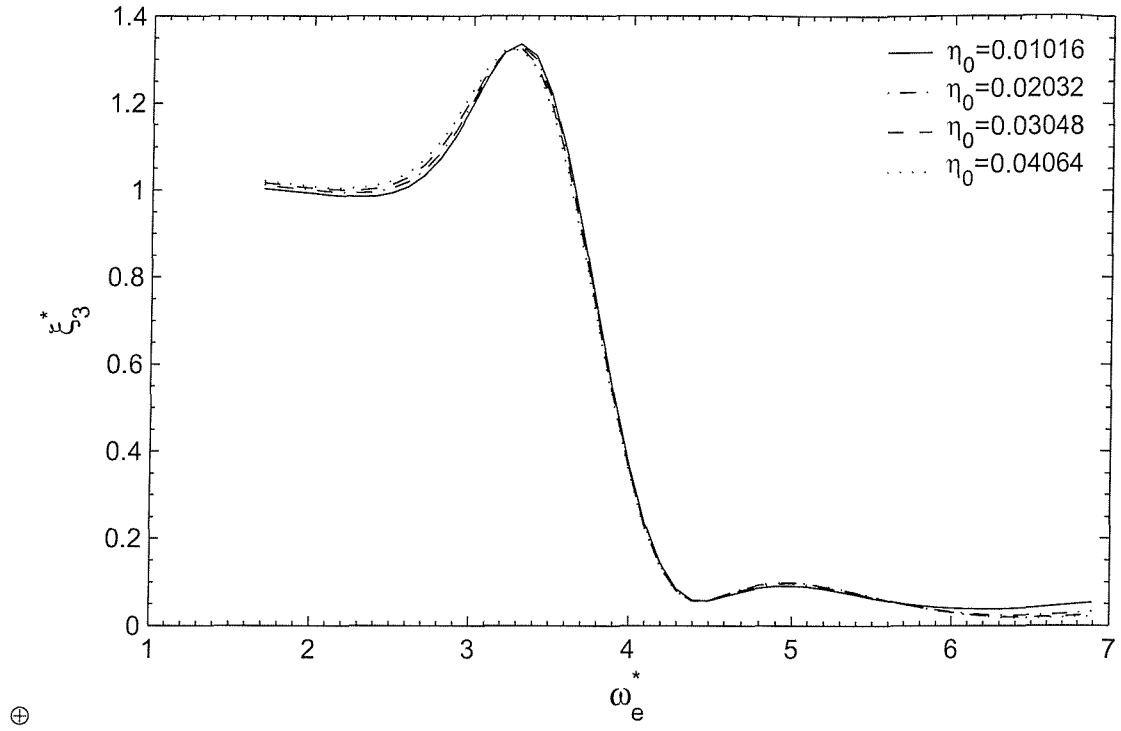

(a) Heave

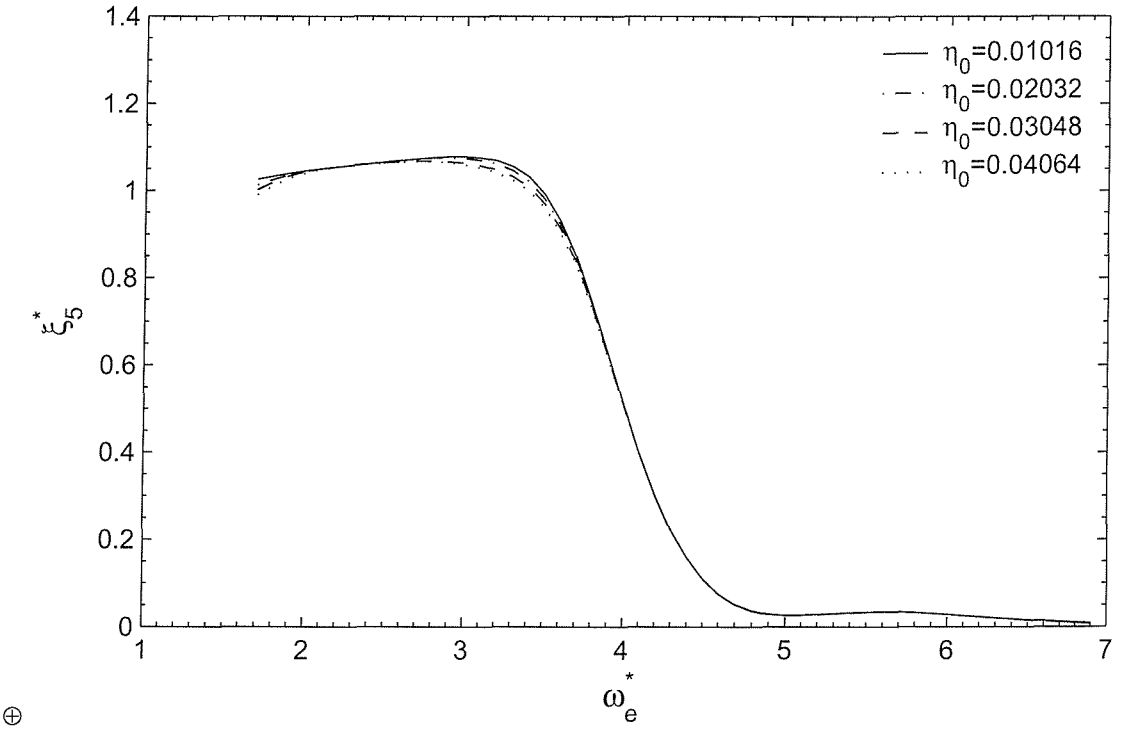

(b) Pitch

Figure 5.14: *Effect of Wave Amplitude on the Motions of a Series 60 ($C_B = 0.7$) Model Travelling with Forward Speed $F_n = 0.2$ in Head Waves.*

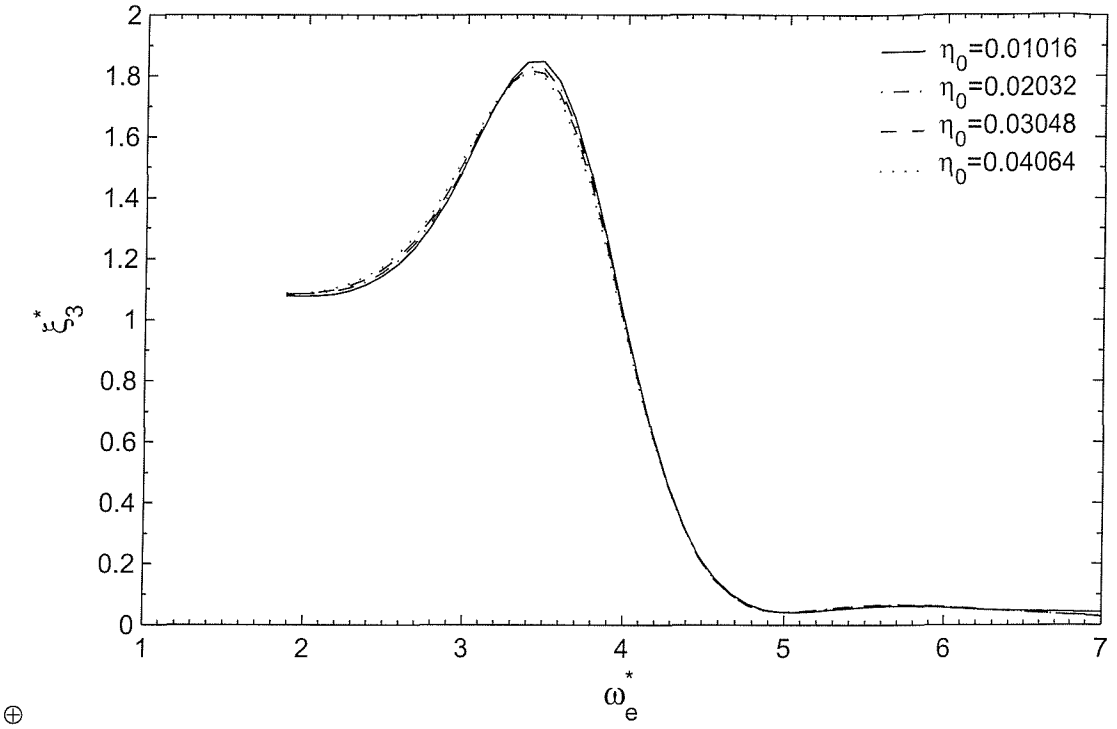

(a) Heave

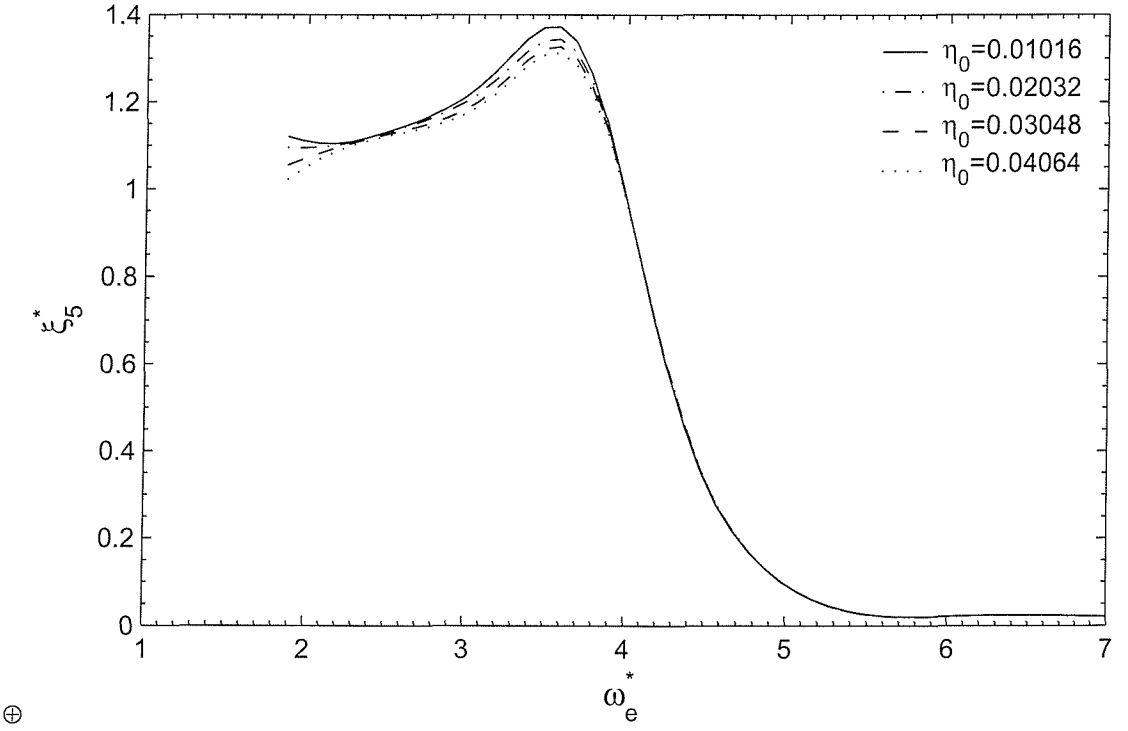

(b) Pitch

Figure 5.15: *Effect of Wave Amplitude on the Motions of a Series 60 ($C_B = 0.7$) Model Travelling with Forward Speed $F_n = 0.3$ in Head Waves.*

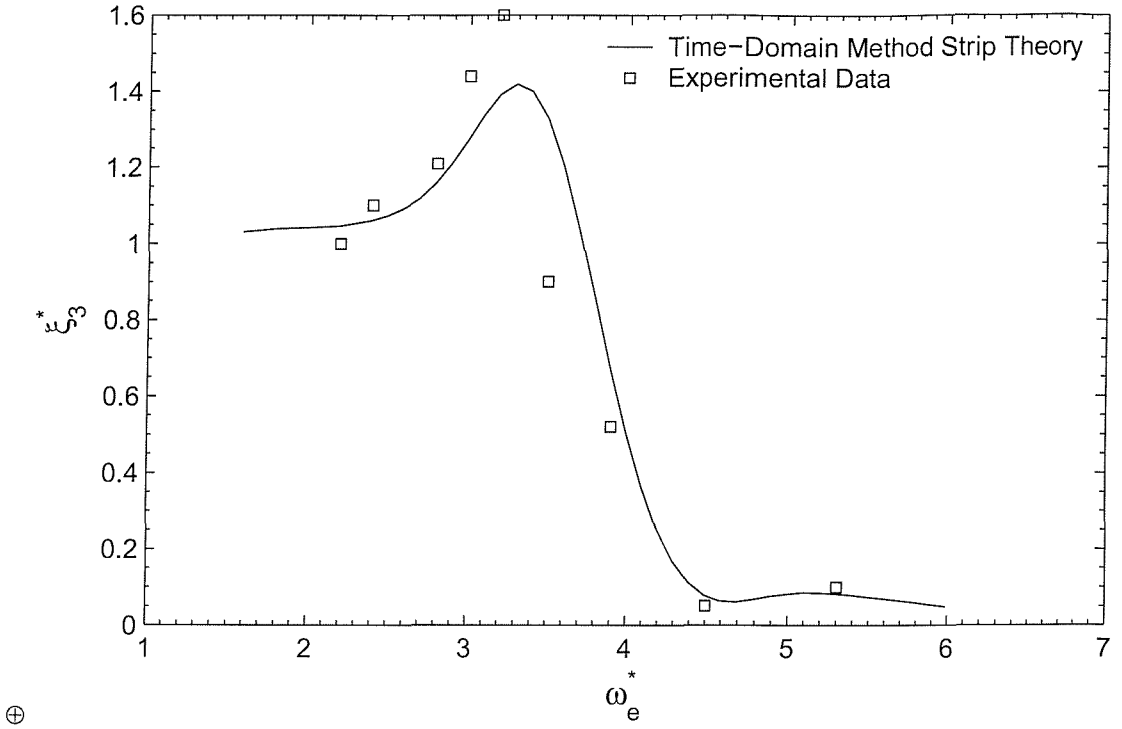

(a) Heave

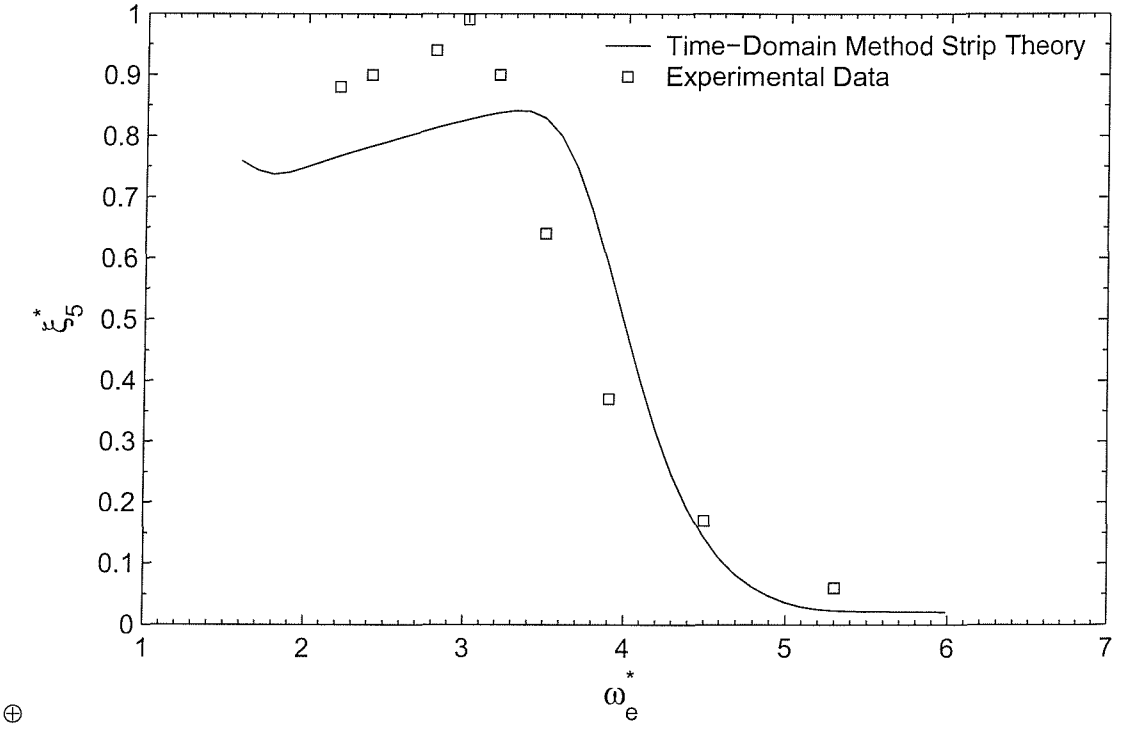

(b) Pitch

Figure 5.16: *Comparison of the Motions of a Series 60 ($C_B = 0.7$) Model Travelling with Forward Speed $F_n = 0.2$ in Oblique Waves ($\mu = 135°$).*

model advancing in oblique sea ($\omega_0 = 4.0$ and heading angle $\mu = 135°$), this process is clearly illustrated in Figures (5.17(a)) and (5.17(e)). The drift of yaw motion results in the change of heading angle. Therefore oscillatory amplitude of roll motion increases quickly after a short period of simulation time, meanwhile amplitude of pitch motion decrease gradually. This is shown in Figure (5.17(c)) and Figure (5.17(d)) respectively. Figure (5.17(b)) indicates that heave motion is not as sensitive to the heading angle as roll and pitch motions.

Figure (5.18) shows the motions of the same ship model in beam waves. Drifts of sway and yaw motion are inevitable. In contrast to the trends in quartering waves, the amplitude of roll motion decreases after transient period and the amplitude of pitch motion increases.

Salvesen, *et al* [56] pointed out that, in the case of sway, yaw and roll motion, the added-mass and damping coefficients are significantly affected by viscosity, especially the roll-damping coefficient B_{44} even in the absence of bilge keels. Hence, the necessary correction of roll-damping coefficient must be made to take account of the viscous effect. However, it needs an iterative computational process which is difficult to implement in the time stepping scheme. So the roll motions shown in all figures are computed with un-corrected roll-damping coefficient. Undoubtedly, the prediction does not agree well with reality.

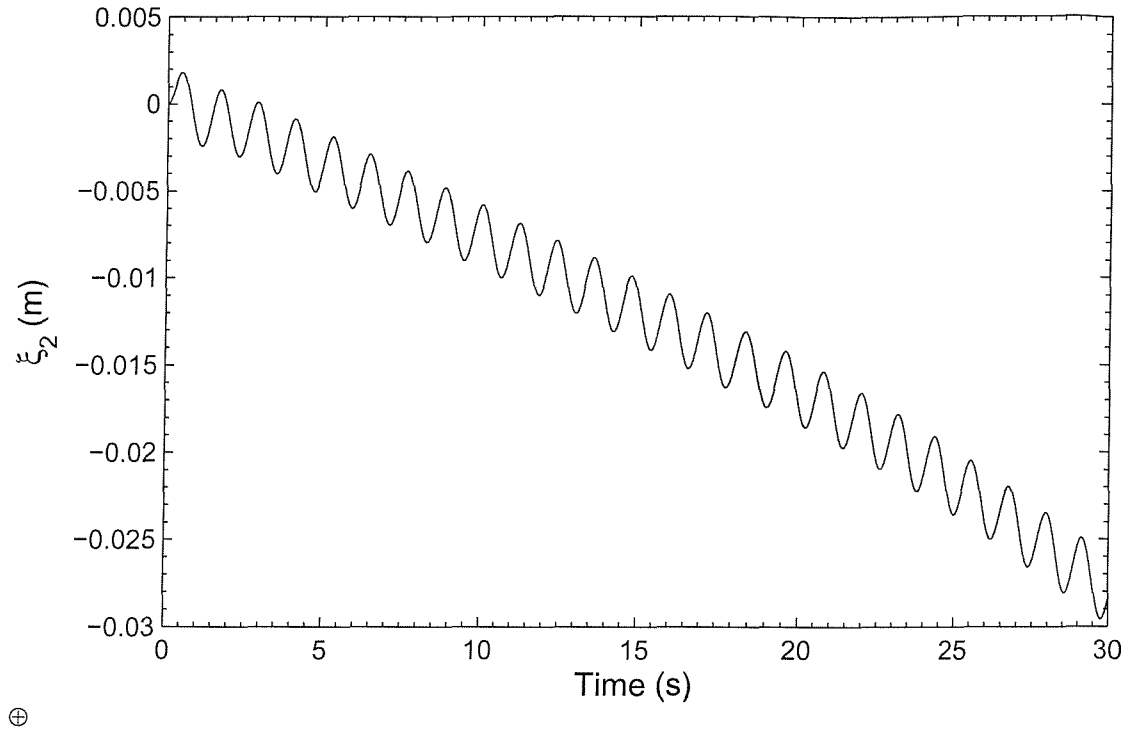

(a) Sway

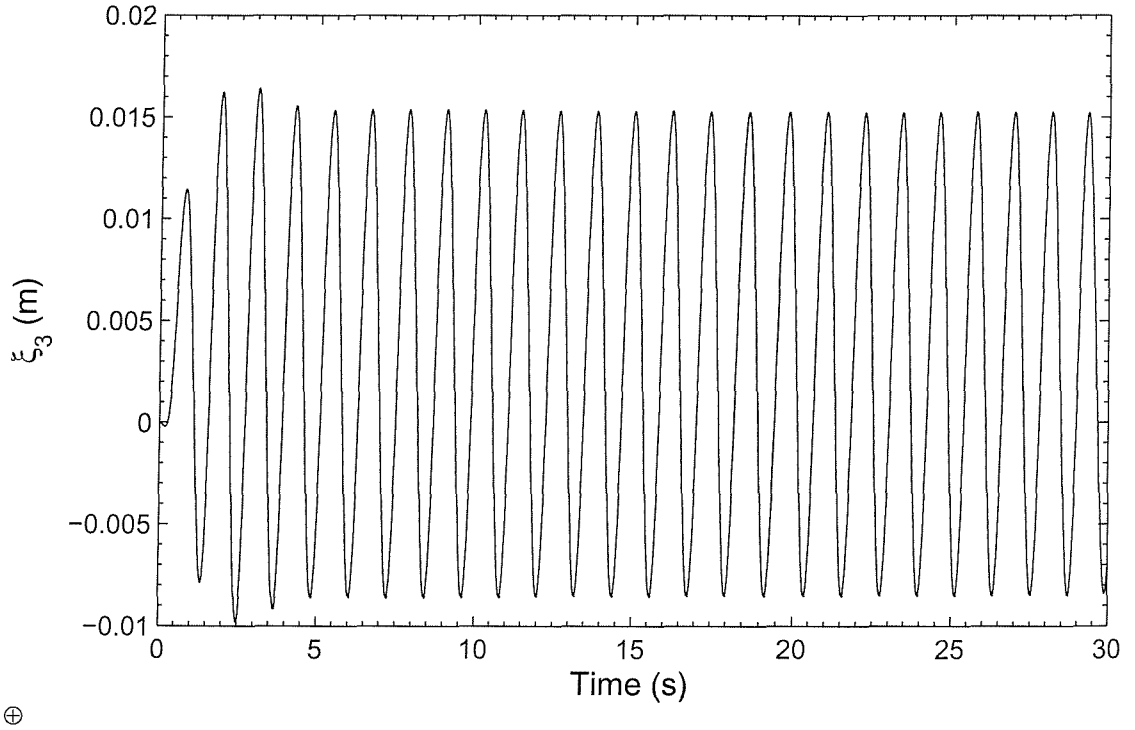

(b) Heave

Figure 5.17: *Motion Histories of a Series 60 ($C_B = 0.7$) Model Travelling with Forward Speed $F_n = 0.2$ in Oblique Waves ($\mu = 135°$, $\omega_0 = 4.0$ rad/s).*

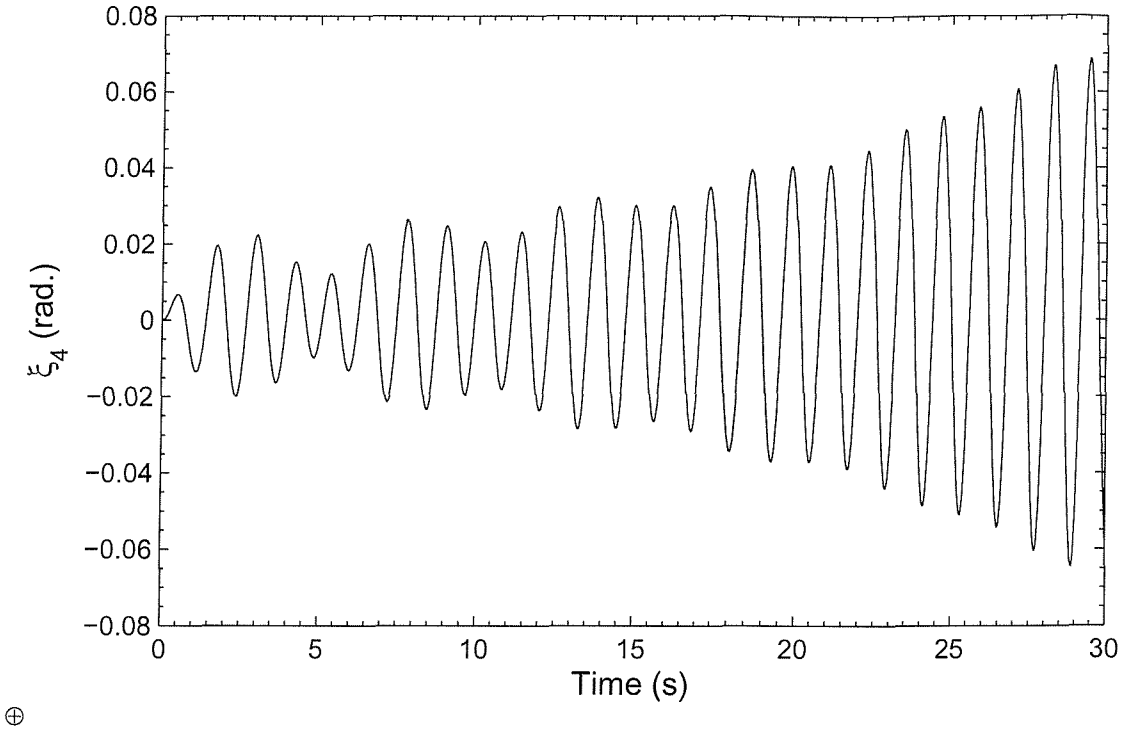

(c) Roll

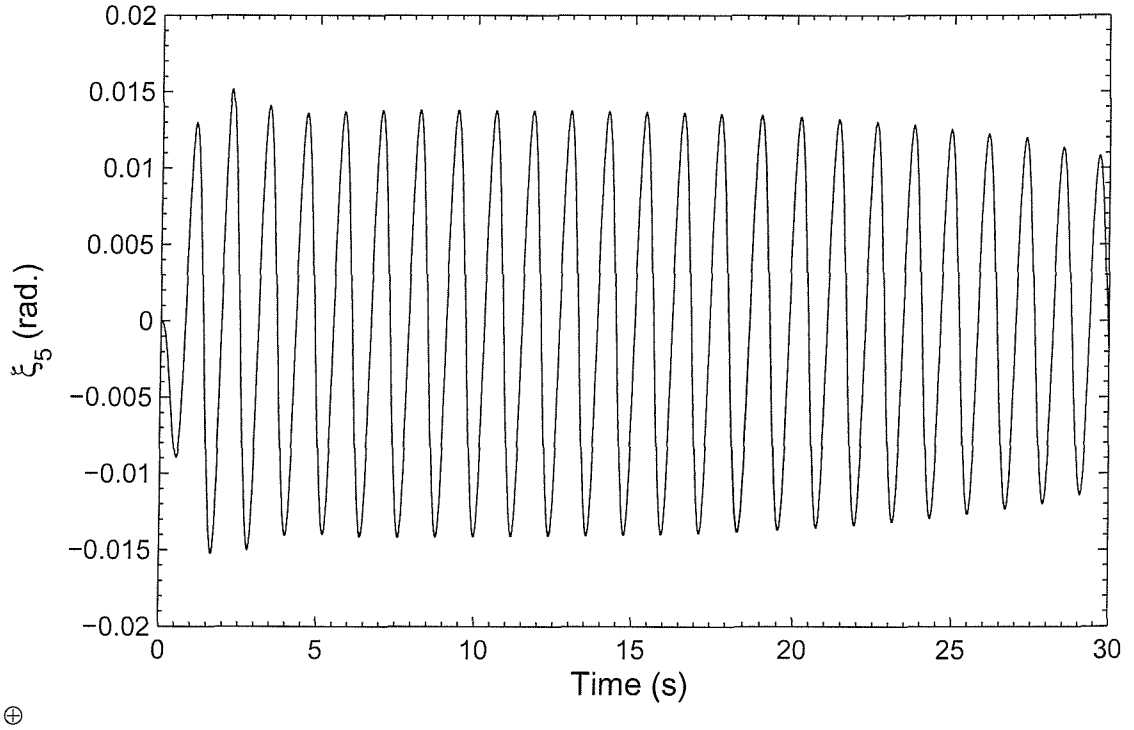

(d) Pitch

Figure 5.17: *Continued.*

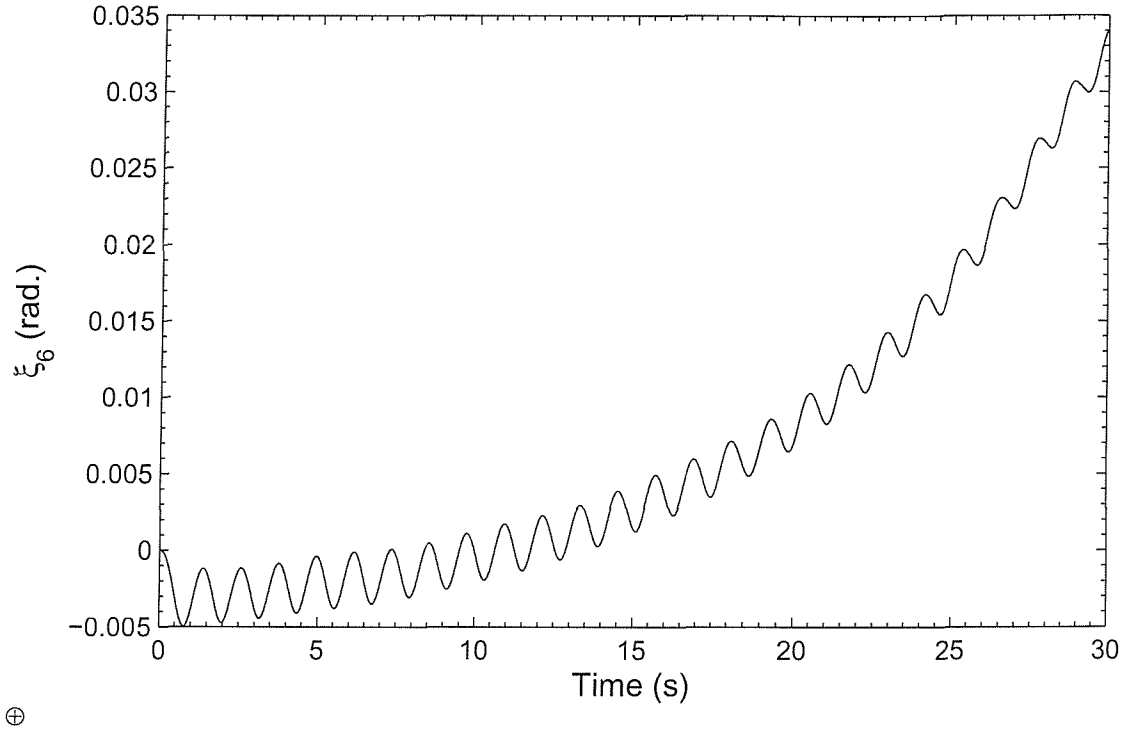

(e) Yaw

Figure 5.17: *Continued.*

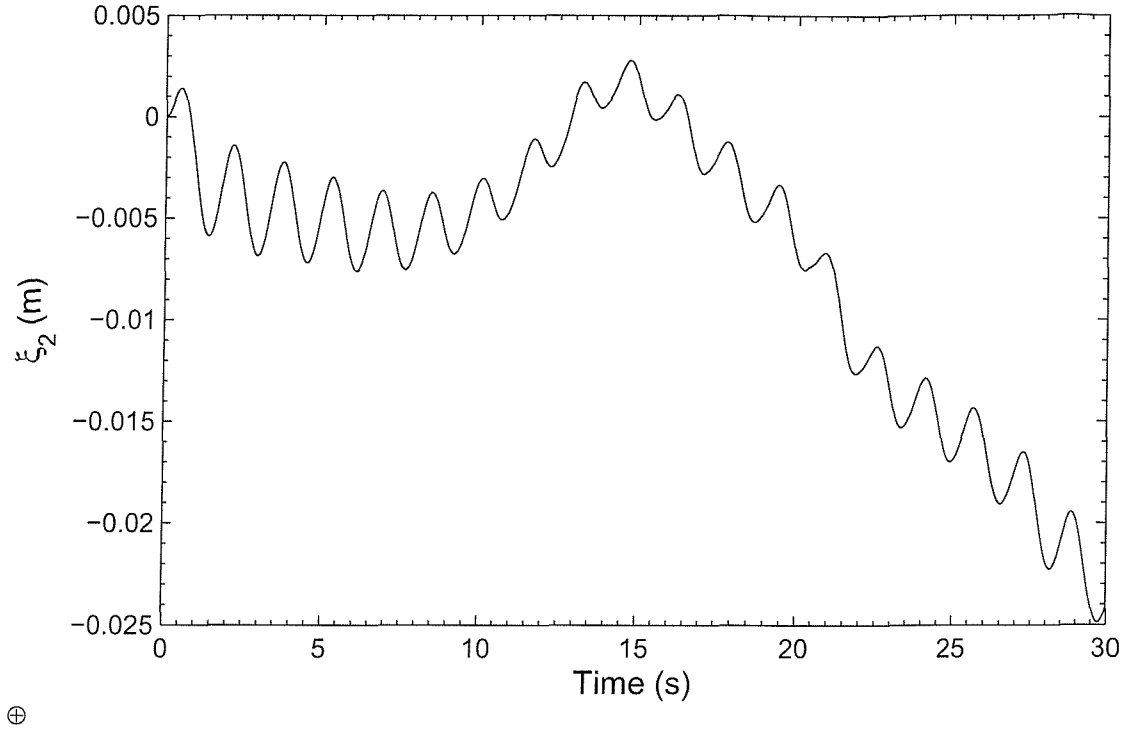

(a) Sway

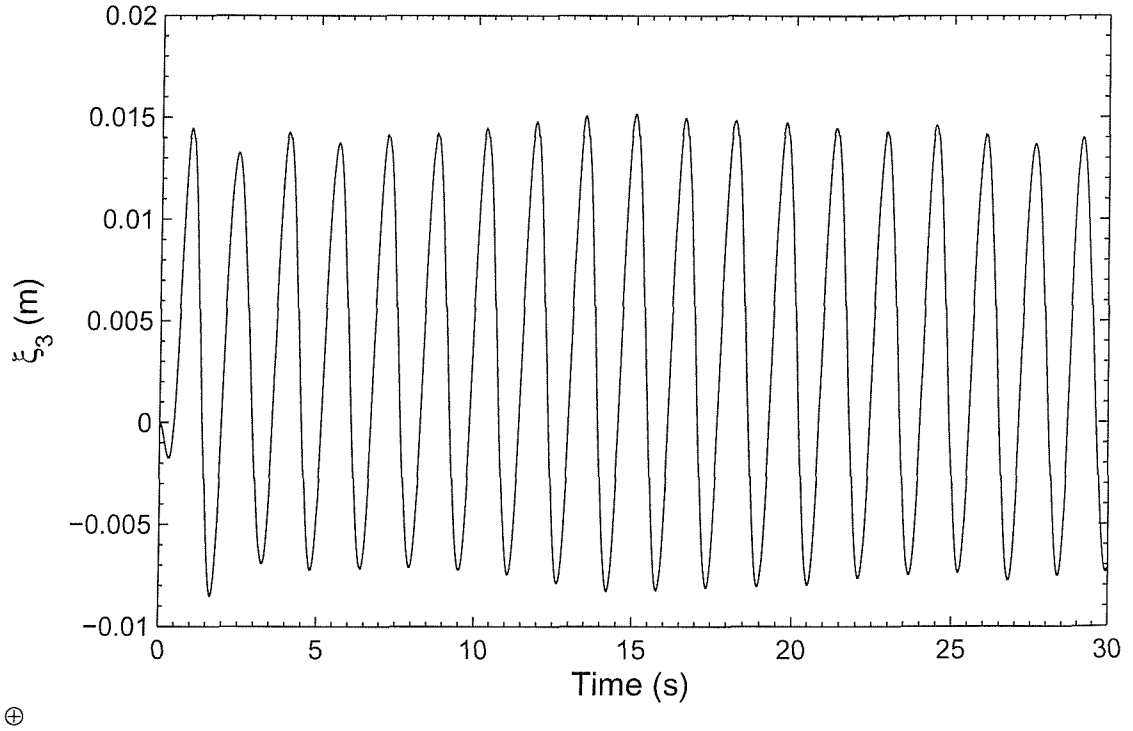

(b) Heave

Figure 5.18: *Motion Histories of a Series 60 ($C_B = 0.7$) Model Travelling with Forward Speed $F_n = 0.2$ in Oblique Waves ($\mu = 90°$, $\omega_0 = 4.0$ rad/s).*

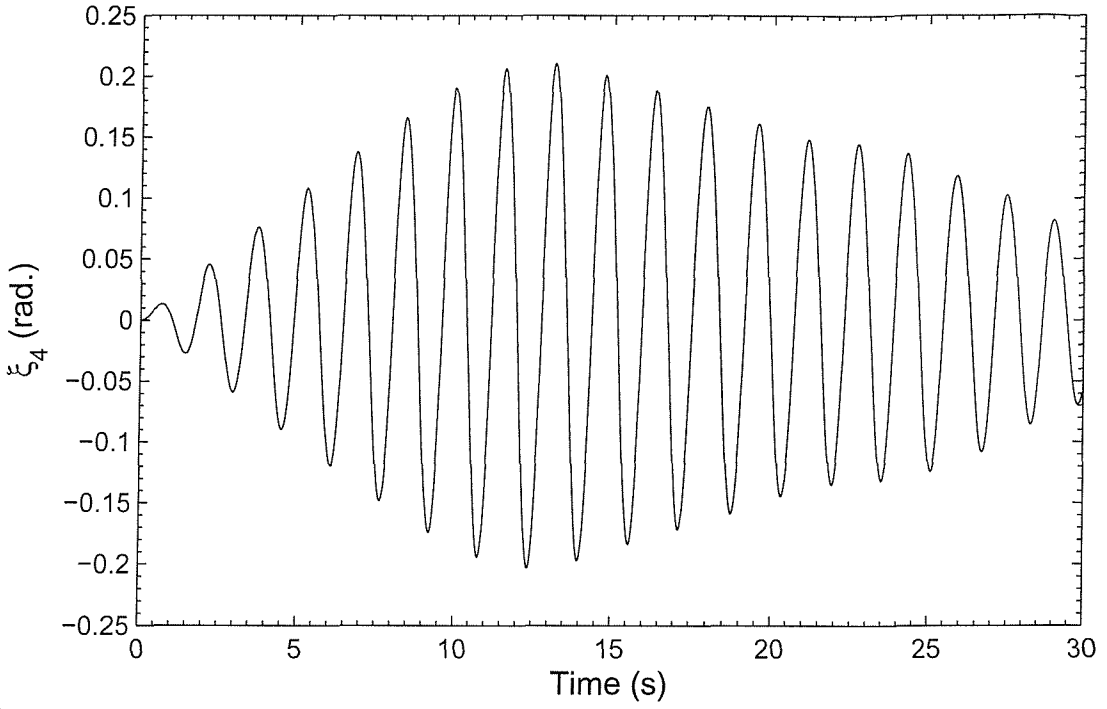

(c) Roll

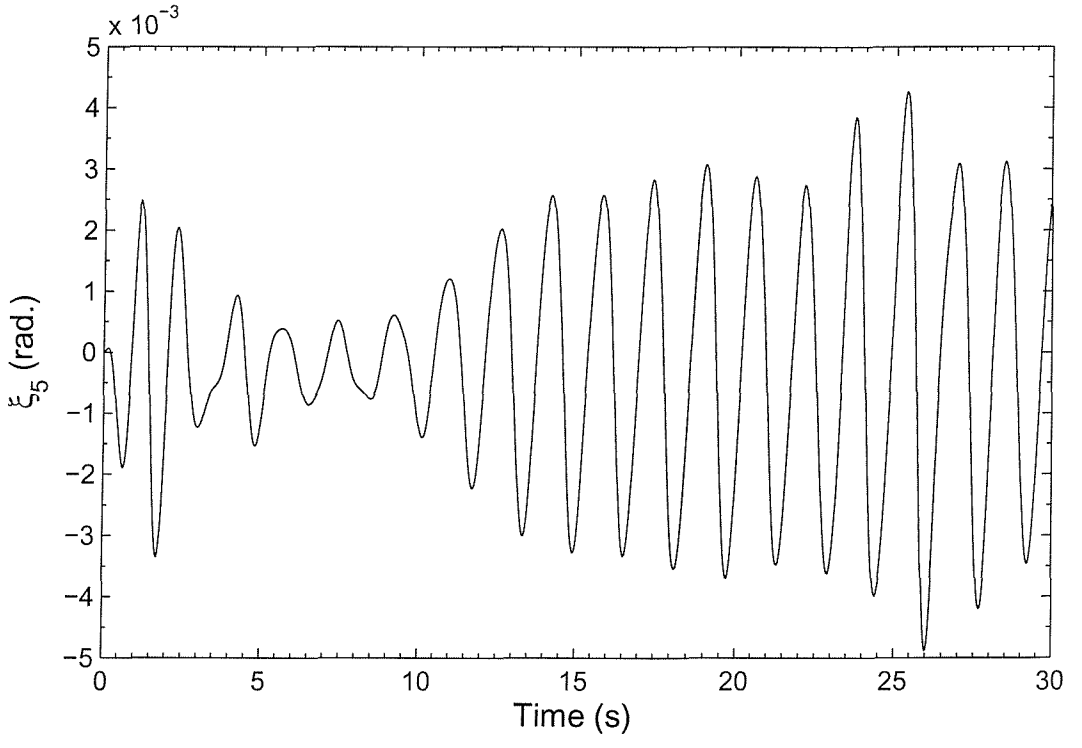

(d) Pitch

Figure 5.18: *Continued.*

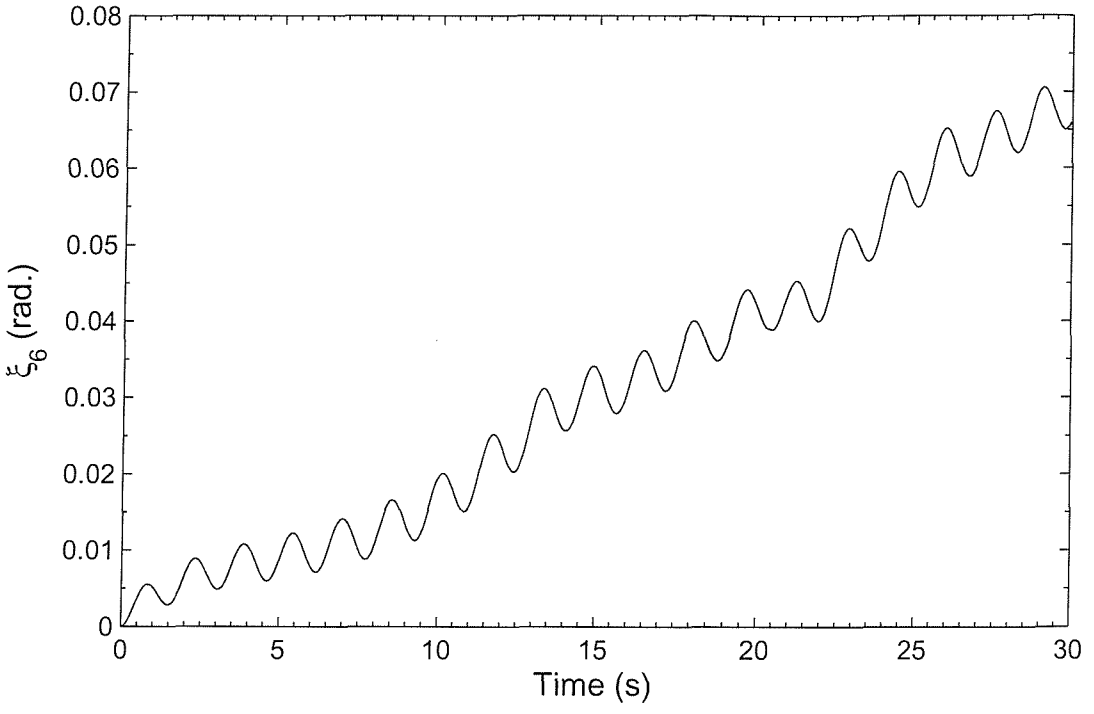

(e) Yaw

Figure 5.18: *Continued.*

Chapter 6

Concluding Remarks

6.1 Summary of Investigation

In this thesis a new time-domain strip theory, based on the traditional strip theory of Salvesen, Tuck and Faltinsen [56], is developed. The so-called body-exact approach is used. This body-exact approach is similar, but not entirely the same, as those previously seen in three-dimensional seakeeping computation methods. The free-surface boundary condition is still linearised about the undisturbed fluid flow, while the body boundary condition is applied on the instantaneous submerged hull surface. This new method not only captures certain non-linearities associated with the body boundary condition, but also retains numerical simplicity compared with the three-dimensional methods. Heave and pitch predicted motions of a Series 60-ship model were presented for regular head waves. Comparison of the new predictions with experimental data and numerical results (produced by other techniques) indicate significant improvements in the low frequency range and at higher forward speeds, *e.g.* $F_n = 0.3$. Predicted motions at different incident wave amplitudes were compared and non-linearities were found in the region of the resonant frequency.

The practical utility of this new time-domain strip theory method must be demonstrated by the validity and accuracy of its prediction. This is the focus of much of the work presented in this thesis. The developed computer program has been verified to demonstrate that the code is "reasonably" bug free and the output is numerically correct. The program has been validated through comparison of the numerical predictions with physical results. Verification and validation are carried out systematically on each of the four key stages of the program, namely:

- Extraction of instantaneous submerged hull surface at each time step,
- Conformal Mapping of sections of various shapes,
- Calculation of two- and three- dimensional hydrodynamic coefficients,
- Predictions of motions in regular head waves.

Accurate extraction of instantaneous submerged hull surface is the basis of all the following computations. Base on the techniques of computational geometry, an efficient and robust algorithm was developed in §4.2. The program was verified extensively to ensure satisfying performance, which were demonstrated in Section §4.2 and Appendix A.

A ship undergoes oscillatory motions of six degrees of freedom during the simulation, which means the wetted sections can vary continuously and assume quite distinct shapes. The degree of geometric variation means that the Lewis mapping is not applicable for computing two-dimensional hydrodynamic coefficients and forces. A multi-parameter conformal mapping method was used to replace the Lewis mapping. The selected Westlake and Wilson [71] conformal mapping technique is able to map sections with asymmetry, but requires further verification and systematic validation. In Section §4.4 this was achieved by extensively investigating the sections of the Series 60 cargo ship with and without heel angle. Numerical instability under certain conditions was identified. Measures

necessary to improve numerical accuracy and reduce instability have been provided. Computational effort was also assessed; guidelines for selecting number of coefficients were suggested.

Section §4.5 continues the validation of the multi-parameter conformal mapping technique by addressing the sensitivity of the numerical methods to the number of mapping parameters and the heel angle. Convergent computations were successfully achieved.

Three-dimensional hydrodynamic coefficients computed by the time-domain strip theory were compared in Section §4.6 with both experimental data and predictions based on a three-dimensional frequency-domain Green function method. Desired accuracy and better performance over the Green function method were demonstrated. Once again the sensitivity of the three-dimensional hydrodynamic coefficient to the number of mapping parameters and the heel angle was addressed. Convergent computations were achieved again, by which the program was validated.

In the last chapter new methods of computing hydrodynamic forces were presented. This provided exciting forces in better agreement with experimental data and three-dimensional results. The Newmark-β direct integration method was used to solve the coupled equations of ship motions. The influence of the integration time step was studied and a preferred step size was recommended. Predictions for pitch motion were extremely good in both head waves and oblique waves. Although the predictions for heave motion were not of the same quality as those for pitch motion, they were still in fairly good agreement with the experimental data and clearly better then those given by three-dimensional frequency-domain Green function method. Non-linearities were found when comparing the predicted motions at different incident wave amplitudes, which evidenced that a portion of important non-linearities was captured by this time-domain strip

theory method.

Finally, motion histories of a Series 60 ship model advancing in an oblique wave were presented. The results were meaningful and incredibly stable except for the expected drifting that occurred in sway and yaw motions.

6.2 Future Developments

Although the results obtained so far are quite encouraging, there are a number of areas needing further research.

Correct extraction of wetted hull surface is crucial for time-domain methods. Present method was designed for ships with transom stern and so lacks generality. By resorting to computer graphic theory, more general algorithms may be able to be developed to accommodate various ship hull forms. However, it might not be considered as seakeeping research.

Diffraction forces need to be validated. Great disparities between the phase angles given by time-domain strip theory and three-dimensional Green function method have to be carefully examined.

The affect of changing the underwater part of the hull surface is not prominent. Non-linearities are only found in the resonant frequency range. This may be due to the incident wave amplitude not being large enough. More computations on other hull forms are needed. For example, the NPL monohull is quite different from the Series 60 hull form.

The predictions of lateral motions in oblique seas are not yet effective. The methods for inhibiting sway and yaw drift need to be developed. Application of a virtual rudder moment might be an effective method. Methods for correcting the roll-damping coefficient in the time domain should be investigated.

In addition, since the eventual objective of this work is to predict the large-amplitude motions of a ship in large seaway, the free surface elevation might not be negligible. The instantaneous wetted surface may have to be extracted relative to the instantaneous free surface instead of the calm water surface.

Appendix A

Intersection of Reference Plane and Ship Hull

In this appendix additional examples are presented to demonstrated the robust performance of the numerical algorithm which computes the intersection of reference plane and ship hull (see §4.2). The original sections are shown as solid lines and the intersections are shown as dashed lines. The hull form chosen to test this algorithm was a frigate, which has already been used by Westlake and Wilson [72]. In order to simplify the calculation, the sections are extrapolated to the maximum depth of the ship, and the phantom offsets above the deck are added.

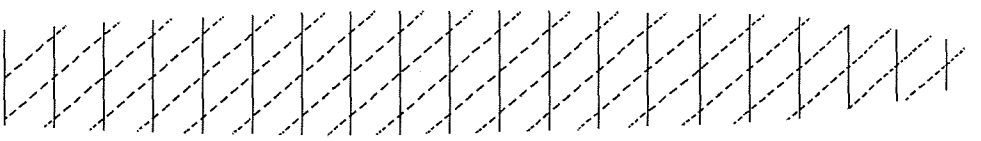

(a) Top View

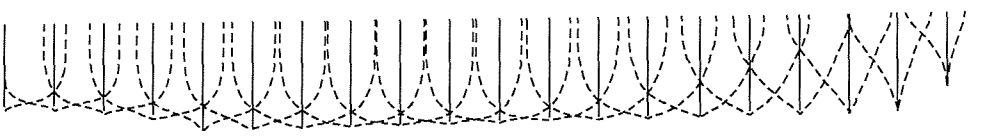

(b) Starboard View

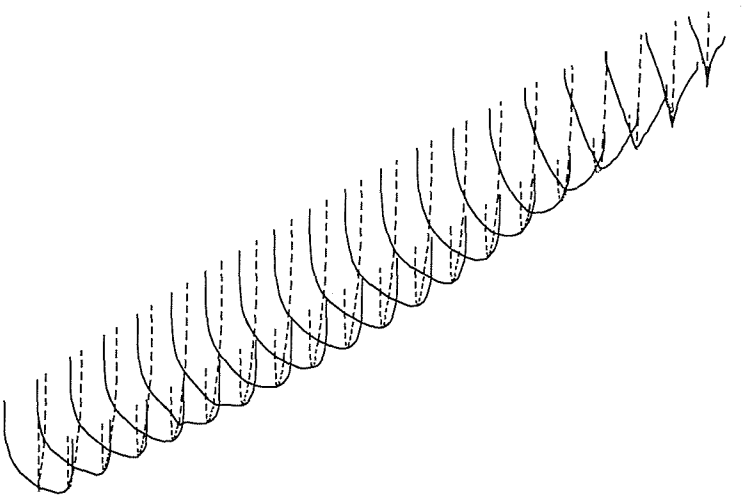

(c) 3D View

Figure A.1: *Intersections of Hull and Reference Planes* ($\xi_5 = 0°, \xi_6 = 50°$)

(a) Top View

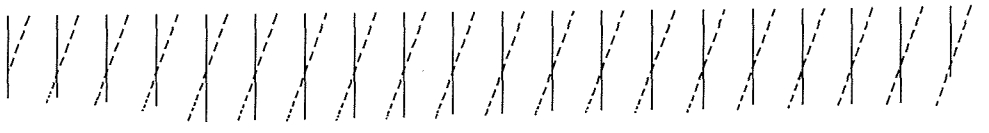

(b) Starboard View

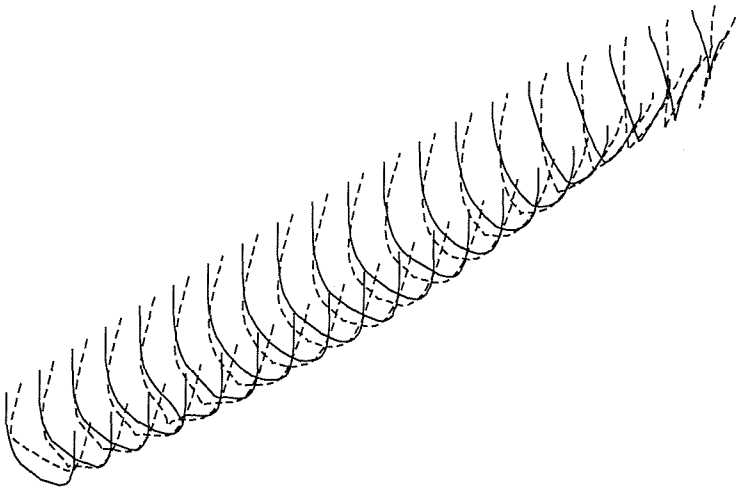

(c) 3D View

Figure A.2: *Intersections of Hull and Reference Planes* ($\xi_5 = 20°, \xi_6 = 0°$)

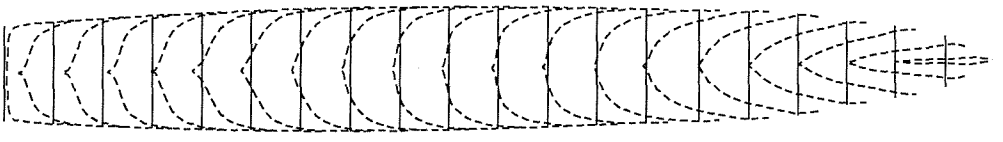

(a) Top View

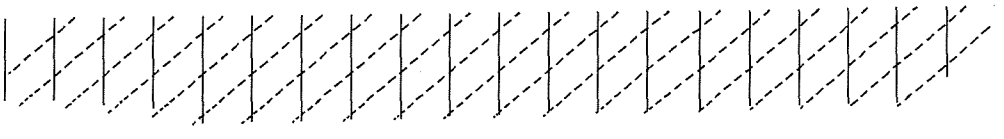

(b) Starboard View

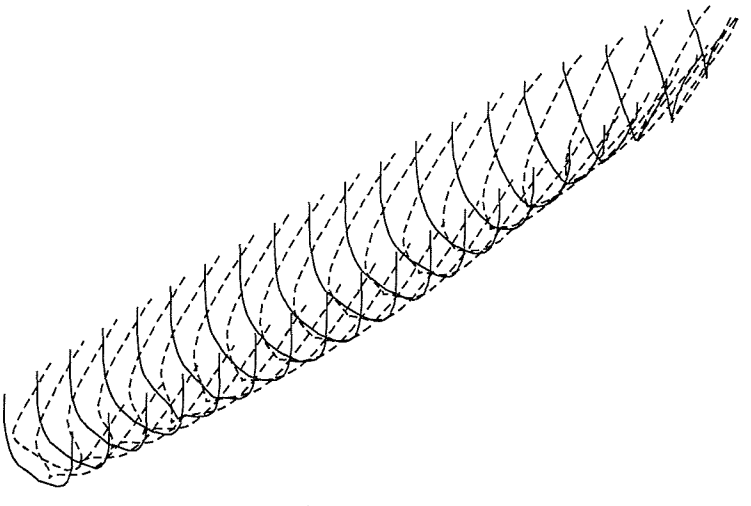

(c) 3D View

Figure A.3: *Intersections of Hull and Reference Planes* ($\xi_5 = 50°, \xi_6 = 0°$)

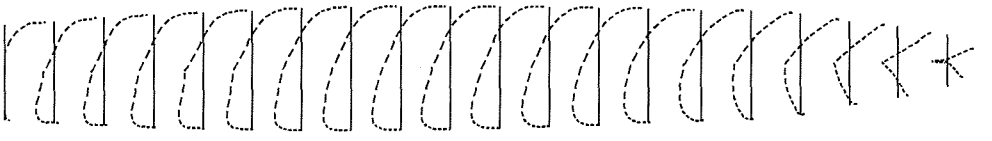

(a) Top View

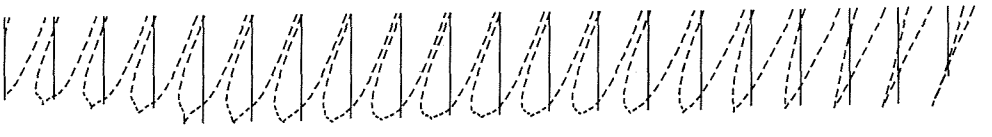

(b) Starboard View

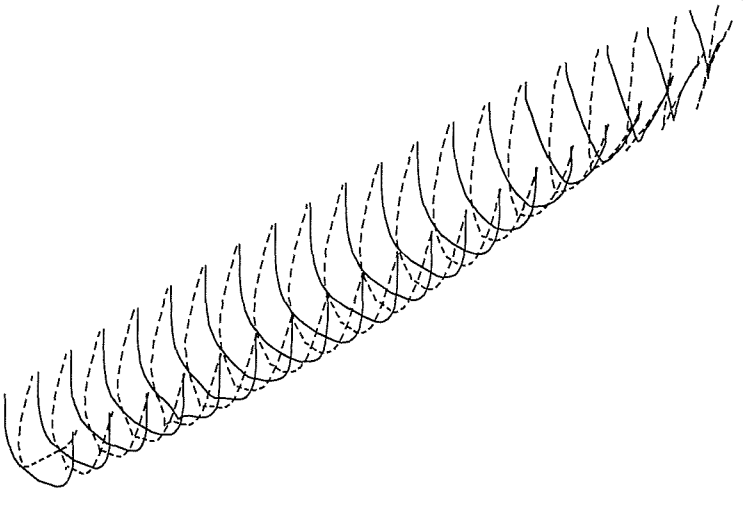

(c) 3D View

Figure A.4: *Intersections of Hull and Reference Planes* ($\xi_5 = 20°, \xi_6 = 20°$)

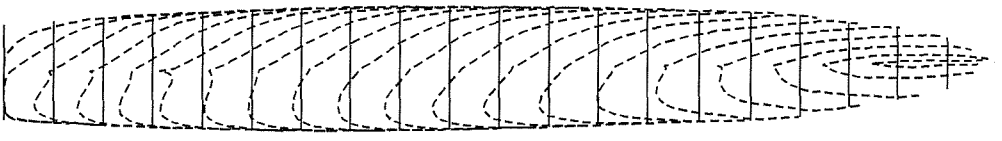

(a) Top View

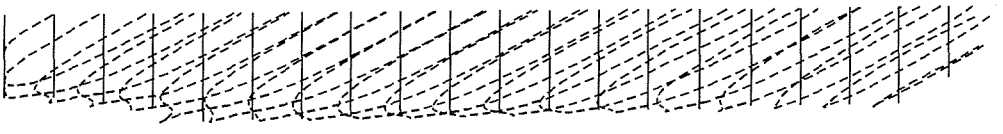

(b) Starboard View

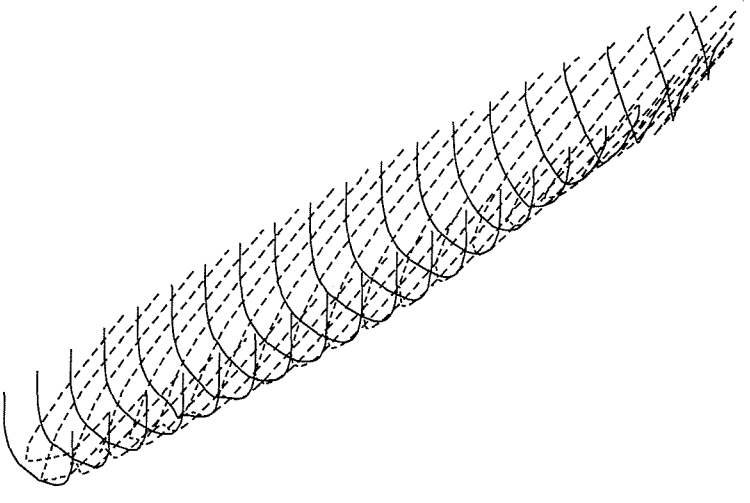

(c) 3D View

Figure A.5: *Intersections of Hull and Reference Planes* ($\xi_5 = 50°, \xi_6 = 50°$)

Appendix B

Geometric Data of the Sections of a Rationalised Series 60 Hull Form

This appendix contains the geometric data (Draught T, Area A and Beam B) of each section of a rationalised series 60 ($C_B = 0.7$) ship model at heel angles $0°$ and $20°$. These data are necessary for computing Lewis mapping coefficients, which in turn act as initial value for computing multi-parameter conformal mapping coefficients (see §4.4).

Section	$\xi_4 = 0°$			$\xi_4 = 20°$		
	B	T	A	B	T	A
1	0.000e+00	0.000e+00	0.000e+00	3.436e-04	2.800e-02	2.901e-07
2	8.604e-02	1.740e-01	1.253e-02	9.365e-02	1.653e-01	1.272e-02
3	1.901e-01	1.740e-01	2.789e-02	2.072e-01	1.740e-01	2.845e-02
4	2.884e-01	1.740e-01	4.334e-02	3.112e-01	1.853e-01	4.430e-02
5	3.596e-01	1.740e-01	5.563e-02	3.840e-01	1.964e-01	5.681e-02
6	3.946e-01	1.740e-01	6.317e-02	4.201e-01	2.066e-01	6.425e-02
7	4.285e-01	1.740e-01	7.051e-02	4.550e-01	2.166e-01	7.142e-02
8	4.306e-01	1.740e-01	7.152e-02	4.577e-01	2.193e-01	7.239e-02
9	4.328e-01	1.740e-01	7.253e-02	4.603e-01	2.221e-01	7.335e-02
10	4.350e-01	1.740e-01	7.353e-02	4.629e-01	2.248e-01	7.431e-02
11	4.350e-01	1.740e-01	7.350e-02	4.629e-01	2.247e-01	7.428e-02
12	4.350e-01	1.740e-01	7.345e-02	4.629e-01	2.245e-01	7.423e-02
13	4.350e-01	1.740e-01	7.266e-02	4.623e-01	2.213e-01	7.345e-02
14	4.349e-01	1.740e-01	7.184e-02	4.617e-01	2.180e-01	7.263e-02
15	4.263e-01	1.740e-01	6.693e-02	4.488e-01	2.092e-01	6.814e-02
16	4.165e-01	1.740e-01	6.179e-02	4.359e-01	2.003e-01	6.338e-02
17	3.796e-01	1.740e-01	5.097e-02	3.977e-01	1.895e-01	5.322e-02
18	3.424e-01	1.740e-01	4.012e-02	3.614e-01	1.787e-01	4.275e-02
19	2.590e-01	1.740e-01	2.537e-02	2.875e-01	1.705e-01	2.773e-02
20	1.576e-01	1.740e-01	1.077e-02	1.902e-01	1.652e-01	1.210e-02
21	6.049e-02	2.800e-02	7.395e-04	7.979e-02	2.800e-02	1.016e-03

Table B.1: *The Series 60 Hull Form Sectional Geometric Data*

Bibliography

[1] P. A. Bailey, W. G. Price, and P. Temarel. A unified mathematical model describing the manoeuvring of a ship travelling in a seaway. *Transactions of the Royal Institution of Naval Architects*, 140:131–149, 1998.

[2] K. J. Bathe and E. L. Wilson. *Numerical Methods in Finite Element Analysis.* Prentice-Hall, Inc., Englewood Cliffs, New Jersey, 1976.

[3] R. Beck and A. Reed. Modern seakeeping computations for ships. In *Proceedings of 23rd Symposium on Naval Hydrodynamics*, pages 1–45, Val de Reuil, France, September 2000.

[4] R. F. Beck and S. Liapis. Transient motions of floating bodies at zero foward speed. *Journal of Ship Research*, 31(3):164–176, 1987.

[5] H. B. Bingham, F. T. Korsmeyer, J. N. Newman, and G. E. Osborne. The simulation of ship motions. In *Proceedings of 6th International Conference on Numerical Ship Hydrodynamics*, pages 561–579, Iowa City, USA, August 1993.

[6] R. E. D. Bishop, W. G. Price, and K. Y. Tam. The representation of hull sections and its effects on estimated hydrodynamic actions and wave responses. *Transactions of the Royal Institution of Naval Architects*, 121:115–126, 1979.

[7] R. E. D. Bishop, W. G. Price, and P. Temarel. Hydrodynamic coefficients of some swaying and rolling cylinders of arbitrary shape. *International Shipbuilding Progress*, 27(307):54–65, 1980.

[8] D. S. Burnett. *Finite Element Analysis.* Addison-Wesley Publishing Company, Reading, Massachusetts, 1976.

[9] M. S. Chang. Computations of three-dimesional ship-motions with forward speed. In *Proceedings of 2nd International Conference on Numerical Ship Hydrodynamics*, pages 124–135, Berkeley, USA, September 1977.

[10] X. B. Chen, L. Diebold, and Y. Doutreleau. New green-function method to predict wave-induced ship motions and loads. In *Proceedings of 23rd Symposium on Naval Hydrodynamics*, pages 66–81, Val de Reuil, France, September 2000.

[11] C. A. L. Conceição, W. G. Price, and P. Temarel. The influence of heel on the hydrodynamic coefficients of ship like sections and a trawler form. *International Shipbuilding Progress*, 31(355):56–66, 1984.

[12] W. E. Cummins. The impulse response function and ship motions. *Schiffstechnik*, 9:101–109, 1962.

[13] C. W. Dawson. A practical computer method for solving ship-wave problems. In *Proceedings of 2nd International Conference on Numerical Ship Hydrodynamics*, pages 30–38, Berkeley, USA, September 1977.

[14] R. Eatock Taylor and C. S. Hu. Multipole expansions for wave diffraction and radiation in deep water. *Ocean Engineering*, 18(3):191–224, 1991.

[15] A. B. Finkelstein. The initial value problem for transient water waves. *Communications on Pure and Applied Mathematics*, 10(4):511–522, 1957.

[16] W. Frank. Oscillation of cylinders in or below the free surface of deep fluids. Technical Report 2375, Naval Ship Research and Development Center, Washington, D.C., 1967.

[17] W. Froude. The rolling of ships. *Transactions of the Institution of Naval Architects*, 2:180–229, 1861.

[18] J. Gerritsma. Shipmotions in longitudinal waves. *International Shipbuilding Progress*, 7(66):49–71, 1960.

[19] J. Gerritsma. Distribution of hydrodynamic forces along the length of a ship model in waves. Technical Report 144, Ship Hydraulics Laboratory, Delft University of Technology, Delft, Netherlands, 1966.

[20] J. Gerritsma and W. Beukelman. The distribution of the hydrodynamic forces on a heaving and pitching ship model in still water. In *Proceedings of 5th Symposium on Naval Hydrodynamics*, pages 219–251, Bergen, Norway, September 1964.

[21] J. Gerritsma and W. Beukelman. Comparison of calculated and measured heaving and pitching motions of a series 60, $c_B = 0.70$ ship model in regular longitudinal waves. In *Proceedings of 11th International Towing Tank Conference*, pages 436–442, Tokyo, Japan, October 1966.

[22] M. D. Haskind. The hydrodynamic theory of ship oscillations in rolling and pitching. In *Technical and Research Bulletin*, No. 1-12, pages 3–43. The Society of Naval Architects and Marine Engineers, New York, 1953.

[23] Y. Huang and P. D. Scalvounos. Nonlinear ship motions. *Journal of Ship Research*, 42(2):120–130, 1998.

[24] D. A. Hudson. *A Validation Study on Mathematical Models of Speed and Frequency Dependence in Seakeeping of High Speed Craft.* PhD thesis, School of Engineering Sciences, University of Southampton, Southampton, United Kingdom, 1999.

[25] R. B. Inglis and W. G. Price. A three dimensional ship motion theory – comparison between theoretical predictions and experiment data of the hydro-

dynamic coefficients with forward speed. *Transactions of the Royal Institution of Naval Architects*, 124:141–157, 1982.

[26] R. B. Inglis and W. G. Price. A three dimensional ship motion theory: Calculation of wave loading and responses with forward speed. *Transactions of the Royal Institution of Naval Architects*, 124:183–192, 1982.

[27] W. P. A. Joosen. Slender body theory for an oscillating ship at forward speed. In *Proceedings of 5th Symposium on Naval Hydrodynamics*, pages 167–183, Bergen, Norway, September 1964.

[28] W. Kaplan. *Advanced Calculus.* Addison-Wesley Press Inc., Cambridge, Massachusetts, 1952.

[29] M. Kashiwagi, A. Mizokami, H. Yasukawa, and Y. Fukushima. Prediction of wave pressure and loads on actual ships by the enhanced unifed theory. In *Proceedings of 23rd Symposium on Naval Hydrodynamics*, pages 368–384, Val de Reuil, France, September 2000.

[30] B. K. King, R. F. Beck, and A. R. Magee. Seakeeping calculations with forward speed using time-domain analysis. In *Proceedings of 17th Symposium on Naval Hydrodynamics*, pages 577–596, Hague, Netherlands, August-September 1988.

[31] B. V. Korvin-Kroukovsky. Investigation of ship motions in regular waves. *Transactions of the Society of Naval Architects and Marine Engineers*, 63:386–435, 1955.

[32] B. V. Korvin-Kroukovsky and W. R. Jacobs. Pitching and heaving motions of a ship in regular waves. *Transactions of the Society of Naval Architects and Marine Engineers*, 65:590–632, 1957.

[33] C. A. Kriloff. A new theory of the pitching motion of ships on waves, and of the stresses produced by this motion. *Transactions of the Institution of Naval*

Architects, 37:326–368, 1896.

[34] D. Kring, Y. F. Huang, P. Sclavounos, T. Vada, and A. Braathen. Nonlinear ship motions and wave-induced loads by a rankine method. In *Proceedings of 21st Symposium on Naval Hydrodynamics*, pages 45–63, Trondheim, Norway, June 1996.

[35] F. M. Lewis. The inertia of water surrounding a vibrating ship. *Transactions of the Society of Naval Architects and Marine Engineers*, 37:1–20, 1929.

[36] W. M. Lin and D. Yue. Numerical solutions for large-amplitude ship motions in the time domain. In *Proceedings of 18th Symposium on Naval Hydrodynamics*, pages 41–66, Ann Arbor, Michigan, August 1990.

[37] A. R. J. M. Lloyd. *Seakeeping: Ship Behaviour in Rough Weather*. Ellis Horwood Ltd., Chichester, Sussex, England, 1989.

[38] J. H. Michell. The wave resistance of a ship. *Philosophical Magazine*, 45:106–123, 1898.

[39] D. Nakos and P. Sclavounos. On steady and unsteady ship wave patterns. *Journal of Fluid Mechanics*, 215:263–288, 1990.

[40] D. Nakos and P. Sclavounos. Ship motions by a three-dimensional rankine panel method. In *Proceedings of 18th Symposium on Naval Hydrodynamics*, pages 21–40, Ann Arbor, Michigan, August 1990.

[41] D. E. Nakos, D. Kring, and P. D. Scalvounos. Rankine panel methods for transient free-surface flows. In *Proceedings of 6th International Conference on Numerical Ship Hydrodynamics*, pages 613–632, Iowa City, USA, August 1993.

[42] J. N. Newman. A linearized theory for the motion of a thin ship in regular waves. *Journal of Ship Research*, 5(1):34–55, 1961.

[43] J. N. Newman. A slender-body theory for ship oscillations in waves. *Journal of Fluid Mechanics*, 18:602–618, 1964.

[44] J. N. Newman. *Marine Hydrodynamics*. The MIT Press, Cambrilge, Massachusetts, 1971.

[45] J. N. Newman. The theory of ship motions. *Advances in Applied Mechanics*, 18:221–283, 1978.

[46] J. N. Newman. Transient axisymmetric motion of a floating cylinder. *Journal of Fluid Mechanics*, 157:17–33, 1985.

[47] J. N. Newman and P. Sclavounos. The unified theory of ship motions. In *Proceedings of 13th Symposium on Naval Hydrodynamics*, pages 373–394, Tokyo, October 1980.

[48] J. N. Newman and E. O. Tuck. Current progress in the slender body theory for ship motions. In *Proceedings of 5th Symposium on Naval Hydrodynamics*, Bergen, Norway, September 1964.

[49] N. M. Newmark. A method of computation for structural dynamics. *ASCE Journal of Engineering Mechanics*, 85:67–94, 1959.

[50] T. F. Ogilvie. Recent progress toward the understanding and prediction of ship motions. In *Proceedings of 5th Symposium on Naval Hydrodynamics*, pages 3–80, Bergen, Norway, September 1964.

[51] T. F. Ogilvie. Singular-perturbation problems in ship hydrodynamics. *Advances in Applied Mechanics*, 17:91–188, 1977.

[52] T. F. Ogilvie and E. O. Tuck. A rational strip theory of ship motions: Part 1. Technical Report 013, Department of Naval Architecture and Marine Engineering, University of Michigan, Ann Arbor, Michigan, 1969.

[53] J. Pawlowski. A nonlinear theory of ship motion in waves. In *Proceedings of 19th Symposium on Naval Hydrodynamics*, pages 33–58, Seoul, Korea, August 1992.

[54] A. S. Peters and J. J. Stoker. The motions of a ship, as a floating rigid body, in a seaway. *Communications on Pure and Applied Mathematics*, 10(3):399–490, 1957.

[55] W. R. Porter. Pressure distributions, added-mass and damping coefficients for cylinders oscillating in a free surface. Technical Report Ser. 82 Issue 16, Institute of Engineering Research, University of California, Berkeley, 1960.

[56] N. Salvesen, E. O. Tuck, and O. Faltinsen. Ship motions and sea loads. *Transactions of the Society of Naval Architects and Marine Engineers*, 78:250–287, 1970.

[57] P. D. Sclavounos. The diffraction of free-surface waves by a slender ship. *Journal of Ship Research*, 28(1):29–47, 1984.

[58] P. D. Sclavounos, D. C. Kring, Y. Huang, D. A. Mantzaris, S. kim, and Y. Kim. A computational method as an advanced tool of ship hydrodynamic design. *Transactions of the Society of Naval Architects and Marine Engineers*, 105:375–397, 1997.

[59] P. D. Sclavounos and D. E. Nakos. Stability analysis of panel methods for free surface flows with forward speed. In *Proceedings of 17th Symposium on Naval Hydrodynamics*, Hague, Netherlands, August-September 1988.

[60] M. St. Denis and W. J. Pierson. On the motions of ships in confused seas. *Transactions of the Society of Naval Architects and Marine Engineers*, 61:280–357, 1953.

[61] J. J. Stoker. *Water Waves.* Interscience Publishers Inc., New York, 1957.

[62] F. Tasai. On the damping force and added mass of ships heaving and pitching. Technical Report 8, Research Institute for Applied Mechanics, Kyuchu University, Japan, 1960.

[63] R. Timman and J. N. Newman. The coupled damping coefficients of symmetric ships. *Journal of Ship Research*, 5(4):1–7, 1962.

[64] F. H. Todd. Some further experiments on single-screw merchant ship forms - series 60. *Transactions of the Society of Naval Architects and Marine Engineers*, 61:516–589, 1953.

[65] F. Ursell. On the heaving motion of a circular cylinder on the surface of a fluid. *Quarterly Journal of Mechanics and Applied Mathematics*, 2(2):218–231, 1949.

[66] F. Ursell. On the rolling motion of cylinders in the surface of a fluid. *Quarterly Journal of Mechanics and Applied Mathematics*, 2(3):335–353, 1949.

[67] G. van Leeuwen. The lateral damping and added mass of an oscillating ship model. Technical Report 65S, Netherlands Ship Research Centre TNO, Delft University of Technology, Delft, Netherlands, 1964.

[68] J. H. Vugts. The hydrodynamic forces and ship motions in oblique waves. Technical Report 150S, Netherlands Ship Research Centre TNO, Delft University of Technology, Delft, Netherlands, 1971.

[69] J. V. Wehausen. The motion of floating bodies. *Annual Review of Fluid Mechanics*, 3:237–268, 1971.

[70] J. V. Wehausen and E. V. Laitone. Surface waves. In *Encyclopaedia of Physics*, volume IX. Springer-Verlag, Berlin, 1960.

[71] P. C. Westlake and P. A. Wilson. A new conformal mapping technique for ship sections. *International Shipbuilding Progress*, 47(449):5–22, 2000.

[72] P. C. Westlake, P. A. Wilson, and P. A. Bailey. Time domain simulation of ship motions. *Transactions of the Royal Institution of Naval Architects*, 142:57–76, 2000.

[73] G. X. Wu and R. Eatock Taylor. The numerical solution of the motions of a ship advancing in waves. In *Proceedings of 5th International Conference on Numerical Ship Hydrodynamics*, pages 529–538, Hiroshima, Japan, September 1989.

[74] R. W. Yeung. The transient heaving motion of floating cylinders. *Journal of Engineering Mathematics*, 16(2):97–119, 1982.